

# Mesoporous Metal-oxides for Dye Sensitized Solar Cells and Photocatalysts

Xiong, Yuli

*Award date:*
2013

*Awarding institution:*
University of Bath

# Mesoporous Metal-oxides for Dye Sensitized Solar Cells and Photocatalysts

Yuli Xiong

A thesis submitted for the degree of Doctor of Philosophy

University of Bath
Department of Chemistry

August 2013

# Acknowledgements

Foremost I would like to thank my supervisor Dr. Karen Edler for her enthusiastic and consistent support throughout the application process prior to my arrival in the UK and for continued support and supervision that has been invaluable during the PhD. Along with Karen, I would like to thank my second supervisor Dr. Petra Cameron for her support and the regular reminders to always try and look at other perspectives.

I would also like to thank all the members of the Edler and Cameron's group, past and present, who have helped me learn new experimental methods and develop my theoretical understanding over the past three years. Particular thanks go to Thomas Risbridger and Robben Jaber for their help when I started.

The financial supports, for fees and subsistence, were generously provided by the Overseas Research Student Scholarship from University of Bath and China Scholarship Council. I am deeply grateful for their assistances, without which I would have been unable to undertake postgraduate research in the UK. Furthermore, I would like to both acknowledge the ISIS and Diamond research facilities, and the beamline scientists employed therein.

Personally, I would like to thank my friends and family both in China and in UK. Such support has made relocation half a world away much easier to adjust. Particular thanks go to my mother, Yunliang Zhao, and sister, Ting Xiong, who have been of great importance in helping me stay focused during the times of my research, and my boyfriend, Dr. Daping He, for his help and care in both life and experiments.

Last, but by no means least, I would like to thank my father, Weiquan Xiong, for his patience, care, motivation, love and encouragement in the past to make me a very happy person. God bless him with happiness in heaven.

# Table of Content

**Abbreviations** ..... **1**

**Abstract** ..... **3**

**Chapter 1 Introduction** ..... **5**

**1.1 Mesoporous Titania** ..... **7**

1.1.1 Soft template method ..... 8
1.1.2 Nanocasting method ..... 10
1.1.3 Combined soft and hard template method ..... 10
1.1.4 Template free method ..... 11
1.1.5 Removal of organic components ..... 12

**1.2 Dye sensitized solar cells** ..... **12**

1.2.1 Structure and theory of DSSC ..... 14
*1.2.1.1 Structure of DSSC ..... 14*
*1.2.1.2 Electron-transfer processes ..... 15*
*1.2.1.3 Efficiency parameters ..... 16*
1.2.2 Strategy to improve efficiency ..... 18
*1.2.2.1 Substrates ..... 18*
*1.2.2.2 Photoelectrode ..... 19*
*1.2.2.3 Dye ..... 20*
*1.2.2.4 Electrolyte ..... 21*
*1.2.2.5 Counter electrode ..... 21*
*1.2.2.6 Post treatment and morphology modification ..... 22*
1.2.3 $TiO_2$ photoelectrodes in DSSC ..... 23
*1.2.3.1 $TiO_2$ photoelectrode prepared by doctor blading and screen printing ..... 24*
*1.2.3.2 $TiO_2$ photoelectrodes prepared by dip and spin coating ..... 30*
*1.2.3.3 1D $TiO_2$ nanoarrays as photoelectrodes ..... 32*

**1.3 Titania photocatalysts** ..... **33**

1.3.1 Theory of photocatalysis ..... 34
1.3.2 Titania photocatalysts ..... 35
*1.3.2.1 $TiO_2$ particle photocatalysts ..... 36*
*1.3.2.2 $TiO_2$ film photocatalysts ..... 38*
1.3.3 Doping of titania as visible-light photocatalyst ..... 39
*1.3.3.1 Theory of $TiO_2$ doping ..... 40*
*1.3.3.2 Metal-doped $TiO_2$ ..... 41*
*1.3.3.3 Nonmetal-doped $TiO_2$ ..... 42*

**1.4 Summary** ..... **43**

**Chapter 2 Analysis Theory and Experimental** ..... **46**

**2.1 Analysis Theory** ..... **46**

2.1.1 X-ray Scattering ..... 46
*2.1.1.1 Theory ..... 46*

*2.1.1.2 WAXS & SAXS* ..... *49*
*2.1.1.3 GISAXS & X-ray Reflectivity* ..... *52*
*2.1.1.4 Measurement* ..... *56*
2.1.2 Neutron reflectivity ..... 58
*2.1.2.1 Theory* ..... *58*
*2.1.2.2 Measurement* ..... *59*
2.1.3 Spectroscopic ellipsometry analysis ..... 59
*2.1.3.1 Theory* ..... *59*
*2.1.3.2 Measurement* ..... *62*
2.1.4 Dynamic light scattering ..... 63
*2.1.4.2 Theory* ..... *63*
*2.1.4.2 Measurement* ..... *66*
2.1.5 UV-Vis spectroscopy ..... 66
*2.1.5.1 Theory* ..... *66*
*2.1.5.2 Measurement* ..... *69*
2.1.6 Electron Microscopy ..... 69
*2.1.6.1 Theory* ..... *69*
*2.1.6.2 SEM & TEM* ..... *71*
*2.1.6.3 Measurement* ..... *74*
2.1.7 Atomic force microscopy ..... 75
*2.1.7.1 Theory* ..... *75*
*2.1.7.2 Measurement* ..... *76*
2.1.8 $N_2$ adsorption and desorption ..... 77
*2.1.8.1 Theory* ..... *77*
*2.1.8.2 Measurement* ..... *81*
2.1.9 TGA & DSC ..... 82
*2.1.9.1 Theory* ..... *82*
*2.1.9.2 Measurement* ..... *83*
2.1.10 Solar cell characterization ..... 83
*2.1.10.1 I-V curve* ..... *83*
*2.1.10.2 IPCE* ..... *84*
*2.1.10.3 Measurement* ..... *85*
**2.2 Experimental ..... 85**
2.2.1 Chemicals and apparatus ..... 85
2.2.2 Substrate cleaning and blocking-layer preparation ..... 88
2.2.3 Fabrication of DSSCs ..... 88
**Chapter 3 Results and Discussion ..... 90**
**3.1 Meso-$TiO_2$ powder made from water-ethanol solution ..... 90**
3.1.1 Experimental ..... 91
3.1.2 Results and discussion ..... 92
*3.1.2.1 SAXS* ..... *92*
*3.1.2.2 TGA* ..... *93*
*3.1.2.3 XRD* ..... *94*
*3.1.2.4 $N_2$ adsorption and desorption* ..... *95*
3.1.3 Conclusion ..... 96
**3.2 Ordered meso-$TiO_2$ thin films by dip coating from aqueous solution ..... 97**

3.2.1 Experimental ..... 98
3.2.2 Results and discussion ..... 98
*3.2.2.1 SAXS & GISAXS ..... 98*
*3.2.2.2 AFM ..... 100*
*3.2.2.3 Ellipsometry measurements ..... 101*
3.2.3 Conclusion ..... 102
**3.3 ZnO films self-assembled at air-liquid interface ..... 102**
3.3.1 Experiments ..... 103
3.3.2 Results and Discussion ..... 104
*3.3.2.1 TGA & DSC ..... 104*
*3.3.2.2 XRD ..... 105*
*3.3.2.3 FESEM & EDS ..... 106*
*3.3.2.4 TEM ..... 107*
*3.3.2.5 $N_2$ adsorption isotherm ..... 108*
*3.3.2.6 Mechanism for film formation ..... 109*
3.3.3 Conclusion ..... 110
**Chapter 4 Ordered Mesoporous Titania and Nanoparticle Composite Films prepared by doctor-blading for DSSC ..... 112**
**4.1 Experimental ..... 112**
**4.2 Results and Discussion ..... 115**
4.2.1 Ordered meso-$TiO_2$ powder ..... 115
*4.2.1.1 SAXS ..... 115*
*4.2.1.2 XRD ..... 116*
*4.2.1.3 TEM ..... 116*
*4.2.1.4 $N_2$ adsorption and desorption ..... 117*
*4.2.1.5 TGA ..... 118*
4.2.2 Ordered meso-$TiO_2$ and nanoparticle composite films ..... 119
*4.2.2.1 XRD ..... 119*
*4.2.2.2 SEM ..... 120*
*4.2.2.3 AFM ..... 122*
*4.2.2.4 $N_2$ adsorption and desorption ..... 124*
*4.2.2.5 Reflection spectra ..... 126*
4.2.3 Ordered meso-$TiO_2$ and nanoparticle composite films in DSSC ..... 127
*4.2.3.1 Optimization of Dye Uptake Time ..... 127*
*4.2.3.2 DSSC based on meso-0 electrodes with various initial layers ..... 127*
*4.2.3.4 DSSC based on meso-$TiO_2$ and nanoparticle composite films ..... 129*
**4.3 Conclusion ..... 131**
**Chapter 5 Ordered S-Doped Meso-$TiO_2$ Thin Film Prepared by Dip-coating for Photocatalyst ..... 133**
**5.1 Experimental ..... 133**
**5.2 Results and Discussion ..... 134**
5.2.1 SAXS and GISAXS ..... 134
5.2.2 XRD ..... 137

5.2.3 TEM ..... 138
5.2.4 FESEM & EDS ..... 141
5.2.5 AFM ..... 142
5.2.6 TGA ..... 143
5.2.7 $N_2$ adsorption and desorption ..... 144
5.2.8 Ellipsometry measurement ..... 145
5.2.9 UV-Vis transmission and absorbance ..... 146
5.2.10 Water contact angle ..... 146
5.2.11 Photocatalytic activity ..... 147
**5.3 Conclusion ..... 149**

**Chapter 6 S-Doped Mesoporous $TiO_2$ Films Prepared by Dip-coating for DSSC ..... 151**

**6.1 Experimental ..... 151**

**6.2 Results and Discussion ..... 152**

6.2.1 The effects of "filling pore" process ..... 152
*6.2.1.1 GISAXS ..... 152*
*6.2.1.2 TEM ..... 153*
*6.2.1.3 AFM ..... 154*
*6.2.1.4 Ellipsometry measurement ..... 155*
6.2.2 S-Doped Meso-$TiO_2$ Multilayer Films for DSSC ..... 156
*6.2.2.1 GISAXS ..... 156*
*6.2.2.2 Film thickness ..... 158*
*6.2.2.3 AFM ..... 158*
*6.2.2.4 UV-Vis absorbance ..... 161*
*6.2.2.5 $N_2$ adsorption and desorption ..... 162*
*6.2.2.6 IV and IPCE ..... 163*
**6.3 Conclusion ..... 164**

**Chapter 7 Meso-$TiO_2$ and Nanowire Composite Films Self-assembled at Air-Water Interface for DSSC ..... 167**

**7.1 Experimental ..... 167**

7.1.1 Free-standing surfactant/$TiO_2$ films from titania precursor ..... 167
7.1.2 Free-standing titania films from titania colloidal solutions ..... 168
7.1.3 Free-standing titania films for DSSC ..... 169
**7.2 Results and Discussion ..... 170**

7.2.1 Free-standing $TiO_2$/surfactant films from titania precursor ..... 170
*7.2.1.1 Neutron reflectivity of interfacial films ..... 170*
*7.2.1.2 TGA of dried film ..... 175*
7.2.2 Free-standing titania films from titania colloidal solution ..... 176
*7.2.2.1 Titania seed solution ..... 176*
*7.2.2.2 Morphology ..... 177*
*7.2.2.3 TGA ..... 178*
*7.2.2.4 XRD ..... 179*
*7.2.2.5 TEM ..... 180*
*7.2.2.6 $N_2$ adsorption and desorption ..... 181*
*7.2.2.7 Mechanism for film formation ..... 183*

7.2.3 Free-standing titania films in DSSCs ..... 184
**7.3 Conclusion ..... 186**
**Chapter 8 Conclusion and Future Work ..... 189**
**8.1 Meso-$TiO_2$ powder made from water-ethanol solution ..... 189**
**8.2 Ordered mesoporous titania and nanoparticle composite films prepared by doctor-blading for DSSC ..... 189**
**8.3 Ordered meso-$TiO_2$ thin films by dip coating from aqueous solution ..... 190**
**8.4 Ordered S-Doped meso-$TiO_2$ thin film prepared by dip-coating for photocatalyst ..... 191**
**8.5 S-Doped meso-$TiO_2$ films prepared by Dip-coating for DSSC ..... 191**
**8.6 Meso-$TiO_2$ and nanowire composite films self-assembled at air-water interface for DSSC ..... 192**
**8.7 ZnO films self-assembled at air-liquid interface ..... 193**
**8.8 Overall summary ..... 193**
**References ..... 195**

# Abbreviations

| | |
|---|---|
| DSSC | Dye sensitized solar cells |
| CB | Conduction band |
| VB | Valence band |
| 1D | One-dimensional |
| 2D | Two-dimensional |
| CMC | Critical micelle concentration |
| EISA | Evaporation induced self-assembly |
| CASH | Combined assembly of soft and hard template |
| CIGS | Copper-indium-gallium-selenide |
| PV | Photovoltaic |
| TCO | Transparent conducting oxide |
| FTO | Fluorine-doped tin oxide |
| AM | Air mass coefficient |
| IPCE | Incident photon-to-current efficiency |
| $\eta_{global}$ | Global conversion efficiency |
| $J_{sc}$ | Short circuit photocurrent |
| $V_{oc}$ | Open circuit photovoltage |
| FF | Fill factor |
| HOMO | Highest occupied molecular orbit |
| LUMO | Lowest unoccupied molecular orbit |
| XRD | X-ray diffraction |
| WAXS | Wide angle X-ray scattering |
| SAXS | Small-angle X-ray scattering |
| GISAXS | Grazing incident SAXS |
| DLS | Dynamic light scattering |
| SEM | Scanning electron microscopy |
| FESEM | Field-emission SEM |
| TEM | Transmission electron microscopy |
| EDS | Energy dispersive spectroscopy |
| SAED | Selected-area electron diffraction patterns |
| AFM | Atomic force microscope |

| | |
|---|---|
| RMS | Root mean square |
| HRTEM | High resolution TEM |
| BET | Brunauer–Emmett–Teller |
| BJH | Barret-Joyner-Halenda |
| TGA | Thermogravimetric analysis |
| DSC | Differential scanning calorimetry |
| QE | Quantum efficiency |
| EQE | External QE |
| IQE | Internal QE |

# Abstract


## Mesoporous metal-oxides for dye sensitized solar cells and photocatalysts

The development of mesoporous titania (meso-$TiO_2$) films is a considerable research goal in the field of mesoporous material development due to their proven applicability in solar cells and phtocatalysts. In this work, the meso-$TiO_2$ films were fabricated through different methods and these home-made titania structures were applied in DSSCs and photocatalysts.

Meso-$TiO_2$ powders were first prepared from ethanol/water or ethanol solvent. The meso-$TiO_2$ made from the ethanol/water solvent did not have an ordered mesostructure, but that made from ethanol solvent had 2D-hexagonal mesostructure. Films were prepared by adding ordered meso-$TiO_2$ particles into paste formulations of P25 nanoparticles with weight proportion ranging from 0 to 100%. These were used to form films by doctor blading, and the influence of paste composition on film structure, morphology, porosity, optical properties and cell performance were investigated.

Secondly, ordered meso-$TiO_2$ films were fabricated by dip coating from aqueous or ethanol solvent. Both films had cubic mesostructures, but the film coated from aqueous solvent was not uniform. The film formed from ethanol solvent was doped with sulphur. The effects of doping on the mesostructure, morphology, structure, optical properties and photocatalytic activity were studied. The thickness of films was increased by repeated coating. The number of layers had an influence on the mesostructure, morphology, optical properties and cell performance when these films were applied in DSSCs

Finally, a novel method was adopted to prepared meso-$TiO_2$ films. Molecular titania precursors or titania colloidal seeds were used as the titania source. Both of them can be used to prepare free-standing hybrid films at air-water interface by a self-assembly method, however the one synthesised from the molecular titania precursor did not contain very much titania and became a powder after calcination. In contrast, after calcination, the films formed from the colloidal titania solution remained intact, and were composed of mixtures of $TiO_2$ nanoparticles

and nanowires with mesopores arising from interparticle porosity. These films were applied in DSSCs. This interfacial method was also successfully extended to prepare free-standing ZnO films from a molecular precursor. After calcination, the free-standing ZnO films were found to be composed of rough spheres formed by flocculation of smaller nanoparticles.

# Chapter 1 Introduction

Metal oxides, such as $TiO_2$, ZnO, $CeO_2$, $ZrO_2$, $Nb_2O_5$, have been extensively studied as photoelectrodes in DSSCs or photocatalysts. Among them, $TiO_2$ and ZnO are the two most widely investigated materials in view of the electronic configuration and recombination probability.[1] The VB of $TiO_2$ is composed primarily of oxygen 2*p* orbitals hybridized with Ti 3*d* states, while the CB is made up of pure 3*d* orbital of titanium, and therefore, the transition probability of electrons to the VB is decreased which ultimately decrease the ($e^-$–$h^+$) recombination probability. In the case of ZnO, which has completely filled 3*d* orbitals, the VB consists of only *d* orbitals and CB consists of hybridized *s*–*p* orbitals. The electronic configuration of ZnO again leads to the reduced ($e^-$–$h^+$) recombination probability.

Titania has three crystalline phases in nature, including rutile ($E_g$=3.05 eV), anatase ($E_g$=3.23 eV), and brookite ($E_g$=3.26 eV). The rutile phase has greater thermodynamic stability although the anatase phase is thermal stable less than 600 °C. The anatase phase has the highest active performance in many applications compared to the other two phases.[2] Moreover, titania is cheap, nontoxic, chemically inert and absorbs only below 388 nm making it invisible to most of the solar spectrum, thus reducing the recombination rate of photoinjected electrons,[3] so it has a wide range of applications, such as photovoltaic devices, photocatalysts, and photochemical-splitting of water. Due to the quantum effects in nanotechnology, the specific surface area and surface-to-volume ratio increase remarkably as the size of materials decreases. Additionally, the movement of electrons and holes in semiconductor nanomaterials and the transport properties related to phonons and phonons are largely affected by the size and geometry of the materials.[4] So, considerable efforts have been devoted to the fabrication of nanosized titania and titania with nanostructures.[5] Compared to titania crystallites, titania with 1D or 2D nanostructure is considered to have some advantages in electronic and photonic devices. Titania with a 1D structure, such as rods, belts and tubes, is well-known for its efficient transport of electrons and excitons,[6, 7] but the low surface area of one-dimensional nanoarrays limits the improvement in many applications and some modifications have been made to improve the

surface area.[8, 9] Titania with a 2D structure, such as ordered mesostructures with high surface area, are another promising material in mesoscopic physics and fabrication of nanoscale devices, as it facilitates reaction/interaction between the devices and the interacting media.

Similarly to $TiO_2$, ZnO has a band gap around 3.3 eV. Also, it is cheap, nontoxic and thermal stable. Different nanostructured ZnO particles, including rods, tubes, spheres and mesoporouss materials, have been synthesized and applied into many areas, such as sensors, piezoelectric transducers, solar cells, photocatalyst and transparent conducting films.[10] However, the stability of ZnO when interacting with acid or base is not as good as titania and this problem is still not overcome.

Titania is normally prepared from the hydrolysis reaction of titanium alkoxides, shown in Figure 1-1. The first step is a substitution of one alkoxy group by hydroxyl group in the hydrolysis reaction. Then, oxo- and hyroxo-bridges are formed in the process of condensation reactions.[11] Both of the reactions are very quick and the relative ratio can be changed by the hydrolysis conditions, such as water/alkoxide ratio, catalyst, reaction temperature, alkyl groups in the alkoxide and chelating addition.[12] [13] Increase of the water/alkoxide ratio and reaction temperature will fasten the hydrolysis process. The hydrolysis of titanium alkoxide in the presence of an acid catalyst shows a slower reaction speed. The alkoxide with higher alkyl groups are slower to hydrolyse and also slower to diffuse, as condensation requires partial hydrolysis and diffusion, higher alkoxide tends to produce smaller condensates which favours the diffusion. So, under the same condition, the reaction speed of $TiCl_4$, $Ti(OCH(CH_3)_2)_4$, $Ti(OCH_2CH_2CH_2CH_3)_4$ is TiCl4 > $Ti(OCH(CH_3)_2)_4$ > $Ti(OCH_2CH_2CH_2CH_3)_4$. After the addition of a chelating complex, the alkoxide precursor is altered to form oligomers, then slower the whole hydrolysis and condensation process, The oligomers can even stabilize in aqueous solution,[13] such as $[CH_3CH(O\text{-})CO_2NH_4]_2Ti(OH)_2$ and $[(CH_3)_2CHO]_2Ti(C_5H_7O_2)_2$.

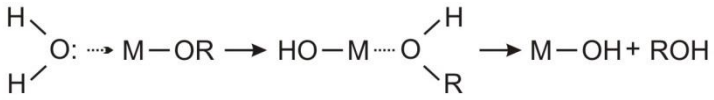

(hydrolysis)

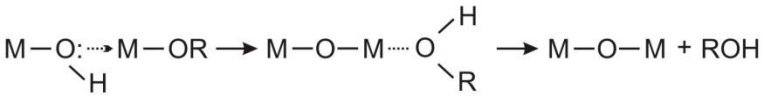

(Alcohol condensation)

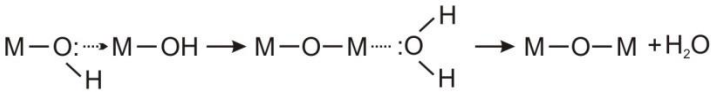

( Water condensation)

**Figure 1-1 Hydrolysis, alcoxidation and oxolation reactions of titanium alkoxides.**

The majority of the work in this thesis is concerned with the fabrication of mesoporous titania films through different methods and application of home-made titania structures in DSSCs and photocatalysts. Thus, chapter 1 gives an introduction to mesoporous titania, describes DSSC and the application of titania in DSSC, and titania photocatalysts. Chapter 2 is about the principles of analysis and how these techniques were used to characterise the materials prepared in the thesis. Chapter 3 is the experimental part, which gives lists of materials and the apparatus used for the experiments. Three small experiments and results that relate to the major projects of this thesis are also shown in chapter 3. Chapter 4 is about the preparation of ordered mesoporous titania and nanoparticle composite films by doctor-blading and their application in DSSC. Chapter 5 is about ordered S-doped mesoporous titania thin films prepared by dip-coating and their application in photocatalysts. Chapter 6 concerns S-doped mesoporous titania multilayer films prepared by dip-coating and their application in DSSC. Chapter 7 reports synthesis of mesoporous titania and nanowire composite films self-assembled at air-water interface and their application in DSSC. The last chapter covers the conclusions of the work done during this PhD and suggests some areas for future work.

## 1.1 Mesoporous Titania

According to the definition of IUPAC,[14] porous solids are classified into three groups based on their pore diameter, namely microporous (< 2 nm), mesoporous (2 - 50 nm), and macroporous (> 50 nm) materials. For microporous materials, the pore size is too small to allow organic molecules with diameter > 2 nm to pass through, while the macroporous materials usually has a low surface area. Mesoporous materials, especially mesoporous titania, have a suitable pore size that allows organic compounds to enter the pores and a high surface area that favours the loading of organic species, which helps the active performance of DSSCs and photocatalyst.[2, 15, 16] When the pores arrange regularly, it shows various mesostructures such as 2D-hexagonal, lamellar, or cubic, presented in Figure 1-2.

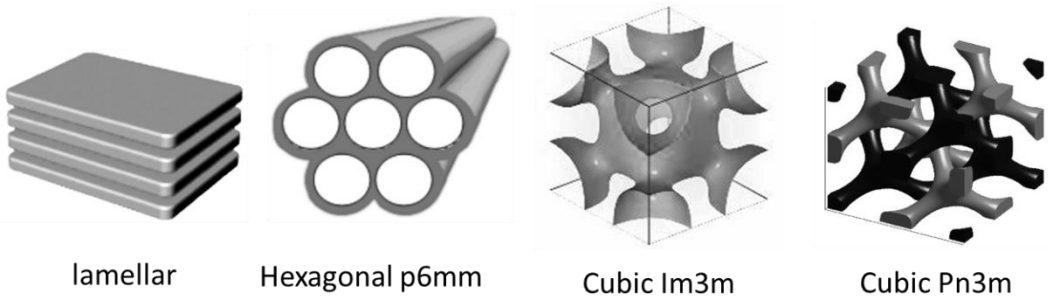


**Figure 1-2 Ordered mesoporous structure.**

Mesoporous titanias have been prepared by various techniques and successfully applied into DSSCs and photocatalysts. Here, we simply define the mesoporous titania into five types according to the method used to obtain pore domains, namely soft template methods, nanocasting methods, combined soft and hard template methods, template free methods and removal of organic compounds methods. For the templating methods, all involves condensation of a titania precursor directed by a template to guide the formation of mesostructure. Then, the templates are removed to obtain open pores by calcination or washing process. The soft-templating method is the most popular templating way due to itss convenience to carry out and the mesostructure and pore size are easy to tune. Some typical examples are described below.

### *1.1.1 Soft template method*

Amphiphilic or surfactant molecules, which display a polar head and non-polar tail, tend to aggregate in solvents where one of these parts is insoluble.

Above the CMC, the amphiphilic molecules form micelles. A combination of molecular geometry and entropic interactions drives the solution to self-assemble into colloidal systems, presenting different packing ordering upon the progressive increase of surfactant concentration.[17] These ordered molecules can be used as a soft template to guide the formation of mesoporous materials.

The soft template method can be easily carried out in water by sol-gel method or in an organic solvent by EISA.[16] The formation of mesostructured materials via EISA method begins with a homogeneous solution of inorganic precursor and surfactant in ethanol/water solvent. The concentration of surfactant is much lower than the CMC. During the evaporation of solvent, the concentration of surfactant increases continuously and drives self-assembly of inorganic-surfactant micelle aggregates when the concentration of surfactant is higher than CMC and their further organization into mesostructured hybrids.[18] The pore domains are formed after the removal of surfactants and the inorganic crystallites form the wall networks. The surfactant in this process serves as the template to guide the formation of mesostructured materials. The EISA approach is now widely used to prepare mesostructured titania films due to the controllable hydrolysis process which is the critical issue of fabrication ordered mesoporous titania.[2, 4] However, the pores can easily collapse during the removal of template by calcination if the inorganic walls are too thin, not sufficiently condensed or undergo a structural change (eg from amorphous to crystalline) during the high temperature calcination step.

Alberius et al. prepared ordered mesostructured titania films by using Pluronic P123 as the template in the EISA method.[19] By varying the volume ratio between the surfactant and inorganic precursor species, titania film with cubic, 2D-hexagonal, and lamellar structure were synthesized. The regions over which the three phases were obtained correspond well with those of the water−block copolymer binary phase diagram when considered in terms of the volume fraction of copolymer incorporated.

Chen et al. fabricated mesoporous anatase titania beads with controlled morphology and physical properties templated by hexadecylamine from a combined sol-gel and solvothermal method.[20] The monodispersity and spherical shape of the beads could be tuned by varying the amount of surfactant in the

sol-gel process. The diameter of the beads could be controlled in the range of 320 - 1150 nm by adjusting the water/ethanol ratio of the solvent. The anatase crystallite size, specific surface area (89 - 120 $m^2/g$), and pore size (14 - 23 nm) were adjusted through the amounts of ammonia, when the precursor beads were treated in ethanol/water solution with the addition of ammonia under 160 °C thermal treatment.

### *1.1.2 Nanocasting method*

In the technique of nanocasting, the titania starting sol is infiltrated into a porous hard template such as alumina membranes, ordered mesoporous silica, or ordered mesoporous carbon.[21] After crystallization by calcination, the template can be removed by calcination in air or treated with alkaline solution. An advantage of this method is that crystalline titania can be intentionally prepared with different mesostructures,[22] but it can be difficult to penetrate the precursor solution into the porous template.

Zhang et al. prepared mesoporous titania by using mesoporous silica KIT-6 as the hard template.[23] They studied the effects of three parameters, precursor/template ratios, calcination temperatures and immersion time in solvent during the process of template removal, on the crystallization of the titania. Owing to the template confinement effect, mesoporous anatase titania with high surface area 207 $m^2/g$ instead of rutile phase was obtained after calcination at 750 °C.

Mokaya et al. fabricated metal oxides (titania, zirconia, alumina and magnesia) templated by hollow spheres of mesoporous carbon.[24] After the removal of the template by calcination, the porous metal oxides showed predominantly hollow sphere morphology with a high surface area. Anatase titania formed after calcination at 500 °C had a specific surface area of 100$m^2/g$ and a mean pore diameter of 6.0 nm.

### *1.1.3 Combined soft and hard template method*

In order to combine the advantages of soft and hard template method, the combined soft and hard template method was adopted.[25-27] A soft template is used to direct the pore structure and the hard template is used to support the nanostructure during calcination process. This is also a good way to make porous titania with a hierarchical structure.[28]

Lee et al. fabricated highly crystalline mesoporous titania templated by CASH method.[29] Firstly, the as-prepared powder templated by poly(isoprene-block-ethyleneoxide) was prepared using the EISA method. Then, samples were calcined at 700 °C under Ar atmosphere and the organic template became carbon as a hard template to support the mesostructure. The carbon was finally removed by calcination at 450 °C in air to obtain well crystallized metal oxides. The as-prepared, carbonized and calcined titania had a 2D-hexagonal mesostructure and the d-spacing shifted from 31.4, to 27.3 to 24.2 nm. The calcined titania had a well-crystallized anatase structure and specific surface area of 89 $m^2/g$ with a big pores of diameter ~ 22.9 nm.

Wang et al. fabricated titania nanotubes with a mesoporous wall from assembly of a soft template and the nanocasting method by filling surfactant templated titania precursor solution into alumina membranes.[30] The specific surface area, pore volume, pore size and crystallite size of mesoporous titania walls could be tuned by variation of the surfactant type in the precursor solution and the template removal approaches. The dimensions of the nanotube could be changed by simply tuning the pore size of the alumina membranes and the viscosity of the starting sol.

### *1.1.4 Template free method*

Mesoporous titania with or without hierarchical structure can also be obtained by a simple template-free approach, but it is difficult to obtain long range ordering for porous materials, as the mesoporous structure is formed because of the voids between particles or aggregations of particles.[31]

Liu et al. synthesized mesoporous titania through nitric acid-catalysed hydrolysis and polycondensation reactions of titanium(IV) *n*-butoxide.[32] The as-prepared amorphous titania had a high specific surface area of 470 $m^2/g$ and a pore volume of 0.28 $cm^3/g$. After calcination at 450 °C for 4 h, anatase mesoporous titania was formed with a specific surface area of 106 $m^2/g$ and an average pore size of 4.8 nm.

Yu et al. prepared bimodal mesoporous titania by a hydrothermal method using tetrabutylorthotitanate as the precursor.[33] The effects of hydrothermal temperature and time on microstructure were investigated. With the increase of hydrothermal temperature and time, the crystallite size and pore size increased

and specific surface areas, pore volumes and porosity steadily decreased. However, after hydrothermal treatment, all samples had two types of pores: one was intra-aggregate pores with pore diameters 4 - 8 nm and the other with inter-aggregate pores with pore diameters 45 - 50 nm.

Li et al. fabricated urchinlike titania hollow spheres with tunable chamber structure through solvothermally reacting $TiOSO_4$ in glycerol, alcohol, and ethyl ether.[34] The morphology, size, and interior structure were controlled by the variation of alcohol solvent and reaction time. They can be tuned from solid (12 h), to sphere-in-sphere (1 day), to hollow core−shell (14 days) structures with reaction time. The outside-sphere diameter grew from 2.0, to 2.4, to 5.2 μm, so could also be tuned by choosing the alcohol solvent.

### *1.1.5 Removal of organic components*

The method of removal of organic components is not a well-defined approach to prepare mesoprous films. The reason why it is included here is because this is the traditional way to make mesoporous titania films for DSSCs. Porous domains are formed by the removal of organic component from a paste of colloidal titania particles with mixtures of organic porogens. This method was firstly used by Grätzel in 1991.[35] They prepared titania colloidal paste first by mixing titania nanoparticles with organics and then made films by the doctor blade method which were calcined to obtain a mesoporous film. DSSC based on these films has a high efficiency as the mesoporous film has a large surface area that can absorb more dye molecules compared to solid films. The details of how to make this type of mesoporous film will be explained later in section 1.2.3.1.

## 1.2 Dye sensitized solar cells

It is clear that access to economically viable renewable energy sources is essential for the development of a globally sustainable society. The mean global energy consumption rate was 13 TW in the year 2000. Assuming a kind of “business-as-usual” circumstance with rather optimistic but reasonable assumptions of population growth and energy consumption, the projection is 28 TW in 2050 for the global energy demand.[36] [37] Solar energy, besides fusion, has the largest potential to satisfy the future global need for renewable energy sources. From the $1.7 \times 10^5$ TW of solar energy that strikes the earth’s surface, a

practical terrestrial global solar potential value is estimated to be about 600 TW.[38] Thus, even if 10% of sunlight could be converted to alternative and usable energy forms, there would be no worry about the energy supply line. PV solar cells are one of the devices that permit direct conversion of sunlight to electricity.

With the huge potential, solar cell production has grown at about 30% per annum over the past 15 years. Based on the nature of the material, maximum conversion efficiency obtainable, and the associated cost of photovoltaic power, Martin Green has classified various photovoltaic solar cells into three major categories, shown in Figure 1-3: first, second and third generation photovoltaics.

Most of the solar cells on the market now are "first generation photovoltaics", made out of the highest purity materials with the least structural defects (such as crystalline silicon) and considered to be a "mature" technology.[39] They are somewhat expensive to produce because of the high processing costs needed to create silicon cells with sufficient purity and long range order.

Second generation devices, for example, multi-crystalline or amorphous Si, CdTe and CIGS, are based on thin film technologies. They are generally deposited from vacuum or by chemical vapour deposition, and include CdTe or CIGS technologies.[40] Their efficiencies and cost are lower, but they can be created in much thinner, light weight formats compared to silicon cells. Disposal at end-of-life is a consideration, because of the toxicity of Cd, Te, Ga, and Se.

DSSCs are referred to as third-generation PV systems, which have excellent potential for DSSC to deliver solar electric power at very low costs. DSSCs are a type of low-cost solar cells belonging to the group of thin film solar cells. They are based on a semiconductor formed between a photo-sensitized anode and an electrolyte, a photoelectrochemical system. This cell, also known as the Grätzel cell, was invented by Grätzel and O'Regan at the École Polytechnique Fédérale de Lausanne in 1991.[35]

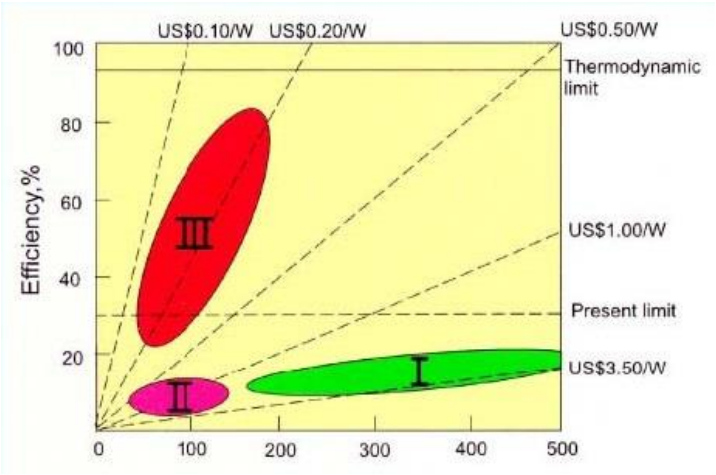


**Figure 1-3 Classification of photovoltaic solar cells.[41] Reprinted with permission from Ref. 41.**

## *1.2.1 Structure and theory of DSSC*

### 1.2.1.1 Structure of DSSC

A typical structure of a DSSC is shown in Figure 1-4. A DSSC is basically a thin-layer solar cell formed by a sandwich arrangement of two TCO electrodes. The mesoporous nanocrystalline titania film electrode is deposited on a TCO substrate and a monolayer of dye is adsorbed onto the titania layer. The counter electrode is composed of platinum film deposited onto another TCO substrate. The inter-layer space is filled with an organic electrolyte containing a redox meditator, usually an iodide/tri-iodide ($I^-/I_3^-$) redox couple.

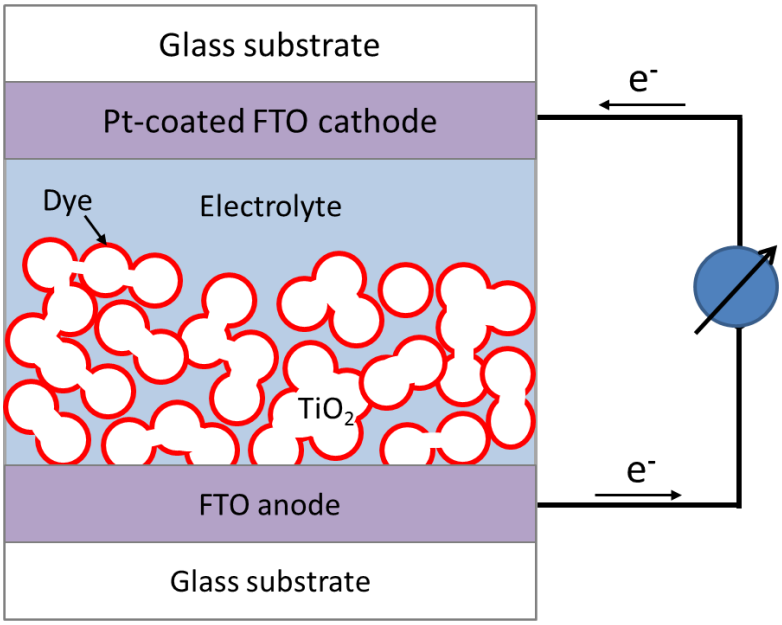


**Figure 1-4 Typical structure of a DSSC.**

### 1.2.1.2 Electron-transfer processes

The mechanism of operation of a DSSC is based on electron-transfer processes. Figure 1-5 shows the electron-transfer processes in a DSSC.

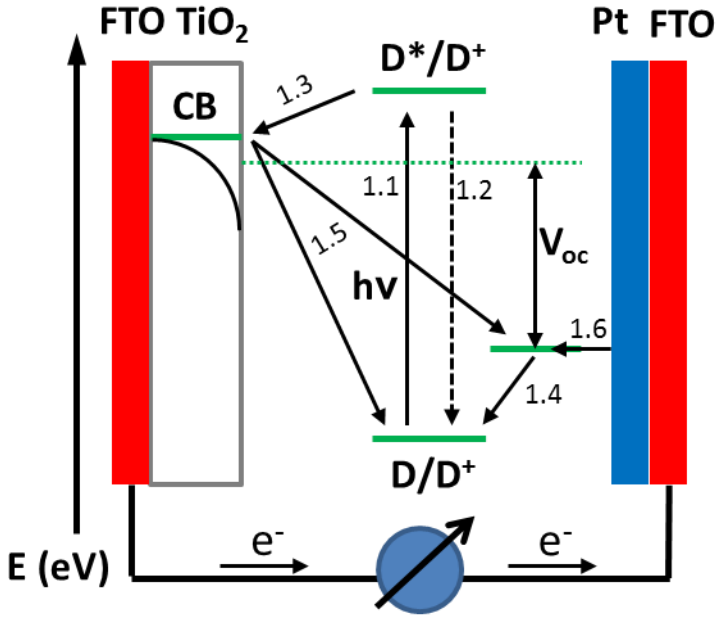


**Figure 1-5 Energy band structure and major electron-transfer processes in DSSC.**

At the anode, the absorption of the light by the dye (*D*) leads to formation for its electronically excited state (*D**).

$$D + h\nu \rightarrow D^{*} \text{ (Photoexcitation)} \qquad 1.1$$

The molecule in the excited state can decay back to the ground state by undergoing relaxation, injecting electrons into the conduction band of titania.

$$D^* \rightarrow D + h\nu \quad \text{(Relaxation)} \qquad 1.2$$

$$D^* \rightarrow D^+ + e_{cb}^- \ (TiO_2 \text{ charge injection}) \qquad 1.3$$

The injected electrons travel through the mesoporous network of titania particles to reach the back-collector electrode to pass through the external circuit. The oxidized dye is reduced rapidly to the ground state by the donor $I^-$ present in the electrolyte

$$2D^+ + 3I^- \rightarrow 2D + I_3^- \quad \text{(Regeneration of dye)} \qquad 1.4$$

In the absence of a redox mediator to intercept and rapidly reduce the oxidized dye, recombination with the electrons of the titania layer takes place, without any measurable photocurrent. This recombination also occurs in the unefficient regeneration process of $I^-$.

$$D^+ + e^-(TiO_2) \rightarrow D \ \text{(Recombination)} \qquad 1.5$$

The electrons reaching the counter-electrode through the external circuit reduce in turn the oxidized ($I^-$) so that the entire sequence of electron transfer reactions involving the dye and the redox mediator $I_3^-$ is rendered cyclic

$$I_3^- + 2e^- \rightarrow 3I^- \ \text{(Regeneration of } I^-) \qquad 1.6$$

If the cited reactions alone take place, the overall effect of irradiation with sunlight is to drive the electrons though the external circuit.

### 1.2.1.3 Efficiency parameters

AM1.5 solar light is almost universally used when characterizing DSSCs. The air mass coefficient (AM) defines the direct optical path length through the Earth's atmosphere. It can be used to help characterize the solar spectrum after solar radiation has travelled through the atmosphere.

$$AM = 1/\cos z \qquad 1.7$$

"AM1.5", 1.5 atmosphere thickness, corresponds to a solar zenith angle of 48.2. While the AM number for mid-latitudes during the middle parts of the day is less than 1.5 in summer, higher figures apply in the morning and evening and at other times of the year. Therefore AM 1.5 is useful to represent the overall yearly average for mid-latitudes. Consequently, the solar industry uses AM1.5 for all standardized testing of solar cells.

In order to fully understand and improve the efficiency of DSSC, several important parameters are used to characterize it. Incident photon-to-current efficiency (*IPCE*) is the most important factor, which corresponds to the photocurrent density produced in the external circuit under monochromatic illumination of the cell divided by the photon flux that strikes the cell.[42]

$$IPCE(\lambda) = LHE(\lambda)\varphi_{inj}\eta_{coll} \qquad 1.8$$

Here, *LHE(λ)* is the light-harvesting efficiency for photons of wavelength *λ*; $\varphi_{inj}$ is the quantum yield for electron injection from the excited sensitizer in the conduction band of the semiconductor oxide; and $\eta_{coll}$ is the electron collection efficiency.

The overall conversion efficiency ($\eta_{global}$)of the DSSC is determined by the photocurrent density measured at short circuit ($J_{sc}$), the open-circuit photovoltage ($V_{oc}$), the fill factor of the cell (*FF*), and the intensity of the incident light ($I_s$).

$$\eta_{global} = \frac{J_{sc}V_{oc}FF}{I_s} \qquad 1.9$$

Where the $I_s$ is the total solar power incident on the cell, 1000 W/m$^2$ for AM 1.5.

The fill factor can assume values between 0 and 1 and is defined by the ratio of the maximum power ($P_{max}$) of the solar cell divided by $V_{oc}$ and $J_{sc}$.

$$FF = \frac{P_{\max}}{J_{sc}V_{oc}} \qquad 1.10$$

$P_{max}$ is the product of the photocurrent and photovoltage at the voltage where the power output of the cell is maximal. The value of the fill factor reflects the extent of electrical and electrochemical losses occurring during operation of the DSSC, which includes the sheet resistances of the substrate and counter electrode, electron transport resistance through the photoanode, ion transport resistance, and the charge-transfer resistance at the counter electrode. Typical values for the fill factor range from 0.75 to 0.85 and there is little room for improvement and the optimization of the *FF*.

The precise $J_{sc}$ value produced by the solar cell in AM 1.5 solar light can be derived by integrating the IPCE spectra over the spectral distribution of the standard AM 1.5 $I_S$, where *e* is the elementary charge.

$$J_{sc} = \int eIPCE(\lambda)I_s(\lambda)d\lambda \qquad 1.11$$

### *1.2.2 Strategy to improve efficiency*

The most straightforward way to increase $J_{sc}$ is to absorb a greater fraction of the incident light which is correlated with the sensitizer absorption capability.

The factors that affect $V_{oc}$ are much more complicated than $J_{sc}$. Referring to the energy band structure and the carrier transfer processes in Figure 1-5, the $V_{oc}$ is calculated by the following equation:[43]

$$V_{oc} = \frac{E_{CB}}{q} + \frac{kT}{q} In(\frac{n}{N_{CB}}) - \frac{E_{redox}}{q} \qquad 1.12$$

where $n$ is the number of the electrons in titania, $N_{CB}$ is the effective density of states, $E_{CB}$ is the conduction band energy level of titania, $E_{redox}$ is the highest occupied molecular orbital (HOMO) level of the redox couples, $k$ is a constant, $T$ is the temperature and $q$ is the unit charge. $n$ is determined by the balance between electron injection and charge recombination, $V_{oc}$ is affected by electron injection, charge recombination, and the values for semiconductor of $E_{CB}$ and $E_{redox}$. So, several methods can be used to increase $V_{oc}$: (1) reduce the charge recombination between redox couple and the injected electrons in the titania conduction band; (2) reduce charge recombination between the oxidized sensitizer and the injected electrons in the semiconductor conduction band; (3) increase the electron injection efficiency; (4) increase the semiconductor $E_{CB}$; (5) downshift the $E_{redox}$.[43]

Over the last two decades, the research area dealing with DSSCs is expanding very rapidly and attracting scientist from different disciplines: Chemists to design and synthesize suitable donor–acceptor dyes and study structure–property relationships; 2) physicists to build solar cell devices with the novel materials, to characterize and optimize their performances, and to understand the fundamental photophysical processes; and 3) engineers to develop new device architectures. The synergy between all the disciplines will play a major role for future advancements in this area.[44]

#### 1.2.2.1 Substrates

As mentioned before, the DSSCs have a sandwich structure involving two TCO substrates. The requirements for the TCO substrates are low sheet resistance (nearly temperature independent, to the high temperatures used for sintering of the $TiO_2$ layer, 450 - 500 ˚C) and a high transparency to solar

radiation in the visible-IR region. Typical sheet resistance of the TCO used is 5-15 $\Omega/cm^2$, found for materials such as tin-doped indium oxide (ITO) and fluorine-doped tin oxide (FTO).

Due to the recombination which occurs predominantly in the region of the FTO substrate,[45] a dense titania layer deposited onto the FTO substrate before the titania photoelectrode has been found to improve device efficiency significantly. The blocking layer increases efficiency firstly through enhancing the bonding strength between the FTO substrate and the porous-titania layer, and secondly, by blocking the charge recombination between electrons emanating from the FTO and the $I_3^-$ ions present in the $I^-/I_3^-$ redox couple. This layer is usually applied by spray pyrolysis, and is typically around 100 nm thick. Especially in the operation of liquid electrolyte DSSC using organic dyes, Grätzel et al. found that the device efficiency can be increased by over 160 % under simulated full sun illumination and more than doubled at lower light intensities by incorporation of a compact layer.[46]

#### 1.2.2.2 Photoelectrode

One of the commonly used wide gap semiconductor for the DSSC photelectrode is titania, because titania is stable, nontoxic and has an energy gap of ~ 3.2 eV. An important requirement for the semiconductor is high transport mobility of the charge carrier to reduce the electron-transport resistance. Many other wide-band gap oxide semiconductors have also been examined as potential electron acceptors for DSSCs, such as ZnO and $SnO_2$,. An excellent review on nanostructured photoelectrodes for DSSCs was published by Zhang and Cao.[47]

Although titania has been mostly used as the photoelectrode, ZnO with different nanostructures has been actively sought as a replacement due to the similar bandgap and conduction band edge of this oxide.[1] Yang et al. prepared a dense array of oriented, crystalline ZnO nanowires by mild aqueous chemistry with a surface area up to one-fifth as large as a nanoparticle cell. The direct electrical pathways provided by the nanowires ensure the rapid collection of electrons generated throughout the device, and an efficiency of 1.5 % was demonstrated, limited primarily by the surface area of the nanowire array.[48] Pellin et al. prepared high surface area ZnO nanotube photoanodes templated by anodic aluminium oxide for use in DSSC. Compared to similar ZnO-based

devices, ZnO nanotube cells showed exceptional photovoltage and fill factors, in addition to power efficiencies up to 1.6 %, which may result from the higher surface area allowing absorption of more dye.[49] Some other binary metal oxides such as $Fe_2O_3$, $ZrO_2$, $Nb_2O_5$, $Al_2O_3$, and $CeO_2$ and ternary compounds such as $SrTiO_3$ and $Zn_2SnO_4$ have been tested as photoelectrodes in DSSC in several groups, but their efficiency is not comparable with titania.

### 1.2.2.3 Dye

Along with the mesoporous oxide layer, a key component of the DSSC is the photosensitizer ("dye") that absorbs the solar radiation and injects electrons into the conduction band of the oxide substrate. A number of desirable properties of the dyes are: strong light absorption in the visible and near-IR region; good solubility in organic solvents; presence of suitable peripheral anchoring ligands; suitable disposition of HOMO and lowest unoccupied molecular orbit (LUMO) of the dye molecule; good thermal stability; and good chemical stability.[50] Examples of dyes that function well in DSSCs are coordination complexes of Ru and Os, squaraines, porphyrins, perylenes, pentacene, cyanines, and coumarins.[51-53]

As the properties of the dye greatly affect the electron injection and charge recombination, hundreds of dyes have been synthesized and tested in DSSCs so far. The most efficient DSSC demonstrated to date have all been based on ruthenium dyes developed by the Grätzel group, such as the N3 and N719 molecules, shown in Figure 1-6.[54] But due to the fact that Ru is toxic and in low abundance, there are many works going on to replace Ru-based dyes with more sustainable materials. To design a good quality dye, many factors need to be considered. Firstly, the dye should absorb strongly from the blue end of the visible spectrum to the near infrared to harvest more light. Secondly, it should have anchoring groups to strongly bind the dye onto the semiconductor surface. Thirdly, the LUMO level of dye must be higher than conducting band energy of titania, so that the process of charge injection in titania conduction band can take place efficiently. Fourth, the HOMO level of dye must be more negative than that of redox couple to keep the efficient transfer to regenerate dyes. Finally, unfavourable dye aggregation should be avoided and photostable, and electrochemical and thermal stability are also required. [50, 51]

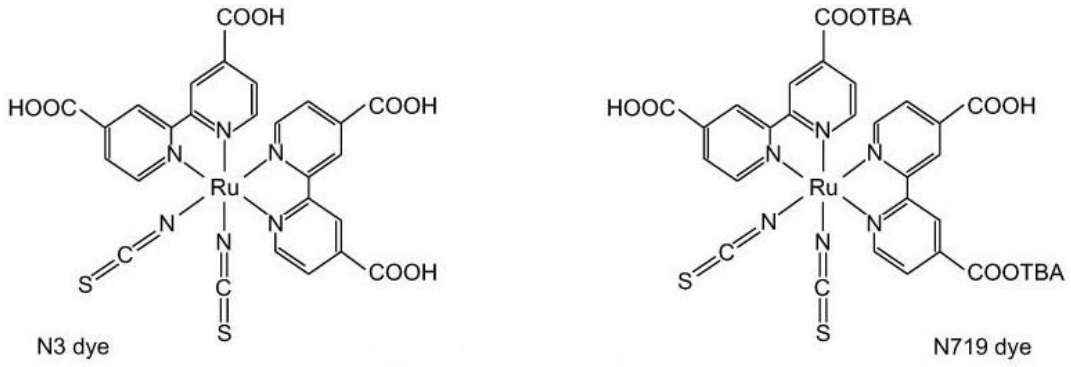


**Figure 1-6 Structure of N719 and N3 dye.**

### 1.2.2.4 Electrolyte

The electrolyte plays a very important role in the DSSC by facilitating the transport of charge between the working and counter electrodes. The ideal electrolyte solvent is one that has very low viscosity, negligible vapour pressure, high boiling point and high dielectric properties.[50] From industrial perspective, factors such as robustness, environmental sustainability, and easy processing are also important. A typical electrolyte used in DSSC is $I^-/I_3^-$ couple.

Although the $I^-/I_3^-$ redox couple has ideal kinetic properties [38] in regenerating the oxidized dye and in inhibition of the recombination of an excited electron to the electrolyte, various redox couples including $Br_3^-/Br^-$,[55] Co(II)/Co(III),[56, 57] $Fe^{2+}/Fe^{3+}$,[58] triethanolamines,[59] pseudohalogen couples,[60] and mixed systems of redox couples have been employed to substitute $I^-/I_3^-$ to enhance the durability and efficiency of DSSCs. Electrolyte can be based on different solvents, such as water, ethanol, acetonitrile and its morphology can be gelated, polymerized, or dispersed within polymeric materials, such as poly(ethylene oxide). Organic and inorganic solid hole conductors are also of great interest, as solid-state solar cells are safer and more durable compared to the liquid ones as they are less likely to leak releasing material into the environment.

### 1.2.2.5 Counter electrode

To balance the charge and regenerate the key components, the oxidized form of the mediator needs to be reduced by the electrons flowing through the external circuit passing through the counter electrode. To reduce losses, the counter-electrode materials should show good electrocatalytic properties. As an electrode material, Pt is the most commonly used material.

Due to the fact that Pt is an expensive material, carbonaceous materials such as active carbon,[61] carbon black,[62] carbon nanotube,[63, 64] and graphite, conducting polymers such as poly(3,4-ethylenedioxythiophene),[65] polyaniline,[66] or polymer-carbon/Pt composites [67-69] are also used for the electrodes in DSSCs. Kitamura et al. synthesized thin films of poly(3,4-ethylenedioxythiophene)–poly(4-styrenesulfonic acid) by a layer-by-layer self-assembly method. The film is highly adhesive to the substrate and has a controllable thickness and showed high cathodic activity. The achieved efficiency of 4.71 % was only a factor of 8 % lower than that of the cell using conventional thermally deposited Pt on FTO glass counter electrodes.[70] Zhao et al. prepared highly uniform and transparent polyaniline electrodes by a facile in situ polymerization method. They also fabricated a novel bifacially active transparent DSSC using polyaniline, which showed conversion efficiencies of 6.54 and 4.26 % corresponding to front- and rear-side illumination, respectively. Meanwhile, the efficiency of the same photoanode employing a Pt counter electrode was 6.69 %.[71] In 2011, Grätzel et al. brought a new breakthrough on counter electrode technology by demonstrating a promising way to reduce the cost and improve the efficiency of DSSC. They found that commercial graphene nanoplatelets in the form of optically transparent thin films on FTO exhibited high electrocatalytic activity toward the $I_3^-/I^-$ redox couple in an ionic liquid. Furthermore, the cell with the graphene electrode without optimized parameters yielded an efficiency of 4.4 % and fill factor of 0.60 when compared to Pt electrode, 5.7 % and 0.75. They predict that the graphene composite is a strong candidate for replacing both Pt and FTO in cathodes.[72]

#### 1.2.2.6 Post treatment and morphology modification

To obtain high-efficiency DSSCs, techniques including $TiCl_4$ treatments for the photoelectrodes, light-scattering layers and an anti-reflecting film on TCO-substrates also have been introduced because of their significant influences on the energy-conversion efficiency.

A $TiCl_4$ treatment of a porous titania electrode is a common method employed during DSSC fabrication to enhance the surface roughness factor and necking of the titania particles thus augmenting dye adsorption and resulting in a higher photocurrent.[73]

Boden et al. reported an anti-reflection film for use as the top layer for DSSC with aim of increasing the light harvesting efficiency from sun light integrated for the entire day.[74] There are two types of anti-reflection film, (1) flat laminate and (2) moth-eye nanostructured film. The former is formed by laminating several thin films with their refraction index increasing toward the inside, while the latter is bioinspired from the nanostructured compound eye of insects.[75-77]

A further improvement that is used in good cells is to have a scattering layer deposited on top of the first layer. This causes any light that passes through the dye layer without being absorbed to be scattered, which increases the average optical path length of the light in the film, improving the chances that it will be absorbed.[78-80] Typically, the underlying layer is prepared from small nanoparticles (10 - 30 nm) and the scattering layer from a top layer of larger particles (200 - 400 nm) or by adding large scattering particles into a nanoparticle matrix. Koo et al. studied the effect of scattering particle size on light scattering efficiency in DSSC.[80] They used two types of rutile titania particles with the size of 300 and 500 nm respectively as a scattering overlayer for bilayered photoelectrode. The global efficiency for the main-layer film was improved differently when two types of scattering layer introduced. This is because significant improvement and strong size-dependence upon deposition of scattering overlayer on the titania main-layer film are related with the quantity and wavelength of transmitted light and the difference in reflectivity of scattering particles. However, using large particles always results in a low surface area with a reduced dye loading,[81] so using large particles with a high surface area such as mesoporous titania secondary particles in the scattering layer is a good way to improve both the dye loading and scattering effects in DSSC. Zhang et al. fabricated anatase titania microspheres with exposed mirror-like plane facets through ahydrothermal process.[82] The photoanode composed of these $TiO_2$ microspheres as the scattering layer showed an improved efficiency when applied in a DSSC due to the superior light scattering effect of microspheres and excellent light reflecting ability of the mirror-like plane facets.

### *1.2.3 $TiO_2$ photoelectrodes in DSSC*

Over the last two decades, the research area dealing with DSSCs has expanded very rapidly and many strategies have been used to improve the

efficiency of solar cells.[44] The morphology and structure of the titania photoelectrode is one of the most studied areas.

DSSC designs using titania have been continuously renovated since 1991 to enhance the efficiency by increasing the light-scattering properties of the metal oxide film, suppressing charge recombination, improving the interfacial energetic, and altering the particle morphology. Several excellent reviews have been published on the preparation, characterization and working theory.[3, 83-86]

Traditional mesoporous titania films made by doctor blading and screen printing methods are still used by most of researchers. Improvements of the morphology of the titania film or functionalization of the titania powder that compose the photoelectrode are under intensive consideration. In the case of studies of morphology design, the multilayer deposition method provides the possibility to make photoelectrodes with different structures,[81] dip or spin coating methods facilitate the preparation of mesostructured titania thin films,[2, 87] and the formation of 1D nanoarrays provides a totally different geometry from the multilayer or dip/spin coated photoelectrodes.[88] To functionalize the titania powder, mesoporous nanoparticles, titania with a hierarchical or 1D structures, and doping have been utilized to improve the cell performance arising from different aspects.[47]

#### 1.2.3.1 $TiO_2$ photoelectrode prepared by doctor blading and screen printing

The traditional way to prepare the titania photoelectrode is made by the doctor blade method or a screen printing approach from a titania colloidal paste. These methods are used because they are easy to carry out and do not have any requirements for specialist facilities to realize a highly efficient photoactive layer.

Figure 1-7 shows the process of film deposition via the doctor blade technique. After preparation of the paste (procedure 1), films can be made by doctor blading. To mask electrical contact strips, 0.5 cm width of the conducting glass plate was covered along the length of each edge with adhesive scotch tape. The viscous titania colloidal paste was then spread on the top of TCO substrates and the thickness of the film was controlled by the scotch tape (procedure 2). After that, the film is annealed and forms mesoporous titania film due to the presence of voids formed among the necked titania nanoparticles by the

combustion of organic binders in the annealing process (procedure 3 and 4). Usually, a titania film with a thickness of 10 - 15 μm can be obtained.

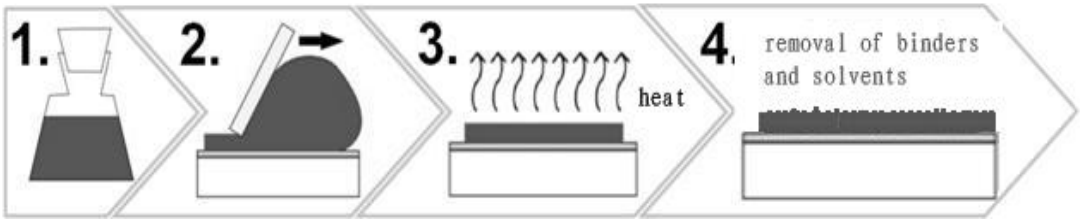


**Figure 1-7 Procedure of film deposition via the doctor blade technique [89] Reprinted with permission from Ref. 89.**

Screen-printing techniques were also first adopted to prepare the porous $TiO_2$ films used for DSSCs by the Grätzel group.[90] The screen-printing method is often chosen for the preparation of titania films with controllable thickness and uniform morphologies in large-scale production. The technique consists of three elements (Figure 1-8): the screen, which is the image carrier, the squeegee and titania paste. The screen uses a porous mesh, made of porous fabric or stainless steel stretched tightly over a frame made of metal. The titania paste is placed on top of the screen. The paste is then forced through the fine mesh openings using a squeegee that is drawn across the screen, applying pressure and thereby forcing the paste through the open areas of the screen. The paste will pass through and form an image on the printing substrate. The diameter of the threads and the thread count of the mesh will determine how much of the semiconductor paste is deposited onto the conductive glass substrate.[91]

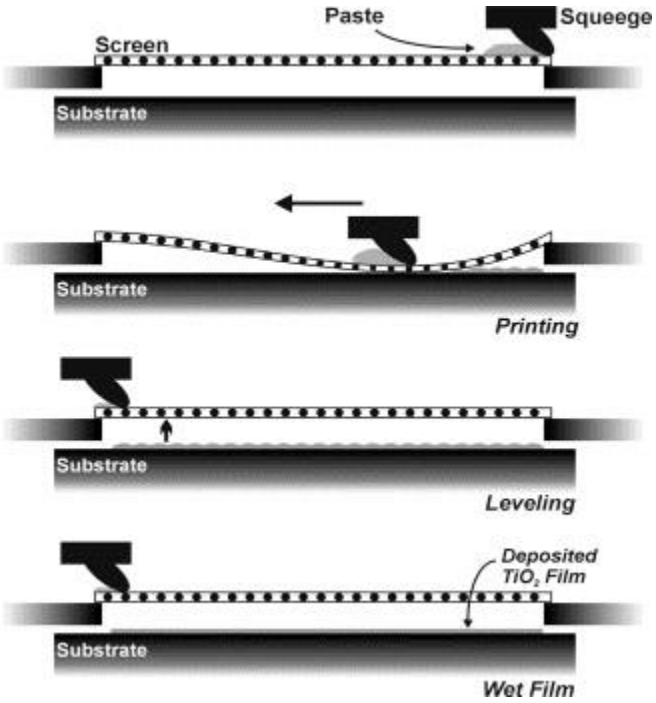


**Figure 1-8 Schematic representation of the screen-printing process.[91] Reprinted with permission from Ref. 91.**

One of the most important factors in the quality of the films made by the doctor-blade or screen-printing techniques is the quality and characteristics of the titania paste. The titania paste can be greatly affected by its composition. Pastes are usually made using ethyl cellulose and terpineol as the solvent. The influences of weight ratio of composition on characteristics of DSSCs were studied by Dhungel et al.[92] They optimized the titania paste using a nanocrystalline titania powder (particle size ~ 20 nm), ethyl cellulose and terpineol by comparing the performance parameters of the DSSCs fabricated using pastes of different compositions. The paste prepared with 26 % titania powder, 15 % ethyl cellulose gel and 59 % terpineol in a liquid state gave a conversion efficiency as high as 7.27 %, so was found the best for application in DSSCs.

Instead of ethyl cellulose as the binder, poly vinyl butyral, poly(ethylene glycol), Triton X-100 etc. can be used as the binder and water, diethylene glycol etc. can serve as the solvent in titania paste formation. Different morphologies and nanostructrues of titania powder in colloidal paste can be used, such as nanoparticles, mesoporous titania nanoparticles, or titania with a hierarchical or 1D structures.

- **$TiO_2$ nanoparticles**

Titania nanoparticles (home-made or commercial) are the traditional titania source for titania colloidal paste and application in DSSCs. The first titania photoelectrodes prepared by either doctor-blading or screen-printing were made from titania nanoparticle pastes. After the initial work, the titania nanoparticle paste served as the standard colloidal paste and became industrialized. Further work regarding the nanoparticle paste turned to the design of the morphology of photoelectrode and doping of titania nanoparticles.

An excellent work about the morphology design of photoelectrodes was done by Wang et al.[81] Photoelectrodes with six different structures, with layers of nanoparticles, light-scattering particles, and mixture of nanoparticles and light-scattering particles at a desirable sequence and thickness, were designed and investigated. The profiles of photocurrent action spectra were related to the light scattering and the suppression of light loss due to the back-scattering by large particles near the conducting glass layer. The results showed that a multilayer structure is better than the mono- and double-layer structure and the adoption of the scattering layer can improve the cell performance.

Kim et al. also used multilayer deposition techniques to fabricate multi-layered titania electrodes to improve the light harvesting efficiency of dye-adsorbed titania electrodes prepared by the doctor blade technique.[93] They used three different structures of titania electrodes in DSSCs which were fabricated with layers of nanoparticles and light-scattering particles. The best efficiency of 6.03 % under AM 1.5 was attained by a multi-layer structure cell using a 123-nm thick titania layer for the light-scattering layer and 9-nm thick titania layer for the dense layer.

Both metal and non-metal elements were successfully doped into titania and DSSC made from these showed an improved efficiency. Ko et al. prepared Al and W-doped titania and applied them as photoelectrodes in DSSC.[94] For Al-doped titania electrodes an increased open voltage and a reduced short current were found, , but the W-doped titania had an opposite effect. However, the efficiency of dye-sensitized solar cells fabricated with doped titania was pronounced better than that of undoped $TiO_2$, because the doping modifications led to significant

changes in powder aggregation, charge transfer kinetics, and dye adsorption characteristics.

Ma et al. synthesised needle-like N-doped titania nanocrystals and nanoparticles from commercial titania powders.[95] The N-doped DSSCs achieved a high conversion efficiency of 10.1 % and 4.8 % using an organic electrolyte and an ionic liquid electrolyte, respectively, contributing to the synergetic effect of higher dye uptake, faster electron transport and higher photovoltage.

- **Mesoporous $TiO_2$**

Ordered mesoporous materials prepared by surfactant templating possess extraordinarily large surface areas and well-arranged channels or pores, thus allowing higher dye loading and better electrolyte diffusion in the DSSCs applications.

Gajjela et al. made mesoporous titania powder templated by various cationic surfactants with a surface area of 90 - 135 $m^2/g$ and applied these powders as the photoelectrodes for DSSC.[96] The DSSC with the highest efficiency of 7.5 %, short current of 14.2 $mA/cm^2$, open voltage of 748 mV and fill factor of 70.83 % was obtained from cetyltrimethylammonium bromide (CTAB)-templated mesoporous titania. Zhao et al. synthesized cubic mesostructured titania with uniform pore diameters of ~16.0 nm, and a specific surface area of 112 $m^2/g$ by using polystyrene-b-poly(ethylene oxide)-b-polystyrene as the template and obtained an efficiency of 5.45 %.[97]

Ho et al. synthesized ordered mesoporous titania particles using Pluronic P123 as the template and made the as-prepared precursor gel into a paste with the addition of 5 wt. % P25 nanoparticles, which acted as scattering centres and active binders to prevent formation of microcracks. The DSSCs they made from the colloid paste displayed an efficiency of 6.5 %.[98]

With different templates, researchers can prepare mesoporous titania particles with various pore sizes. Won et al. synthesized mesoporous titania particles with the same high surface area (210 $m^2/g$) but different pore sizes of 6.8 and 3.0 nm, respectively.[99] With the mesoporous titania having larger pores, the photo-conversion efficiency was increased significantly to 6.71 %, compared with 5.62 % using P25 nanopowders, and 3.05 % using titania having small pores, because bigger pores can afford more accessible sites for dye adsorption as the

dye molecules have a size around 2 nm. Thus pore size will affect the amount of dye uptake and thus affect the photovoltaic performance of DSSCs.

- **$TiO_2$ with a hierarchical structure**

Titania with a hierarchical structure normally is in a powder form with a size in the submicro or micrometer level. It has secondary nanostructure that is composed of primary nanoparticles or nanostructures.

Liao et al. fabricated anatase titania spheres consisting of nanorods and nanoparticles by an acid thermal method.[100] The DSSC based on these hierarchically structured titania spheres as the photoelectrode shows a short current of 18.78 mA/cm$^2$, open voltage of 826 mV, and a high efficiency of 10.34 %. Compared to P25 nanoparticle photoelectrodes, the improved efficiency is mainly attributed to a higher surface area, higher light scattering effects from the sphere structures, and faster electron transport rates and slower recombination rates from the nanorod structure.

Gajjela et al. prepared mesoporous titania particle templated by CTAB and used the submicron-sized mesoporous titania aggregates as a photoelectrode in a DSSC.[101] The DSSC showed an efficiency of 9.00 % at 1 sun and 10.84 % at 0.16 sun illumination due to the multi-functional properties of the hierarchically structured titania such as high dye uptake, efficient light scattering and enhanced charge collection.

Huang et al. synthesized submicrometer-sized mesoporous titania beads by a combined sol-gel and solvothermal process and applied them as the scattering layer in a bilayered photoelectrode for DSSC.[102] A high efficiency of 8.84 % was obtained with the mesoporous beads as a scattering layer, compared with an efficiency of 7.87 % for the electrode with the scattering layer of 400-nm titania particles, of similar thickness. This is because the mesoporous structure offers a high surface area of 89.1 m$^2$/g and the submicrometer sized beads structure has good scattering effects.

- **$TiO_2$ with a 1D structure**

In general, titania nanowires or nanotubes will not be used to make films by doctor blading or screen printing directly. Firstly, nanowires or tubes have a relative large size which makes it difficult to obtain crack-free films. Secondly, the

techniques to make 1D nanowire or tube arrays are mature. However titania nanorods have a smaller size and can be used as the titania powder source for colloidal paste and applied in DSSCs.

Jiu et al. fabricated anatase titania nanorods with lengths of 100 − 300 nm and diameters of 20 - 30 nm via a hydrothermal process.[103] The effects of addition of Pluronic F127 on the morphology of nanorods wes studied. When these rods were applied as photoelectrodes in DSSC, a high conversion efficiency of 7.29 % was obtained from a cell made using titania single crystalline anatase nanorods. Compared to a P25 nanoparticle electrode, the improved efficiency of the DSSC was due to better light scattering effects, the single crysatalline phase to reduce the grain boundary resistance and efficient electron transfer in the 1D nanostructures.

### 1.2.3.2 $TiO_2$ photoelectrodes prepared by dip and spin coating

Mesoporous titania thin films are very promising materials to act as electrode in DSSCs. Randomly oriented nanocrystalline titania particles are usually used to prepare photoelectrodes with a thickness of 10 - 15 μm. However template-assisted dip or spin coating techniques based on EISA mechanism can be used to obtain thin films (thickness < 4 μm) with ordered porosity.[104-107]

As described in Figure 1-9, the dip-coating process can be separated into three stages. Firstly, the substrate is immersed into the solution of the coating materials, then once the substrate has remained inside the solution for several seconds, it is withdrawn at a constant speed, while a thin wet layer is formed on the substrate. Finally, the solvent evaporates from the liquid, forming the thin film.

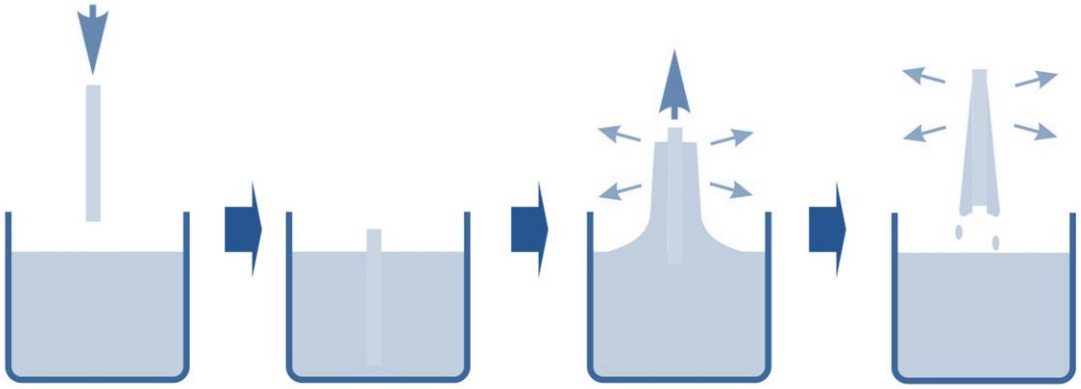

**Figure 1-9 Schematic representation of film formation via the dip-coating process.**

Spin coating is a procedure used to apply uniform thin films to flat substrates. Similar to the dip-coating process, the spin coating process, shown in Figure 1-10 can be divided into three steps. Firstly, the coating solution is applied onto the wafer or substrate; then, the solution is spread out and wet thin layer is formed, when the substrate rotates at a constant rate. Finally, the solvent in the fluid evaporates and thin solid films are obtained.

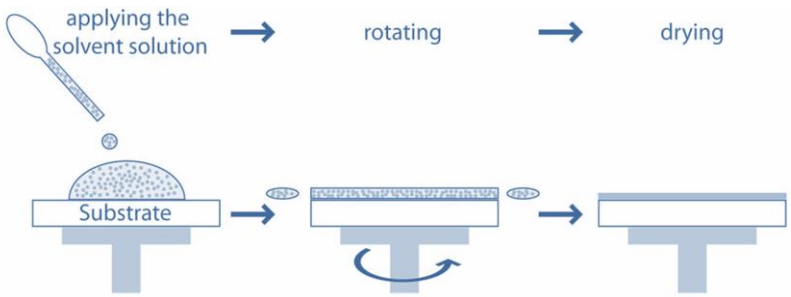


**Figure 1-10 The process of film formation via the spin coating technique.**

The film thickness can be controlled by the withdrawal or spinning speed and viscosity of precursor solutions. Usually, uniform films are obtained by dip or spin coating, so they are popular ways of preparing thin films for research purposes, such as ordered mesoporous thin films.

Grätzel group fabricated organized mesoporous titania films templated by Pluronic P123 via multilayer dip-coating. Sensitized by N-945 dye, the 1μm-thick titania film was applied as a photoanode in a DSSC and showed enhanced solar conversion efficiency by about 50 % compared to that of traditional films of the same thickness made from randomly oriented anatase nanocrystals. This is because the high surface area of the film facilitated the higher dye loading and the pores increased the accessibility of dyes to the redox couple and electrons.[108]

The film thickness is one of the important factors that affect the efficiency of DSSC and many studies were carried out to prepare thicker organized films by dip or spin coating. In 2008, the Grätzel group prepared ordered mesoporous titania films with a thickness up to 2.3 μm by increasing the number of successively deposited layers and found that the solar performance of multilayer films sensitized with N945 dye scaled linearly for 1 - 3 layer films, but approached a plateau for thicker films.[105] At the same time, Chi et al. prepared mesoporous titania films with a thickness up to 3.5 μm templated by Pluronic P123. The highly

transparent multilayer mesoporous film showed a large pore size of 8.9 nm with a specific surface area of 129.4 $m^2/g$. An efficiency of 6.01 % was obtained whenthis film was applied in a DSSC.[109] In 2011, the thickness of an ordered mesoporous titania film deposited by dip coating reached 4 μm by Dewalque et al.[106] The influence of the template on the film organization and porosity was studied in terms of long-range order, percentage of porosity, pore size and pore connectivity. An excellent efficiency of 6.1 % was obtained for a 4 μm thick film sensitized by N719. Zhang et al fabricated thick titania films (up to 5.08 μm) with an ordered orthorhombic pore organization by spin coating.[110] The influence of film thickness on the cell performance was studied. With the increase of thickness, the efficiency of DSSC improved. The maximum efficiency was 6.02 %, when a film of 5.08 μm in thickness was applied in a DSSC sensitized by N719. However, this method is not as popular as the traditional way for several reasons. Firstly, not everyone can repeat the experiments to obtain such organized film as the EISA method has critical environmental requirements; Secondly, the efficiency is still not as high as the DSSC based on 10 μm titania film; Thirdly, it is much more complicated than doctor blading or screen-printing methods.

#### 1.2.3.3 1D $TiO_2$ nanoarrays as photoelectrodes

Titania in the form of 1D nanoarrays, such as nanotubes, nanorods and nanowires, is normally made by an anode oxization method, templating method or a hydrothermal method. The effective transport and movement of charge carriers in nanoarrays benefit efficient cells.

Zhu et al. fabricated titania nanotube arrays from electrochemically anodized Ti foils.[111] The nanotube arrays were several micrometers in length, with typical wall thicknesses and intertube spacings of ~ 9 nm and pore diameters around 30 nm. The calcined nanotubes contained an anatase phase with crystallite size ~ 30 nm. The thickness of nanotube films affected the photoconversion processes. However, the nanotube arrays showed similar transport time but higher charge-collection efficiency compared to nanoparticle films with the same thickness. Also, the nanotube arrays showed higher light scattering effects. These contribute to the improved efficiency of this DSSC compared to those prepared using nanoparticle photoelectrodes.

Kang et al synthesized titania nanotube arrays by a templating method, filling titania precursor solution into porous alumina.[112] After calcination, the anatase nanotube arrays had an external diameter ~ 295 nm, tube length 6 -15 μm, and wall thickness 21 - 42 nm. When this nanoarray was applied into a DSSC using N719 dye, it yielded an efficiency of 3.5 % and IPCE of 20 % at 520 nm.

Feng et al. prepared single crystal rutile titania nanowire arrays directly onto an FTO substrate through a non-polar solvent/hydropholic substrate reaction.[113] By changing the reaction time from 2, 4, 8 to 22 h, the length of nanowire varied from 2, 3.2, 3.8 to 4 μm. The nanowire array with a length of 2-3 μm achieved a global efficiency of 5.02 % when applied into a DSSC using N719 dye.

Liu et al. fabricated single crystal rutile titania nanorods on FTO substrate by a hydrothermal method.[114] The diameter, length, and density of the nanorods could be tuned by varying the growth parameters, such as growth time, growth temperature, initial reactant concentration, acidity, and additives. For a photoelectrode composed of 4 μm-long titania nanorods, an efficiency of 3% was achieved after $TiCl_4$-treatment.

## 1.3 Titania photocatalysts

Solar energy, besides nuclear fusion, has the largest potential to satisfy the future global need for renewable energy sources. Generally, two types of approaches are adopted to utilize sun light. One is transformation of solar energy to electricity, such as in the photovoltaic solar cells discussed above. The other is to make use of sun light as a source of chemical energy. Except for the photosynthesis of plants on the earth, photocatalysis is the major technique to take advantage of sun by means of a photochemical process.[115]

In 1972, Fujishima and Honda proposed the photocatalytic splitting of water on titania electrodes under UV light.[116] This event opened a new story of heterogeneous photocatalysis. Since then, intensive research in understanding the fundamental processes and improving the photocatalytic activity have been performed by scientists and engineers. At first, those studies were often concerned about energy transfer and storage. After 1980s, application to environmental remediation has been one of the most active areas in heterogeneous photocatalysis.[117] Research from the last decade has

demonstrated that photocatalysis can decompose most of the organic pollutants in the gas phase, pure organic liquid phases or aqueous solutions.[118] This is exciting news for modern society, because many environmental problems occur along with the civilization of society including water and air pollution. The elimination of toxic and hazardous chemical pollutants has become a major concern.

### *1.3.1 Theory of photocatalysis*

In the process of photocatalysis, organic pollutants in the fluid phase are firstly absorbed to the surface of catalyst and then decomposed in the presence of an energetic light source and an oxidising agent such as oxygen or air.[119] Figure 1-11 illustrates the mechanism of titania photocatalysis, where P represents the organic pollutants.

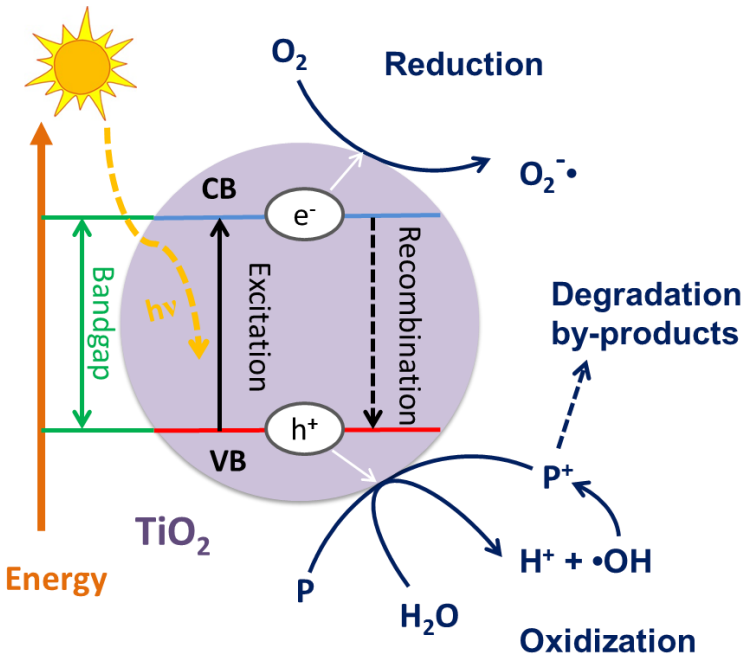


**Figure 1-11 Mechanism of titania photocatalysis.**

When titania absorbs the energy of a photon with sufficient energy (equivalent or higher than the band gap energy of the catalyst), an electron in the valance band can overcome the band gap and reach the conduction band, leaving a vacancy in the VB. This event generates a negative electron ($e^-$) in the CB and a positive hole ($h^+$) in the VB, shown in equation 1.13. The recombination of the electron and hole can also happen at the same time. To benefit the

photocatalyzed reaction, the recombination process must be prevented as much as possible. The electron in the conduction band reduces oxygen adsorbed on the catalyst (titania), shown in equation 1.14. This process prevents the recombination of an electron–hole pair. The positive hole can oxidize organic pollutant directly (equation 1.15) or react with water to produce •OH radicals (equation 1.16). The resulting hydroxyl radical is a very strong oxidizing agent (standard redox potential +2.8 V) and can oxidize most organics (equation 1.17).[120] According to the theory above, the relevant reactions at the semiconductor surface causing the degradation of organics can be expressed as follows.

$$TiO_2 + h_v \rightarrow e^- + h^+ \qquad 1.13$$

$$e^- + O_2 \rightarrow O_2^-\bullet \qquad 1.14$$

$$h^+ + \text{organic} \rightarrow \text{intermediates} \rightarrow CO_2 \qquad 1.15$$

$$h^+ + H_2O \rightarrow \bullet OH + H^+ \qquad 1.16$$

$$\bullet OH + \text{organic} \rightarrow \text{intermediates} \rightarrow CO_2 \qquad 1.17$$

### *1.3.2 Titania photocatalysts*

There are several requirements for materials that can serve as photocatalysts and the most important one concerns the band gap energy. An effective material should have suitable conduction and valance band energy to reduce oxygen in eauation 1.14 and generate •OH radicals in equation 1.16. Several metal oxide and sulphide semiconductor have suitable band gap energies for photocatalytic processes, such as $TiO_2$ ($E_g$ =3.2eV), $WO_3$ ($E_g$ =2.8eV), $SrTiO_3$ ($E_g$ =3.2eV), ZnO ($E_g$ =3.3eV) and ZnS ($E_g$ =3.6eV). However, among these semiconductors, titania has proven to be the most suitable for widespread environmental applications due to its excellent photocatalytic activity and stability. Many factors affect the degradation performance, such as catalyst loading, pH and temperature of the solution and surface morphology of photocatalyst,[117] because there is a direct relationship between degradation of the organic compounds and surface coverage of the catalysts. The surface morphology, such as particle size and structure, is the most studied aspect. According to the geometry, titania photocatalysts can be classified into two groups, titania particles and film photocatalysts.

### 1.3.2.1 $TiO_2$ particle photocatalysts

There are numerous investigations on the synthesis of anatase nanoparticles with sizes ranging from 5 nm to several micrometres and a variety of shapes or nanostructures for photocatalysis. These aim to achieve high photocatalytic activity and adsorption efficiencies by virtue of their induced shape- and size-dependent properties. Some typical examples of titania photocatalysts are listed below.

- **$TiO_2$ nanoparticles**

Particle size is an important parameter for catalysis in general since it directly impacts the specific surface area of a catalyst.

Xu et al. studied the effects of particle size with a range from 49 μm to 30 nm on the photoreactivity of titania anatase nanoparticles by degradation of methylene blue.[121] Results showed that the photocatalytic activity of titania increased as the particle size of titania became smaller due to the larger surface area of the nanocrystallites. However, this does not mean the photocatalytic activity always increased with the decrease of particle size, especially for nanoparticle with a size under 30 nm. Wang et al. also did a systematic study of the particle size effect on the photocatalytic performance of titania nanocrystallites by degradation of chloroform.[122] Anatase titania particles with different sizes (6, 11 and 21 nm) were prepared by a hydrothermal synthesis method. The surface area increased when the particle size decreased. However the highest photoreactivity was obtained by titania with a particle size of 11 nm. This is because the increased surface area also improved the surface electron-hole recombination rate in the nanocrystalline titania.

- **Mesoporous $TiO_2$**

Mesoporous materials are known for their high surface area, so mesoporous or ordered mesoporous titania nanoparticles have attracted much attention due to this property.

Peng et al. fabricated mesoporous anatase titania nanoparticles by using CTAB as a template from a hydrothermal method.[123] The mesoporous titania after calcination at 400 °C had a particle size 7 - 27 nm and a crystallite size of 3.1 nm. Moreover, it had specific surface area of 318 $m^2/g$ with a mean pore diameter of

2.5 nm. When testing this material by degradation of Rhodamine B, it showed much better photocatalytic activities than Degussa P25 due to the large surface area, small particle size, and well-crystallized anatase mesostructure.

Zhou et al. prepared ordered mesoporous anatase through an evaporation-induced self-assembly technique.[124] After calcination at 700 °C, it still had a large pore diameter (10 nm), high specific surface area (122 $m^2/g$), and high total pore volumes (0.20 $cm^3/g$). The obtained mesoporous titania showed better photocatalytic performance than that of Degussa P25 for degradation of 2,4-dichlorophenol under UV irradiation. This enhancement is attributed to the well-ordered large-pore mesoporous structure, which facilitates mass transport, the large surface area offering more active sites, and high crystallinity that favours the separation of photogenerated electron-hole pairs.

- **$TiO_2$ with a hierarchical structure**

Titania with hierarchical structures has been used as promising photocatalysts, because the textural mesopores and intrinsically interconnected pore systems of the macrostructures are able to efficiently transport guest species to framework binding sites.[125]

Macro/mesoporous titania fabricated with or without template shows a better photocatalytic activity than Degussa P25. Wang et al. prepared macro/mesoporous titania using a non-ionic polymeric surfactant as the template and calcined at different temperatures.[126] The obtained materials had macropores of around 2–4 μm in width and around 50 μm in length. The calcination temperature had a great influence on the structures and photocatalytic activity. At 350 °C, the calcined sample had a surface area of 201 $m^2/g$, porosity of 60 %, a mean pore diameter of 5.7 nm and anatase crystallite size of 5.8 nm. This sample showed the highest photocatalytic activity by ethylene decomposition, and was much better than P25. Higher temperature calcination decreased the photoreactivity a little because of the destruction of the hierarchical structure and the decrease of the specific surface area.

However, Yu et al. fabricated macro/mesoporous titania without using any template.[125] The obtained materials had macropores with a similar size as Wang's work. They also discussed the influence of calcination temperature on the structures and photocatalytic activity. At 300 °C, the calcined sample had a

surface area of 206 $m^2$/g, a mean pore diameter of 3.7 nm and anatase crystallite size of 5.9 nm. This sample showed the highest photocatalytic activity for degradation of acetone. Higher temperature calcination decreased the phtotoreactivity a little, but all of the samples showed a better photocatalytic activity than Degussa P25 anatase nanoparticles.

- **$TiO_2$ with a 1D nanostructure**

For 1D nanostructured crystals, the effective transport and movement of charge carriers are favoured throughout the crystal length, leading to improved delocalization and enhancing photocatalytic reaction efficiencies.

Joo et al. prepared anatase titania nanorods by a sol-gel reaction between titanium(IV) alkoxide and oleic acid with the addition of stabilizing surfactants.[127] The diameter of the nanorods produced could be adjusted by changing the of amount of surfactants. Titania nanorods with a surface area of 198 $m^2$/g. exhibited a higher photocatalytic activity to inactivate E. coli than the Degussa P25 nanoparticles because of the quantum confinement effect of the nanorods.

Wu et al. fabricated well-defined single-crystalline anatase titania nanobelts with 60 − 400 nm wide, ~ 10 nm thick, and up to 25 μm long in dimension.[128] The influence of the special shape and the surface structure of the nanobelts in photocatalytic degradation of methyl orange aqueous solutions were studied in detail. Compared to nanosphere with a similar surface area, the nanobelts had a better charge separation because of a more efficient carrier movement and facilitated pathway for transport of charge carriers throughout the longitudinal direction of the rod.

### 1.3.2.2 $TiO_2$ film photocatalysts

In order to avoid the use of titania powder, which requires later separation from the water, various researchers began to work on ways of immobilizing titania particles, for example in thin film form. Generally, titania nanoparticle thin films are deposited from titania nanoparticle suspensions, while mesoporous films prepared from titania precursor solution by dip or spin coating, and titania 1D arrays are normally synthesized by an anodic oxidation approach.

- **$TiO_2$ nanoparticles**

Chae et al. prepared transparent anatase titania nanoparticle films from a titania nanoparticle suspension by spin coating.[129] They believe the particle size affected the photocatalytic activity of films. The titania films prepared from 7-nm-sized nanoparticles showed a higher photocatalytic performance in decomposing 2-propanol, which was 1.6 times better of that of films derived from Degussa P25, while the films made from 15- and 30-nm titania showed lower photocatalytic efficiencies than Degussa P25.

- **Mesoporous $TiO_2$**

Yoshiaki et al. fabricated ordered mesoporous anatase titania film using the EISA method by dip coating.[130] Samples showed a cubic mesostructure after calcination at different temperatures. The calcination temperature affected the porous property of the films and photoactivity. The optimal films, in photodegradation of methylene blue and lauric acid, contained ananoparticle of size 7.5 nm and an open grid-like network integrating pores of size 5.5 nm after calcination for 10 min at 600 °C in air. The high active performance was because this film had a high porosity and pores were completely accessible.

- **1D $TiO_2$ nanoarrays**

Liu et al. prepared highly ordered nanotube arrays consisting of tubes around 100 nm in diameter from potentiostatic anodization of Ti foil.[131] Anatase titania nanoarrays with three lengths, 0.21, 12, and 17 μm, were prepared by adjusting anodizing time. The photocatalytic activity in the degradation of phenol showed a dependence on the length of the nanotube arrays. Short nanotube arrays had better catalytic activity than the long one due to the reduced recombination effects. When compared with Degussa P25 film, all the nanotube array samples showed a much better photocatalytic activity owing to the improved electron transport and reduced charge recombination.

### *1.3.3 Doping of titania as visible-light photocatalyst*

Given the requirement for UV light activation of titania and the fact that UV light only accounts 3 % of the solar spectrum,[132] researchers became interested in modifying the materials so that they would become activated by visible light (e.g. room light) for applications for indoor use or by solar light for outdoor use.

Titania doped by metal and non-metal elements was proved to be an effective way to extend the spectral response to visible light.

### 1.3.3.1 Theory of $TiO_2$ doping

The mechanism of metal and non-metal doped titania photocatalysis is displayed in Figure 1-12. The generation of electron-hole pairs in pure titania requires energy $hv_1$ which is equal to the band gap energy. For metal-doped titania, a new energy level forms below the conducting band of titania by the dispersion of metal nanoparticles in the titania matrix.[133] Moreover, transition metal doping improves the trapping of electrons to inhibit electron-hole recombination during irradiation. The energy for electron excitation now equals $hv_2$. In the case of non-metal doping, impurity energy levels above the valence band are formed and energy $hv_3$ is required to generate the electron-hole pair, although there are still some issues which are not understood about the non-metal doping mechanism.[134] Due to the shift of CB or VB energy level, the band gap energy of metal or non-metal doped titania is smaller. Visible light has a larger wavelength than the UV light, which affords a lower level of energy than UV light. For pure titania, the bad gap is too large to generate electron-hole pairs under the visible light irradiation, but the doped titania has a smaller band gap for the generation of electron-hole pairs. Some typical examples of doped titania photocatalysts are listed here.

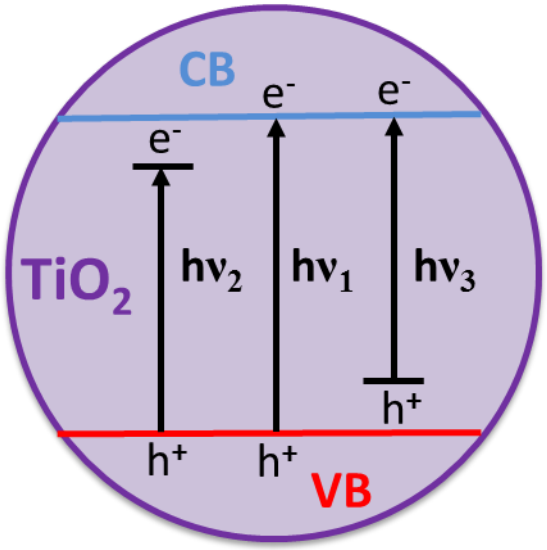


**Figure 1-12 Mechanism of titania photocatalysis: $hv_1$: pure titania; $hv_2$: metal-doped titania and $hv_3$: nonmetal-doped titania.**

### 1.3.3.2 Metal-doped $TiO_2$

The modification of titania by doping with transition metal ions such as V, Fe, Cr, Co, Ni, Cu, Mn etc., brings about a red shift in the absorption pattern of the titania catalyst allowing it to use solar irradiation more effectively.[135, 136] The ions can also be implanted into titania networks with different nanostructures by various techniques.

Klosek et al. fabricated a V-doped titania nanoparticle film from a sol-gel approach, which was very active under visible light (396-450 nm).[137] It had a comparable photoactivity in ethanol degradation under UV illumination as an undoped titania catalyst, but much better catalytic performance under visible-only irradiation. The excited vanadium centres donate an electron to the titania conduction band under visible irradiation, which allows the oxidation of surface adsorbed molecules.

Yu et al. fabricated Fe-doped mesoporous titania nanorods from a hydrothermal method.[138] By using the Fe-doped titania nanorods with an atomic ratio of Fe/Ti ($R_{Fe}$) in the range of 0.1 - 1.0%, the photocatalytic activity improved compared to undoped titania nanorods and Degussa P25 nanoparticles. This is because $Fe^{3+}$ can act as a temporary electron or hole-trapping site that enhance the transfer and transport of the charge carrier and Fe-doping shifts the absorption edge into the visible-light range.

Yu et al. fabricated an ordered and well-crystallized cubic Im3m mesoporous Cr-doped titania photocatalyst using the EISA method.[139] The doping $Cr^{3+}$ was embedded into the anatase nanocrystal framework through substitution of $Ti^{4+}$ and a marked red-shift of Cr doped titania was observed. The film showed a high photocatalytic activity under visible light illumination in degradation of methylene blue, because of the absorption in the visible light region and the open mesoporous architecture with a large surface area, good anatase crystallinity and a 3D-connected pore system.

Mokaya et al. prepared a W-doped mesoporous titania photocatalyst by a hydrothermal process.[140] The percentage of $WO_3$ in the composite was increased from 1 to 40 wt. %, which decreased the size of the anatase crystals but had little effect on the porosity properties. The photocatalytic activities in trichloroethylene degradation were higher than commercial Degussa P25 for samples with

loadings of up to 5 wt. % $WO_3$, possibly due to the coupling effect of the two semiconductors and enhanced charge separation.

#### 1.3.3.3 Nonmetal-doped $TiO_2$

However, metal-doping in titania does not produce materials with long-term stability and not all metal dopants result in a positive change of photocatalytic activity.[135] Non-metallic elements were proved to be another effective way to extend the spectral response to visible light. Moreover, these materials are more stable and almost all of the non-metal elements used so far were reported to improve photocatalytic activity under visible light irradiation, such as B,[141] C,[142] N,[143] S,[144] F [145], P,[146] and I.[147]

In 2001, Asahi et al. published a paper in the journal *Science* on an N-doped titania photocatalyst.[143] They discussed the possibility of dopants such as C, N, F, P, S for O but found that N is the most effective candidate. N-doped titania films were prepared by sputtering a titania target in $N_2$ gas and its photoactivity was tested by methylene blue degradation under visible light. Also, N-doped titania powder was prepared by treating titania powder under $NH_3$ atmosphere at 600 °C and its photoactivity was tested by acetaldehyde degradation under visible light. Both of them had better photocatalytic performance than pure titania due to the absorption in visible light region.

Li et al. prepared F-doped titania by spray pyrolysis from an aqueous solution of $H_2TiF_6$.[148] The photocatalytic activity in decomposition of acetaldehyde and trichloroethylene showed a pronounced improvement compared to Degussa P25 under visible-light irradiation, although F-doping had less effect on the optical absorption properties of bulk titania. This is because two kinds of oxygen vacancies (*F* and $F^+$ centres) were formed by F-doping and the excitation of the absorption bands of these oxygen vacancies induced the visible-light-driven photocatalysis.

Zhang et al. prepared a S-doped titania photocatalyst by a mechanochemical method.[144] Samples were prepared by grinding a S and titania mixture which was then calcined at 400 °C in Ar atmosphere. Under irradiation of visible light, the samples showed good photocatalytic performance in NO destruction, due to the absorption in visible-light region.

Hong et al. fabricated an I-doped titania photocatalyst by direct hydrolysis of tetrabutyl titanate through iodine-doping.[147] After calcination at 400 °C, the I-doped titania nanoparticles with a mean diameter of ~5 nm showed strong absorption in the 400 − 550 nm range. Compared to undoped titania and Degussa P25 catalyst, they had a more pronounced photoactivity in phenol degradation under UV and visible light illumination, in particular the photoactivity was 4 times higher than that of Degussa P25 under visible light irradiation. This is because of the band gap narrowing effects of doping and because a certain amount of $Ti^{3+}$ surface states/cation vacancies have been generated to maintain the electroneutrality when $I^{5+}$ substituted for $Ti^{4+}$. The existence of surface states of $Ti^{3+}$ can slow down the recombination of the electron−hole pairs.

Wu et al. prepared C-doped titania nanotubes, nanowires and nanorods from titanate nanotubes.[149] The morphology of C-doped titania could be adjusted by the calcination temperature. The three types of 1D C-doped titania catalysts exhibited enhanced photocatalytic activity for degradation of toluene under both visible and simulated solar light irradiation compared with that of Degussa P25. This is due to the 1D nanostructure contributing to the efficient carrier transport and the band gap narrowing effects of C-doping.

## 1.4 Summary

In summary, various modifications of the geometry of nanosized materials were carried out to improve the active performance of photocatalyst and DSSC. The property of surface area plays an important role in the improvements of efficiency of photocatalysis and light-to-current conversion, as it facilitates reaction/interaction between the devices and the interacting media, which mainly occurs on the surface or at the interface and strongly depends on the surface area of the material. Mesoporous material is well-known for its high surface area compared to nanoparticles or nanoarrays. Moreover, as fabricating of mesoporous silica well-developed in Edler group,[150 151] mesoporous titania will be a good extension of the previous works. So, this work focused on the preparation of mesoporous titania films through different methods and application of home-made titania structures in DSSCs and photocatalysts..

For DSSCs, many high-efficient solar cells were made from titania photoelectrodes based on nanoarrays or nanoparticles, but efficiency is not the only way to judge whether or not these materials have better advantages than others with relatively low efficient cell performance. The efficiency of solar cells are highly dependent on the purity of materials, such as dye, electrolyte and very sensitive to the humidity of air.[50] Also, the traditional mesoporous titania film formed by removal of organics that used as the standard cells was due to the larger surface area of mesoporous titania film than bulk nanoparticles film. Considering the surface area, the titania with mesoporous structure still has an advantage over nanoparticles or nanoarrays, so we propose using ordered 2D-hexagonal meso-$TiO_2$ aggregates as the scattering particles in DSSC. These mesoporous particles can function as light scatterers without sacrificing the internal surface area needed for effective dye-uptake when applying them in DSSC. This will be described in Chapter 4.

Mesoporous titania thin films have proved to enhance phototocatalytic activity under UV light, but solar photocatalysts are more attractive than UV-Vis phototcatalysts, as it brings many conveniences for outdoor use under sun light. Also, the non-metal dopants have better stability than metal dopant, so mesoporous titania films doped by non-metal elements should be a good candidate for solar photocatalysts. Reports regarding non-metal doped mesoporous titania thin films have been scarce, so we first report a synthesis S-doped mesoporous titania films with a cubic mesostructure by dip-coating and then apply these films into a solar photocatalyst, which is shown in chapter 5.

For solar cells prepared from thin mesostructured titania film by dip coating, the efficiency is still far away from that achieved by DSSC based on the typical 10 μm thick titania film due to the relative low thickness. However, mesostructured photoelectrodes prepared by dip coating have a higher efficiency compared to nanoparticle films with the same thickness. Moreover, some of the doped titanias, such as N, have been applied into DSSC and showed a promising increase in efficiency.[152] Ordered mesoporous S-doped titania films were first successfully made and then used as a photocatalyst, so these films were also applied in a DSSC in the hope of improving the efficiency of the DSSC. Multiplayer coating is

required to make thicker film to obtain higher efficiency DSSC, and studied of this are reported in chapter 6.

As well as the popular, commonly used approaches to prepare mesoporous titania films, a novel method was adopted to prepare free-standing mesoporous films and applied these films into DSSC. The growth of unsupported films is a promising route to manufacture robust, thick films having a large area.[153] The first report of surfactant-templated titania films was by Henderson et al.[154] Their films could be easily seen by eye but were too fragile to remove from the solution surface. $TiO_2/ZrO_2$ films with a nanorod structure fabricated by Kan et al. were thicker and could be transferred to a glass substrate, although the structure completely collapsed during calcination.[155] After that, a series of titania binary oxide films were fabricated by Ji et al.[156] The interfacial films before calcination had either a lamellar or mesoporous structure with morphologies described as particle, ribbon or pieces, but the stability of these films to calcination was not reported. The only application of free-standing titania films published so far was as a photocatalyst reported by Ji et al.[157] They used $TiO_2$/ZnO hybrid films to degrade methylene blue dye but the photocatalytic performance was worse than that of a commercial photocatalyst due to the amorphous structure. In chapter 7, free-standing titania films were successfully made at the air-liquid interface. After calcination, the film is composed of mesoporous nanoparticles and nanowires having an anatase structure. This novel membrane was applied into DSSC for the first time and the results are reported in chapter 7.

# Chapter 2 Analysis Theory and Experimental

This chapter covers the methods of analysis and experimental used in this thesis.The characterization techiniuqes include X-ray scattering, neutron reflectivity, spectroscopic ellipsometry, dynamic light scattering, UV-Vis spectroscopy, electron microscopy, atomic force microscopy, $N_2$ adsorption and desorption, TGA & DSC, and solar cell characterization. A brief description of the theory behind each technique is given, followed by details of the equipment used for this research. All the chemicals and apparatus used in this thesis are listed and the whole experimental story during the experiments is explained, although some of the experimental details in the three major projects were described into the other chapters.

## 2.1 Analysis Theory

### *2.1.1 X-ray Scattering*

#### 2.1.1.1 Theory

When electromagnetic radiation interacts with matter, (Figure 2-1) several things happen, such as transmission, reflection, refraction, absorption, diffraction and scattering. It depends on the property of light and samples. Many techniques use this characteristic to obtain information of samples. X-ray diffraction (XRD) and small-angle X-ray scattering (SAXS) were based on scattering and diffraction to obtain structural information on short and long range ordering. For grazing incident SAXS (GISAXS), as well as scattering and diffraction, reflection should also be considered. Ellipsometry analysis (described in section 2.3) is mostly based on refraction and reflection to obtain the optical properties and thickness of film samples. Dynamic light scattering is based on scattering and diffraction to obtain the particle size of sample in liquid (described in section 2.4). For UV-Vis spectroscopy, transmission, reflection and absorption are commonly used (described in section 2.5). For electron microscopy, scattering, transmission and diffraction can be observed (described in section 2.6).

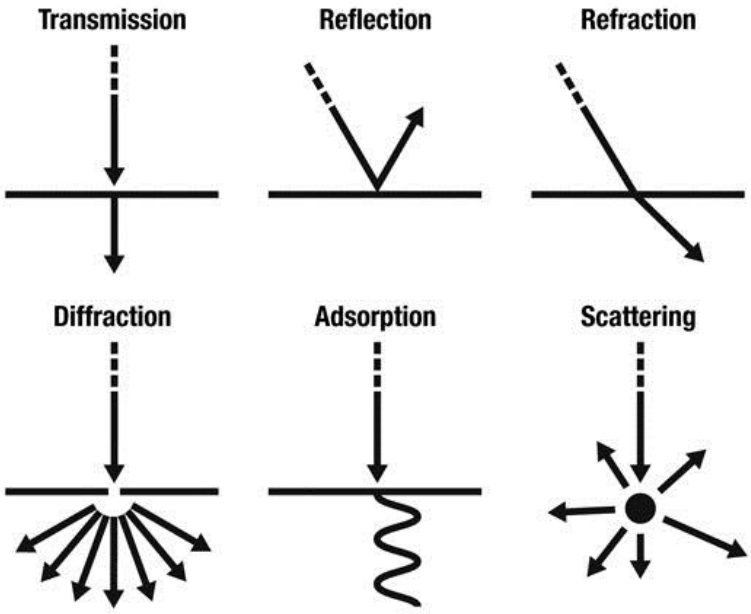


**Figure 2-1 when electromagnetic radiation meets matter, different things occur.**

X-rays are electromagnetic radiation, which has both wave-like and particle-like properties, with wavelengths from 0.01 to 10 nm. X-rays are usually produced from a copper target tube with energy of 5 - 100 keV. More powerful X-rays can be obtained from an electron synchrotron or electron storage ring by accelerating electrons up to several GeV.[158]

The scattering of X-rays is characterized by the resultant change in its momentum, *p*, and energy, *E*, where *h* is Planck constant, $\upsilon$ is the wave frequency and $\lambda$ is the wavelength.[159]

$$E = h\nu \quad \text{(Planck's hypothesis)} \qquad 2.1$$

$$\lambda = \frac{h}{p} \quad \text{(Broglie's proposal)} \qquad 2.2$$

As shown in Figure 2-2, the scattered waves have a wavevector, $k_f$, and angular frequency, $\omega_f$, so the momentum transfer can be expressed as

$$p = \hbar k_i - \hbar k_f = \hbar Q \qquad 2.3$$

Where the reduced Planck's constant is $\hbar = h/2\pi$, and wave vector difference

$$Q = k_i - k_f \qquad 2.4$$

And, similarly, the energy transfer is

$$E = \hbar\omega \qquad 2.5$$

$$\omega = \omega_i - \omega_f \qquad 2.6$$

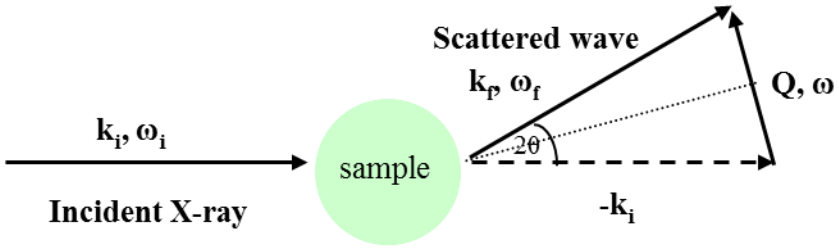


**Figure 2-2 Geometry of scattered X-ray by a sample through an angle of 2θ.**

In inelastic scattering, the scattered waves have a lower energy than incident beam, because the momentum is transferred when they collide inelastically with electrons ($\omega > 0$, $E > 0$). In elastic scattering, the scattered waves have the same frequency and wavelength as the incident X-rays ($\omega = 0$, $E = 0$, $|k_i| = |k_f| = \frac{2\pi}{\lambda}$), so

$$Q = k_f - k_i = \frac{4\pi \sin\theta}{\lambda} . \qquad 2.7$$

This scattering is the main type of scattering and can give rise to diffraction effects, which is the basis of wide-angle X-ray scattering (WAXS) or XRD, SAXS and GISAXS.

The incident wave with a single direction of propagation is deflected and propagates in new and other directions due to coherent scattering, constructive and destructive interference effects. This phenomenon is known as diffraction. The constructive interference only happens in a few directions when the scattered waves scatter according to Bragg's law. Figure 2-3 shows the diagram of Bragg diffraction.

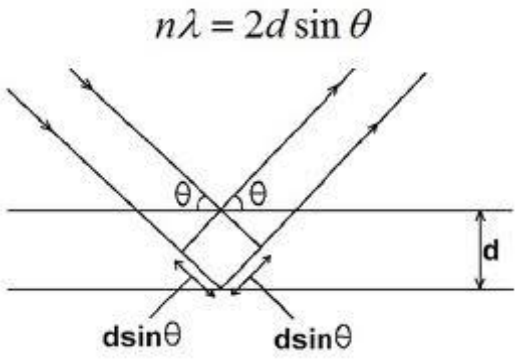


**Figure 2-3 Schematic diagram of Bragg diffraction.**

Bragg's law provides the condition for a plane wave to be diffracted by a family of lattice planes:

$$2d\sin\theta = n\lambda \qquad 2.8$$

where *n* is an integer, *d* is the spacing of parallel lattice planes and $2\theta$ is the diffraction angle, the angle between the incoming and scattered X-ray beams.

### 2.1.1.2 WAXS & SAXS

Both small and wide angle X-ray scatters (WAXS and SAXS) consist of three basic parts: an X-ray source, a sample holder, and an X-ray detector, as shown in Figure 2-4

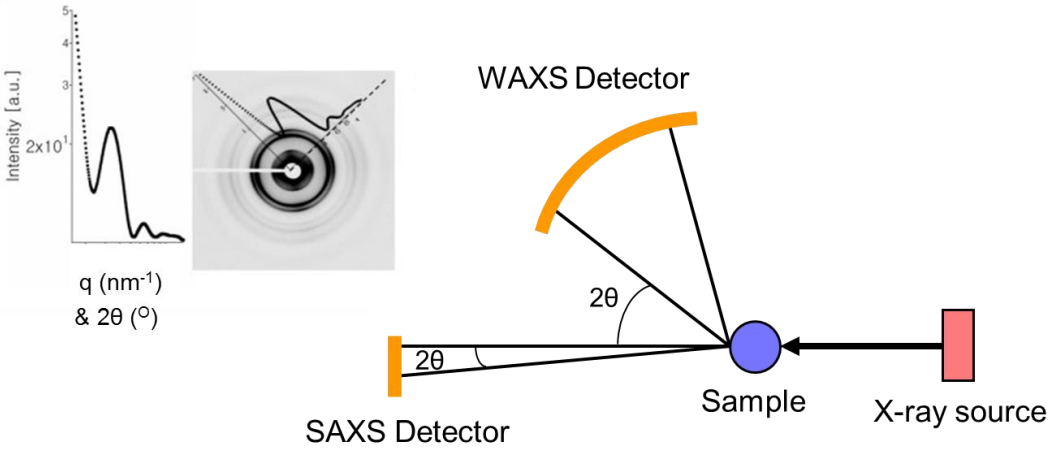


**Figure 2-4 Schematic diagram of WAXS and SAXS.**

Characteristic X-ray spectra of the target material are emitted under electron-target interaction, when an electron beam strikes the target. The electron beam usually is produced by a heated cathode, when a high voltage is applied.

Then, the spectra are filtered by foils or a crystal monochromator to obtain monochromatic X-rays. These X-rays are collimated and directed onto the sample. When X-rays pass through the sample, elastic and inelastic scatterings occur. Elastic scattering only has direction change, so it can give rise to diffraction effects. The intensity of the reflected X-rays is recorded by a detector.

Wide-angle X-ray diffraction contains structural information and is usually presented as a function of $2\theta$. However, small-angle X-ray scattering contains information on relatively large scale structures and is usually presented as functions of $Q$. The relationship between $Q$ and $\theta$ is shown in equation 2.7.

The unit cell is given by the lattice parameters in crystals: the length of the cell edges are denoted as $a,b,c$ and the angles between them are denoted as $\alpha$, $\beta$, and $\gamma$. Vector and lattice planes can be given using the Miller index notation, written as ($hkl$) to describe the individual plane. Combined with the Bragg equation, Table 2-1 lists the relationship between $d$ value and lattice index of seven crystal systems. Every diffraction peak corresponds to a d-spacing. Once all d-spacings have been determined, automated search/match routines compare the d-spacings of the unknown to those of known materials. Because each material has a unique set of d-spacings, matching these d-spacings provides an identification of the unknown crystalline sample.

**Table 2-1 The relationship between d value and lattice index of seven crystal systems.[160]**

| ***System*** | ***d value*** | ***Essential symmetries*** |
|---|---|---|
| Cubic | $\frac{1}{d^2}=\frac{h^2+k^2+l^2}{a^2}$ | a=b=c<br>α=β=γ=90° |
| Tetragonal | $\frac{1}{d^2}=\frac{h^2+k^2}{a^2}+\frac{l^2}{c^2}$ | a=b≠c<br>α=β=γ=90° |
| Orthogonal | $\frac{1}{d^2}=\frac{h^2}{a^2}+\frac{k^2}{b^2}+\frac{l^2}{c^2}$ | a≠b≠c<br>α=β=γ=90° |
| Hexagonal | $\frac{1}{d^2}=\frac{4}{3}\frac{h^2+k^2+hk}{a^2}+\frac{l^2}{c^2}$ | a=b≠c<br>α=β=90° |
| Trigonal | $\frac{1}{d^2}=\frac{(h^2+k^2+l^2)\sin^2\alpha+2(hk+kl+hl)(\cos^2\alpha-\cos\alpha)}{a^2(1-3\cos^2\alpha+2\cos^3\alpha)}$ | a=b=c<br>α=β=γ≠90° |
| Monoclinic | $\frac{1}{d^2}=\frac{h^2}{a^2\sin^2\beta}+\frac{k^2}{b^2}+\frac{l^2}{c^2\sin^2\beta}-\frac{2h\cos\beta}{ac\sin^2\beta}$ | a≠b≠c<br>α=β=90°≠γ |
| Triclinic | none | a≠b≠c<br>α≠β≠γ |

In periodically ordered but locally-amorphous samples, the group of atoms in the “unit cell” is taken in the broad sense to include the regions of discontinuous density, for example the pore, or crystalline regions. The type of the long range order can be easily detected according to the positions of the Bragg diffraction peaks in the small angle range. Some typical ratios of q values relative to the periodic structure are listed in Table 2-2.

**Table 2-2 Typical mesostructures found in surfactant templated inorganic materials and their diffraction properties.**

| *Crystal system* | | *Diffraction properties (peak ratios of q)* |
|---|---|---|
| Wormlike | | One peak |
| Lamellar | | 1 (001) : 2 (002) : 3 (003) : 4 (004) : 5 (005) … |
| Hexagonal | $p6mm$ | 1 (100) : $\sqrt{3}$ (110) : 2 (200) : $\sqrt{7}$ (210) : 3 (300) … |
| Orthorgonal | $c2mm$ | $\sqrt{2}$ (110) : 2 (200) : $\sqrt{8}$ (220) : $\sqrt{10}$ (310) : 4 (400) … |
| Cubic | $Pm\bar{3}n$ | $\sqrt{2}$ (110) : 2 (200) : $\sqrt{5}$ (210) : $\sqrt{6}$ (211) : $\sqrt{8}$ (220) : $\sqrt{10}$ (310) : $\sqrt{12}$ (222) : $\sqrt{13}$ (320) : $\sqrt{14}$ (321) … |
| | $Im\bar{3}m$ | $\sqrt{2}$ (110) : 2 (200) : $\sqrt{6}$ (211) : $\sqrt{8}$ (220) : $\sqrt{10}$ (310) : $\sqrt{12}$ (222) : $\sqrt{14}$ (321) : 4 (400) … |
| | $Fd\bar{3}m$ | $\sqrt{3}$ (111) : $\sqrt{8}$ (220) : $\sqrt{11}$ (311) : $\sqrt{12}$ (222) : 4 (400) : $\sqrt{19}$ (331) : $\sqrt{24}$ (422) … |
| | $Fm\bar{3}m$ | $\sqrt{3}$ (111) : 2 (200) : $\sqrt{8}$ (220) : $\sqrt{11}$ (311) : $\sqrt{12}$ (222) : 4 (400) : $\sqrt{19}$ (331) : $\sqrt{20}$ (420) : $\sqrt{24}$ (422) … |
| | $Pm\bar{3}m$ | No space group extinction; 1 (100) : $\sqrt{2}$ (110) : $\sqrt{3}$ (111) : 2 (200) : $\sqrt{5}$ (210) : $\sqrt{6}$ (211) : $\sqrt{8}$ (220) : 3 (300) … |
| | $Ia\bar{3}d$ | $\sqrt{6}$ (211) : $\sqrt{8}$ (220) : $\sqrt{14}$ (321) : 4 (400) : $\sqrt{20}$ (420) : $\sqrt{22}$ (332) : $\sqrt{24}$ (422) : $\sqrt{26}$ (431) : $\sqrt{32}$ (440) … |
| | $Pn\bar{3}m$ | $\sqrt{2}$ (110) : $\sqrt{3}$ (111) : 2 (200) : $\sqrt{6}$ (211) : $\sqrt{8}$ (220) : 3 (221) : $\sqrt{10}$ (310) : $\sqrt{11}$ (311) : $\sqrt{12}$ (222) : $\sqrt{14}$ (321) … |

### 2.1.1.3 GISAXS & X-ray Reflectivity

The basis of reflectivity is measuring the intensity or reflectivity of radiation from an interface during specular reflection, which states the incident angle $\theta_i$ and reflected angle $\theta_f$ are equal with respect to the surface normal.

Figure 2-5 shows the reflection geometry between two homogeneous media with refraction indices $n_0$ and $n_1$ respectively. Both the reflected and refracted rays are in the plane of incidence. The $z$ components of the incident wave

vectors ($k_{iz}$) and reflected wave vectors ($k_{fz}$) on the surface are able to be calculated as

$$k_{iz} = \frac{2\pi \sin\theta_i}{\lambda} \qquad 2.9$$

$$k_{fz} = \frac{2\pi \sin\theta_f}{\lambda} \qquad 2.10$$

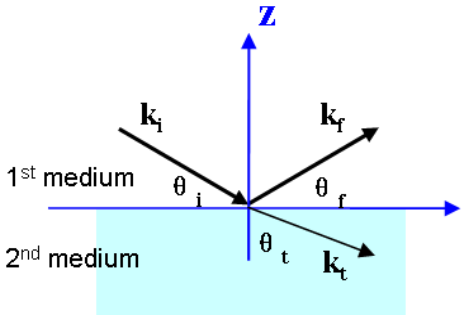


**Figure 2-5 Reflection geometry between two homogeneous media.**

The refractive index of the 1st medium is $n_0$ and the second is $n_1$, so the refractive index $n$, $n = \frac{n_1}{n_0}$, is the ratio of the wave vectors in the two media at the interface. If we consider the first medium is air or vacuum, whose refractive index is equal to 1, the refractive index $n$ is equal to the refractive indice $n_1$.

The refractive index can also be described as:

$$n = 1 - \lambda^2 A - \lambda B i \qquad 2.11$$

Where $A = N_b / 2\pi$ and $B$ can be ignored as it is much smaller than $A$ for most materials. So the refractive index $n$ can be written as:

$$n \approx 1 - \frac{N_b \lambda^2}{2\pi} \qquad 2.12$$

For X-rays,

$$N_b = r_e \times \rho_e \qquad 2.13$$

Where $N_b$ is the scattering length, $r_e$ is the radius of the electron cloud and $\rho_e$ is the electron density. This gives a scattering length density that increases with the atomic number of atoms within the sample. Because $N_b$ is positive for most materials, refractive index of many materials is smaller than 1. Thus total external reflection is usually observed. From Snell's Law we can know:

$$n_1 \sin\theta_t = \sqrt{(n_1^2 - n_0^2 \cos\theta_i^2)} \qquad 2.14$$

At total reflection, the critical glancing angle $\theta_c$ is equal to the incident angle $\theta_i$ and the refracted angle $\theta_t$ is 0, so:

$$\cos\theta_c \approx 1 - \frac{N_b \lambda^2}{2\pi} \qquad 2.15$$

As the refractive index of X-rays is slightly smaller than 1, so total external reflection occurs for grazing angles of incidence $\theta_i$ smaller than a critical angle $\theta_c$. This can be used to enhance surface sensitivity, as below this critical angle an evanescent wave propagates at the surface with a penetration depth of only a few nanometres.[161]

Interfacial structures are probed by specular reflectivity via plotting reflectivity against the scattering vector. The difference between the incident and reflected wave vectors is $Q$,

$$Q = k_i - k_f = k_{iz} - k_{fz} \qquad 2.16$$

In specular reflection, $\theta_i = \theta_f$, so the

$$Q = \frac{4\pi \sin\theta_i}{\lambda} \qquad 2.17$$

For a single layer, fringes are visible in the reflectivity pattern, which is typically fitted by a model. However, this has not been used in this work. If a sample has multiple layers of different scattering length density, the reflectivity profile of an interface becomes more complicated. Due to the elastic nature of scattering, the incident and reflected beams can constructively or destructively

interact with each other. So the incident wave propagates in new and other directions after reflecting and the information gained from a reflectivity scattering curve corresponds to depth profile perpendicular to the interface, along the z-axis.[162] These interferences can give rise to Bragg diffraction, if the sample has long range order with a periodic structure, such as a hexagonal, cubic or lamellar phase. Except if the sample is highly aligned next to the interface some of the peaks will be missing from the pattern due to that orientation meaning that the scattering plane doesn't intersect the detector.

GISAXS is a scattering geometry based on the diffraction and specular reflection from surfaces.[163] Figure 2-6 shows the schematic diagram of GISAXS.

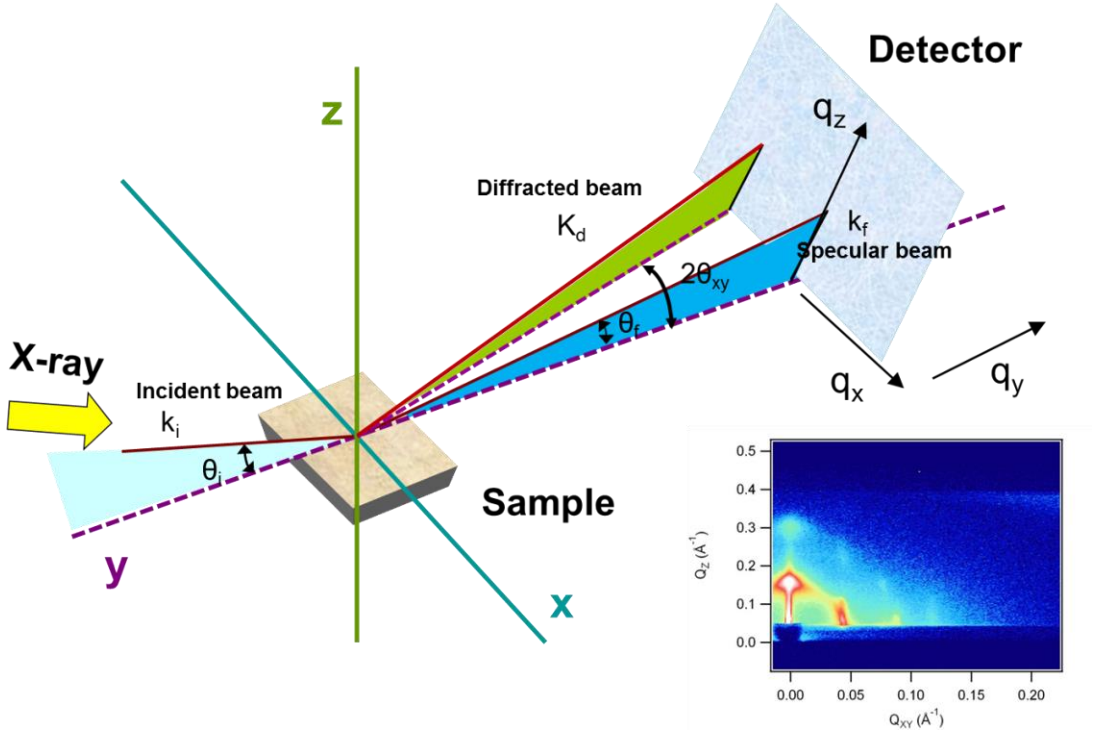


**Figure 2-6 Schematic diagram of GISAXS.**

The intensity of the specularly reflected and diffracted beam as a function of both the vertical and horizontal components was recorded by the detector. The components of the scattering vector are given by,[164]

$$q_{x,y,z} = \frac{2\pi}{\lambda}\begin{bmatrix} \cos(\theta_f)\cos(2\theta_{xy})\cos(\theta_i) \\ \cos(\theta_f)\sin(2\theta_{xy}) \\ \sin(\theta_f)+\sin(\theta_i) \end{bmatrix} \qquad 2.18$$

where $\theta_i$ is the incident angle, $\theta_f$ is the reflected angle, $2\theta_{xy}$ is the

diffraction angle and $\lambda$ is the X-ray wavelength. GISAXS patterns showing diffraction spots or arcs are indexed using the rules for identifying ordered mesostructures outlined above in section 2.1.2. If the patterns do not show diffraction spots, then the images can be analysed by taking cuts through the data perpendicular to and parallel to the specular ridge of scattering (Figure 2-7). The "detector cut" parallel to the specular ridge can be analysed to provide information about the vertical structure of the film while the in-plane cut can provide information about the lateral film structure.[165-167] In Figure 2-7 below, the anisotropy in the scattering suggests that the film is compressed in the vertical direction as the scattering peaks at 0.09 $Å^{-1}$ in this direction, while a sharper diffraction ring is seen at 0.03 $Å^{-1}$ in the in-plane cut. The film is better ordered in-plane as peaks can be seen at ~ 0.03 and 0.06 $Å^{-1}$.

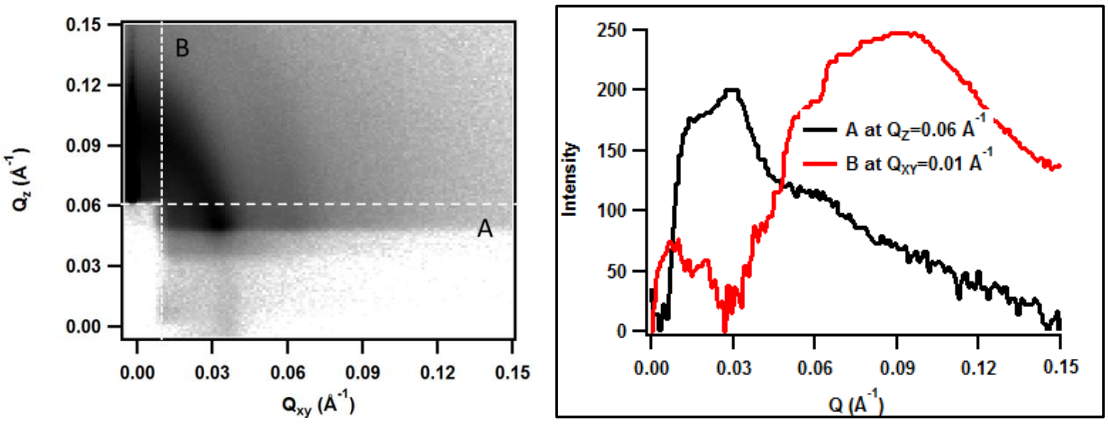


**Figure 2-7 GISAXS image (left) and corresponding intensity profile in the $Q_z$ and $Q_{xy}$ directions (right).**

### 2.1.1.4 Measurement

SAXS patterns in this project were measured either in–house or at a synchrotron. In-house measurements were made using an Anton Paar SAXSess system on a PANalytical PW3830 X-ray generator. Synchrotron small angle X-ray scattering experiments were performed using non-crystalline diffraction beamline (I22) instrument at the Diamond Light Source, UK. Table 2-3 gives the I22 beamline specifications.[168]

**Table 2-3 I22 beamline specifications.**

| *Specifications* | *Parameter* |
|---|---|
| Energy range | 3.7-20 keV |
| d-spacing range | 1-5000 Å |
| Photon beam size at sample | 320(H)× 70(V) μm |
| Beam divergence at 12 keV | 50(H)× 70(V) μrad |

An Anton Paar SAXSess small angle X-ray scattering instrument with a measurable Q range of 0.077 - 2.70 $Å^{-1}$ was used to perform SAXS measurements at University of Bath. Line and pin-hole X-ray sources (15.4 nm) on a Cu X-ray tube, operated at 40 kV and 50 mA were used. An elliptical focusing mirror was utilized to further enhance the flux. Collimation is achieved using a block collimator with a roughness of less than 0.14 μm/cm and the flight path from source to detector is in a chamber evacuated to below 5 mbar. X-rays are detected by a reusable Europium excitation based image plate (size: 66 × 200 mm) with a 42.3 $μm^2$ pixel size. After exposure the image plate is read by a Perkin Elmer Cyclone reader using OptiQuant software. The powder samples were put in a sample holder between two pieces of Sellotape™ and held in place by two copper plates and measured at 25 °C. The background was tested by using two pieces of Sellotape™ illuminated for the same time as the sample and subtracted during the data analysis.

XRD analyses of the samples in a 0.3 mm borosilicate glass capillary was performed on a Bruker D8 powder diffractometer using monochromatic Cu Kα radiation (15.4 nm) and with generator voltage and current of 40 kV and 40 mA respectively. X-ray scans were made between 2θ angles of 20 and 60 or 70 °. A scan speed of 3 s per step and a step size of 0.025 ° were used.

GISAXS experiments on film samples on silicon wafers were performed to observe the film structure on the I07 beamline at the Diamond Light Source in Oxford, UK. I07 is a high-resolution X-ray diffraction beamline for investigating the structure of surfaces and interfaces. The entire sample scattering was recorded in air. GISAXS patterns were collected with $Q_z$ range of 0 - 0.5 $Å^{-1}$ and $Q_{xy}$ range of 0 - 0.25 $Å^{-1}$ at an incident angle of 0.25 º, using an energy of 12.5 keV (λ = 1.0 Å). A 54 × 182 channel detector (Pilatus 2M) with a vertical alignment was used to

collect data during experiments. Pattern of silver behenate prepared by spin coating on silicon wafer were used for calibration.[169] The silver behenate has a lamellar structure with a d-spacing of 58.380 Å in (001) plane. The image of raw data is expressed in the units of pixels, and then we can obtain the value ratio between pixels and Å according to the known d-spacing of silver behenate. So we can modify the raw image from pixels to Å.

## *2.1.2 Neutron reflectivity*

### 2.1.2.1 Theory

Neutrons are neutral particles that are unaffected by the charge of the orbital electrons.[170] They interact with the nucleus of the atom via the strong nuclear force. Specular neutron reflection provides information about inhomogeneities normal to an interface or surface.

The basis of a neutron reflection experiment is the variation of specular reflectivity with the wave vector transfer (*Q*), perpendicular to the surface or interface (described in section 2.1.3).[171] This can be achieved in two ways: either by using a single monochromatic wavelength and varying the grazing angle of incidence or by using a fixed angle of incidence and a range of wavelengths sorted by time-of-flight.

It is horizontal interfaces at various depths through the sample that cause the reflection. The information gained from a reflectivity scattering curve corresponds to depth profile perpendicular to the interface, along the z-axis.

In specular reflection, $\theta_i = \theta_f$ , combining with equation 2.9 and 2.10, so

$$Q_z = 4\pi \sin\theta_i / \lambda \qquad 2.19$$

With the same frequency and wavelength of incident and reflected waves, constructive and destructive interference are found to occur giving rise to diffraction, so that the incident wave propagates in new and other directions after reflecting. In diffraction patterns, it contains the structure information based on the theory of Bragg equation. Some details of Bragg equation are described above in the section 2.1.1. Where no diffraction peaks are visible the reflectivity is typically fitted as a series of layers stacked on the surface,[172] however this has not been used in this work.

### 2.1.2.2 Measurement

Neutron reflectivity measurements of the films grown at the air/water interface and dip-coated films on silicon wafer were performed on INTER instruments (Target Station II, detailed schematic diagram in Figure 2-8 at the ISIS Pulsed Neutron Source facility within the Rutherford Appleton Laboratories. For the INTER instrument, it operated at lower frequency of 10 Hz by taking 1 in 5 pulses from the existing ISIS synchrotron. The INTER reflectivity views the grooved surface of the cold coupled methane moderator giving the best possible flux gains without compromising resolution or signal to noise.

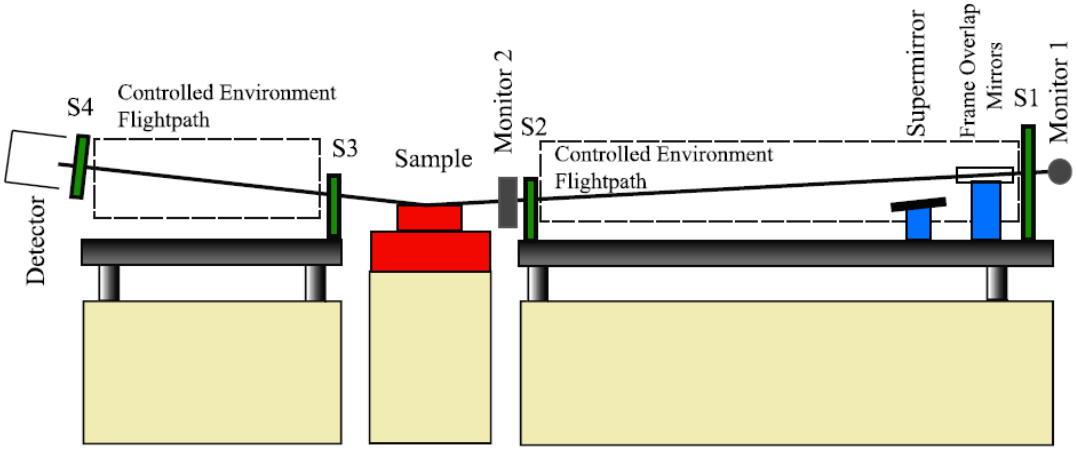


**Figure 2-8 Schematic representation of the INTER reflectivity on Target II at ISIS.[173]**

In the neutron reflectivity experiment of the films grown at the air/water interface, the solution is prepared by pouring a film formation solution into a 4 x 15 cm PTFE trough to provide a meniscus above the edge of the trough, and then the scattering data was collected on this air/solution interface. The incident angle used was either 0.7 or 2.3 °, with data being collected between 0.01 and 0.1 $Å^{-1}$ or 0.03 and 0.4 $Å^{-1}$ in $D_2O$ at 25 °C in 3 min patterns.

## *2.1.3 Spectroscopic ellipsometry analysis*

### 2.1.3.1 Theory

Light can be described as an electromagnetic wave composed of mutually perpendicular electric and magnetic fields that are always orthogonal to the propagation direction. Normally, the magnetic field is ignored due to its

unchanged nature. When the electric field of light follows a specific path and traces out a distinct shape at any point, the light is defined as polarized light.[174]

When polarized light meets matter, reflection and transmission occur at the surface. There are different paths for electric fields parallel and perpendicular to the sample surface due to the various properties of the surface, meaning light can be separated into p- and s polarized vectors. The direction of the p polarized component is parallel to the plane of incidence and the s-polarized component is perpendicular to the plane of incidence. Ellipsometry mainly measures how the p- and s- components change upon reflection.[175]

Figure 2-9 shows the reflection geometry between two multiple interfaces, such as a film-covered surface.

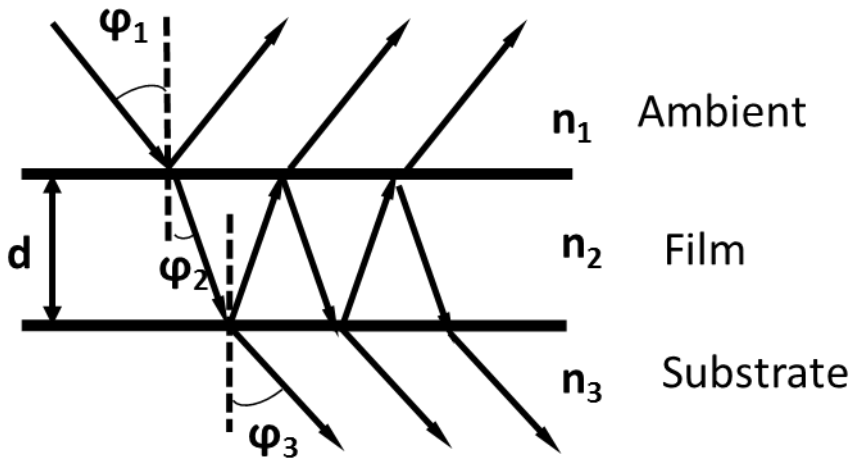


**Figure 2-9 Light reflects and refracts in film-covered surface.**

According to Snell's law, we have

$$n_1 \cos\varphi_1 = n_2 \cos\varphi_2 = n_3 \cos\varphi_3 \qquad 2.20$$

where $n_1$, $n_2$ and $n_3$ are the complex refractive index of first (ambient), second (film) and third (substrate) medias, respectively. $\varphi_1$ is the incident angle of light, $\varphi_2$ and $\varphi_3$ are the refraction angle at the film and substrate surfaces respectively.

The distance d between two media (film thickness) can be expressed as:

$$\delta = 2\pi d n_2 \cos\varphi_2 / \lambda \qquad 2.21$$

where $2\delta$ is the phase difference between two reflection waves and $\lambda$ is the wavelength of incident light.

If $r_{1p}$ and $r_{1s}$ are the Fresnel coefficients for the components *p* and *s* of light at film surface and $r_{2p}$ and $r_{2s}$ are the Fresnel coefficients for the components *p* and *s* of light at substrate surface, then

$$r_{1p} = (n_2 \cos\varphi_1 - n_1 \cos\varphi_2)/(n_2 \cos\varphi_1 + n_1 \cos\varphi_2) \qquad 2.22$$

$$r_{2p} = (n_3 \cos\varphi_2 - n_2 \cos\varphi_3)/(n_3 \cos\varphi_2 + n_2 \cos\varphi_3) \qquad 2.23$$

$$r_{1s} = (n_1 \cos\varphi_1 - n_2 \cos\varphi_2)/(n_1 \cos\varphi_1 + n_2 \cos\varphi_2) \qquad 2.24$$

$$r_{2s} = (n_2 \cos\varphi_2 - n_3 \cos\varphi_3)/(n_2 \cos\varphi_2 + n_3 \cos\varphi_3) \qquad 2.25$$

The amplitude and phase changes in polarization are commonly written as:[176]

$$\rho = \tan\varphi \times e^{i\Delta} = \frac{E_{rp}/E_{rs}}{E_{ip}/E_{is}} \qquad 2.26$$

where $\rho$ is the change of polarization between the input and output light, $\tan\varphi$ is the amplitude ratio upon reflection, $\Delta$ is the phase shift, $E_{ip}$ and $E_{is}$ are the *p*- and *s*-components of incident light, $E_{rp}$ and $E_{rs}$ are the *p*- and *s*-components of reflected light. Moreover,

$$E_{rp} = E_{ip}(r_{1p} + r_{2p}e^{-i2\varphi})/(1 + r_{1p}r_{2p}e^{-i2\delta}) \qquad 2.27$$

$$E_{rs} = E_{is}(r_{1s} + r_{2s}e^{-i2\varphi})/(1 + r_{1s}r_{2s}e^{-i2\delta}) \qquad 2.38$$

Combining the equations from 2.19 to 2.27, we find that

$$\rho = f\,(n_1,\ n_2,\ n_3,\ \mathrm{d},\ \varphi_1,\ \lambda) \qquad 2.29$$

Usually, $n_1$, $\lambda$ and $\varphi_1$ are known, $n_3$ can be independently obtained, so $n_2$ and *d* are closely related to each other.

During ellipsometry measurements, the changes in light polarization can be used to determine the properties of the sample, such as film thickness and optical constants. In the ideal case of bulk materials without any surface layers, the refractive index $N$ can be calculated from the equation:[177]

$$N = \tan\phi[1 - \frac{4\rho}{(1+\rho)^2}\sin^2\phi] \qquad 2.30$$

where $\rho$ is the change of polarization between the input and output light, $\phi$ is the incident angle. However, there is typically a surface oxide or roughness on most materials which adds errors in the direct inversion formula. So, a model analysis is normally performed, after the sample is measured.[178]

Experimental data are obtained by testing under different wavelengths. A model is based on the equation 2.29 which describes each layer of material with thickness and optical constants. If these values are unknown, an estimate is given for the purpose of the initial calculation. The calculated values are compared to experimental data. Finding the best match between the model and the experiment is typically achieved through regression analysis. The best answer provides the optical constants and thickness parameters of the sample.

The ellipsometry instrument has components including a laser light source, polarization generator, sample stage, polarization analyser, and detector, shown in Figure 2-10.[179]

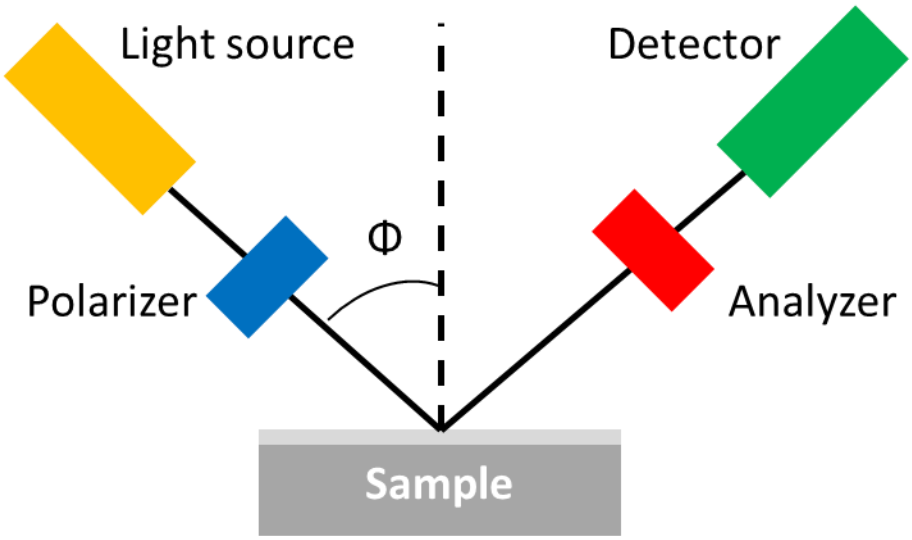


**Figure 2-10 Schematic diagram of ellipsometry instrument.**

### 2.1.3.2 Measurement

Film samples were tested using an ellipsometry measurement on an alpha-SE Ellipsometer from J.A. Wollam Co. under the control of software CompleteEASE. The instrument uses a laser with wavelength in the range of 380 - 900 nm and an incident angle of 70 º was used. For one sample, different areas

were tested to obtain the average value of film thickness and refractive index. Results were fitted by the model Absorbing films on Silicon contained in the CompleteEASE software according to the manual book, as the S-doped titania film absorbs some lights in the visible region. Fitting process was automatically done by software when a suitable model was chose. Figure 2-11 shows an example of ellipsometry data and fitted by CompleteEASE software. The amplitude and phase changes are Psi and Delta respectively.

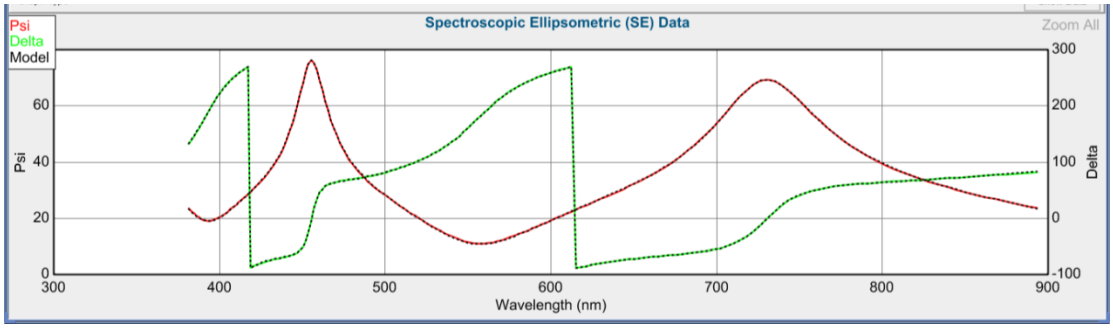


**Figure 2-11 An example of ellipsometry data and fitted by CompleteEASE software. The amplitude and phase changes are Psi and Delta respectively.**

The refractive index was used to calculated the porosity of the mesoporous titania thin films through the following equation [180] :

$$\mathrm{P} = \left(1 - \frac{n^2 - 1}{n_T^2 - 1}\right) \times 100\% \qquad 2.31$$

where $n$ is the refractive index measured by ellipsometry and $n_T$ is the refractive index of anatase titania ($n_T = 2.55$).

## *2.1.4 Dynamic light scattering*

### 2.1.4.2 Theory

When particles are suspended in a liquid, the particles are constantly moving due to Brownian motion. The movement of particles is random, driven by collisions with the molecules or atoms of the liquid that surrounds the particle. Moreover, the movement speed of particles is in proportion to particle size. Based on this theory, Dynamic light scattering (DLS) measures Brownian motion and links it to the size of the particles by illuminating the particles with a laser and analysing the intensity variations in the scattered light.[181]

For stationary particles, if we put a detector close to the particle, the detector will show speckle patterns consisting of bright and dark areas, because of the constructive and destructive interferences between incident laser and scattered lights. However, the particles in a liquid are randomly moving, which will induce the intensity fluctuation of the brightness in speckle patterns. By measuring the rate of the intensity variation, the size of the particles can be worked out from the correlation function.[182]

If we compared the intensity signal of a particular part of the speckle pattern at one point in time (say time = t) to the intensity signal a very short time later (t + dt), we will find the two signals are very similar or strongly correlated. Then, if we compare the original signal at t to intensity at t + 2dt, the two signals are still well correlated but not as strong as at t+dt.[182] If we compare the original signal intensity to itself then we will have perfect correlation. The perfect correlation is reported as 1 and no correlation is 0. So, if larger particles are being measured, the intensity of the speckle pattern will change more slowly due to the slower movement in Brownian motion. Oppositely, the intensity change from smaller particles will be quicker. The change of signal intensity can be expressed by the correlation function. Figure 2-12 shows the correlation function for large and small particles.

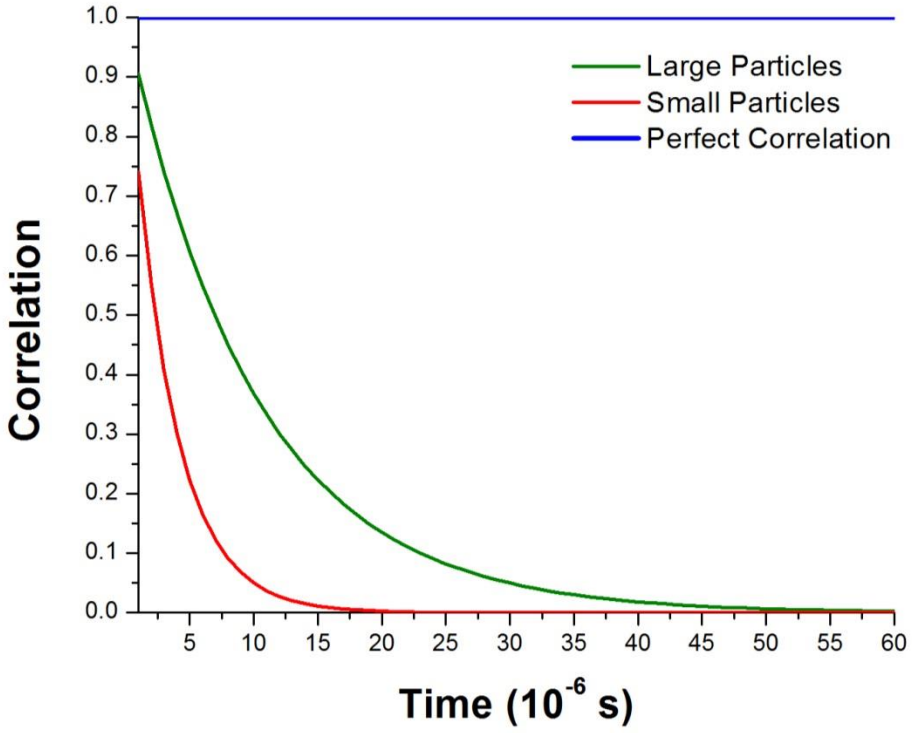


**Figure 2-12 Exponential decay of the correlation function.**[183]

Figure 2-13 shows a typical DLS system. It consists of a laser, a cell, a detector, an attenuator, a correlator and computer equipped with specialist software. The laser is used to provide a light source to illuminate the particle sample in liquid within a cell. Most of the light passes through the sample and some of it is scattered back. A detector, either at position 173 or 90º, is used to measure the intensity of the scattered beam. The detector at 180 º cannot be used, as it will block the laser. The angle < 90 º is not adopted due to the incident beam passed from sample will affect the results However, if too much light is detected, the detector will be overloaded. So, an attenuator is used to reduce the intensity of the laser and hence decrease the scattering intensity. The scattering intensity signal from the detector is passed to the correlator. The correlator compares the correlation function over time and this information is then passed to a computer to analyse the data and obtain size information.

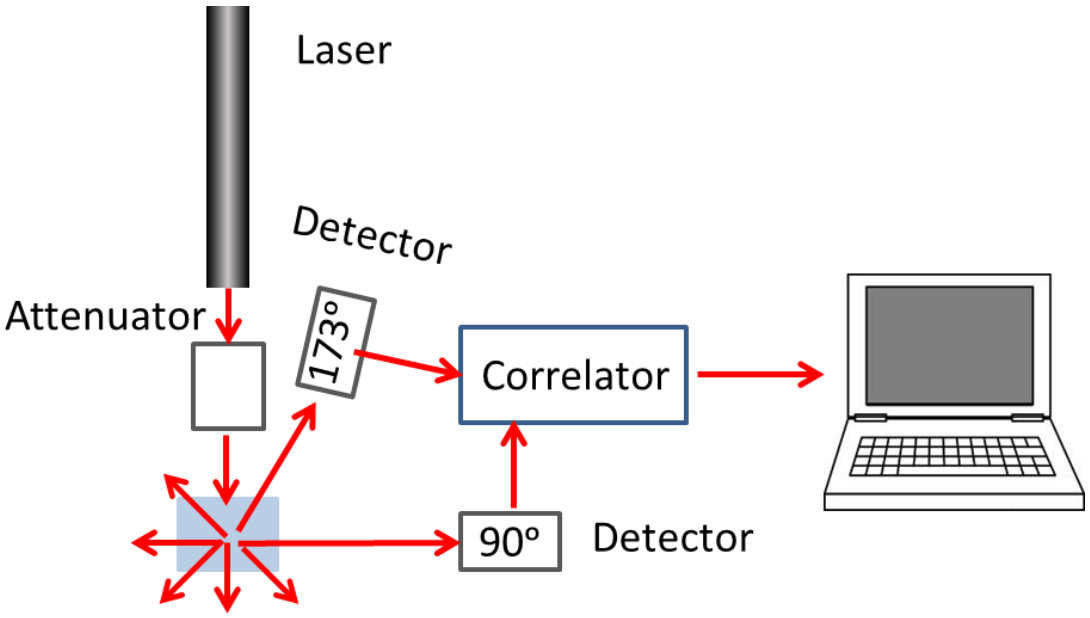


**Figure 2-13 Schematic diagram of DLS system.**

#### 2.1.4.2 Measurement

A Zetasizer Nano from Malvern was used in this work to estimate the particle size. The backscatter detector (173 º) was used in this instrument. Because the backscatter is being measured, the incident beam does not need to pass through the entire sample, which can reduce the multiple scattering effects, as it will affect the track of light and then affect the intensity and direction of lights that we are interested.

During testing, 1.5 ml of the titania colloidal solution was put into the cell and measured several times at room temperature. Then the particle size and polydispersity was calculated by the Zetasizer software and the average results were chosen. To obtain a consistent estimate of particle size, it is normal to do a dilution series and plot a graph to find the size at zero concentration, but we did not do this for titania colloidal solution as we want to check the size of titania clusters in the colloidal solution, rather than the size of a single titania particle.

### *2.1.5 UV-Vis spectroscopy*

#### 2.1.5.1 Theory

If a beam of monochromatic light passes through a transparent medium, part of the light is absorbed and the transmitted beam has a lower intensity than the intensity of the incident beam. When the medium is a transparent solution, shown

in Figure 2-14, the relationship between absorbance and concentration of the absorbate is described in the Beer-Lambert law,[184] written as:

$$A = \log\left(\frac{I_0}{I}\right) = \varepsilon c L \qquad 2.32$$

Where $A$ is the absorption, $I_0$ is the intensity of incident beam, $I$ is the intensity of transmitted beam, $c$ is the concentration of solute, $L$ is the path length and $\varepsilon$ is the molar absorption coefficient. The molar absorption coefficient is constant for a particular solute and varies depending on the wavelength of the incident beam, so it can be figured out by plotting the adsorption against the concentration of solute. In other words, the beam adsorption is proportional to the concentration of solute in a particular solute at a fixed wavelength of incident beam and path length.

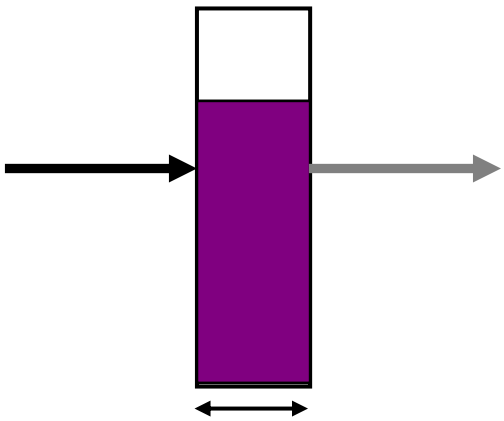

**Figure 2-14 A schematic representation of Beer-Lambert adsorption.**

In order to be able to determine dye concentration, the molar adsorption coefficient was required for dye N719 in 0.1 M KOH according to the Beer-Lambert Law. The data for UV/Vis adsorption of a range of amounts of N719 dissolved into 0.1 M KOH was kindly supplied by Thomas Risbridger. Under a fixed wavelength of 528 nm, the adsorption intensity is measured as a function of concentration of KOH, shown in Figure 2-15. The slope of this curve is the value of the molar adsorption coefficient, 9694.7 ± 152 L/mol cm.

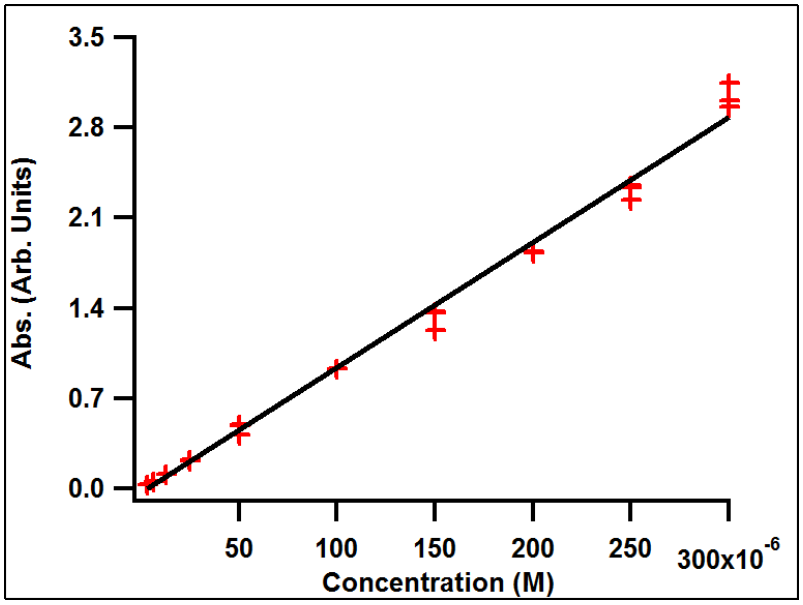


**Figure 2-15 Adsorption as a function of N719 concentration in 0.1M KOH solution under 528 nm illumination.**

In Figure 2-16 (left), when a beam of light hits a rough surface, the light is reflected at different angles (diffuse reflection) rather than just one angle as in the case of specular reflection. The most general mechanism by which a surface gives diffuse reflection is that most of the diffused light is not from surface but results from scattering centres beneath the surface, illustrated in Figure 2-16 (right). If the light illuminates the surface of the sample, a small part of the "primary" light is reflected by the first scatterer and most of it enters the sample. This light meets the second scatterer and produces a number of "secondary" reflections. Still some of the light can pass through the second scatterer to meet the third scatterers, and so on. These generate a lot of random reflections which finally arrive at the surface and exit in different directions.

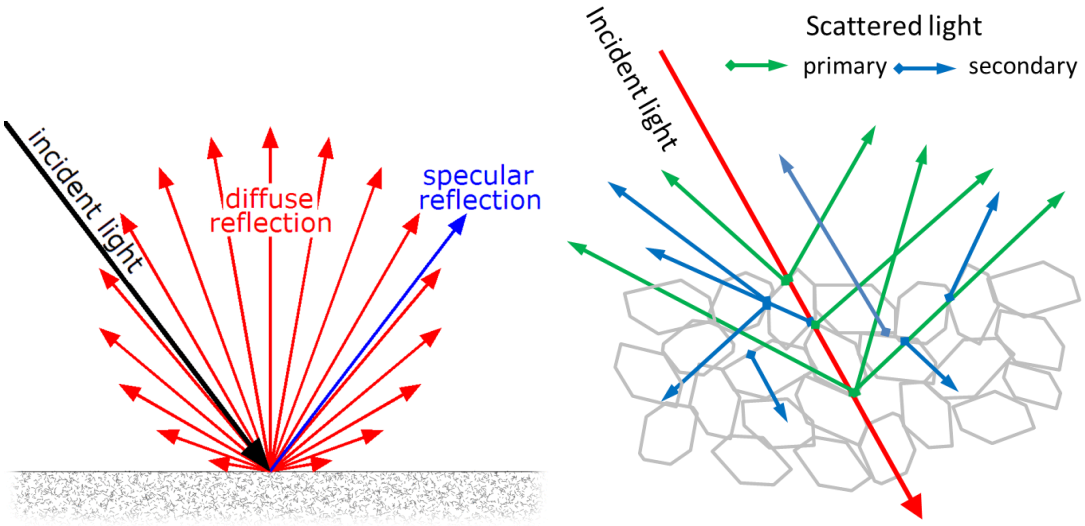


**Figure 2-16 Diffuse and specular reflection from a glossy surface (left); General mechanism of diffuse reflection by a solid surface (right).**

#### 2.1.5.2 Measurement

For film transmission and absorbance measurements, air was used for baseline correction. Samples were tested using an UV/Vis spectrometer (Varian, Cary 50 Probe). For dye desorption measurements, the adsorbed dye molecules were desorbed by using 0.1 M KOH solution. In this case, the 0.1 M KOH solution was used for baseline correction. Based on the Beer-Lambert law, the adsorbed dye amount was measured with the dye solution held in 1 cm thick quartz cuvettes. For reflection measurements, the film sample was tested using a UV-VIS-NIR instrument from Ocean Optics. The uncoated FTO glass substrate was used for the baseline correction.

The photocatalytic activity of the thin films with area ~3 $cm^2$ on Si wafer was monitored by immersing the samples into 100 ml of 5 µM methylene blue aqueous solution under 1 sun illumination from a TS Space Systems solar simulator. The films were allowed to reach an adsorption-desorption equilibrium for 1 h before sun irradiation. The concentration of MB solution was determined by measuring the visible light absorbance at 650 nm using the UV/Vis spectrophotometer. 3 mL of solution was used for testing but returned to the solution after the UV-Vis measurement.

### *2.1.6 Electron Microscopy*

#### 2.1.6.1 Theory

When an electron beam strikes the atoms in a sample (Figure 2-17), individual incident electrons undergo two types of scattering.[185] These are determined by the mass ratio of the electrons and colliding solids. If the electrons pass close to the nucleus of the atom, the directions of electrons change or they may even be backscattered. In this process, the kinetic energy and velocity of electrons remains the same as primary beam, so it is elastic scattering. When incident electrons interact with the atomic electrons of the sample, they collide with and displace electrons from their shells of target atoms. This interaction leads to energy "loss" from the incident electrons so is inelastic scattering. It places the sample in an unstable state and makes scanning electron microscopy possible.

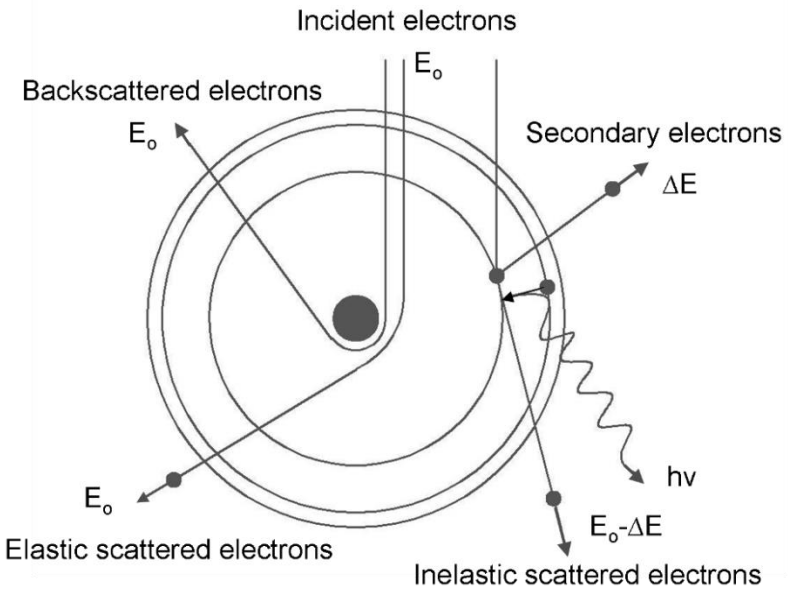


**Figure 2-17 Illustration of interaction of electrons with an atom.**

An incident electron may excite an electron in an atom in the sample during specimen interaction and lose most of its energy. The excited electron moves towards the surface of the sample and finally escapes from the surface if it still has sufficient energy. These excited electrons, named secondary electrons, can be used in scanning electron microscopy (SEM), because their production is topography related.[186] Due to their low energy after excitation (5 eV), only the secondary electrons very near the surface (< 10 nm) can escape from the sample undergoing elastic and inelastic collisions. Any changes in the topography in the sample that are larger than the depth of sample that can yield the changes of

secondary electrons can therefore be distinguished. So, the collection of secondary electrons reflects the topography of specimen.

Excluding that the secondary electrons are the most common signal used in SEM, backscattered electrons are also used in SEM imaging. The production of backscattered electrons has a direct relationship with the atomic number of the sample. The higher the atomic number, the more backscattered electrons are produced and collected, so the image of areas containing atoms with a higher atomic number appears brighter than those containing lower elements.

When the sample is thin enough, some of the incident beam can transmit through the specimen without any interactions with the specimen. These transmitted electrons are used in transmission electron microscopy (TEM) imaging. The amount of transmitted electrons is primarily determined by the thickness of the sample. Thick areas are darker than thin areas due to fewer transmitted electrons. The atomic number also plays an important role in the transmission of areas of a sample with the same thickness. Higher atomic number elements have more electrons that increase the chance of being scattered when the incident electrons pass through, so areas of atoms with higher atomic numbers are darker than those containing lower elements.

Another part of the incident electrons, are elastically scattered by atoms in the specimen, but transmitted through the remaining portion of the specimen. Some of them are scattered according to Bragg's Law, so these electrons contain information about the specimen. All scattered electrons that were incident at the same angle are scattered by the same atomic plane. These scattered electrons can be collated to form a pattern of spots by using magnetic lenses and are used in TEM diffraction mapping. This pattern yields information on the orientation and crystal structure of the specimen.

As was mentioned above, inelastic scattering places the atom in an excited state. Excess energy is set free as X-rays, cathodoluminescence or Auger electrons, when the atom returns back to ground state. The energy of the X-ray is characteristic of the element from which the X-ray was emitted. So, these X-rays can be collected for qualitative elemental analysis by energy dispersive spectroscopy (EDS) X-ray detectors in SEM or TEM instruments.

#### 2.1.6.2 SEM & TEM

All of the electron microscopies have some similar basic components: an operating vacuum; an electron source; electron lenses for forming an electron probe; systems for defining the probe position; detectors to detect the signals, and an imaging forming system. A discussion of the vacuum systems is outside the scope of this thesis. More information can be obtained through papers and books.[187-190]

A thermionic source, especially the V-shape tungsten source, is traditionally used and a schematic diagram is shown in Figure 2-18. The filament is heated until a stream of electrons is produced. The positive potential acts as an electrostatic lens, accelerating the electrons. Meanwhile, the electrons are repelled toward the optical axis due to the negative potential of the cap and exit the gun area through the small hole in the Wehnelt cap to be used in SEM or TEM mode. Although the conventional tungsten filament is capable of providing the relatively large total current required for SEM and low magnification imaging in TEM, it cannot generate high intensity probes, to obtain high magnification imaging, because of the inherently low brightness. High resolution electron microscope mapping can be obtained by replacing the heated tungsten thermionic electron source with a high-brightness probe such as a field-emission (FE) cathode. A cold-FE source is simply a sharply pointed piece or single crystal of tungsten. The point is so sharp that it favours producing a very thin electron beam (less than 1 nm thick) which means higher current density. Although the total current intensity of a FE source normally is as high as the thermionic source, its brightness is far higher due to the much larger emission current density.[191]

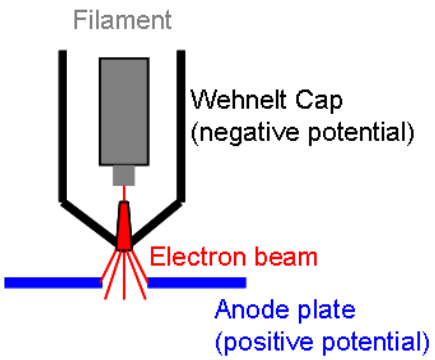


**Figure 2-18 Schematic diagram of electron gun.**

In SEM, the electron beam is focused to a probe by a condenser lens. The beam passes through the deflection coils in the objective lens and scans the surface of the sample. When the beam interacts with the sample, signals produced are collected by the detector and used to modulate the intensity of a synchronously scanned TV screen. The geometry of an SEM is shown in Figure 2-19. In EDS measurements, characteristic x-ray intensity is measured relative to lateral position on the sample.

In TEM (Figure 2-19), the beam is confined to a spot by condenser lenses, passes the condenser aperture and “hits” the sample surface. The electrons are elastically scattered and transmitted through the thin sample. The transmitted beam is converged by an objective lens and passes the objective aperture, which is used to choose transmitted electrons that will form the image in the microscope. Finally, the beam is expanded by a projector lens onto imaging devices. Different types of images can be obtained in TEM by using the apertures properly to choose different types of electrons. As a result, diffraction patterns are shown if the aperture is used to select the scattered electrons. If the unscattered beam is chosen, a bright field image is obtained; if the diffracted beams are chosen, a dark field image is obtained.[192]

The EDS X-ray detector in an SEM or TEM can supply information for qualitative and quantitative analysis, elemental mapping and line profile analysis. The presence of an element in the sample can be obtained by comparing the EDS spectrum with known characteristic X-ray energy values. Variations in x-ray intensity at any characteristic energy value indicate the relative concentration for the applicable element across the surface. One or more element maps or line profiles can be recorded simultaneously using image brightness or plots of intensity as a function of the local relative concentration of the elements present.[190]

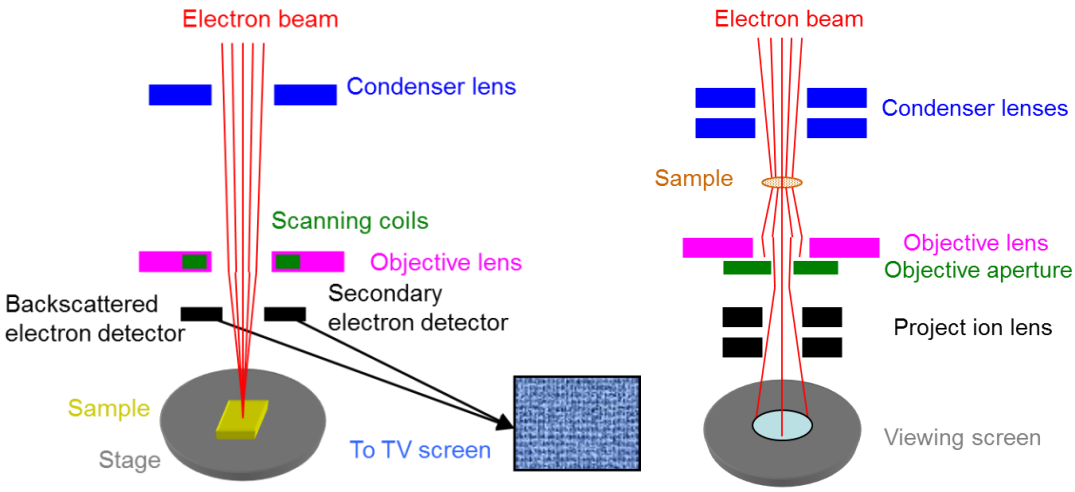


**Figure 2-19 Schematic diagrams of SEM (left) and TEM (right).**

### 2.1.6.3 Measurement

Scanning electron microscopy images were taken either at the Centre for Electron Optical Studies at the University of Bath using a Japanese Electron Optics Laboratory JEOL JSM6480LV or at Wuhan University of Technology using Hitachi Field-Emission SEM (FESEM) S-4800. For samples imaged by the JEOL JSM6480LV, the surface morphologies of film samples were studied in situ under an operating voltage of 20 kV. For cross-sectional samples, they were polished carefully using nano-diamond polishing slurry to obtain a smooth surface and coated with chromium to prevent charging of the samples before imaging in the SEM. High resolution surface morphology and EDS of film samples at section 3.4.2.3 of chapter 3 and section 5.2.4 of chapter 5 was measured directly by the S-4800 operated at 10 kV.

Transmission electron microscopy images were also taken at the Centre for Electron Optical Studies at the University of Bath. Images and diffraction patterns were collected using a Japanese Electron Optics Laboratory JEOL 1200 EX operated at 120 kV. Instrument settings and images were established using the fluorescent screen of the TEM instrument before final collection using a CCD camera. High resolution TEM (HRTEM) was taken at Wuhan University of Technology using a JEM-2100F instrument.

Solid samples for TEM were ground to a fine powder then placed in a test tube and dispersed in dry ethanol by sonication for several minutes. A clean pipette was then used to place a drop of this dispersion onto a carbon film

mounted on a copper TEM grid. The dispersion was allowed to dry in air, thereby depositing powdered material on the TEM grid once the ethanol had evaporated.

## *2.1.7 Atomic force microscopy*

### 2.1.7.1 Theory

The atomic force microscope (AFM), invented in 1986, is an indispensable analytical tool for imaging, measuring, and manipulating materials at the nanoscale, due to its unique potential in surface characterization and moderate price.[193] In AFM, the forces between the probe and sample are measured and converted to a signal that reflects the surface properties, which is collected by the detector and converted into an image by software, as shown in Figure 2-20 (left). The movement of samples is performed by a piezoceramic scanner, by which the tip and sample are brought close together so that the probing interactions can be measured with a detector. The detector signal is used for feedback control to adjust the tip-sample distance during scanning. AFM can be operated in different modes, depending on its application. In general, imaging modes, displayed in Figure 2-20 (right), are divided into static (also called contact) modes on the basis of the cantilever deflection and dynamic (non-contact or "tapping") modes where the cantilever is vibrated.[194]

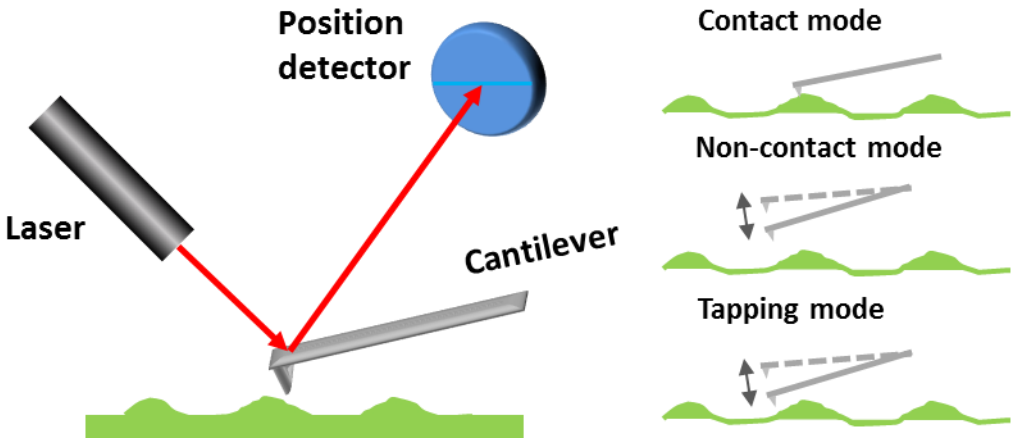


**Figure 2-20 Schematic diagrams of AFM (left) and different imaging modes (right).**

In contact model, the sample is in contact with the tip and the repulsive force experienced by the tip is measured by recording the cantilever deflection. The force between the tip and the surface is kept constant during scanning by adjusting the sample position to maintain a constant deflection according to the

surface performance. However, the mechanical contact between tip and sample limits its application in soft materials since these can be damaged by the force of the tip.[195] In dynamic modes, the sample surface is scanned with the sharp probe at a distance of a few nanometers, where the tip-sample force interaction causes a change in the amplitude, the phase, and the resonance frequency of the oscillating cantilever. During scanning, the cantilever is oscillated at a frequency close to its resonant frequency where the amplitude of oscillation is typically a few nanometers (< 10 nm) for non-contact mode and higher than 10 nm (typically > 20 nm) for tapping mode. For non-contact mode, attractive long-range forces above the sample surfaces, such as van der Waals forces (which are strongest from 1 nm to 10 nm above the surface), decrease the resonance frequency of the cantilever. By combining the decreased resonant frequency with the feedback loop system, the tip maintains constant oscillation amplitude or frequency by modifying the average tip-to-sample distance, which allows the software to construct the structural image of the sample surface. However, a rigid sample normally has a few monolayers of liquid on its surface under ambient conditions, which interrupts the Van der Waals force from being detected in the range of the fluid layer and prevents high-resolution surface imaging with non-contact AFM. The tapping model overcomes this problem. During oscillation, the tip is moved toward the surface until it begins to lightly touch the surface and lifts off. When the oscillating cantilever begins to intermittently contact the surface, the oscillation amplitude of the cantilever is reduced by the energy loss of contacting the surface. The reduction in oscillation amplitude is used to identify and measure surface features.[196]

#### 2.1.7.2 Measurement

Surface profiles of film samples were measured by Easyscan 2 FlexAFM from Nanosurf using tapping mode, in the Chemistry Department at the University of Bath. Scanning parameters were set by the Nanosurf Easyscan 2 control software, which also provides some functions of image analysis such as estimating the area root mean square (RMS) roughness. Before testing, the position of a laser was adjusted carefully to maximize the signal being collected by the detector. During scanning, a Nanosurf Isostage with a compact active vibration isolation system was used to protect all of the scans against vibration

disturbances and an Acoustic Enclosure 300 was used to provide acoustic protection from light, electric and air flow disturbances. For one sample, different areas were scanned to obtain the average value of RMS and 512 points and 1 second per line were set to obtain relatively high resolution images. Film samples were put in the sample stage and tested in situ, different sizes of area can be chosen in the software.

### *2.1.8 $N_2$ adsorption and desorption*

#### 2.1.8.1 Theory

When a solid is exposed in a closed space to a gas or vapour at some definite pressure, the solid begins to adsorb the gas by the physical (van der Waals) and chemical forces acting between the solid and molecules of the gas.[197] The quantity of gas taken up by a solid sample can be expressed in moles per gram of solid as equation 2.33.

$$n = f(p, T, gas, solid) \qquad 2.33$$

The amount adsorbed depends on the mass *m* of the sample, the temperature *T*, the pressure *p* of the vapor, and the nature of the solid and gas. If the other factors except pressure are fixed, the equation simplifies to

$$n = f(p)_{T,gas,solid} \qquad 2.34$$

If the temperature is below the critical temperature of the gas, the alternative form is more useful

$$n = f(p/p^o)_{T,gas,solid} \qquad 2.35$$

where $p^0$ is the saturation vapour pressure of the adsorptive gas. Both of equation 2.34 and 2.35 are expressions for the adsorption isotherm. After tens of thousands of adsorption isotherms were recorded, Brunauer, Emmitt and Teller (BET) originally grouped those isotherms into six types,[198] indicated in Figure 2-21.

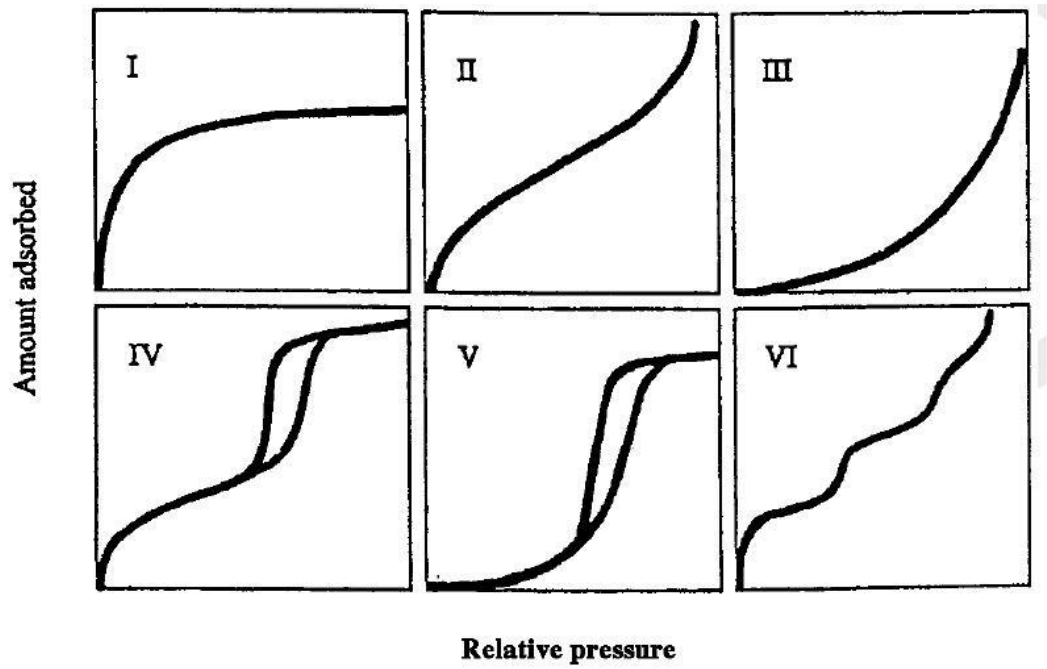


**Figure 2- 21 IUPAC classification of physisorption isotherm types.[199] Reprinted with permission from Ref. 200.**

Type IV represents adsorption isotherms with hysteresis (Figure 2-22), which is associated with capillary condensation taking place in mesopores (pore diameter 2 ~ 50 nm). Such isotherms are generally characteristic of mesoporous materials, such as the surfactant templated materials studied in this work.

A typical Type IV isotherm is shown in Figure 2-22 and the features labelled correspond to particular adsorption or desorption processes. In the lower relative pressure region, the monolayer adsorption starts from point A and is complete at point B, corresponding to an inflection of the adsorption isotherm. Then multilayer adsorption begins on the walls of the pores until point C, which is the start of the hysteresis loop. After that, the curve begins to deviate upwards (CD) until at higher pressures (point E), when the capillary condensation commences in the finest pores, and wider and wider pores are filled with the increasing pressure until the saturation vapour pressure is approached. The amount adsorbed along the desorption branch (EFC) is always greater than along the adsorption branch (CDE) at any given relative pressure, thus a hysteresis loop appears, which is a characteristic feature of type IV isotherm.

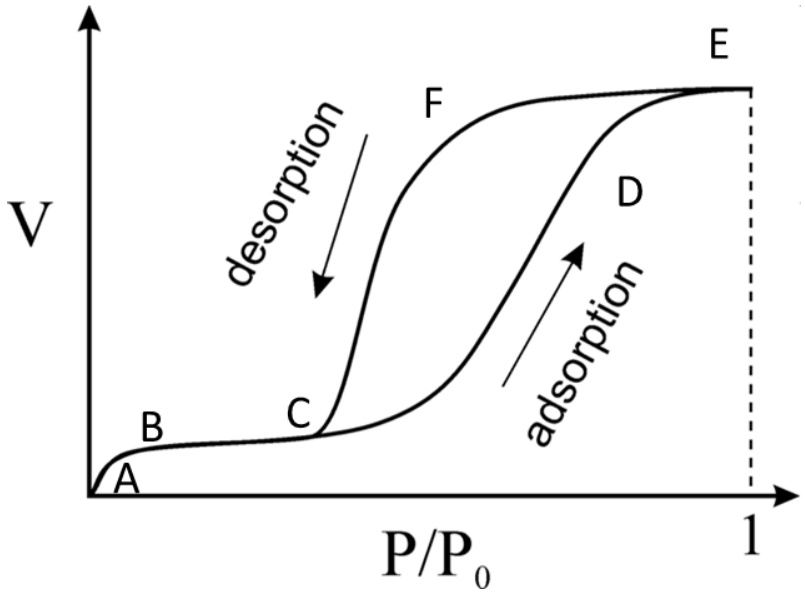


**Figure 2-22 Type IV adsorption and desorption isotherms.**

A general explanation of hysteresis has been offered by Foster assuming an open pore structure of the adsorbent.[200] At the beginning of the hysteresis region, there is an adsorbed film on the walls of the capillaries. As the pressure increases, more adsorption takes place and the film becomes thick enough to bridge the pore. Then, a liquid meniscus is formed and capillary condensation sets in immediately until all capillaries of this size are filled. Thus the ascending branch of the loop corresponds to adsorption and capillary condensation occurring simultaneously but the descending branch represents capillary condensation primarily, which means a delay in the formation of the meniscus during the adsorption process is responsible for the phenomenon of hysteresis. Due to the tensile strength effect, the nitrogen hysteresis loop closure takes place at around 0.42. Because an improved pressure will induce a decreased tension, so there is a minimum pressure where the liquid condensed in the pores can exist. Using nitrogen as adsorbate, the relative pressure is around 0.42.

Due to the differences of pore shape, four types of hysteresis loops were recognized according to IUPAC classification,[201] shown in Figure 2-23. Types H1 and H4 are two extreme types, and type H2 and H3 are regarded as intermediate between two extremes. Type H1 is characteristic of porous materials with narrow distribution of pore size. Type H2 is for pores similar to those of type H1 but without a uniform pore size. Most common mesoporous materials and catalysts belong to the two types.[108, 202, 203] The Type H4 loop is characteristic of slit-like

pores with a uniform distribution, while type H3 is associated with slit-like pores which are not well-defined. Graphene oxide,[204, 205] nanotubes,[206, 207] and zeolites [208, 209] belong to these two types.

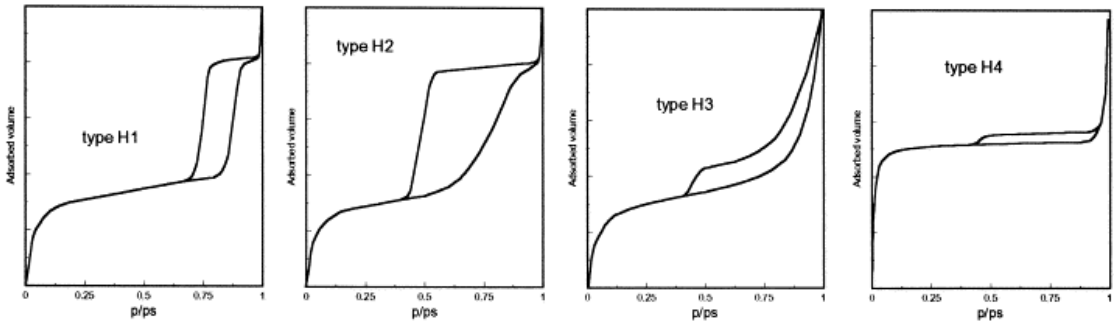


**Figure 2-23 Types of hysteresis loops.[210] Reprinted with permission from Ref. 211.**

The best known theory used for evaluation the specific surface area from the adsorption isotherm is the BET model which is based on a kinetic model put forward by Langmuir.[211] If *n* (in moles) is the amount adsorbed on 1g of adsorbent and $n_m$ is the monolayer capacity, then

$$\frac{n}{n_m} = \frac{Bp}{1+Bp} \qquad 2.36$$

where *B* is an empirical constant in practice. This equation, known as the Langmuir equation, is based on the dynamic equilibrium state and confined to a monolayer adsorption. In a dynamic equilibrium state, the rate of molecules of adsorbent condensed on to bare sites is equal to the rate of molecules evaporating from occupied sites. Some other assumptions, such as that absorbate molecules only interact with the adsorption site without lateral interaction between the adsorbate molecules and that all adsorption sites are equal, are also included in the Langmuir adsorption.[212] The Langmuir model usually applies to solids with a type I isotherm with few adsorbed molecular layers. Moreover, this mechanism also applies to the multilayer adsorption taken into account by the BET model. The BET equation is expressed as:

$$\frac{p/p^o}{n(1-p/p^o)} = \frac{1}{n_m c} + \frac{c-1}{n_m c}\frac{p}{p^o} \qquad 2.37$$

where in practice *c* is a constant and related to the strength of the interaction between the adsorbate molecules and adsorbent.

By plotting the absorbed amount and relative pressure as in equation 2.37, $n_m$ and $c$ can be evaluated. The specific surface (in $m^2/g$) can be calculated according to equation 2.38.

$$A = \frac{v_m}{22414} a_m L \times 10^{-20} \qquad 2.38$$

where $A$ is the surface area, $a_m$ is the area of a single molecule of the adsorbate, (for example the value of $a_m$ for nitrogen at 77 K is 16.2 Å),[2 198] and L is Avogadro's number. 22414 is the volume of one mole of an ideal gas in millilitres. Although real surfaces do not follow the assumptions of BET model, the BET method can nearly give a correct surface area value in the range of relative pressure 0.05 - 0.35.

The basis for the calculation of pore size distribution from the Type IV isotherm is Kelvin equation [213], written as

$$\ln \frac{p}{p^o} = -\frac{2\gamma V_L}{RT} \frac{1}{r_m} \qquad 2.39$$

Where $p/p$ is relative pressure, $V_L$ is the molar volume, $r_m$ is the mean radius of curvature, $\gamma$ is the surface tension, $R$ is the universal gas constant and $T$ is temperature. This equation allows the calculation of the relative pressure at which capillary condensation will occur for a given pore size in the range of 1 - 25 nm. Barret-Joyner-Halenda (BJH) is the most common scheme for calculation of mesopore distribution.[214] The assumed pore geometry in BJH model is cylindrical or slit shaped pores. Based on the Kelvin equation, comparison of the amount of gas adsorbed at different relative pressures to the pore size corresponding to these pressures can then give an indication of a pore size distribution, the relative number of pores of different sizes, in a sample. The upper limit of BJH model arises from the exponential dependence of pore size in which the condensation takes place from the relative pressure. Thus, uncertainty increases when the relative pressure approaches 1. The lower limit at relative pressure around 0.42 is due to the tensile strength effect described above.[215]

### 2.1.8.2 Measurement

Measurements of the nitrogen adsorption isotherms for titania powders or film materials was done by grinding the material into a powder before testing. The

measurements were conducted in the Department of Chemistry at the University of Bath using a BELSORP-mini II instrument to make a free space measurement and for the automated measurement of nitrogen adsorption and desorption from powdered film material at 77 K. The instrument records the amount of gas absorbed measured from the change of gas pressure inside the measuring system by means of the state equation of gas, and then an isotherm was generated by plotting the gas volume absorbed against the relative pressure. Approximately 0.1 g of the sample was ground up and degassed in vacuum at 150 °C for 4 h before measurement. The BET model was used to estimate the surface area and BJH analysis was done to obtain the pore size distribution.

### *2.1.9 TGA & DSC*

#### 2.1.9.1 Theory

Thermogravimetric analysis (TGA) is an analytical technique that can be used to detect and record the changes in the mass of a substance being heated as a function of the temperature by using a thermobalance, while Differential scanning calorimetry (DSC) is a primary technique that can record the amount of heat required to increase the temperature of the sample and the reference material as a function of the temperature. Detailed descriptions of TGA and DSC measurement are readily available from research publications.[216, 217]

TGA instruments can be divided into two general types: vertical and horizontal balance instruments. Normally, a furnace heats the sample at a constant heating rate or holds it at a constant temperature while a sensitive balance monitors the sample weight changes due to decomposition, oxidation, or dehydration etc. The atmosphere used in the TGA experiment plays an important role and can be reactive, oxidizing or inert such as Helium or Argon. The results from thermogravimetric analyses are usually reported in the form of curves relating the mass lost from the sample against temperature. It can be used to identify the composition of multicomponent systems and thermal and oxidative stability of materials among other characteristics.

Based on the mechanism of operation, DSCs can be grouped into two types: heat-flux DSCs and power-compensated DSCs. For heat-flux DSCS, the sample and reference are placed in a furnace and heated by a linear heating rate.

However, owing to the differences of heat capacity of the sample and reference, there would be a temperature difference between the sample and reference. From the differences of heat capacity and temperature, the thermal energy can be obtained on the basis of reference. For power-compensated DSCs, the sample and reference are placed in two furnaces heated by separate heaters. The sample and reference are kept at the same temperature, and the differences in heat required to maintain this temperature is measured. A series of temperatures are tested and plotted as a cure between heat and temperature.

#### 2.1.9.2 Measurement

Analysis of the solvent content and organic content of film materials, which were recovered from the air/solution interface and dried in air, was undertaken using a Perkin Elmer TGA 7 thermogravimetric analyser. The instrument uses a vertical balance accurate to ± 0.005 mg to measure the change in the sample mass during heating. A Perkin Elmer TAC 7/DX thermal analysis controller and Puris software was used for instrument control and data collection in terms of percentage mass and sample temperature. 1 - 10 mg sample was used for TGA experiments. These materials were allowed to dry in air prior to measurement in the temperature range from room temperature to 600 °C at a heating rate of 5 °C /min. TGA and DSC tested in section 3.4 of chapter 3 was measured by NETZSCH STA 449 C in the temperature range from room temperature to 1200 °C at a heating rate of 10 °C /min. Measurements were done in air.

### *2.1.10 Solar cell characterization*

#### 2.1.10.1 I-V curve

To compare solar cells characterized in different laboratories all over the world, a set of standard conditions is necessary to measure the photon to electron conversion efficiency. The standard conditions indicate that the temperature should be 25 ˚C and the solar radiation incident should have a total power density of 1000 W/m$^2$, with an AM 1.5 filter.[44]

Under a constant incident light intensity, the current given out by a cell is measured as a function of voltage by changing the resistance of the load. Figure 2-24 shows the typical I–V curve and power curve for a solar cell. Because Dye Sensitised Solar Cells (DSSCs) have a relatively slow electrical response due to

their high interfacial capacity, the voltage scan should be sufficiently slow to avoid errors in the current measurement due to capacitive charging [38]. The principle of electron transfer and efficiencv parameters were described in chapter one. From 4, the short circuit ($J_{sc}$) is determined at the *V=0* intercept and the open-circuit photovoltage ($V_{oc}$) is found at the *I=0* intercept. The maximum output power ($P_{max}$) is obtained where the value of $|I \times V|$ reaches a maximum. The fill factor of the cell (FF) and overall conversion efficiency $\eta_{global}$ can be calculated according to equation 1.10 and 1.9 respectively.

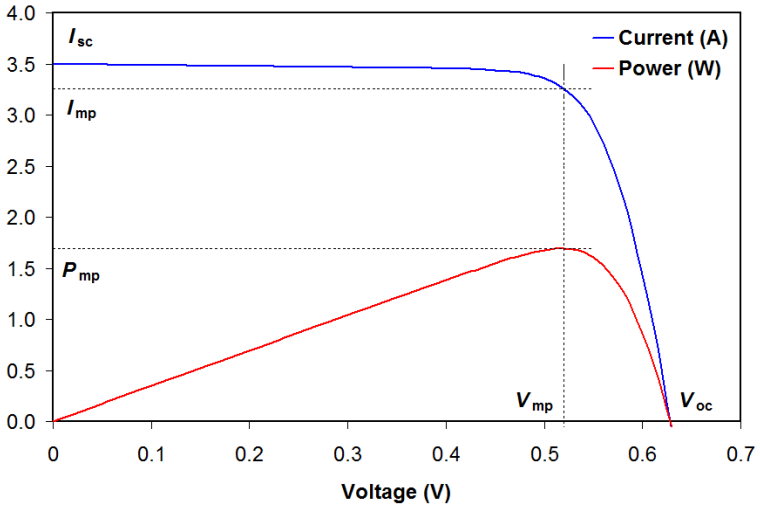


**Figure 2-24 Typical I-V curve and power curve for a solar cell.**

### 2.1.10.2 IPCE

As described in section 1.2.1 of chapter 1, IPCE, also called quantum efficiency (QE) is the ratio of the number of carriers collected by the solar cell to the number of photons of a given energy incident on the solar cell.[218] Quantum efficiency therefore relates to the response of a solar cell to the various wavelengths in the spectrum of light irradiating on the cell. The quantum efficiency may be given either as a function of wavelength or as energy. The ideal Quantum efficiency has a square shape, where the QE value is fairly constant across the entire spectrum of measured wavelengths. However, due to the effects of recombination, reflection and low diffusion length, the QE for most solar cells is reduced.[219]

Two types of quantum efficiency of a solar cell are often considered, external QE (EQE) and internal QE (IQE).[220] EQE is the parameter normally used to

describe cells, which includes the optical losses such as transmission and reflection of cells. The IQE is the efficiency with which light not transmitted or reflected out of the cell can generate charge, which is normally higher than EQE. By measuring transmission and reflection of a cell, the EQE can be corrected to obtain IQE data.

The QE measuring equipment is mainly composed of a light source, monochromator, output signal detector, sample chamber, reference cell and analysing software. The QE at various wavelengths is measured by first measuring a pre-calibrated cell at these wavelengths so the number of photons emitted at each wavelength can be calculated. The cell to be measured is then exposed at the same wavelengths, and the current produced is measured. This information can then be used to calculate the IPCE and described as a percentage vs wavelength.

#### 2.1.10.3 Measurement

IV curves were measured using a Class AAA Solar Simulator (TS-space system) based on metal halide sources, Keithley 2601A series source meter and calibrated with a Si reference solar cell. The testing system is computer-controlled over a USB interface with all the settings accessible through software TSIV.

For IPCE measurement, a 75 W xenon lamp was used as the light source to generate a monochromatic beam. Before measurements, the sample or the photodiode were adjusted to the right place in respect to the light spot of 550nm. Benth2008 software was used to set all the parameters. Calibration was performed using a standard silicon photodiode.

## 2.2 Experimental

### *2.2.1 Chemicals and apparatus*

All chemicals were used without further treatments. Chemicals and apparatus are listed in Table 2-4 and Table 2-5 respectively.

**Table 2-4 Chemicals used in experiments.**

| ***Name*** | ***Description*** |
|---|---|
| Titanium n-butoxide (TIBU) | $Ti(OCH_2CH_2CH_2CH_3)_4$, $\geq$ 99.0%, Acros Organic |

| | |
|---|---|
| Titanium isopropoxide (TIPR) | $Ti(OCH(CH_3)_2)_4$, ≥98.0%, Acros Organic |
| Titanium(IV) chloride | $TiCl_4$, ≥99.9%, Acros Organic |
| Ammonium hexafluorotitanate (TINF) | $(NH_4)_2TiF_6$, ≥99.9%, Sigma Aldrich |
| Titanium(IV) bis(ammonium lactato)dihydroxide solution (TIBDD) | $[CH_3CH(O-)CO_2NH_4]_2Ti(OH)_2$, 50 wt.% in water, Sigma Aldrich |
| Titanium Diisopropoxytitanium bis(acetylacetonate) | $[(CH_3)_2CHO]_2Ti(C_5H_7O_2)_2$, 75 wt. % in isopropanol, Sigma Aldrich |
| P25 | $TiO_2$, particle size ~21 nm, ≥99.5%, Sigma Aldrich |
| Titania paste (Solaronix-paste) | Anatase particle ~15 nm, concentration 11.wt.%, Ti-Nanoxide T, Solaronix |
| Titania paste (Dyesol-paste) | Anatase particle, ~20 nm,18NR-T, Dyesol |
| Zinc Acetate (ZNAC) | $Zn(CH_3CO_2)_2$, ≥98%, Acros Organic |
| Zinc Nitrate Hexahydyate | $Zn(NO_3)_2 \cdot 6H_2O$, ≥98%, Sigma Aldrich |
| Zinc Chloride | $ZnCl_2$, ≥98%, Sigma Aldrich |
| Cetyltrimethylammonium bromide (CTAB) | $(H_3C(H_2C)_{15}(CH_3)_3\text{-}N^+ Br^-$, ≥99.0%, Acros Organic |
| Sodium dodecylsulphate (SDS) | $CH_3(CH_2)_{10}CH_2\text{-}SO_4^- Na^+$, ≥99.0%, Fisher |
| Cetylpyridinium bromide hydrate (CpBr) | $C_{21}H_{38}BrN \cdot xH_2O$, ≥98%, Acros Organic |
| Poly(ethyleneimine) (LPEI) | $(C_2H_5N)x$, $M_W$~750,000, 50 wt. % in $H_2O$, Sigma Aldrich |
| Poly(ethyleneimine) (SPEI) | $(C_2H_5N)x$, $M_W$~2,000, 50 wt. % in $H_2O$, Sigma Aldrich |
| Polyethylene oxide (PEO) | $H(OCH_2CH_2)_xOH$, $M_W$~100,000, Sigma Aldrich |
| Polyacrylamide (PAAm) | $(C_3H_5NO)_x$, $M_W$~10,000, 50 wt. % in $H_2O$, Sigma Aldrich |
| Polyvinylpyrrolidone (PVP) | $(C_6H_9NO)_x$, $M_W$~360,000, Sigma Aldrich |
| Alginate acid sodium salt (AGA) | $(C_6H_8O_6)_x Na$, Sigma Aldrich |
| Pluronic P123 | $H(OCH_2CH_2)_{20}(CH_2CH(CH_3)O)_{70}(CH_2CH_2O)_{20}H$, $M_n$~5800, Sigma Aldrich |

| | |
|---|---|
| Pluronic F127 | $H(OCH_2CH_2)_{100}(CH_2CH(CH_3)O)_{65}(CH_2CH_2O)_{100}H$, $M_n$~12500, Sigma Aldrich |
| N719 dye | $C_{58}H_{86}N_8O_8RuS_2$, Dyesol, B2 |
| Methylene blue (MB) | $C_{16}H_{18}ClN_3S \cdot 3H_2O$, ≥96.0%, Acros Organic |
| Iodine | $I_2$, ≥99.999%, Sigma Aldrich |
| 3-propyl-1-methylimidazolium iodide | $C_7H_{13}IN_2$, ≥95.0%, Merck |
| Guanidine thiocyanate | $NH_2C(=NH)NH_2 \cdot HSCN$, ≥99.0%, Fluka |
| Tert-butylpyridine | $C_9H_{13}N$, ≥99.0%, Sigma Aldrich |
| Hexachloroplatinate | $(NH_4)_2PtCl_6$, ≥99.995%, Sigma Aldrich |
| Acetylacetone | $CH_3COCH_2COCH_3$, ≥99.0%, Sigma Aldrich |
| Terpineol | $C_{10}H_{18}O$, ≥99.5%, Sigma Aldrich |
| Ethyl Cellulose (EC) | 48% in ethoxy, viscosity 5-15 cp, Sigma Aldrich |
| Ethyl Cellulose (EC) | 48% in ethoxy, viscosity 35-50 cp, Sigma Aldrich |
| Sulphuric acid | $H_2SO_4$, ≥98.0%, Fisher |
| Hydrochloric acid | HCl, ≥32.0%, RG, Fisher |
| Acetic Acid (ACOH) | $CH_3COOH$, ≥99.0%, Fisher Scientific |
| Potassium hydroxide | KOH, ≥85.0%, Sigma Aldrich |
| Acetonitrile | $CH_3CN$, HPLC, Fisher |
| Valeronitrile | $CH_3(CH_2)_3CN$, ≥99.5%, Sigma Aldrich |
| t-butanol | $(CH_3)_3COH$, ≥99.7%, Sigma-Aldrich |
| Isopropanol | $(CH_3)_2CHOH$, LRG, Fisher |
| Acetone | $CH_3COCH_3$, AR, Sigma-Aldrich |
| Ethanol (EtOH) | $CH_3COOH$, AR, Fisher |
| DECON 90 | Decon alkaline cleaning fluid |
| Milli-Q water | $H_2O$, 18.2 MΩ cm resistance |
| FTO glass | TEC 15, Asahi |
| Surlyn | SX1170-25PF, 25 μm Solaronix |

**Table 2-5 Apparatus used in experiments.**

| ***Name*** | ***Description*** |
|---|---|
| Dip coater | Nima dip coater, model DSG-75 |

| | |
|---|---|
| Ultrasound bath | FB11020, Fisherbrand |
| Rotary evaporator | Rotavpor R-114, Buchi |
| Waterbath | Waterbath B-480, Buchi |
| Oven | LTE inc. |
| Humudity oven | SPEAR inc. |
| Muffle furnace | CARBOLITE inc. |
| Fridge | LEC inc. |

### *2.2.2 Substrate cleaning and blocking-layer preparation*

Substrates used for making films are FTO glasses, microscope slides and silicon wafers. FTO glasses and microscope slides were cleaned in the following way: 5% Decon 90 (ultrasonic 15min) → Milli-Q water (ultrasonic 15min) → 5% Decon 90 (ultrasonic 15min) →Milli-Q water (ultrasonic 15min) → acetone (ultrasonic 15min) →ethanol (ultrasonic 15min). Silicon wafers were washed with 5% Decon 90 and distilled water first, then activated according to reference.[221]

For FTO glass, a blocking layer of $TiO_2$ is normally applied by the spray paralysis technique to enhance the bonding strength between substrate and the porous titania layer and to block the charge recombination to some extent.[45] The blocking layer solution was made by using a concentration of 0.2 M solution of dispropoxytitanium bis(acetylacetonate) dissolved into isopropanol. The cleaned substrates were preheated to 400 °C on a hot plate. The solution was sprayed onto the surface 16 times with a rate of once per 10 seconds. This process resulted in formation of a uniform dense titania blocking layer with a thickness around 100 nm.

### *2.2.3 Fabrication of DSSCs*

Figure 3-1 shows the photograph and configuration of the DSSC, which were produced by following a variation of the following procedure.

- Dye adsorption: The photoelectrodes were preheated to 80 ºC and they were soaked in an solution of 0.3 mM N719 dye in t-Butanol/Acetonitrile solvent (volume ratio of 1:1) for 20 h at room temperature in blacked out containers. The dye-coated $TiO_2$ films were washed with t-Butanol/Acetonitrile and dried

- Counter electrode preparation: Two drops of 5 mM hexachloroplatinate solution in isopropanol were dropped onto the conducting side of cleaned FTO glass which had two small holes drilled into it. A Pt layer was then deposited onto the FTO glass after being heated at 390 °C for 15 min.
- Electrolyte injection: A hot-melt Surlyn gasket was used, and once the two sides were sealed together, a small quantity of electrolyte was introduced through the drilled holes using a vacuum backfilling system. The electrolyte was consisted of 0.03 M $I_2$, 0.6 M 3-propyl-1-methylimidazolium iodide, and 0.1 M guanidine thiocyanate and 0.5 M tert-butylpyridine in an acetonitrile/valeronitrile solvent with a volume ratio of 85:15.
- Sealing of cells: The cell was sealed using hot-melt Surlyn and a glass cover slip. The dimensions of the active area of the cell were usually about 1 $cm^2$, and the individual glass sides were 1.5 $\times$ 2.5 $cm^2$.

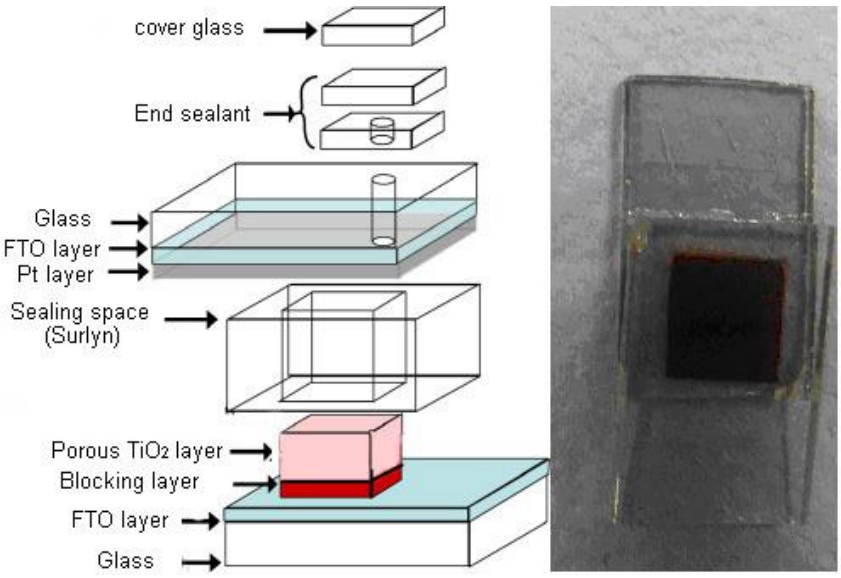


**Figure 3-1 Photograph and configuration [45] of the DSSC. Reprinted with permission from Ref. 45.**

# Chapter 3 Results and Discussion

There are three major projects in this thesis: 1. Fabrication of ordered meso-$TiO_2$ powders and their application in DSSC by the doctor-blading method; 2. Synthesis of ordered meso-$TiO_2$ thin films by dip coating and their use as a photocatalyst and in DSSC; 3. Preparation of meso-$TiO_2$ free-standing films by a self-assembly method at the air-water interface and their use in DSSC. In this chapter, Three other experiments, related to but branching out from the major projects and their results are also discussed here. The first experiment on preparation of meso-$TiO_2$ powder made from a water-ethanol solution was work done before the major project of Chapter 4. The second experiment on ordered meso-$TiO_2$ thin films by dip coating from aqueous solution is work related to the project of Chapter 5 and 6. The third experiment on ZnO films self-assembled at air-liquid interface is an extension of work from the project of Chapter 7.

## 3.1 Meso-$TiO_2$ powder made from water-ethanol solution

From the chapter 1, meso-$TiO_2$ has many potential advantages and ordered meso-$TiO_2$ powder can be prepared by various techniques. The EISA method in soft-templated approach is one of the most used ways to prepare ordered meso-$TiO_2$ powders. However, the EISA method has critical requirements to control the atmosphere and post treatments, such as humidity, aging temperature and time.[222] Also, mesoporous titanias prepared from aqueous solutions are normally not well-ordered, so, if ordered meso-$TiO_2$ could be prepared from aqueous solutions, it would reduce the dependence of structure on the preparation environment.

First a surfactant/polymer was attempted as the template to prepare meso-$TiO_2$ from aqueous solution. CTAB or the mixture of CTAB/SDS were used as the surfactant, with LPEI, SPEI, PAAm or PEO as the polymer, and TIBU, TIPR, TIBDD as the titania precursor, but no mesostructured titania was found, despite adjusting the reagent concentration, pH of the solution, and adding ethanol or ACOH along with the titania precursor to slow the hydrolysis reaction of titania alkoxide. However, if only CTAB was used as the template and water soluble titania precursor (TIBDD) was used to obtain precipitates and the

precipitates were treated under a mild hydrothermal process (40-70 °C) overnight, the as-prepared sample had a partly ordered mesostructure. After calcination, the powder still had pores according to data from $N_2$ adsorption and desorption results, but without ordered mesostructures. The failure of this experiment is due to the rapid hydrolysis reaction of titanium alkoxide, as the hydrolysis of titanium alkoxide is very sensitive to water.[11, 86] So, it is necessary to control the amount of water during the preparation of mesoporous titania.

Pluronic P123 and F127 are two widely acknowledged polymers for templating mesostructured materials. As water is a PEO block selective solvent but ethanol is a good solvent for both the PEO and PPO blocks, the self-assembly behaviour of Pluronic P123 differs greatly between ethanol and aqueous solution.[223] To investigate the influence, P123 and F127 were used as the template to attempt to make meso-$TiO_2$ from aqueous, water-ethanol solution and ethanol. This procedure still did not give a mesostructured sample from aqueous solution, but partly ordered samples were obtained from water-ethanol solution while an ordered meso-$TiO_2$ was synthesised from ethanol only solutions. Also, it was observed that the Pluronic F127 template was more difficult to decompose during calcination compared to Pluronic P123. Two samples prepared under the same condition, were calcined however the sample containing F127 solution was brown while the one synthesised from P123 solution was white, indicating residual carbon inside the titania templated by F127. So, after this, Pluronic P123 was used as the template to make meso-$TiO_2$ powder. In this section, only the partly ordered meso-$TiO_2$ templated by P123 is discussed, while the ordered meso-$TiO_2$ is explained in detail in chapter 4.

### *3.1.1 Experimental*

1.0 g Pluronic P123 was dissolved in a water-ethanol mixed solvent, then the solutions were stored in a bottle sealed by a lid and stirred vigorously for 3 h at room temperature. 1 ml $TiCl_4$ was added dropwise in a wet ice bath followed by vigorous stirring for 20 h. The solution was poured into plastic dishes and evaporated at 40 or 60 ˚C in air for 9 days. The resulting membranes were crushed into a powder and subsequently the template removed by calcination at 450 ˚C for 3 h with a heating speed of 1 ˚C/min in air. Finally, white meso-$TiO_2$ powder samples were obtained.

SAXS, XRD, $N_2$ adsorption and desorption, and TGA were used to characterize the samples.

## *3.1.2 Results and discussion*

### 3.1.2.1 SAXS

Figure 3-2 shows SAXS patterns for a sery of calcined meso-$TiO_2$ powders with different synthesis processes. The SAXS of the as-prepared sample is not tested, as the mesostructure after calcination is the interested point, but the mesostructure of the as-prepared sample from water/ethanol solution is assumed not as good as that from ethanol only solution. As the as-prepared titania powder templated by F127 prepared from ethanol solution has a much better mesostructure ordering than that from water/ethanol solution. The samples are divided into three sets where each set used the same reagents. Set one is sample A and B, set two is C and D, and set three is E and F. From the SAXS patterns, none has well-ordered mesostructures but only a broad shoulder at ~ 0.5 $nm^{-1}$ indicating a d-spacing of about 12.6 nm. For sample A and B, it is found that the nanostructure of sample B aged at 40 °C is more disordered than that at 60 °C. However, from another two sets of samples, the long-rage ordering behaviour under different aging temperature is opposite. Comparing the second set (sample C and D) with the third set (sample E and F), no obvious differences could be noticed. The differences are possibly due to the change in solvent as the self-assembly behaviour of P123 is very sensitive to the volume ratio between ethanol and water,[223] and also the evaporation speed of solvents in different temperatures will be different, which can change the condensation speed of the inorganic structure.[224]

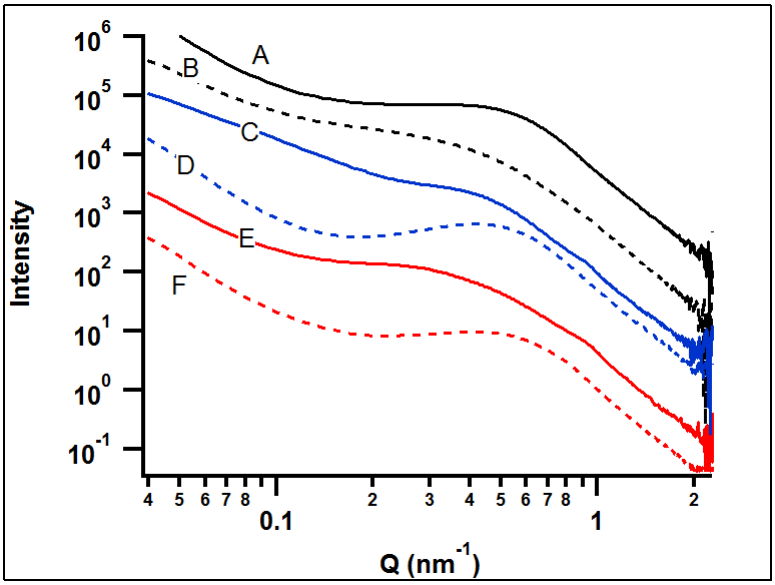


**Figure 3-2 SAXS curves of meso-$TiO_2$ prepared from P123 1g/$TiCl_4$ 1ml in various solvents: A ($H_2O$ 2.5ml/EtOH 2.5ml), C ($H_2O$ 2.5ml/EtOH 5ml), and E ($H_2O$ 5ml/EtOH 2.5ml) were aged at 60 °C, B ($H_2O$ 2.5ml/EtOH 2.5ml), D ($H_2O$ 2.5ml/EtOH 5ml) and F ($H_2O$ 5ml/EtOH 2.5ml) at 40 °C.**

### 3.1.2.2 TGA

Figure 3-3 shows the TGA curves of the as-prepared meso-$TiO_2$ made from P123 1g/$TiCl_4$ 1ml/$H_2O$ 2.5ml/EtOH 2.5ml and aged at different temperatures. Below 130 °C, the mass loss is due to volatile species, such as water, ethanol and HCl. Between 130 and 300 °C, the mass loss is from the combustion of the P123 template. After that stage, a small mass loss occurs due to the continuous removal of residual organic and sintering of $TiO_2$ particles.[225] The as-prepared meso-$TiO_2$ aged at 40 °C has a greater mass loss below 130 °C compared to that aged at 60 °C, as there is more water remaining in samples made at the lower aging temperature. However, the weight ratio between inorganic species and organic compound is almost ~ 1:1 for the two samples, since the same amounts of P123 and $TiCl_4$ are used in reagents in both cases. As the sample aged at 60 °C has a relatively better mesostructure than that at 40 °C, this sample is used for the later characterization.

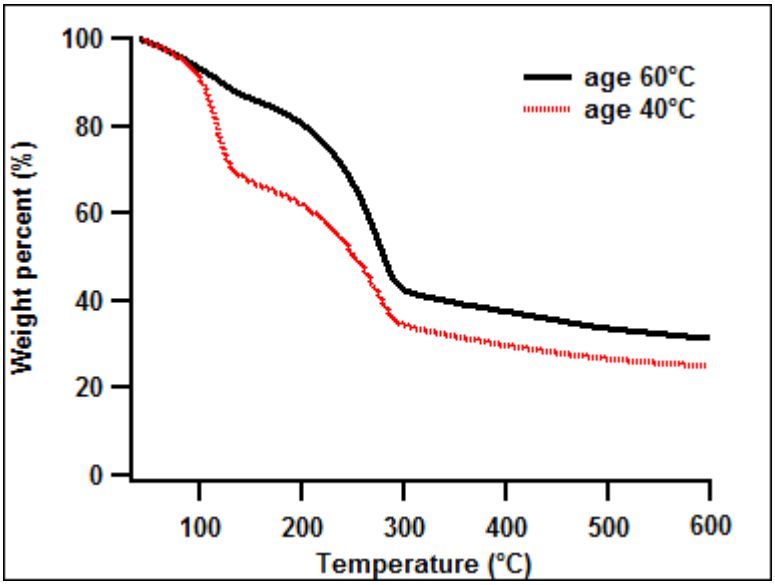


**Figure 3-3 TGA curve of meso-$TiO_2$ made from P123 1g/$TiCl_4$ 1ml/$H_2O$ 2.5ml/EtOH 2.5ml and aged at 40 and 60 °C.**

### 3.1.2.3 XRD

Figure 3-4 shows the XRD curve of meso-$TiO_2$ aged at 60 °C and prepared from P123 1g/$TiCl_4$ 1ml/$H_2O$ 2.5ml/EtOH 2.5ml. All diffraction peaks can be attributed to (101), (004), (200), (116), (220) and (204) planes of the anatase $TiO_2$ (JCPDS card no. 21-1272). The crystallize size calculated according to Scherrer formula [226] is ~ 19 nm. This crystallite size is much larger than the expected wall size in a P123 templated titania,[227, 228] suggesting considerable wall collapse and growth of titania particles during the calcination process.

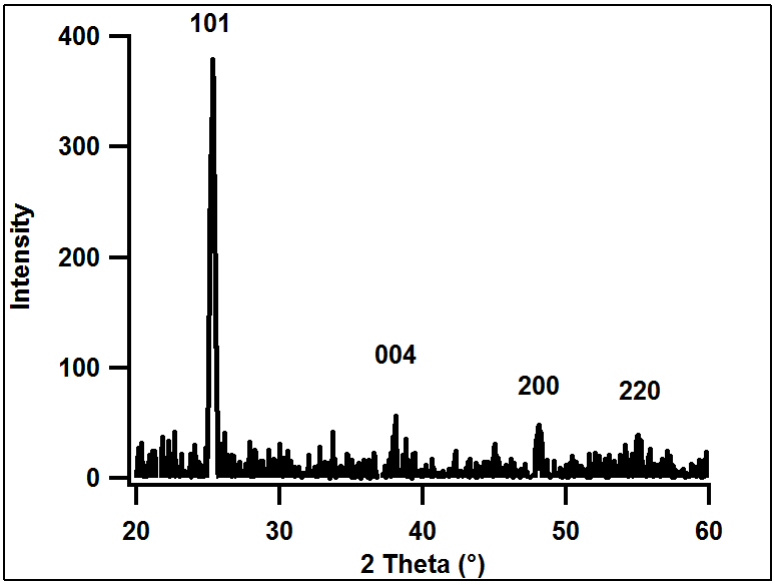


**Figure 3-4 XRD curve of meso-$TiO_2$ aged at 60 °C and prepared from P123 1g/$TiCl_4$ 1ml/$H_2O$ 2.5ml/EtOH 2.5ml.**

### 3.1.2.4 $N_2$ adsorption and desorption

Figure 3-5 shows $N_2$ adsorption and desorption isotherms and BJH pore size distributions of meso-$TiO_2$ synthesized from P123 1g/$TiCl_4$ 1ml/$H_2O$ 2.5ml/EtOH 2.5ml. The BET surface area is 101 $m^2$/g and total pore volume is 0.29 $cm^3$/g. The isotherms show a slow capillary condensation step in the range of 0.4-0.9, indicating the presence of mesopores and a wide distribution of pore size.[229] The pronounced H1 desorption hysteresis loop suggests the existence of mesopores with open-ends having a cylindrical shape in this sample.[230] BJH pore size analyses were performed on the adsorption branch, and the peak pore diameter is 3.1 nm, which is relatively small compared to the size (8.33 nm) of meso-$TiO_2$ prepared via EISA method in chapter 4 and work by others.[231] This is because of the well-crystallized structure and large crystal size (~19 nm) in the sample, which means that the pores collapsed severely during calcination and the crystallites grew out of the geometry of the wall inducing the decrease of pore areas.

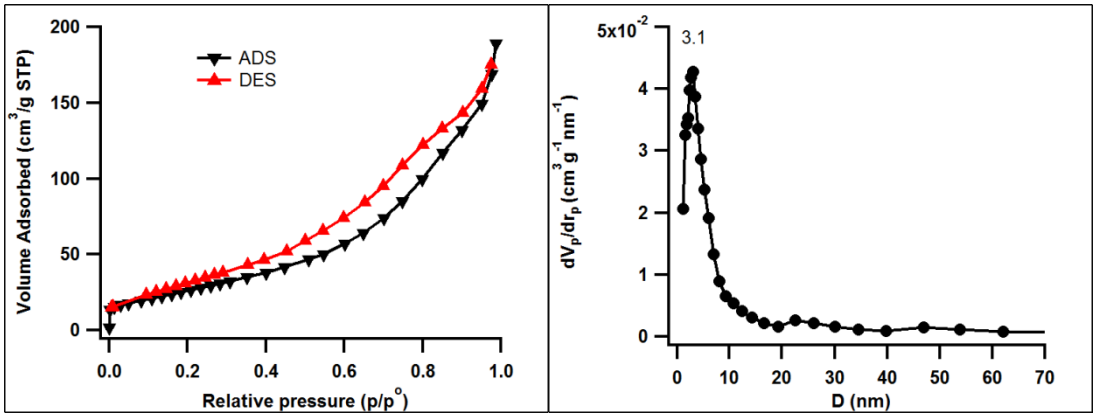


**Figure 3-5 $N_2$ adsorption and desorption isotherms and BJH pore size distribution of meso-$TiO_2$ aged at 60 °C and prepared from P123 1g/$TiCl_4$ 1ml/$H_2O$ 2.5ml/EtOH 2.5ml.**

### *3.1.3 Conclusion*

Meso-$TiO_2$ was made from water-ethanol solution by using the P123 as the template. The effects of volume ratio between ethanol and water, and aging temperatures on mesostructure of calcined samples were studied, but all the samples did not have ordered mesostructure. From the TGA results, the aging temperatures did not affect the inorganic/organic weight ratio in the as-prepared materials. XRD and $N_2$ adsorption and desorption were tested for a typical meso-$TiO_2$ sample which was aged at 60 °C and made from P123 1g/$TiCl_4$ 1ml/$H_2O$ 2.5ml/EtOH 2.5ml. It showed an anatase phase with crystal size around 19 nm. Also, it had a specific surface area 101 $m^2$/g with a mean pore diameter of 3.1 nm. The formation of the relatively small pores was due to the pore collapse during calcination as the titania crystallites in the walls grew, forming the final well-crystallized structure.

Although these meso-$TiO_2$ were not well-ordered, they were well-crystallized and did retain some mesoporosity. These materials therefore should have higher active performance compared to bulk titania, in the photocatalyst or a DSSC, as it had a well-crystallized anatase mesoporous structure. Some further ways could be attempted to improve the long range ordering. Firstly, the pore collapsed severely during calcination which decreases the mesostructural ordering and pore size, so lowering the calcination temperature to 350 or 400 °C may help to retain the mesostructure, as, from TGA results, the organic components had decomposed totally by around 300 °C. Secondly, use of the CASH method could

be attempted to improve the ordering. This method involves carbonization under Ar firstly at 450 °C then calcination in air to remove the carbon at ~ 350 °C. Thirdly, more complex titania compounds could be used in the synthesis solutions to slow the hydrolysis reaction of titanium alkoxide, allowing better interactions with the surfactant templates.

## 3.2 Ordered meso-$TiO_2$ thin films by dip coating from aqueous solution

Ordered meso-$TiO_2$ films have many applications and are generally prepared from EISA method, but the properties of these films are highly dependent on the atmosphere which reduces its repeatability and hinders industrialization. From section 3.2, ordered meso-$TiO_2$ powder was attempted to prepare from aqueous solution but failed. Here, ordered meso-$TiO_2$ film was attempted to prepare from aqueous solution to reduce the dependence on the preparation environment.

From previous work in the Edler group, some colleagues made mesostructured surfactant/polymer films by spray coating onto a silicon wafer using a layer by layer deposition method. So, preparation of an ordered meso-$TiO_2$ film was attempted through the similar method. Surfactants (CTAB or SDS), polymers (LPEI, SPEI, PAAm, PVP or AGA), and water soluble titania salts (TINF or TIBDD) were dissolved in water to prepare stock solutions. Layers of surfactants were sprayed onto the substrate first (in the case of films using two surfactants, for example to make a CTAB/SDS/polymer/$TiO_2$ film, the CTAB was sprayed first, then SDS), then the polymer layer and finally a titania precursor layer. The results showed that the as-prepared CTAB/SPEI/$TiO_2$ film had an ordered structure but no mesostructure was obtained after calcination even after tuning the concentration of reagents. This may be because the mesostructure measured in the as-prepared sample arose only from the surfactant/polymer or the mesostructure totally collapsed during calcination.

During this work, a paper was published by Krins et al.[232] They prepared ordered mesoporous titania films using F127 as the template by capillary coating (withdrawal speed 0.01 - 0.1 mm/min ) from aqueous solutions under controlled temperatures. Moreover, this method did not require ageing processes, which reduced the preparation time of meso-$TiO_2$ film compared to the film made by a

traditional EISA method. This method was attempted, using F127as the template and ordered meso-$TiO_2$ was made by dip coating with a withdrawal speed 10-60 mm/min at room temperature. Mesostructure and morphological properties of these films were tested, but the surface of the films made by this method was uneven and adjustments were needed for further applications. Thus, the fabrication of ordered meso-$TiO_2$ was still done by dip coating using the ethanol based EISA method for our studies of applications of these films as photocatalyst and in DSSC, which is described in detail in chapter 5 and 6.

## *3.2.1 Experimental*

3.0 g Pluronic P123 was added into 30 ml of Milli-Q water under vigorous stirring. After the polymer was totally dissolved, 3 or 5 ml of $TiCl_4$ were added dropwise in a wet ice bath under vigorous stirring to give the precursor solution. The sol-gel solution was then stirred for another 30 min at room temperature before it was used. Films were made on cleaned silicon wafer by dip-coating at room temperature and at a relative humidity of 20 - 30 %. The lowest withdrawal speed for dip coater used is 10 mm/min. Films were finally calcined at different temperatures for 5 min with a ramp speed of 5 °C/min.

SAXS, GISAXS, AFM, and ellipsometry tool were used to characterize these samples.

## *3.2.2 Results and discussion*

### 3.2.2.1 SAXS & GISAXS

Figure 3-6 shows a series of titania films prepared using different synthesis processes. From the SAXS patterns, the film dip coated using a quicker withdrawal speed (60 mm/min) has a less well-ordered mesostructure than those prepared using 10 mm/min withdrawal speed, The withdrawal speed affects the film thickness and evaporation speed, which further influences the condensation speed of the titania within the mesostructure.[222] The films made from a precursor solution with 5 ml titanium salt species has less well-ordered mesostructure than those prepared from solutions containing 3 ml titanium salt, because the inorganic/organic ratio affects the formation mesostructure and too much titania prevents the ordering of the P123 micelle.[19] Zhao et al. studied the effects of the amount of P123 on the mesostructure of titania.[233] During the decrease of amount

of surfactant, the ordering of mesostructure increased and then decreased. Also the calcination temperature affects the mesostructure of the films, as the titania crystallites grow faster at higher calcination temperature causing the pores collapse more easily at higher calcination temperatures. However, none of the films shows well-ordered mesostructures, except the film prepared from 3 ml $TiCl_4$ and calcined at 500 °C with a withdrawal speed 10 mm/min which had a broad shoulder at ~0.4 $nm^{-1}$, indicating a d-spacing of 15.7 nm. So, we chose the 3 ml $TiCl_4$ and withdrawal speed 10 mm/min for later experiments.

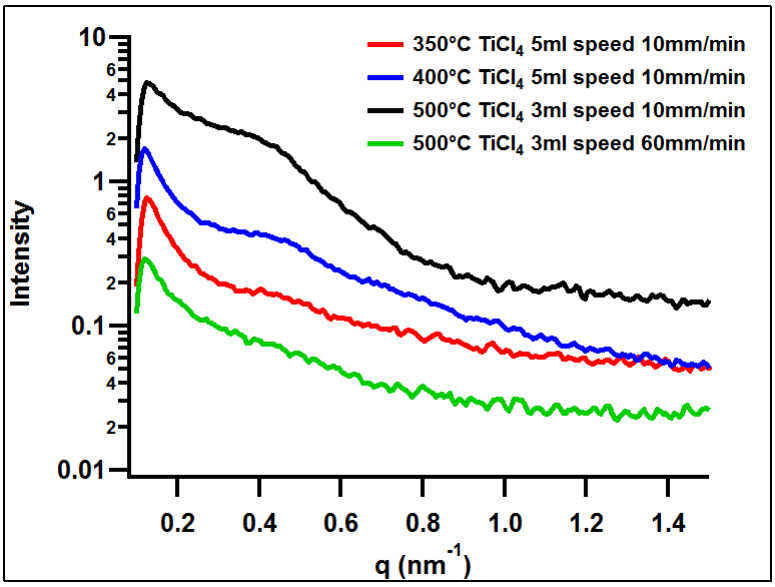


**Figure 3-6 SAXS curves from titania films prepared by dip coating under a range of conditions and solution concentrations.**

Figure 3-7 shows the GISAXS images of titania films prepared from 3 ml $TiCl_4$ and calcined at 350 (left) and 400 °C (right). It is surprised to see the well-ordered mesostructure, as there are many spots in the images. The mesostructure is much better than that found for the film calcined at 500 °C in Figure 3-6, probably due to the lower calcination temperature used to prepare the GISAXS samples. Also the powdered samples tested using transmission SAXS were prepared by scratching film off from the substrate which may also destroy the mesostructure. From the existence of in-plane diffraction and the angle relationship between the spots close to the beam centre, the pores of both films appear to be arranged in a body-centred cubic mesostructure (Im3m) with some shrinkage in the vertical direction to the film surface, which is commonly observed.[234] All diffraction spots are indexed based on this symmetry. These

results are also in accordance with those of Krins et al.[232] However, the degree of mesophase ordering in the film calcined at 400 °C is a little bit worse than the one calcined at 350 °C and it has larger shrinkage in the vertical direction. The unit cell dimensions of the film calcined at 400 °C is a=b=17.2 nm c=11.4 nm, while the one calcined at 350 °C is a=b=17.2 nm c=11.0 nm.

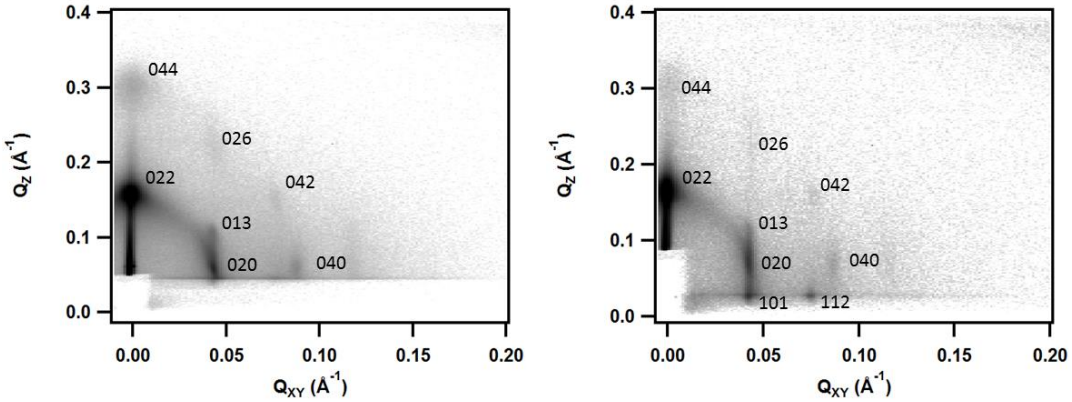


**Figure 3-7 GISAXS images of titania films prepared from 3 ml $TiCl_4$ and calcined at 350 °C (left) and 400 °C (right).**

### 3.2.2.2 AFM

Figure 3-8 shows AFM images of titania films prepared from 3 ml $TiCl_4$ and calcined at 350 and 400 °C. Films do not show a uniform surface, as there are some large macropores visible on the surface. For the film calcined at 400 °C, the open space between particle networks is 1 - 2 µm, while it is 2 - 3 µm for the film calcined at 350 °C, probably due to pore shrinkage at the higher calcination temperature. These suggests the films has a meso/macroporous structure, which is useful in potential applications as it benefits the efficient transport of guest species to framework binding sites.[125] The RMS roughness of the film calcined at 400 °C is 4.5 nm which increases to 10.6 nm for the film calcined at 350 °C, because the macropores are bigger in the film calcined at 350 °C. Compared to the 1-layer film (RMS < 1 nm) made by the EISA method in chapter 6, these samples have a much rougher surface due to the existence of the macropores.

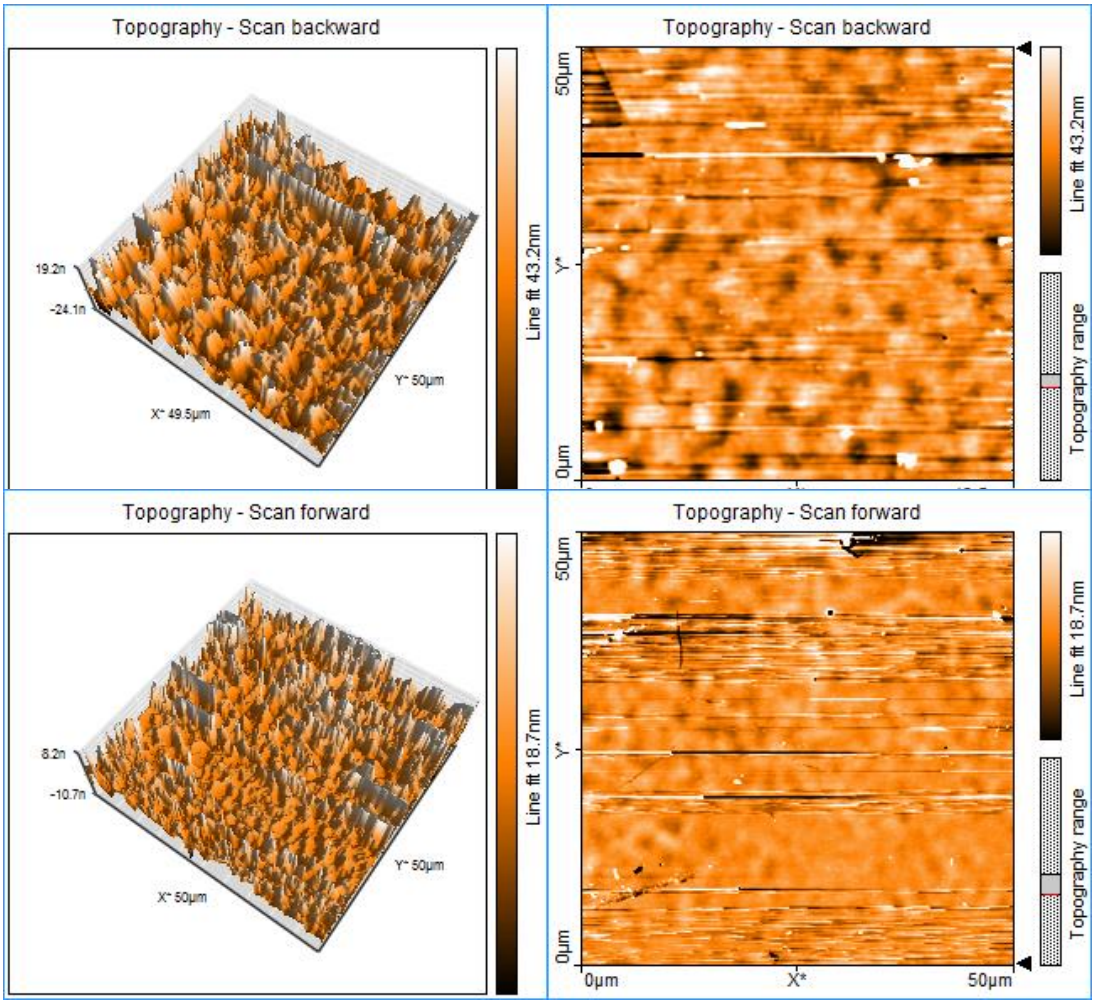


**Figure 3-8 AFM images of titania films prepared from 3 ml $TiCl_4$ and calcined at 350 °C (top) and 400 °C (bottom)**

### 3.2.2.3 Ellipsometry measurements

The films calcined at 350 and 400 °C are not smooth, as we can see many lines on the film from eyes due to the drying differences between various film areas with different thickness, so only an average value for thickness can be found by measuring different areas on the film. The films have similar thicknesses of ~ 130 nm and the variation is around 50 nm, but the two films have a totally different refractive index. The film calcined at 350 °C has a refractive index of 2.52, while the other sample is 1.65. By calculation from equation 2.33, their porosities are 3 % and 69 % for films calcined at 350 and 400 °C respectively. The huge difference is likely to be due to the fact that the template in the film calcined at 350 °C was not totally removed, as this temperature was relatively low, and the sample was held at this temperature for 5 min. Also according to our

previous experiments above the F127 template was more difficult to remove compared to P123. The refractive index of film the calcined at 400 °C was also the same as that found by Krins et al.[232]

### *3.2.3 Conclusion*

Ordered meso-$TiO_2$ films were successfully made by dip coating from aqueous solution without a subsequent ageing process. The withdrawal speed of dip coating, amounts of titanium salt in precursor solution, calcination temperature affected the mesostructure. The film prepared from 3 ml $TiCl_4$ and coated using a withdrawal speed of 10 mm/min had a cubic mesostructure (Im3m symmetry) and shrank in the vertical direction after calcination at 350°C and 400 °C. From the AFM results, the films had a meso/macroporous structure that could benefit the efficient transport of guest species to framework binding sites. The differences between the films calcined at 350 and 400 °C in mesostructure, surface morphology, and refractive index were due to the lower calcination temperature which decreased the degree of film shrinkage, but which also made a rougher surface and did not remove the template totally. However, both of the films had a very rough surface and low thickness ~ 130 nm, which limits their potentials in applications.

The GISAXS results demonstrate that it is feasible by this method to make a highly ordered meso-$TiO_2$ film, although many modifications on preparation process should be made to optimize the other properties of the films. Several possible methods are suggested here. Firstly, the viscosity of precursor solution could be adjusted to change the thickness of the films – solutions with a higher viscosity will produce thicker films. Secondly, pre-treatment of the substrates could be done to obtain a smoother film surface. When dip coating on cleaned glass slide with titania blocking layer on top was attempted, the surface looked smoother compared to the film coated onto cleaned glass slides, so the surface chemistry and the wetting of the synthesis solution on the substrate are also important variables. Thirdly, adjusting the calcination process to totally remove the templates and obtain crystallized anatase titania without pore collapse would help to retain the highly ordered mesostructure.

## 3.3 ZnO films self-assembled at air-liquid interface

ZnO has a similar band gap to that of titania, although it is not as stable as titania, but it is cheaper and has much higher electron mobility than anatase titania.[235] ZnO films are prepared by various methods, such as sputtering,[236] templating,[237] electrochemical deposition.[48] However, no report exists so far about the fabrication of ZnO films via self-assembly methods at air-liquid interface.

The growth of unsupported films, driven by solvent evaporation, is a promising route to manufacture large areas of robust, thick films. From previous experiments in our group, mesostructured surfactant/polymer films were grown at air-water interface and this method was expanded to fabricate free-standing mesostructured silica films templated by CTAB/SPEI.[238, 239] As the interaction between ZNAC and PEI is strong,[240] preparation of free-standing ZnO films templated by surfactant and PEI was attempted. CTAB/PEI, CTAB/SDS/PEI, and CpBr/PEI were all tested as the template. In CpBr/PEI solutions an interfacial film grew, but the others did not form films at all. However, only a little ZnO remained from the free-standing CpBr/PEI/ZnO film after calcination so the film fragmented into powder. The reagents concentration and the polymer (LPEI or SPEI) were varied, but still a free-standing ZnO film could not be obtained.

In chapter 7, the successful use of CTAB/SDS/PEO as a template with titania colloidal solution to make free-standing titania film is reported. Thus here we successfully fabricated free-standing ZnO films using the same template. Free-standing CTAB/SDS/PEO/ZnO films grew spontaneously at the air-water interface with ~ 15% ZnO incorporated inside the film. After calcination at 600 ºC for 3 h, the ZnO had a well-crystallized structure and spherical morphology that was formed by assembled ZnO nanocrystals.

### *3.3.1 Experiments*

CTAB, SDS, PEO, ZNAC were dissolved into Milli-Q water to give 0.1 M CTAB, 0.1 M SDS, 100 g/l PEO and 0.1 M ZNAC stock solutions. To prepare the CTAB/SDS/PEO/ZnO films, a CTAB and SDS solutions were mixed by diluted into water and then PEO and ZNAC solutions were added separately. This mixed solution was poured into a 50 mm diameter polystyrene dish over a piece of plastic mesh after a short period of stirring. Films grew at the air-liquid interface within several hours, were removed from the solution surface by lifting the open

plastic mesh and dried in the air at room temperature. Dried films were then calcined at different temperatures in air for 3 h with a ramp speed of 1 ºC/min and a natural cool down. Reagent concentration was adjusted according to the weight percentage of ZnO in CTAB/SDS/PEO/ZnO films by measuring the films before and after calcination at 600 ºC on an analytical balance. The CTAB/SDS/PEO/ZnO film with the highest weight percentage of ZnO was made from CTAB 1.4 ml/SDS 0.6 ml/PEO 1.6ml/ZNAC 1.8 ml and give a final composition of CTAB 0.0117 M, SDS 0.005, PEO 1.33 wt.% and ZNAC 0.015 M.

XRD, FESEM and EDS, TEM, $N_2$ adsorption, TGA and DSC were used to characterize these samples.

## *3.3.2 Results and Discussion*

### 3.3.2.1 TGA & DSC

Figure 3-9 shows the TGA and DSC curves of as-prepared free-standing ZnO hybrid film. The weight loss around 7 % in the temperature below 100 °C is because the evaporation of water in the film and the crystallization water removed from ZNAC. Between 200 and 400 °C, the mass loss of around 77 % is due to the removal of template and decomposition of ZNAC into ZnO. The TGA became more or less steady around 400 °C, but the formation of ZnO continues up to 550 °C. The DSC curve also supports this, as there is still a small peak at 535 °C corresponding to the ZnO crystallisation.

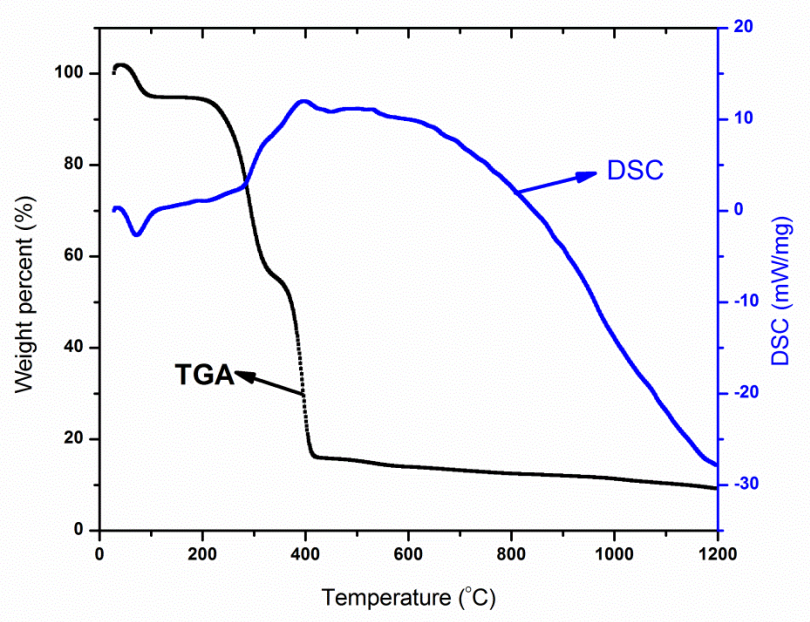


**Figure 3-9 TGA and DSC of as-prepared ZnO hybrid film.**

### 3.3.2.2 XRD

Figure 3-10 shows the XRD of the ZnO film calcined at different temperatures. For ZnO calcined at 600 °C, all diffraction peaks can be attributed to the (100), (002), (101), (102), (110), (103), (200), (112), and (201) planes of the wurtzite ZnO structure (JCPDS card no. 36-1451). For ZnO calcined at 400 and 500 °C, two extra peaks (circled in Figure 3-10) are observed as well as the peaks of wurtzite phase. The extra peaks might be from remaining acetate groups and organics on the ZnO surface,[241] which is also supported by the result from TGA and DSC. Crystallize size was estimated according to the Scherrer formula under the assumption of spherical crystals.[226] By increasing the calcination temperature from 400 to 500, to 600 °C, the crystal size increases from 17.8, to 18.9, to 27.4nm. The crystallite size only changes a little when the calcination temperature increased from 400 to 500 °C, probably due to the blocking effects of remaining compounds in ZnO films preventing diffusion of Zn atoms to form larger crystals.

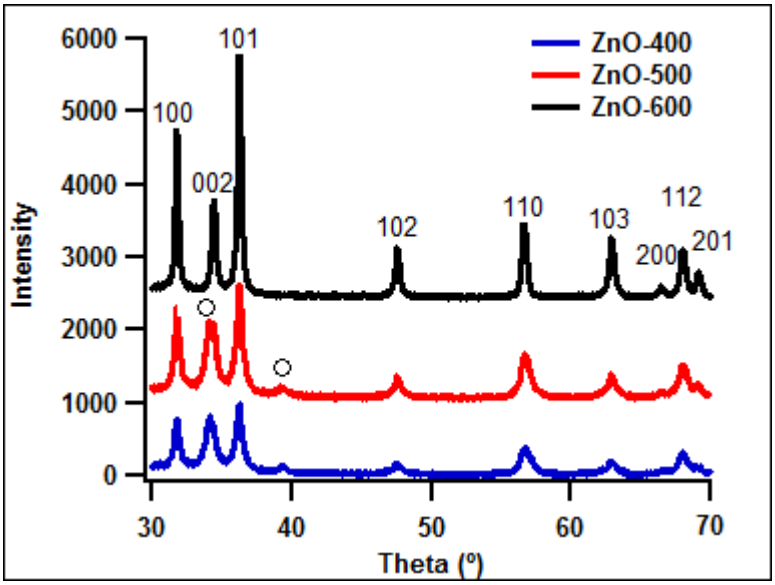


**Figure 3-10 XRD curves of ZnO calcined at 400 (ZnO-400), 500 (ZnO-500) and 600 °C (ZnO-600).**

### 3.3.2.3 FESEM & EDS

Figure 3-11 shows the FESEM images and EDS of a free-standing ZnO film after it was calcined at 600 °C. From image A in Figure 3-11, the film after calcination is not smooth and also cracks due to the relatively low remaining weight of inorganic species after the removal of surfactants (discussed above from the TGA results), which adds the difficulty to form continuous films. Surprisingly, the film is composed of spheres with a uniform size distribution around 100-200 nm, shown in image B. From the magnified image C, the spheres had a rough surface rather than smooth, which will increase the surface area. The rough sphere is assembled by the aggregation of elliptical nanoparticle with size around 50 nm. The EDS analysis of the film showed zinc and oxygen as the only detected elements, without any other elements left from surfactants or acetate groups.

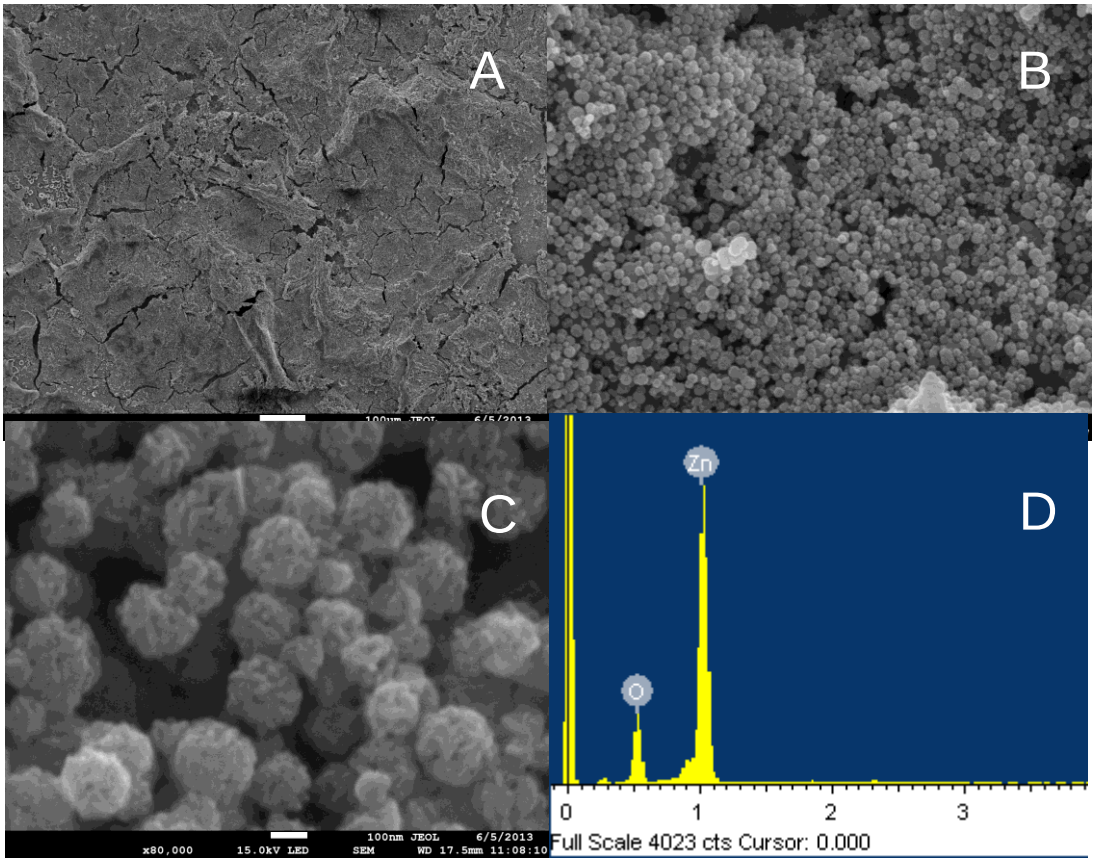


**Figure 3-11 FESEM images and EDS of a ZnO film calcined at 600 °C.**

### 3.3.2.4 TEM

Figure 3-12 shows TEM images and diffraction patterns of ZnO film calcined at 600 °C. From image A, it is clearly seen that the larger spheres have a size around 150 - 200 nm with a rough surface and are composed of elliptical nanoparticles. Image B shows a typical rough sphere with a size of 150 nm. The sphere was formed by aggregated nanoparticles with a long axis of ~ 35 – 50 nm and short axis of ~ 15 - 25 nm in dimension, which is in accordance with the crystal size from the XRD results. It is important to note that that these nanoparticles are nanoporous due to the formation of unsymmetrical pores associated with the interparticle spaces. In image C, the lattice spacing of 0.28 nm is clearly shown in the ZnO nanoparticle, which corresponds with the (100) plane of the wurtzite phase. The diffraction pattern reveals the sample has a well-crystallized structure and it is in the wurtzite phase, because these diffraction spots are attributed to (100), (002), (101), (102), (110), (103), and (200) planes of

the wurtzite phase, respectively. The results of the TEM images and diffraction patterns are totally in agreement with XRD and FESEM results.

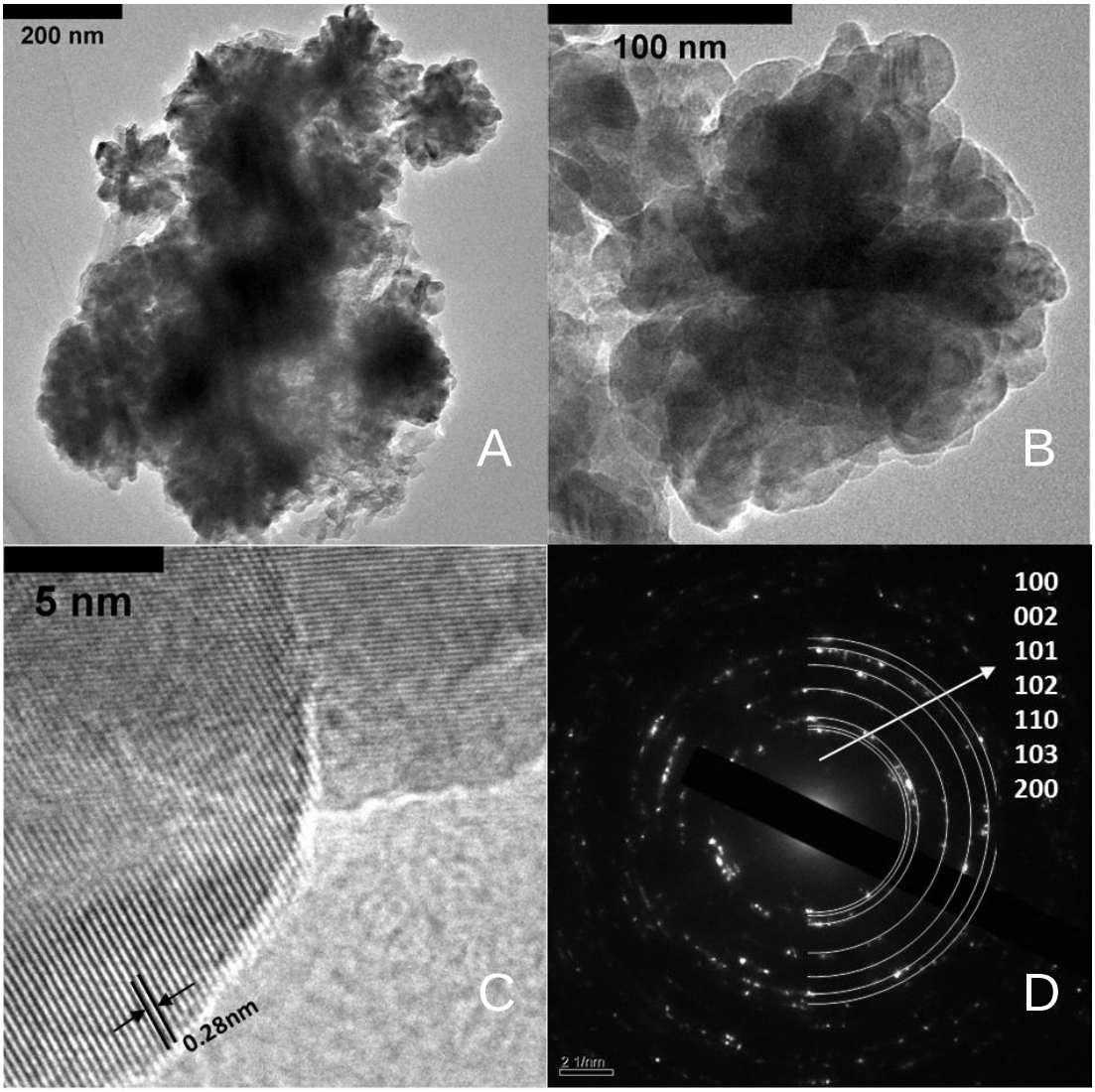


**Figure 3-12 TEM images and diffraction pattern of particls from a ZnO film calcined at 600 °C.**

### 3.3.2.5 $N_2$ adsorption isotherm

Figure 3-13 shows the $N_2$ adsorption isotherm of the ZnO spheres from a powdered film sample. The isotherm is type III, which indicates a lack of a low interaction between $N_2$ and the ZnO surface. The $N_2$ adsorption from some other publications also shows the same curve shape.[242, 243] Due to the low absorbed $N_2$, the desorption branch became minus in the low relative region pressure, so BJH pore size distribution cannot be obtained. The $N_2$ adsorption testing was done twice and both showed the similar results, so the adsorption isotherm is

considered to be believable. The BET surface area is 19.1 $m^2/g$, which is high compared to the surface area of commercial ZnO which is around 4 - 5 $m^2/g$.[244] This is also a comparable result with other preparations of spherical ZnO particles. Chen et al. prepared nano-sized ZnO particles with a surface area of 18.87 $m^2/g$ from the direct calcination of $Zn_4(CO_3)(OH)_6 \cdot H_2O$ at a temperature of 550 °C for 2 h.[245] Barick et al. fabricated ZnO aggregate spheres by refluxing zinc acetate dihydrate using diethylene glycol as a solvent.[246] The spheres with size 150 – 200 nm had a crystal size of 20 nm and surface areas of 20.6 $m^2/g$. From the BJH pore size distribution, the ZnO has mesopores and macropores. The mesoporous are from the voids between the nanoparticle aggregation and the macropores are due to the open space between spheres.

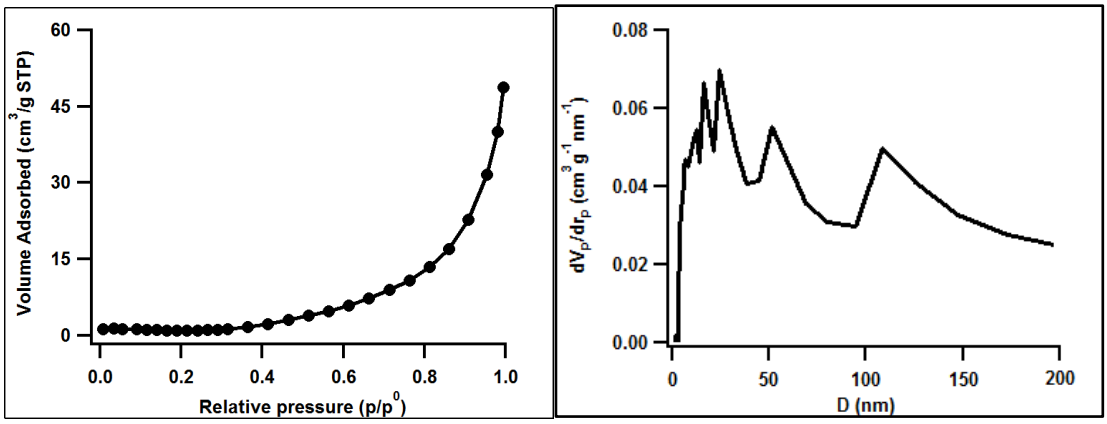


**Figure 3-13 $N_2$ adsorption isotherm and BJH pore size distribution of ZnO calcined at 600 °C.**

### 3.3.2.6 Mechanism for film formation

The overall CTAB/SDS concentration in the film growth solution is 0.0125 M. In our group, people found that 0.01 M CTAB/SDS mixed surfactant solutions contain larger ellipsoidal aggregates (1.5 × 0.5 microns) and small mixed micelles (90% CTAB) in aqueous solution,[247] and the addition of PEO was measured to affect the morphology of micelle aggregates at higher concentrations of CTAB/SDS but was not measured at the concentration used here to form the ZnO film. After adding the ZNAC, the positive charged zinc ions interacts with surfactants or polymer to decrease their surface free energy.[248] The surfactants or polymers with absorbed zinc ions are less soluble so rapidly assemble into large aggregates, and then the absorbed zinc ions form ZnO nuclei gradually. For

the small, largely CTAB surfactant micelles, little zinc ions would be expected to interact due to the electrostatic repulsion force, as the point-of-zero charge (pzc) of ZnO is ~ 9-10 and the ZnO is posive-charged. Although CTAB,[249] SDS,[250] and PEG [251] have all been found to produce elongation effects favouring the growth of ZnO nanoparticles into single crystal nanorods, the ZnO nuclei in the CTAB/SDS/PEO aggregates are trapped in the viscous aggregated structures and so cannot move around to form single crystal nanorods but instead form polycrystalline nanoparticles with elliptical shape. Driven by the solvent evaporation, the ZnO hybrid spheres, micelles and PEO migrated to the surface to form films within a few hours after mixing. This surface layer condenses due to the continuous evaporation of water and the high local concentrations of PEO, wrapped around the spheres play an important role to shield electrostatic repulsion between charged compounds and bind them together.[252] The wet films can be easily lifted by a mesh and dried in air to obtain thick and robust ZnO hybrid films. Dried films with around 15 % ZnO were calcined in air to eliminate the organics and crystallize the structure. During the calcination, the microspheres also shrank giving finally spheres 100 - 200 nm.

### *3.3.3 Conclusion*

Free-standing ZnO films with ~15 % ZnO inside were successfully fabricated via a template-assisted method and a possible mechanism was proposed. The procedure of decomposition of organics and ZNAC was not fully finished until ~ 550 ºC, according to the TGA, DSC and XRD results. After calcination at 600 ºC, the ZnO in the film had a wurtzite phase with a crystal size of 27.4 nm and the film was composed of rough spheres. The spheres had uniform size distribution in the films around 100 - 200 nm and were composed of assembled elongated ZnO nanoparticles. The film calcined at 600 ºC had a surface area around 20 $m^2/g$, which is much higher than commercial ZnO nanoparticles. These properties can make the free-standing ZnO films serve as a promising candidate for many applications.

However, no further work was done on these materials due to the limited time. ZnO aggregated spheres have strong scattering effects, which could improve the efficiency of DSSCs.[253] In our case, the film had many cracks due to the low loading of ZnO in films, so adjustments of synthesis parameters to obtain robust

ZnO film will be the first thing required for future development of these films. After that, the free-standing ZnO could be used as the scattering layer or as the photoelectrode in a DSSC. Moreover, the free-standing ZnO hybrid film before calcination could also have potential for direct use in applications, as PEO is a well-known polymer electrolyte and has been applied in many electronic devices. The incorporation of ZnO in PEO has been studied to improve the photoluminescence of ZnO-PEO films,[254] and the electrical properties of ZnO-PEO-$LiClO_4$ films, which could help the performance of UV emitters and lithium batteries prepared using the ZnO hybrid films developed here.[255]

# Chapter 4 Ordered Mesoporous Titania and Nanoparticle Composite Films prepared by doctor-blading for DSSC

Typical photoelectrodes used in DSSC are around 10 μm thick and prepared from titania nanoparticle by the doctor blade method. Mesoporous titania (meso-$TiO_2$) powders can also be used to prepare photoelectrodes with thickness around 10 μm and these photoelectrodes have shown a promising efficiency when applied into DSSC.[96, 256, 257] Using meso-$TiO_2$ materials as an electrode sensitized by N719 dye in a DSSC, reached an efficiency of 10 % in 2006.[256] Recently, meso-$TiO_2$ has been synthesized for DSSC in micron/submicron particle geometries with hierarchical structures, such as titania aggregates,[101, 258] beads,[202, 257] spheres,[82, 259] and inverse opal structures.[260] These porous structures are composed of primary nano-crystallites that cluster together to form larger secondary particles, thereby functioning as light scatterers without sacrificing the internal surface area needed for effective dye-uptake when applying them in DSSC.

Here, we propose using ordered 2D-hexagonal meso-$TiO_2$ aggregates as the scattering particles in DSSC. The meso-$TiO_2$ particles have large internal pores and an ultrahigh surface area to increase dye loading and the open spaces between large aggregates help ensure efficient electrolyte diffusion.[202, 258, 261] A bilayer photoelectrode was used in a DSSC with the underlying layer made from a commercial titania paste and the scattering layer prepared from meso-$TiO_2$ aggregates, Degussa P25 titania nanoparticles or their mixtures. The influence of film structure, morphology, optical properties and cell performance were investigated in films prepared by adding meso-$TiO_2$ into Degussa P25 nanoparticles with weight proportions ranging from 0 to 100%. The results show an improved photovoltaic performance of the DSSC with meso-$TiO_2$ and the best cell was obtained by incorporating 50 wt.% meso-$TiO_2$.

## 4.1 Experimental

Ordered meso-$TiO_2$ was prepared through an EISA method using TIPR as a precursor,Pluronic P-123 as the surfactant template and HCl and $H_2SO_4$ as the acidic catalysts. 1.0 g of P-123 was dissolved in 40 ml ethanol, to which 1ml HCl (32 %) and 0.2 ml $H_2SO_4$ (98 %) were added. The solution was placed into a bottle sealed with a cap and stirred vigorously for 3 h at room temperature. 2.9 ml TIPR was added dropwise at room temperature followed by vigorous stirring for 20 h at 40 ˚C. The solution was poured into petri dishes and evaporated at 40 ˚C in air under a relative humidity of 55 % for several days. The resulting membranes were crushed into powder and calcined in air at 350 ˚C for 3 h first, followed by a further 3 h at 450 ˚C , using a temperature ramp of 1˚C/min.

TGA, SAXS, XRD, TEM, $N_2$ adsorption and desorption were used to characterized these powder materials.

The calcined meso-$TiO_2$ powders were mixed with commercial Degussa P25 nanoparticles at different weight ratios. The mixtures were ground thoroughly before use and are named meso-X (X= 0, 25, 50, 75 or 100) where X represents the weight percentage of the meso-$TiO_2$ in the mixture.

Titania paste was prepared by mixing titania powder with ethyl cellulose as a binder and terpineol as the solvent. The final weight ratio of titania, ethyl cellulose and terpineol was 3:2:10. The synthesis procedure was done according to the procedure described below in Figure 4-1.

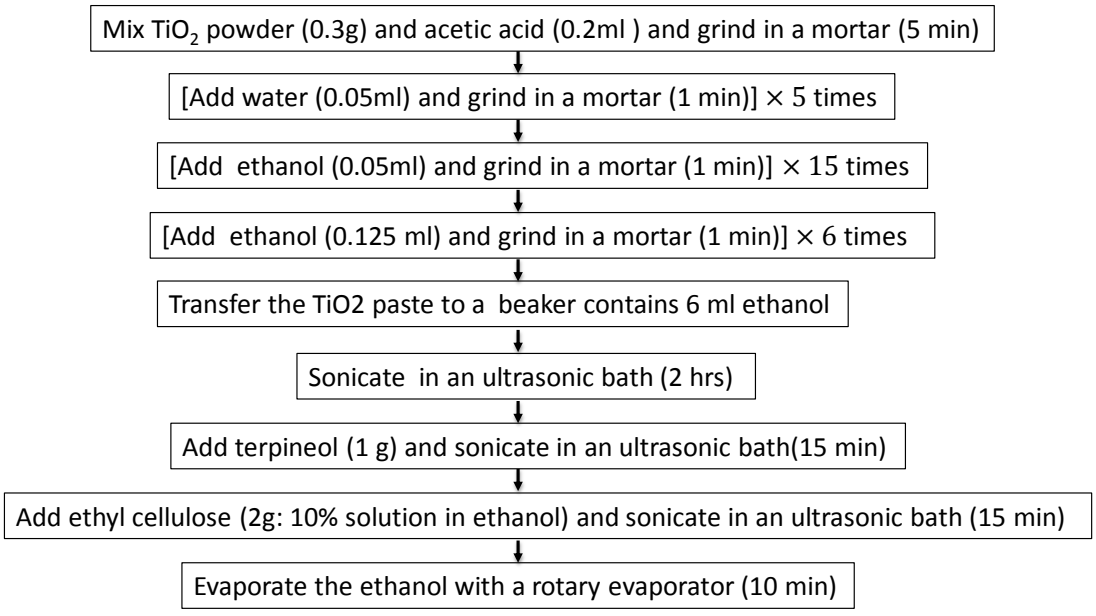


**Figure 4-1 Fabrication scheme for $TiO_2$ pastes.**

A bilayer nanocrystalline $TiO_2$ photoelectrode was prepared to be used in the DSSC. The first layer of nanocrystalline $TiO_2$ was deposited on FTO glass (7.5 × 2.5 $cm^2$) with a blocking layer, using a commercial paste (Ti-Nanoxide T, Solaronix) and the doctor blade method. 'Magic tape' (Scotch) was used to mark out a 1 cm wide strip on the glass and control the film thickness. The slide containing the first layer was then placed on a hotplate for 30 min at 100 ºC. To minimize the effects of the first layer on the cells' performance, the FTO glass slide with a single Ti-Nanoxide layer was cut into 5 small pieces (1.5 × 2.5 $cm^2$). Then the second layer was doctor bladed on top of each piece using one of five different home-made pastes. The bilayer photoelectrodes were treated using the heating procedure, shown in Figure 4-2 to remove organic species from the pastes and open up the pores in the film.

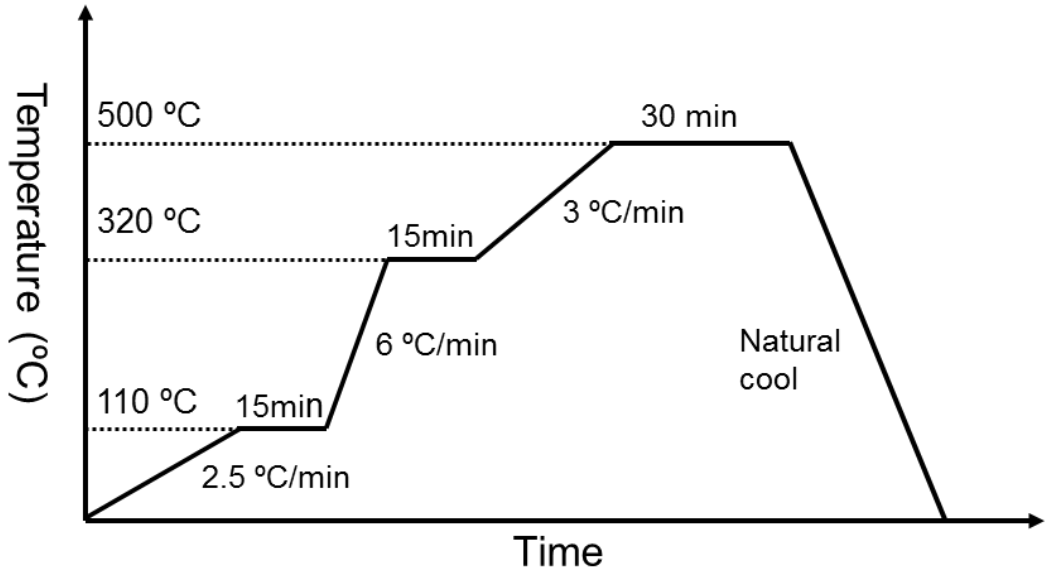


**Figure 4-2 Heating procedure used to obtain a porous titania layer.**

SEM, AFM, and reflectance spectra were used to characterize film samples. XRD and $N_2$ adsorption and desorption were used to test powder samples. The powders were scratched down from the substrates, where the films were doctor-bladed onto glass without the underlayer and calcined using the procedure described above.

The meso-X films were put into DSSC. Quantification of the adsorbed dye was carried out using an UV/Vis spectrometer. In order to optimize the dye

immersion time, a meso-0 film was used to test the adsorbed dye amount as a function of time. IV curves and IPCE were measured to evaluate the cell performance.

## 4.2 Results and Discussion

### *4.2.1 Ordered meso-$TiO_2$ powder*

#### 4.2.1.1 SAXS

Figure 4-3 shows the SAXS patterns of the as-prepared meso-$TiO_2$ sample aged at different time before and after calcination. Both of them display similar curve shape with almost four scattering peaks. A clear shift of the diffraction peaks to a low q was observed suggesting shrinkage of the titania network after the removal of template.[262, 263] For the as-prepared samples, an increase of the ageing time improved the degree of ordering revealed by the decreased peak width of the peak at 0.47 $nm^{-1}$. However, little improvement of mesostructure was observed between as-prepared samples ageing for 6 and 9 days. Considering the preparation time and mesostructure of samples, sample ageing for 6 days were used for later experiments. For a calcined sample aged for 6 days, the peaks in the pattern at q-values of 0.59, 1.02, 1.18 and 1.56 $nm^{-1}$ can be indexed to the (100), (110), (200) and (210) reflections, which correspond to an ordered 2D hexagonal ($p6mm$) mesostructure. The unit cell parameters of the as-prepared and calcined samples aged for 6 days were 15.1 and 12.4 nm respectively, indicating a 17.9 % contraction of the titania network during calcination. From previous reports, SAXS patterns for calcined bulk 2D hexagonal meso-$TiO_2$ usually display only one or two peaks, although the corresponding patterns for as-synthesized samples distinctly show three peaks.[264-266] Additionally, the contraction ratio of hexagonal titania after calcination at 450 ºC here was relatively low in comparison to work by others.[264, 267, 268] Thus, this synthesis produced a very well-ordered stable meso-$TiO_2$ which exhibited only a small amount of shrinkage upon calcination.

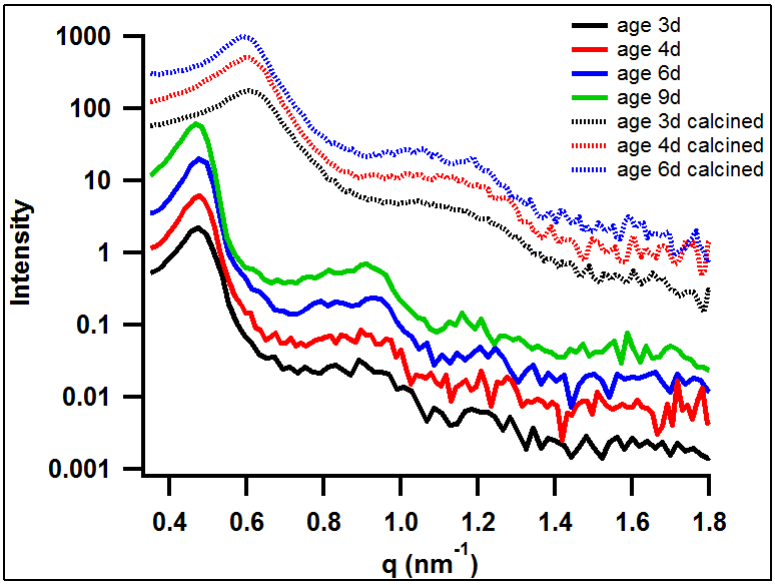


**Figure 4-3 SAXS curves of meso-$TiO_2$ aged for different times during preparation, before and after calcination.**

### 4.2.1.2 XRD

The crystallographic structure of the calcined meso-$TiO_2$ powders was confirmed by XRD analysis (Figure 4-4) All diffractions peaks can be assigned to (101), (004), (200), (116), (220) and (204) planes of the anatase $TiO_2$ (JCPDS card no. 21-1272). The crystallite size calculated according to the Scherrer formula [226] is ~ 7 nm.

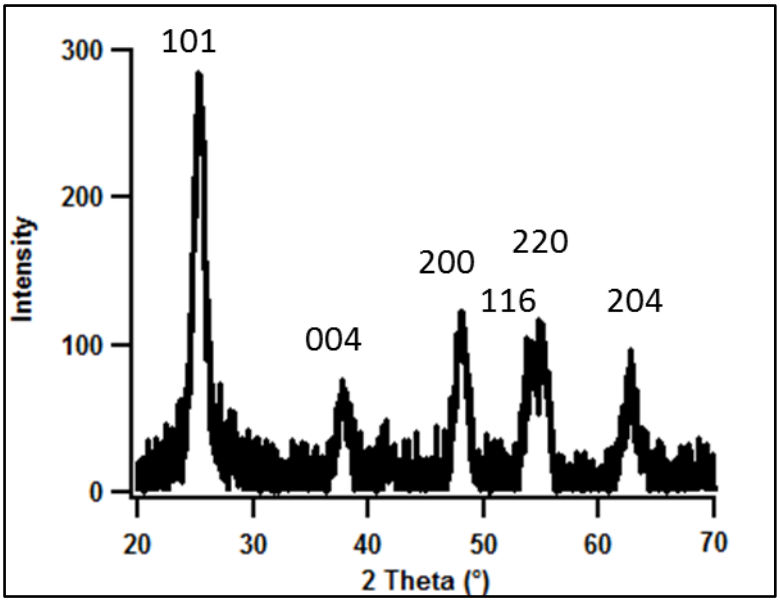


**Figure 4-4 XRD curve of calcined meso-$TiO_2$.**

### 4.2.1.3 TEM

The TEM image in Figure 4-5 shows a highly ordered structure with a degree of periodicity having a d-spacing of 10.6 nm, viewed from the (100) directions, further confirming the 2D hexagonal ($p6mm$) mesostructure suggested by SAXS. The diffraction pattern reveals that the sample has a nanocrytalline structure and is in the anatase phase, because the clear crystal rings in the inset diffraction pattern are attributed to (101), (004), (200), (211) and (204) planes of the anatase phase, respectively. This is in agreement with the XRD result.

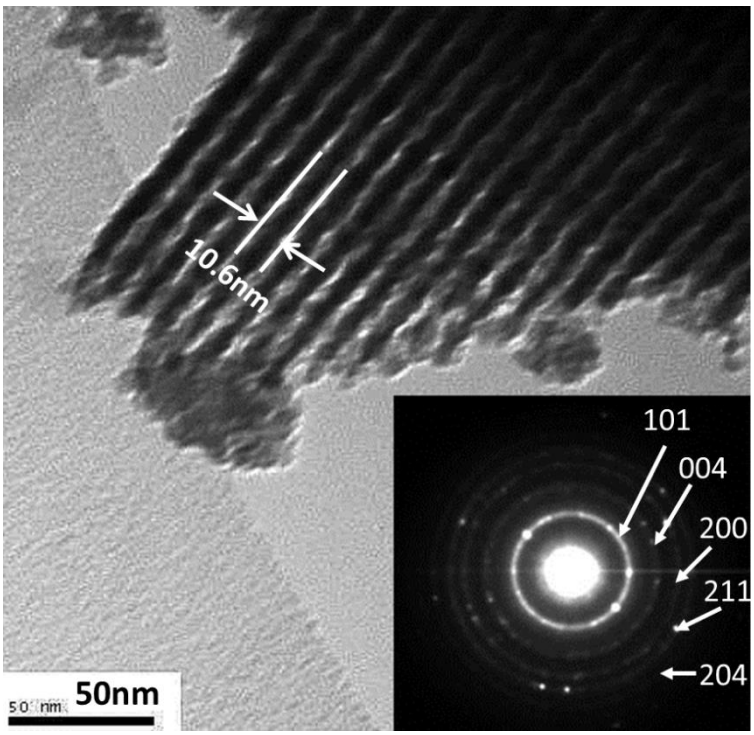


**Figure 4-5 TEM image of calcined meso-$TiO_2$ with the electron diffraction pattern inset.**

#### 4.2.1.4 $N_2$ adsorption and desorption

Figure 4-6 shows the nitrogen adsorption and desorption isotherms and pore size distribution of the meso-$TiO_2$ powder. The isotherms can be classified as type IV with a pronounced H1 hysteresis loop and show a sharp capillary condensation step at a relative pressure of 0.7 - 0.9, suggesting a narrow pore size distribution and the existence of large mesopores with an open-ended cylindrical shape in this sample.[229, 230] The predominant pore size is around 8.33 nm with a total pore volume of 0.28 $cm^3/g$ and they are uniform and narrowly distributed. To the best of our knowledge, such pore sizes are one of the largest for ordered mesoporous titania synthesized using the P123 template without any

swelling agents.[231] The large pores can improve the accessible pore volumes allowing the adsorption of dye molecules on the internal surfaces.[99] The BET surface area of the meso-$TiO_2$ is 121 $m^2/g$, which is also quite high considering the large pore diameter.

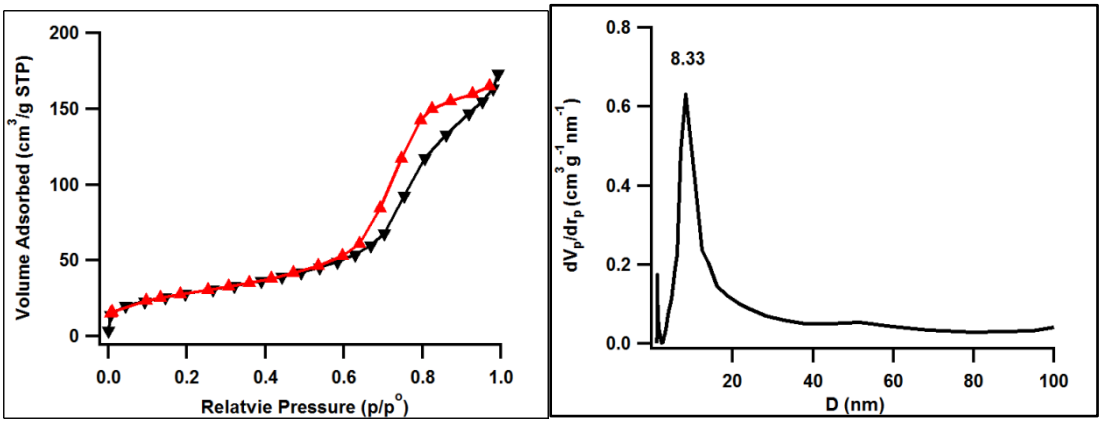


**Figure 4-6 $N_2$ ads/desorption isotherms and BJH pore size distribution of calcined meso-$TiO_2$.**

### 4.2.1.5 TGA

The TGA curve of the as-prepared uncalcined meso-$TiO_2$ is shown in Figure 4-7. Below 130 °C, about 8 % mass loss is due to volatile species, such as water, ethanol and HCl. Between 130 and 300 °C, a mass loss of around 43 % arises from the combustion of the P123 template. After that stage, a small mass loss occur due to the continuous removal of residual organic and sintering of $TiO_2$ particles.[225] The final mass weight at 600 °C is 38 %, which indicates that the $TiO_2$ powders have a composition of about 38 % $TiO_2$,43 % organics and 8% solvent before the heat treatments. To further confirm the removal of organics, the calcined titania was tested by TGA and displayed in Figure 4-7. It has ~5% weight loss in the range of 40-180 ºC due to the evaporation of moisture that absorbed from the air during storing and ~ 3% weight loss at higher temperatures due to the removal of residual carbon.

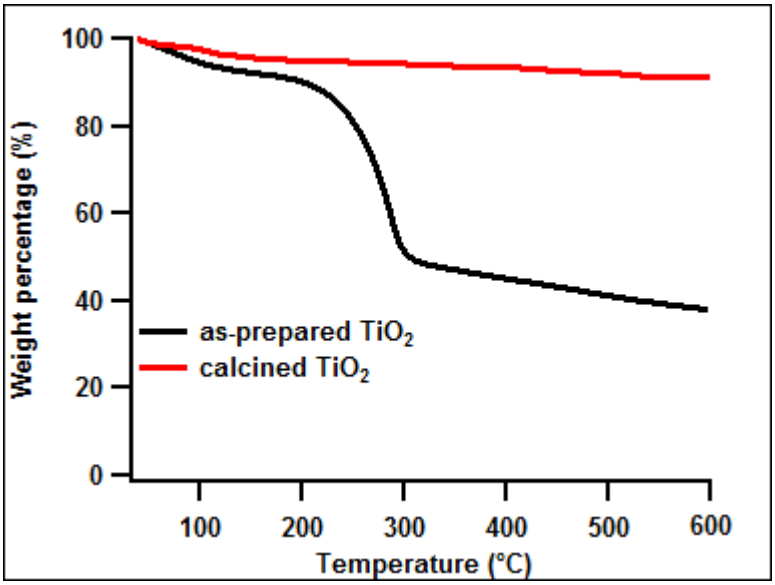


**Figure 4-7 TGA curve of meso-$TiO_2$ before and after calcination.**

## *4.2.2 Ordered meso-$TiO_2$ and nanoparticle composite films*

### 4.2.2.1 XRD

The properties of meso-$TiO_2$/Degussa P25 composite films were also investigated by XRD (Figure 4-8). Only the anatase phase was found in the meso-100 sample, while the other films contained both anatase and rutile phase, as a small amount of the rutile phase is contained in Degussa P25 nanoparticles. According to the following equation: [269]

$$W_R = \frac{I_R}{0.886 I_A + I_R}$$

the mass fraction of rutile ($W_R$) in the samples can be calculated by measuring the intensities of the strongest (110) and (101) diffraction peaks of rutile ($I_R$) and anatase ($I_A$), respectively. The results are listed in Table 4-1. It can be seen that the mass fraction of rutile phase decreases with increasing weight ratio of meso-$TiO_2$.

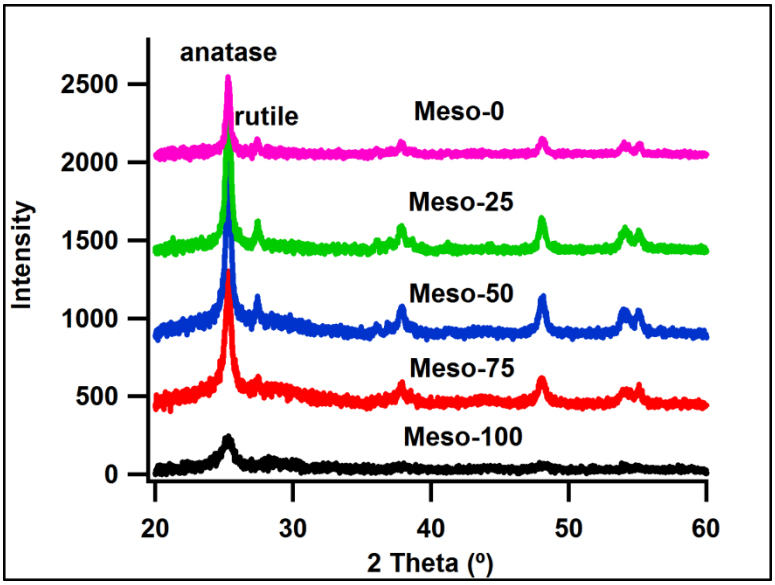


**Figure 4-8 XRD curves of meso-X (X=0, 25, 50, 75 and 100).**

#### 4.2.2.2 SEM

Figure 4-9 shows a SEM image of the top view with inset cross-sectional images of meso-X (X=0, 25, 50, 75 and 100) films. SEM showed that films were homogenous on the micron-scale. With the increase in weight ratio of meso-$TiO_2$, films become rougher as a result of the growing number of secondary titania particles. By adding meso-$TiO_2$, the films look more porous than the meso-0 film according to the magnified SEM surface images. However, the meso-100 layer can be easily peeled off the substrate after calcination, while others are more robust. This is because the film made entirely from meso-$TiO_2$ contains large aggregates with open space between them leading to a weaker and less compact film. From the inset cross-sectional images, it can be seen that the first layer of the five photoelectrodes has exactly the same thickness (5 μm) and morphology, which should remove effects arising from the first layer when comparing the cell performance using different bilayer electrodes. The thickness of the meso-X films is around 5 μm and it is also easily seen that they have a smooth edge except in the case of the meso-100 film due to its loosely compacted structure.

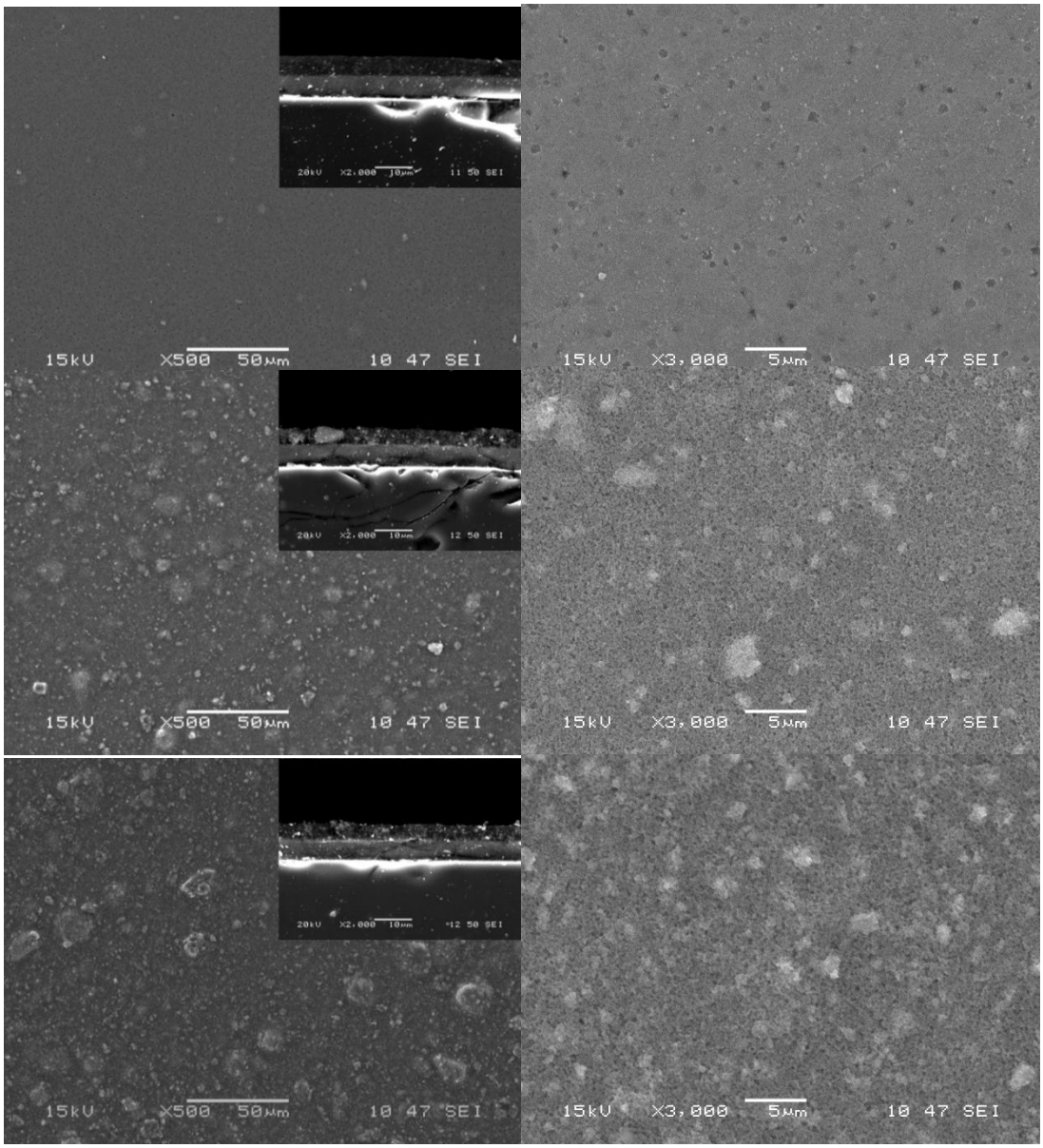
15kV X500 50µm 10 47 SEI
15kV X3,000 5µm 10 47 SEI
15kV X500 50µm 10 47 SEI
15kV X3,000 5µm 10 47 SEI
15kV X500 50µm 10 47 SEI
15kV X3,000 5µm 10 47 SEI

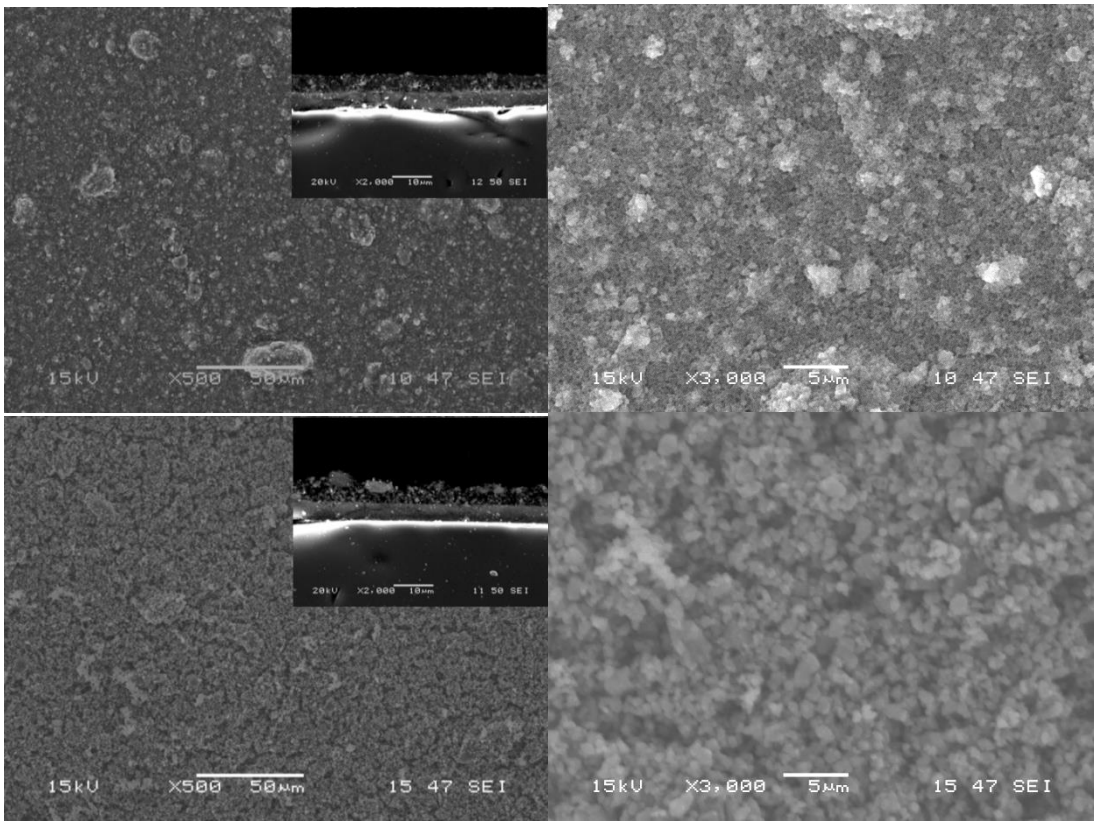


**Figure 4-9 Top view of meso-X films (X=0, 25, 50, 75 and 100) from top to bottom by SEM. Insets: cross-sectional images of the films.**

#### 4.2.2.3 AFM

AFM images of meso-X films were tested to further confirm the SEM results, as displayed in Figure 4-10. With the increase of weight ratio of meso-$TiO_2$, films become rougher with visible larger aggregates. The area root mean square roughness of films is summarized in Table 4-1. The RMS increased from 30.71 to 300.66 nm when the weight ratio of introduced meso-$TiO_2$ varied from 0 to 100, which is in accordance with the SEM results.

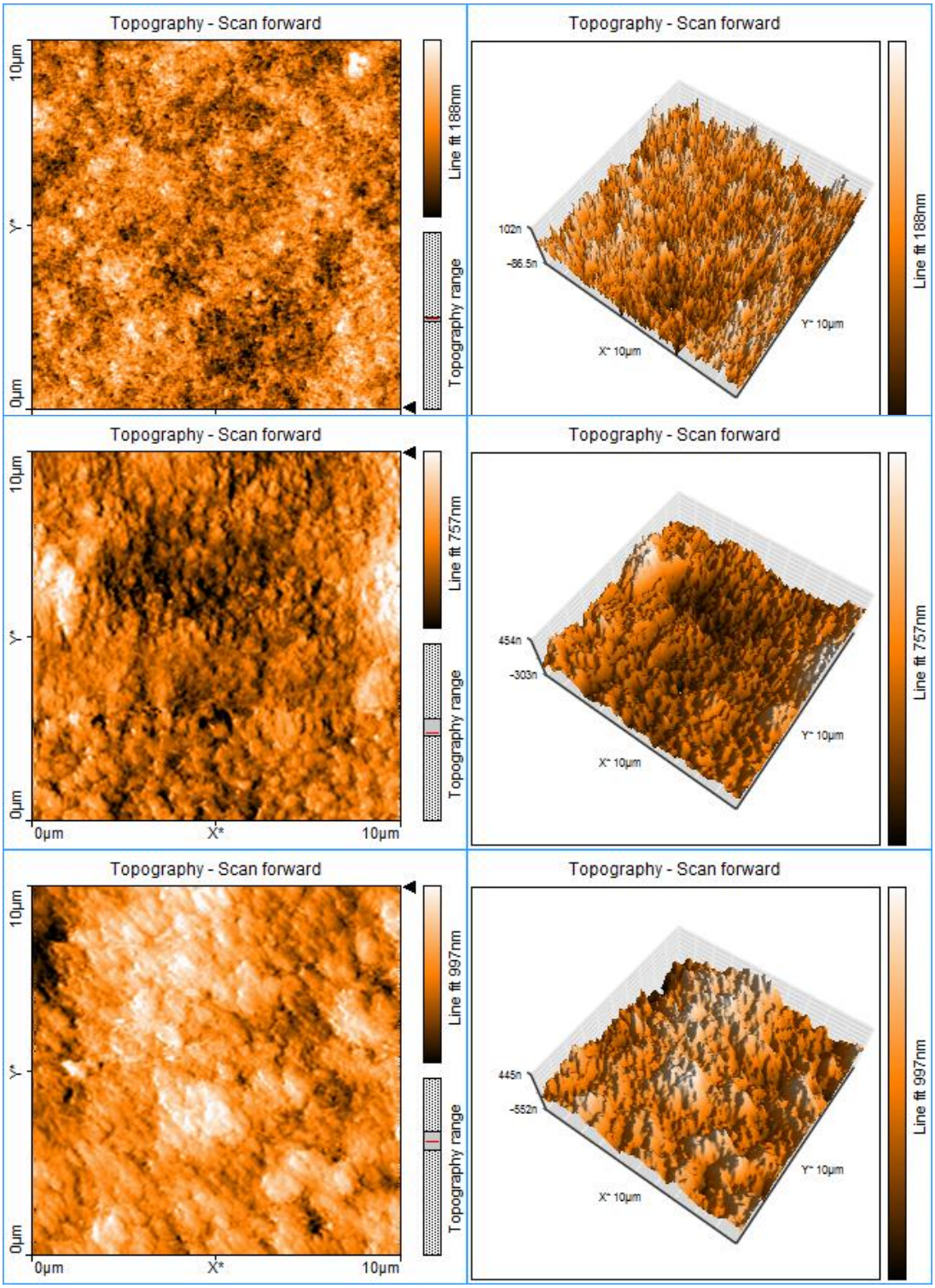
Topography - Scan forward
10µm
Y*
0µm
Line fit 188nm
Topography range
Topography - Scan forward
102n
-86.5n
X* 10µm
Y* 10µm
Line fit 188nm
Topography - Scan forward
10µm
Y*
0µm
0µm
X*
10µm
Line fit 757nm
Topography range
Topography - Scan forward
454n
-303n
X* 10µm
Y* 10µm
Line fit 757nm
Topography - Scan forward
10µm
Y*
0µm
0µm
X*
10µm
Line fit 997nm
Topography range
Topography - Scan forward
445n
-552n
X* 10µm
Y* 10µm
Line fit 997nm

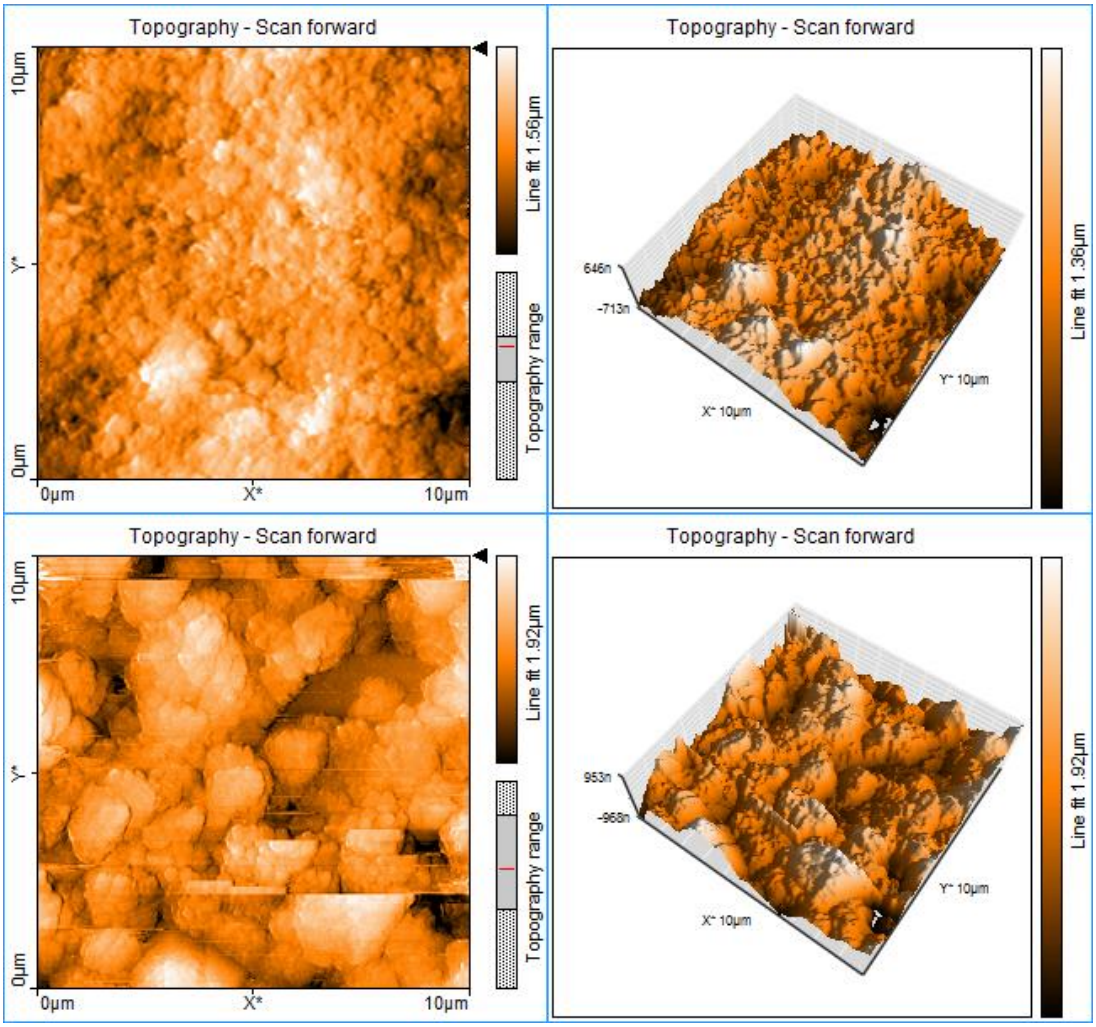


**Figure 4-10 AFM images of meso-X films (X=0, 25, 50, 75 and 100) from top to bottom.**

### 4.2.2.4 $N_2$ adsorption and desorption

Figure 4-11 shows the nitrogen adsorption and desorption isotherms and pore size distribution of meso-X (X=0, 25, 50, 75 and 100) mixtures. As the meso-$TiO_2$ was already calcined at 450 ºC for 3 h prior to mixing with the Degussa P25 in pastes to form the films, the isotherms of meso-100 films look very similar to the meso-$TiO_2$ powder, although the pore size distribution seems wider because the pore size distribution also measured the pores formed by gaps between the meso-$TiO_2$ particles which will be in the same size range as the particle size of the meso-$TiO_2$ became smaller by the grinding. The BET surface area of the meso-100 film is 157 $m^2/g$, which is more than 3 times higher than that of the meso-0 films (46 $m^2/g$). After the introduction of Degussa P25 particles into the meso-$TiO_2$, the shape of sorption isotherms changed and the hysteresis loop

became smaller. The surface area decreased because the Degussa P25 is a non-porous material and as a result has a much lower surface area than meso-$TiO_2$ despite the presence of inter-particle porosity in the P25 materials. The predominant pore size of the meso-100 films is around 8.33 nm arising from the internal pores of meso-$TiO_2$, while the larger pores of Degussa P25 films are caused by the internal space within nanoparticle aggregates and open space between aggregates.[261] No macropores were observed in the meso-100 films because the open space between aggregates is too big to be analysed using in BJH models.[270] The change in composition of the films caused variation in the pore size distribution and pore volumes in the films. The BET surface area and total pore volume of films are summarized in Table 4-1. Obviously, the meso-100 has the highest surface area but with the lowest pore volumes due to the lack of macropores. Meso-50 and meso-75 shares a very similar surface area but the meso-50 has a higher pore volume. Considering the surface area and porosity, the optimum composite is likely to be the meso-50 films with a pore volume of 0.70 $cm^3/g$ and surface area of 127 $m^2/g$.

**Table 4-1 Textural properties of meso-$TiO_2$/Degussa P25 composite films.**

| *Sample* | *Meso-0* | *Meso-25* | *Meso-50* | *Meso-75* | *Meso-100* |
|---|---|---|---|---|---|
| Phase ratio (anatase:rutile) | 80:20 | 85:15 | 90:10 | 95:5 | 100:0 |
| RMS roughness (nm) | 31 ±2 | 100 ±6 | 160 ±8 | 220 ±14 | 300 ±20 |
| $S_{BET}$ ($m^2/g$) | 46 | 69 | 127 | 127 | 157 |
| Pore volume ($cm^3/g$) | 0.39 | 0.26 | 0.70 | 0.65 | 0.33 |
| Thickness (μm) | 4.9+4.6 | 4.9+4.5 | 4.9+4.4 | 4.9+4.5 | 4.9+4.7 |

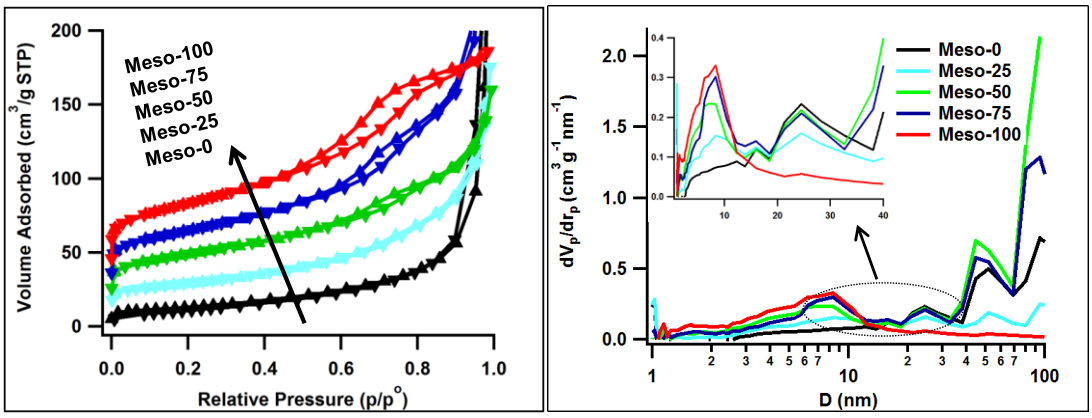


**Figure 4-11 $N_2$ ads/desorption isotherms (left) and BJH pore size distribution (right) of calcined meso-X films.**

### 4.2.2.5 Reflection spectra

To investigate the light scattering effects of the meso-X films for use in DSSC photoanodes, the reflectance spectra of the five photoanodes were compared, shown in Figure 4-12. The meso-100 electrode has the highest reflectance, as it is composed of large secondary particulates with a strong light scattering effect, while the meso-0 film shows the lowest scattering due to a much smaller size of Degussa P25 particles. When adding the meso-$TiO_2$ into the nanoparticle film, the reflectance is greatly improved due to the scattering effects of these large aggregates. The meso-50 anode film shares a similar value with that of the meso-75 anode, despite the meso-75 containing more large aggregated particles. This is because the meso-50 film had a higher number of macropores than the meso-75 film (refer to the BJH pore distribution in Figure 4-11) which could also serve as scattering centres.[271] The inset in Figure 4-12 shows the actual appearance of the meso-X photoanodes. The photoanodes were placed above a sheet with words to demonstrate their transparency. For the Meso-0 sample, the words beneath the photoanode can still be identified, whereas the words under other samples become gradually less clear as the weight ratio of meso-$TiO_2$ was increased and are completely obscured by the meso-100 film because of the intense light scattering effect of the micrometre sized aggregates of meso-$TiO_2$. It is worth mentioning that the transparency of meso-50 and meso-75 films is quite similar.

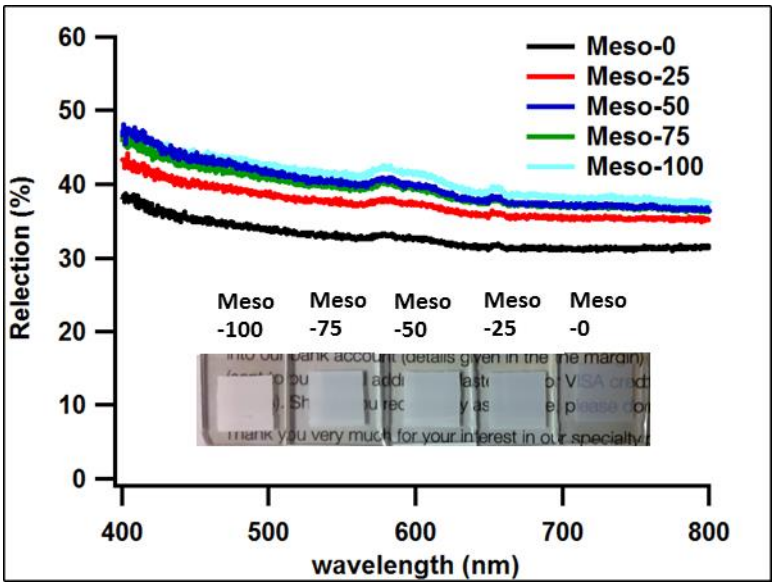


**Figure 4-12 Reflection spectra and photographs of meso-X films**

### *4.2.3 Ordered meso-$TiO_2$ and nanoparticle composite films in DSSC*

#### 4.2.3.1 Optimization of Dye Uptake Time

From the reports,[272] the dye uptake is related to the immersion time in dye solution. To optimize the immersion time, mes-0 film was used to test the dye uptake time in the function of immersion time (Figure 4-13). With the increase of immersion time, the dye uptake should increase and then level off, but it is not shown in this case and several reasons are possible. Firstly, the values calculated are mol/cm$^2$, which do not account for the thickness of the films and the thickness may vary slightly between films. Secondly, the quality of dye aggregates increased in the dye solution when keeping the solution static for longer time, which decreased the concentration of dye solution. To obtain the equilibrium, the absorbed dye in film also decreased. So, 20 h was chosen as the optimized immersion time. This time was then also used for the other films when testing the dye uptake and applied in the manufacture of dye coated films for DSSCs.

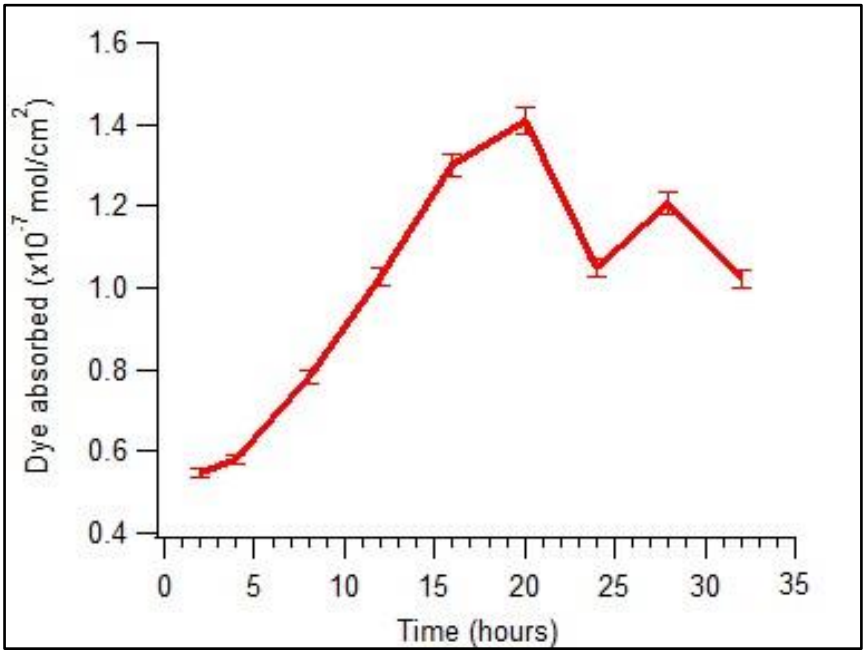


**Figure 4-13 Dye uptake of meso-0 film as a function of immersion time**

#### 4.2.3.2 DSSC based on meso-0 electrodes with various initial layers

The first layer of a bilayered photoelectrode was made either from Solaronix or Dyesol paste. The thickness of the first layer made from Dyesol paste (named DSL 18NR-T) was controlled by one layer of Scotch tape. For initial layer prepared from Ti-nanoxide paste, two thicknesses were adopted and the films were named Ti-Nanoxide or Thick Ti-Nanoxide. The thickness of Ti-Nanoxide film was controlled by one layer of Scotch tape and that of Thick Ti-Nanoxide was controlled by two layers of the tape.

Figure 4-14 shows SEM cross-sectional image of the bilayered photoelectrode prepared from Ti-Nanoxide and DSL 18NR-T films. The SEM cross-sectional image of the bilayer photoelectrode prepared from Thick Ti-Nanoxide is displayed in Figure 4-10 (top). The three photoelectrodes show different thickness of the initial layer and their values were summerized in Table 4-2. The initial layers of Ti-Nanoxide and Thick-Nanoxide films have a thickness of 2.5 and 4.9 µm respectively, while that of DSL 18NR-T has a thickness of 6.0 µm.

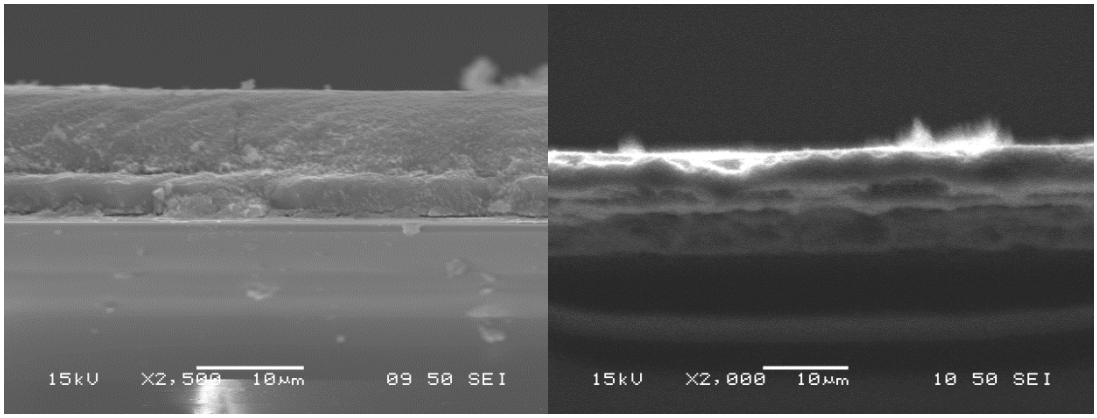


**Figure 4-14 SEM cross-sectional images of a bilayer photoelectrode prepared from a meso-0 film deposited on an initial layer of Ti-Nanoxide (left) and DSL 18NR-T (right).**

DSSC were made from the three types of photoelectrodes and their IV curves are shown in Figure 4-15. The aim of comparing the three types of cells was to find the optimized photoelectrode structure. It is obvious that the cell made from the Thick Ti-Nanoxide film has a higher short current, open circuit voltage, and efficiency, so this structure of phototelectrode was chosen for the later experiments in this chapter. The cell performances are also summarized in Table 4-2. The variation of efficiency was calculated according the results of several

cells produced in the same way as the ones described above. The differences between the three types of cells arise probably from the differences between the initial layers. From the manual descriptions of products, the particle size of film from Dyesol paste is around 20 nm, while that from Solaronix is around 15 nm. Also the thickness and the transparency of the initial layer is different between films, which may affect the passing of lights into the cell.[81]

**Table 4-2 Photoelectric properties of DSSC with bilayer photoelectrodes prepared from a meso-0 film deposited on an initial layer of titania.**

| *Sample* | *Thickness (μm)* | $V_{oc}$ *(mV)* | $J_{sc}$ *(mA/cm$^2$)* | *FF (%)* | *η (%)* |
|---|---|---|---|---|---|
| Thick Ti-Nanoxide | 4.9 + 4.6 | 748 | 9.84 | 56.4 | 4.12 ±0.5 |
| Ti-Nanoxide | 2.5 + 8.0 | 722 | 8.42 | 52.9 | 3.21 ±0.5 |
| DSL 18NR-T | 6.0 + 4.0 | 670 | 6.90 | 54.8 | 2.54 ±0.5 |

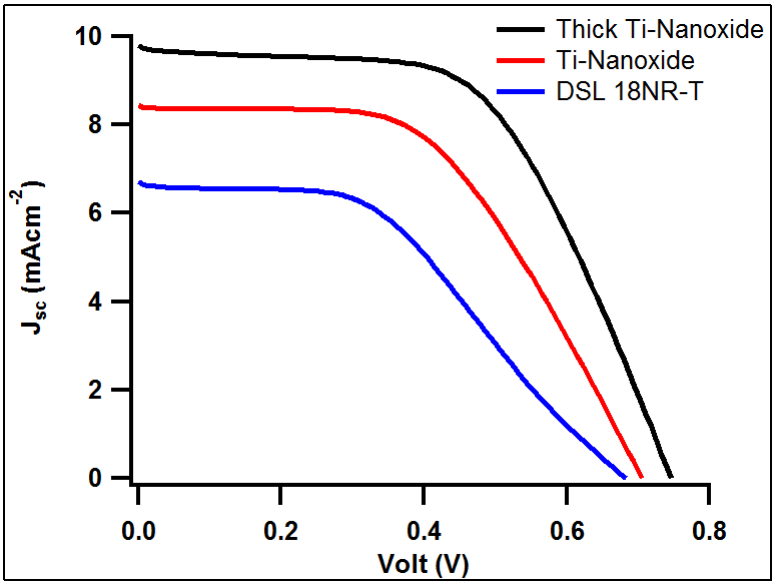


**Figure 4-15 IV curves of DSSC with bilayer photoelectroded prepared from a meso-0 film deposited on various initial layers.**

### 4.2.3.4 DSSC based on meso-$TiO_2$ and nanoparticle composite films

Figure 4-16 shows the IV curves for DSSC prepared with meso-X. Incorporation of the meso-$TiO_2$, increased the short current ($J_{sc}$) 10-15 %, while the fill factor (FF) was not appreciably changed. In contrast, the open circuit

voltage ($V_{oc}$) was decreased slightly by 10–20 mV, possibly because the higher surface area of the films provides more recombination sites. [273, 274] It is also possible that some of the dye adsorbed within the mesopores is not easily accessible to the electrolyte, increasing geminate recombination with the dye. [43] IPCE curves are shown in Fig 4-16. DSSC containing ≥ 25 % meso-$TiO_2$ showed a better photoelectrical response, with IPCEs that were higher than that found for the meso-0 cell over the entire wavelength range 400 – 800 nm. This is also in good agreement with the enhanced light scattering and dye adsorption as discussed above.

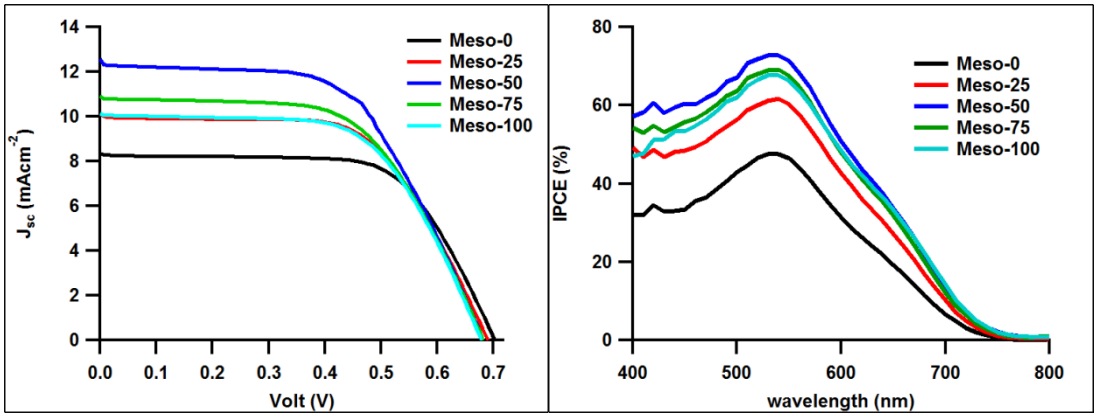


**Figure 4-16 IV curves (left) and IPCE (right) of meso-X solar cells.**

The details of the photoelectrical properties are displayed in Table 4-3. The measurements were repeated on five sets of meso-X cells prepared in the same way, and the other sets of meso-X solar cells shared the same trend, although the efficiency varies due to the manual effects in fabrication of the photoelectrodes and assembling of solar cells. One typical result is shown here. The efficiency found in these DSSC is around 4-5 %, which is not as high as that reported in literature,[98, 101, 258, 260, 261] when they applied meso-$TiO_2$ secondary particles into DSSC. However, the previous studies all used small area cells (0.16-0.36 cm$^2$) and most of them had some post-treatment such as $TiCl_4$ treatment which has been demonstrated to improve efficiency of DSSC. In this work, we focused on 1 cm$^2$ cells and did not use any post-treatment and were the first to apply meso-$TiO_2$ aggregates and P25 nanoparticle mixtures as the scattering layer. The influence of film structure, morphology, optical properties and cell performance were investigated. The total efficiency of the cells increased when meso-$TiO_2$ was added. This is likely to be due to the increased surface area and hence dye

loadings in the composite films as well as the increased light scattering. However, the meso-100 cell with the highest surface area and strongest scattering effects did not show the highest efficiency. This could be attributed to the fact that the meso-100 films had the highest dye loadings but a low porosity, suggesting that loses could be incurred due to poor infiltration of the electrolyte into large aggregates. [275] In addition the meso-100 aggregates may not provide efficient electron transfer pathways for electron extraction. It is reasonable that the meso-25 cell has the second lowest efficiency out of the five cells, which results from its lower surface area and the smaller quantity of big particulates which means less dye loading and weaker scattering effects. The highest efficiency obtained for meso-50 might be attributed to the following facts: firstly, meso-50 films have the highest pore volume, which allows the electrolyte to penetrate into macropores and directly contact dye molecules. Secondly, it shows high dye loadings and strong scattering. It is interesting that the meso-75 cells showed a lower efficiency than meso-50 cells. Meso-75 cells show similar dye loading and scattering effects, and only slightly reduced porosity when compared to meso-50 cell. The issue may be the increase in aggregates in the meso-75 films which do not provide good pathways for electron extraction.

**Table 4-3 Photoelectric properties of meso-X solar cells.**

| ***Sample*** | ***Meso-0*** | ***Meso-25*** | ***Meso-50*** | ***Meso-75*** | ***Meso-100*** |
|---|---|---|---|---|---|
| $J_{sc}$ (mA/cm$^2$) | 8.36 | 9.82 | 11.96 | 10.26 | 9.32 |
| $V_{oc}$ (mV) | 706 | 688 | 680 | 687 | 684 |
| FF (%) | 65 | 62 | 62 | 62 | 65 |
| η (%) | 3.85 ±0.26 | 4.26 ±0.29 | 4.93 ±0.32 | 4.38 ±0.36 | 4.21 ±0.38 |
| IPCE at 530nm (%) | 47.54 | 61.15 | 72.76 | 68.88 | 67.59 |
| Adsorbed Dye (nmol/cm$^2$) | 141 ±2 | 151 ±2 | 172 ±3 | 174 ±3 | 188 ±3 |

## 4.3 Conclusion

Highly ordered anatase 2D-hexagonal mesoporous titania powders with high surface area and large pores were synthesized. The introduction of meso-$TiO_2$ into Degussa P25 titania films, caused the films to become more porous, rougher and have higher surface area. Moreover, the large aggregates of meso-$TiO_2$ in the films benefit the light scattering. Most importantly the amount of dye that could

be adsorbed onto the photoanode increased with the fraction of meso-$TiO_2$. These contributed to an improvement of the photovoltaic performances when meso-$TiO_2$ was added to Degussa P25 nanoparticles in DSSC. Although the meso-100 cell has some superior properties such as high surface area and scattering effects, it did not show the best cell performance likely due to the poor connectivity of microsized meso-$TiO_2$ aggregations that increase the electron diffusion resistance. Considering the porosity, surface area, scattering effects and the degree of compactness of the film, the optimum cell was obtained by introducing 50 wt.% meso-$TiO_2$ , which shows an increase of short current from 8.36 to 11.96 mA/$cm^2$ and efficiency from 3.85 to 4.93 % compared to cell with the Degussa P25 film.

Although some promising results were obtained, there are still some points which could be improved. From section 4.2.3.2, the best morphology of photoelectrode was chosen to make DSSC for the later experiment, but no further research was done to study the reasons for this performance. In the process of titania paste preparation, annealing of the film is needed to remove the organic compounds, although the meso-$TiO_2$ was calcined at 450 °C already. This is not only a waste of energy, used to calcine the titania twice, but also makes the preparation more complicated. To simplify the process, using the as-prepared meso-$TiO_2$ directly in the paste after mixing with organics was attempted, but the film did not adhere to the substrate tightly. Also, some titania precursor solution was added into the paste, but no good film was obtained. This is probably due to the shrinkage of the mesostructure of meso-$TiO_2$ during calcination or the unsuitable composition of organics used to make paste compared to the normal templating solutions. To improve the efficiency of solar cells, several convenient and applicable strategies are possible. Firstly, some post treatment of the photoelectrode, such as exposure to $TiCl_4$ to create better bonding between particles could improve the efficiency. Secondly, the composition of ethyl cellulose, terpineol and titania powder in the pastes could be adjusted to optimise the components to obtain better titania film and improve the cell performance.

# Chapter 5 Ordered S-Doped Meso-$TiO_2$ Thin Film Prepared by Dip-coating for Photocatalyst

It is well known that titania is an efficient photocatalyst under UV light irradiation, however UV only accounts for 3 % of the solar spectrum.[132] So, titania doped by non-metal elements, as an effective way to extend the spectral response to visible light, is of considerable interest for many technological applications.[143] For S-doped titania, it is reported that the band gap can be greatly reduced and that it shows a satisfactory visible light-activated photocatalytic activity.[144, 276-281] S-doped titania nanoparticles have been fabricated using different sulphur sources and preparation methods, but reports regarding S-doped titania thin films have been rare. [144, 276, 282, 283]

Specifically films with a porous nanostructure are crucial for photocatalytic applications, and mesoporous titania can be an efficient photocatalyst due to its ultrahigh surface area and well organized pore structures.[284, 285] It is also expected that a cubic mesoporous film would offer higher photocatalytic efficiency than a hexagonal one since the mesopore channels of cubic mesostructures are open on the surface of the film regardless of the mesophase orientation, whereas those of hexagonal mesophases lie parallel to the substrate and are not open on the film surface.[286, 287]

In this chapter, first the synthesis by dip coating of S-doped titania films with a cubic mesostructure and ultrahigh surface area is discussed. S-doped mesoporous thin films were templated by Pluronic P123 using the EISA approach with sulphuric acid as the sulphur source in the initial sol. Compared to an equivalent undoped film, the S-doped titania film has many superior properties, such as a more ordered mesostructure, bigger pores, higher porosity, narrower band gap and better hydrophilicity, which contributed to a more efficient visible-light photocatalytic activity.

## 5.1 Experimental

1.0 g of Pluronic P123 was dissolved into 12.0 g absolute ethanol and a mixture of 2.86 g HCl (32%) and 0.2 ml $H_2SO_4$ (98%) was added. Then the solution was put into a beaker with a lid and stirred vigorously for 3 h at room

temperature. 5.36 g TIPR was added drop by drop under vigorous stirring. The precursor solution was stirred for another 30 min before it was used. To make a comparison, an equivalent precursor solution without the added $H_2SO_4$ was used to make an undoped titania film. There was essentially no difference in acidity between the two solutions as the overall acid concentration was greater than 10 M in both solutions.

Cleaned silicon wafers or microscope slides were used as the substrates, and a silicon wafer was normally used if not otherwise specified. At first, a series of withdrawal speeds were tested at a temperature and relative humidity of 25 °C and 20-30% respectively, but a slower speed was found to be better to obtain uniform films, so 60 mm/min was chosen for all the films if not otherwise specified. As soon as the withdrawal of the substrate from solution was complete, each sample was placed into a fridge maintained at a temperature of 7 °C and 22 % relative humidity for 24 h, then moved into an oven at 40 °C and 55 % relative humidity for 24 h and finally aged at 100 °C and 22 % relative humidity for 24 h. After that, films were heated at 350 °C for 2 h with a ramp speed of 1 °C/min to remove the template. The final calcination step was taken at 450 °C for 15 minutes with a ramp speed of 5 °C/min to crystallize the structure.

SAXS, GISAXS, TEM, FESEM, EDS, AFM, TGA, $N_2$ adsorption and desorption, ellipsometry instrument, UV-Vis spectrometer, water contact angle, and photocatalytic activity were used to characterize samples.

## 5.2 Results and Discussion

### *5.2.1 SAXS and GISAXS*

According to the report of Alberius et al., [19] a cubic mesostructure of $TiO_2$ films can be obtained when the template volume fraction [$\Phi_T = V_{template}/(V_{template} + V_{inorganic})$] is in the range of 29-36%. In our case, the template volume fraction is 31 %, thus a cubic structure is expected.

Figure 5-1 shows the SAXS patterns of the S-doped and undoped titania before and after calcination. Both of the as-prepared samples have a shoulder ~ 0.39 $nm^{-1}$. From the SAXS of calcined sample, it is obvious that S-$TiO_2$ has a much more ordered structure than $TiO_2$. The titania only has a shoulder peak at ~ 0.42 $nm^{-1}$ indicating a disordered structure, but the S-$TiO_2$ has two strong peaks

at 0.36 and 0.42 $nm^{-1}$ and one shoulder peak at ~0.7 $nm^{-1}$, suggesting a cubic structure (Pn3m symmetry) with a d-spacing of 16.5 nm. From the position of the peak or shoulder in undoped titania, a shift to a lower q from 0.39 to 0.42 $nm^{-1}$ is observed suggesting shrinkage of the titania network after the removal of template for. But little shift is observed for S-doped titania, as it has a shoulder around 0.39 $nm^{-1}$ before calcination and two strong peaks at 0.37 and 0.41 $nm^{-1}$ after calcination. For the as-prepared samples, in both cases only one broad shoulder is displayed. This is probably because the mesostructure of titania/template is not fully condensed prior to calcination and could be destroyed during the process of scratching the film away from the substrates.

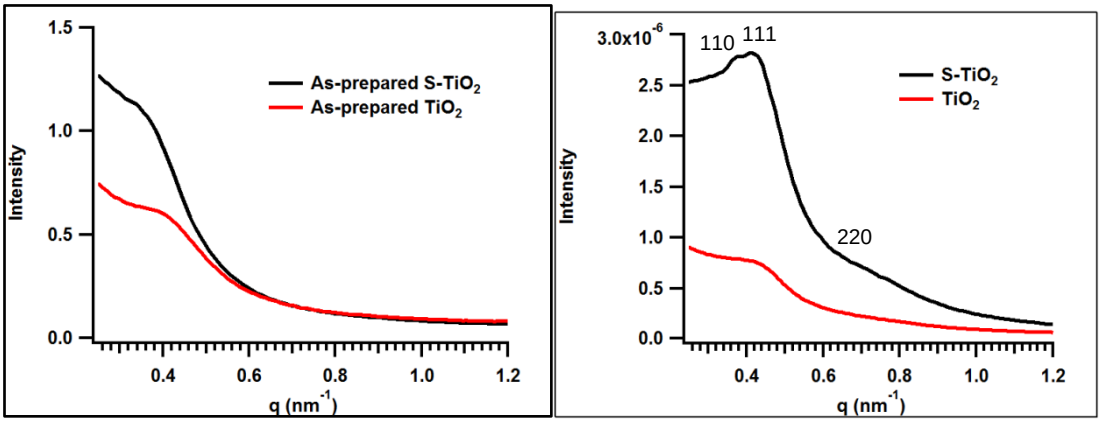


**Figure 5-1 SAXS curves of S-$TiO_2$ and $TiO_2$ before (left) and after calcination (right). The data after calcination has a low intensity due to the small amount of sample available and the difficulty of removing it from the substrate after calcination.**

Figure 5-2 shows the GISAXS and corresponding intensity profile in the $Q_z$ and $Q_{xy}$ directions of the pattern taken from the film before and after calcination. Before calcination (Figure 5-2 (top)), the pattern from the film shows two spots in the vertical direction and two arcs in the scattering. In the cut taken in the vertical direction, as well as peaks at 0.036 and 0.046 $Å^{-1}$, there is one more peak at ~0.067 $Å^{-1}$ and a shoulder at ~ 0.118 $Å^{-1}$, which is in accordance with the SAXS pattern of the film after calcination. These suggest that the film has a cubic mesostructure (Pn3m symmetry) and the peaks are indexed as the (110), (111) and (200) planes, according to the ratio of peak positions. The unit cell size remains almost the same before and after calcination. There is only one peak at 0.036 $Å^{-1}$ and a shoulder at ~ 0.070 $Å^{-1}$ visible in the in-plane direction cut, this is

because the in-plane cut was taken at $Q_z$=0.04 $Å^{-1}$ due to the position of beam-stop and normally more diffraction peaks are seen at the lower $Q_z$ values.

After calcination (Figure 5-2 (bottom)), the film still showed a well-defined structure. In the cut taken in the vertical direction, the degree of ordering become worse, as the clear ring that shows in the as-prepared sample become broadened and shifted to larger Q value ~ 0.088 $Å^{-1}$after calcination. The peak at 0.046 $Å^{-1}$ corresponds to the (111) plane, which is the same as in the as-prepared sample. In this symmetry here is also supposed to be another peak at 0.036 $Å^{-1}$, but it is blocked by the beam-stop. In the cut taken in the in-plane direction, there is one peak at 0.036 $Å^{-1}$ and a broad shoulder at ~0.062 $Å^{-1}$, which is quite similar to the as-prepared sample. The peaks appear stronger and more well-defined than in the as-prepared pattern due to the increased contrast between pore and wall domains after the removal of template. According to the ratio of d-spacings, the peak at ~0.062 $Å^{-1}$ is indexed as the (211) plane of the Pn3m phase. Noticeably, we do not observe any shrinkage of mesostructure after calcination for the S-doped titania film, because the doping of S helps the maintenance of mesostructure, despite it being very common for films to show a shrinkage in the vertical direction after calcination.[288] The GISAXS results for the calcined S-doped film are also in agreement with the SAXS results. The size of the unit cell for the as-prepared and calcined S-doped titania film is a=b=c=24.7 nm in both cases.

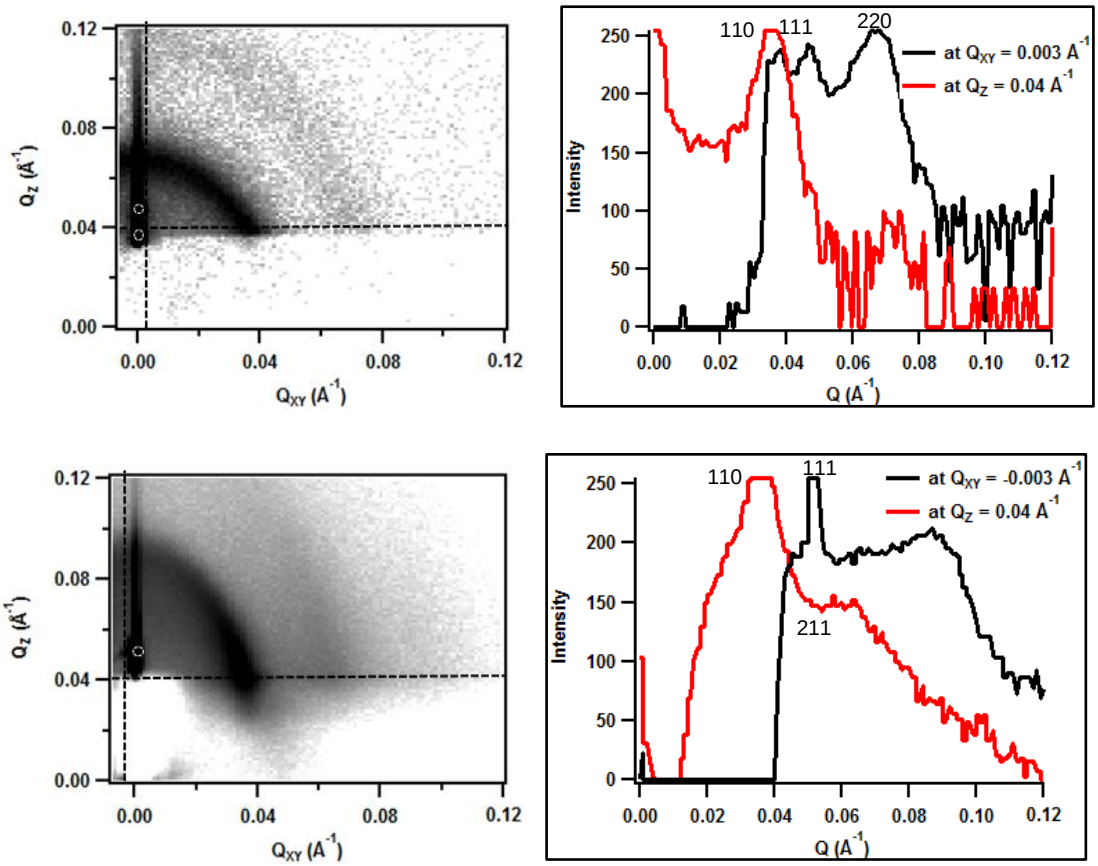


**Figure 5-2 GISAXS image (left) taken at 0.25° incident angle and corresponding intensity profile in the $Q_z$ and $Q_{xy}$ directions as indicated by the lines on the GISAXS patterns (right) of S-$TiO_2$ film before (top) and after calcination (bottom).**

### *5.2.2 XRD*

Figure 5-3 shows the XRD curves of S-$TiO_2$ and $TiO_2$ film powder. The primary peak of anatase phase at $2\theta$=25° is obviously found in both samples. The $TiO_2$ film is better crystallized than S-$TiO_2$, since only one obvious peak is clearly observed in S-$TiO_2$ with a relatively broad shape, indicating the mesostructured wall is composed of nanosized anatase nanocrystallites. Also no other peaks were observed, suggesting the sulfur was grafted into the lattice rather than interacting on the surface of titania. The crystal size, calculated according to the Scherrer equation,[226] are around 4.5 and 6.0 nm respectively.

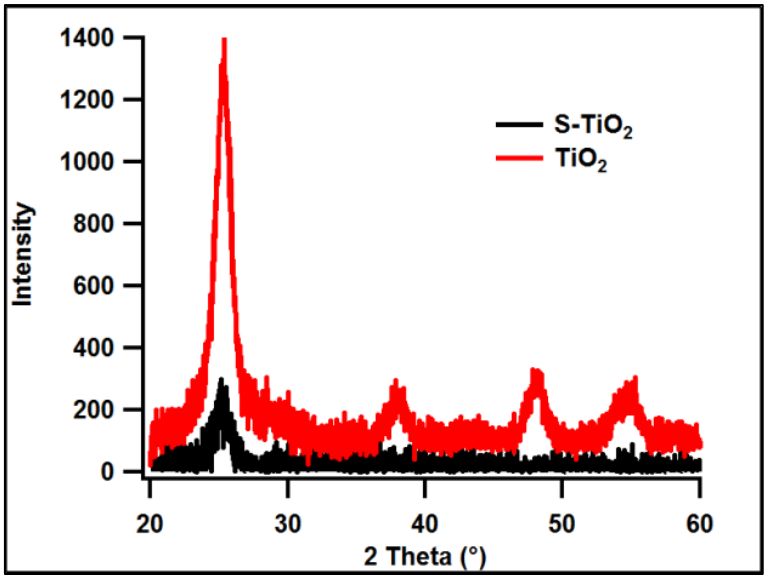


**Figure 5-3 XRD curves of S-doped and undoped titania.**

### *5.2.3 TEM*

The porous structure and the morphology of the materials were further studied by TEM in Figure 5-4. Figure 5-4.A and B show a well-ordered pore structure in the S-doped titania from the (111) and (110) orientation of the cubic phase (Pn3m symmetry) with a linear array of pores arranged at regular intervals. The orientation and pore entrance of the individual pores are clearly visible. The high level of ordering of the cubic Pn3m phase is also demonstrated by the well-defined Fourier Transfer images of the mesostructure of the film. The *d* spacing of the cubic mesostructured film was found to be ~16 nm, which is in accordance with GISAXS results. In Figure 5-4.C, the pores have a well-defined shape. The mesostructured film has 7-9 nm pores and 4-6 nm walls. Also, we do not observe unidirectional shrinkage of the cross-sectional pore structure, which helps retain the well-ordered structure even after calcination. From Figure 5-4.D, a typical pore and walls is displayed at high magnification. The pore has a very regular shape and composed of a 7.0 nm diameter void and 4.7 nm thick wall. It can be noticed that the wall areas are composed of highly-crystalline anatase nanoparticles. The titania lattice spacing of 0.35 nm corresponding to the (101) anatase crystal plane is also clearly seen in the nanoparticles, which is in good agreement with the XRD studies. The anatase nanoparticles are randomly embedded into the mesoporous walls of the thin films. In comparison, the pure titania material had a wormlike mesostructure from Figure 5-4.E. In Figure 5-4.F,

the pore unit cell does not have pores with well-defined shape and the pore size is smaller due to the larger crystallites in the mesoporous wall domains. Usually, the anisotropic crystallization and growth of crystalline particles are apt to produce particles which exceed the geometry of the inorganic framework and will lead to the obvious distortion or deterioration of the ordered mesopore structures.[289] In our case, the anatase crystals in S-doped titania film have a relatively smaller size than in the pure titania and so occupy the limited space within the channel walls, resulting in a crystallized well-ordered structure.

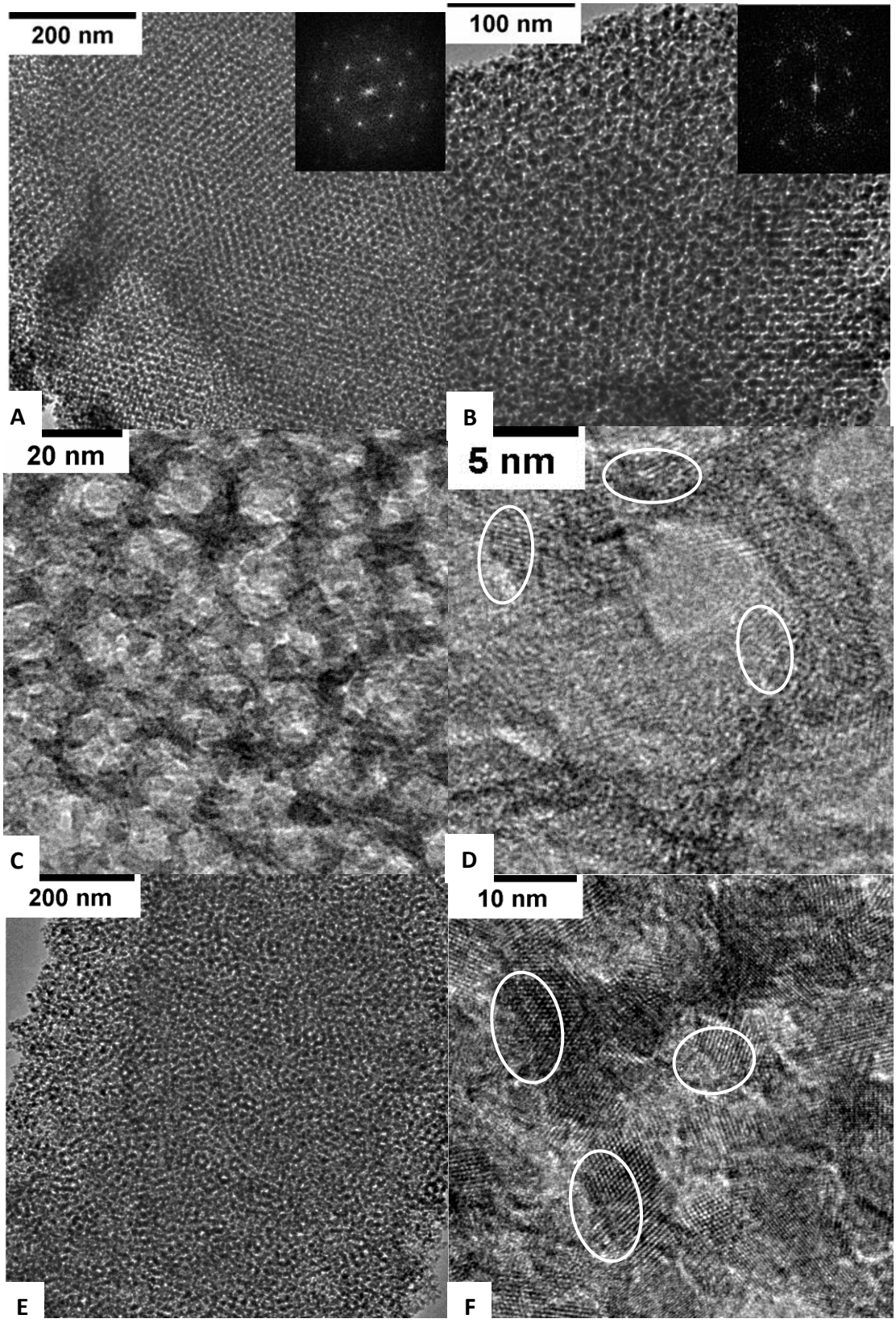


**Figure 5-4 TEM images of S doped (A, B, C, D) and undoped titania (E, F).**

### *5.2.4 FESEM & EDS*

Figure 5-5 shows the FESEM images of S-doped (left top) and undoped (right top) titania films. Both of them display a smooth surface and have a high porosity with the mesopores open to the film surface. Compared to the titania film, it is clearly seen that the S-$TiO_2$ film has an extremely flat surface and the mesopores are perpendicular to the surface plane, uniform in size and regularly distributed. From the magnified images, many pores in the pure titania film collapsed due to the crystallization of the pore walls during calcination.[264] Noticeably, the S-$TiO_2$ film retains a good pore structure with the pore diameter around 7.5-9.5 nm, wall thickness around 5.5-7.5 nm and the pore repeat spacing around 16-18 nm. These correspond with the SAXS, XRD and TEM results. EDS elemental analysis (Figure 5-5 (bottom)) identified the presence of sulphur in the doped titania film. The relative low signal intensity of O, Ti and S atoms is because the signal of Si substrate is too strong. The atomic ratio between Ti and S is 1:0.19, which is quite similar to the theoretical value calculated from the concentration of the reagents used in the synthesis. According to the reagent quantity, the atomic ratio between Ti and S should be 1:0.2. Elemental mappings of O, Ti and S show that these elements are uniformly distributed over the whole region, demonstrating the good dispersion of the sulphur in the titania film.

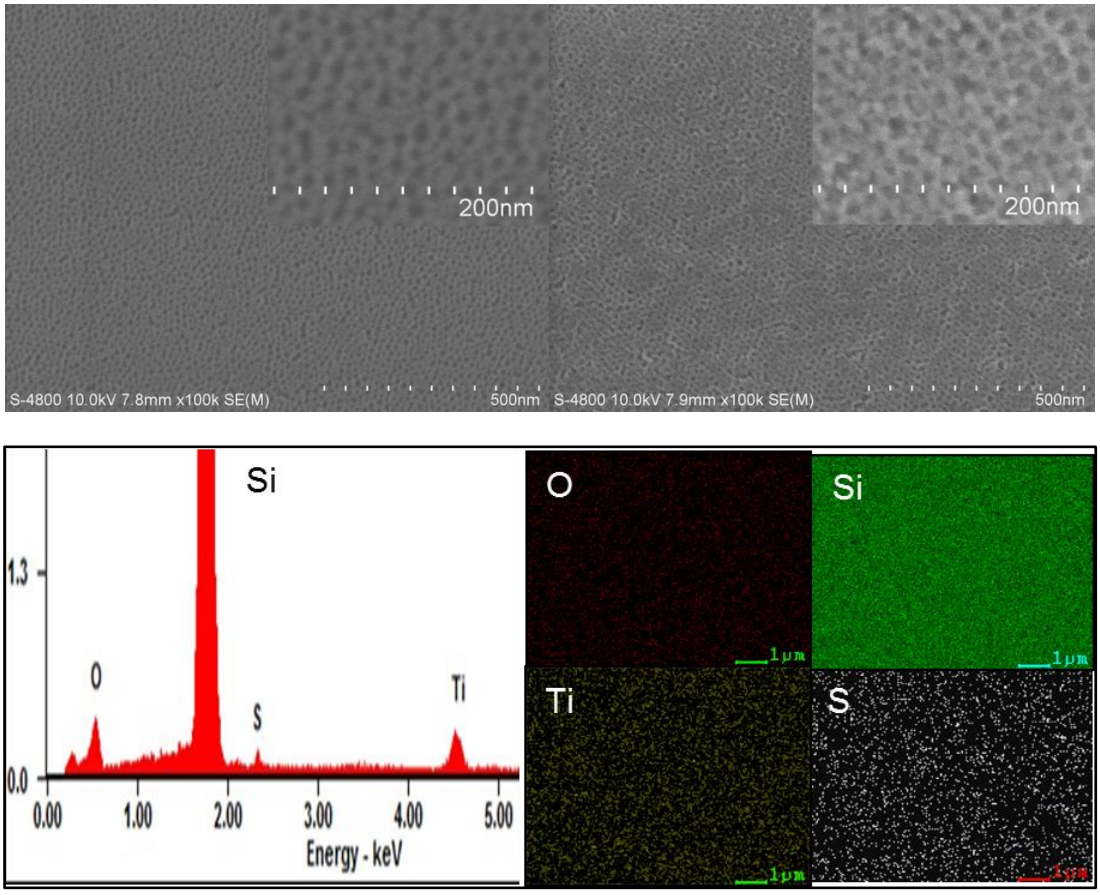


**Figure 5-5 FESEM images of S doped (left top) and undoped (right top) titania films; EDS and element mapping of S doped titania film (bottom).**

### *5.2.5 AFM*

The surface morphology of the S-doped and undoped films was also tested using AFM (Figure 5-6), which emphasizes both the extreme flatness of the top surface and the fact that the pores are open to the surface. The RMS roughness was calculated and both films had a RMS roughness less than 1nm. However, it is obvious that the undoped titania has a rougher surface than S-$TiO_2$, probably due to the pore collapse in the surface during calcination and crystallisation.

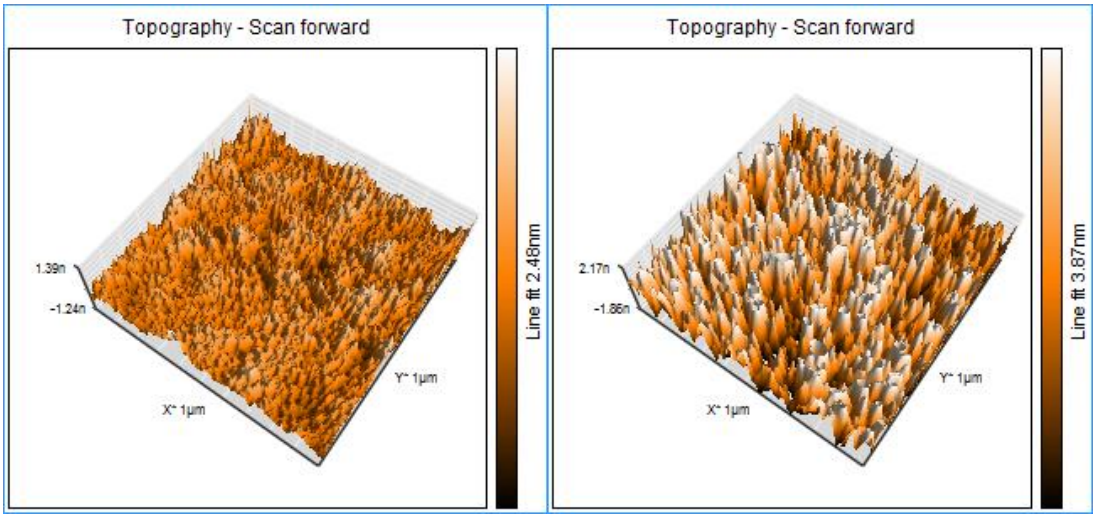


**Figure 5-6 AFM images of S doped (left) and undoped titania (right).**

### *5.2.6 TGA*

TGA curves of as-prepared and calcined doped and undoped titania are displayed in Figure 5-7. For the as-prepared samples, in the temperature range of 40-180 ºC, weight loss occurs due to the evaporation of solvent. The mass loss of S-doped titania (~13%) is higher than pure titania (~5%), because more water was left in the as-prepared sample. The sulphuric acid became concentrated during the evaporation steps and ageing process, and concentrated sulphuric acid is known to assist the maintenance of water in the film. Then, a sharp decrease occurs in the range of 180-300 ºC from the combustion of the template. After this, at higher temperatures, a small amount of weight loss happens due to the continuous removal of residual organic and sintering of titania particles.[225] It is clear that most of the organic template is removed from the films upon calcination at 300 °C, which is in good agreement with results reported in the literature.[264, 279] After calcination at 350 ºC, the remaining mass of the inorganic network for the S-doped titania film is 62 % and 68 % for $TiO_2$. Considering the weight differences of water found in the as-prepared samples the amount of inorganic species in the as-prepared films is similar. Calcined S-$TiO_2$ and $TiO_2$ were also tested to confirm the removal of organics. For both samples, they show similar curves. They have ~5% weight loss in the range of 40-180 ºC due to the evaporation of moisture that absorbed from the air during storing and ~ 5% weight loss at higher temperatures due to the removal of residual carbon.

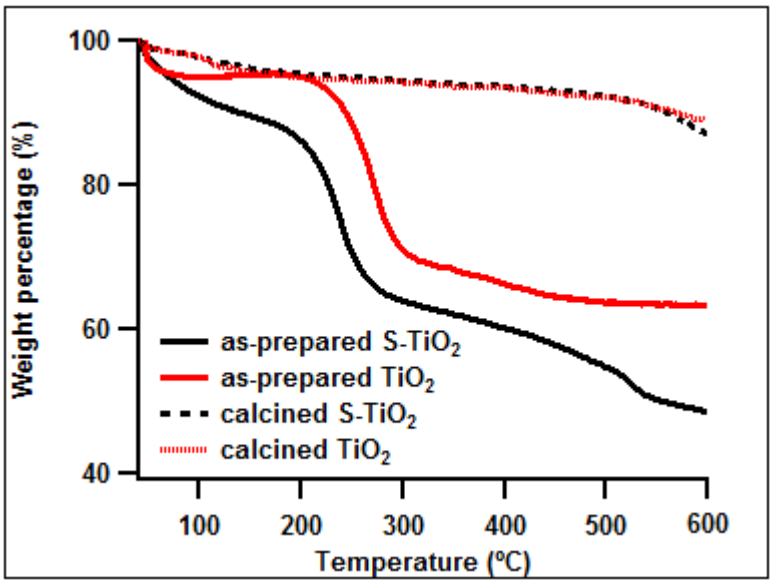


**Figure 5-7 TGA curves of as-prepared and calcined S doped and undoped titania.**

### *5.2.7 $N_2$ adsorption and desorption*

Figure 5-8 shows the nitrogen adsorption–desorption isotherms and pore size distribution of S-doped and undoped titania films. Their isotherms can be classified as type IV, which is the characteristic type for mesoporous materials. Also, it shows a sharp capillary condensation step at a relative pressure of 0.55-0.75, suggesting a narrow pore size distribution.[229] A pronounced H1 desorption hysteresis loop suggests the existence of large mesopores with open-ended ended cylindrical shapes in this sample.[230] The shape of the isotherms for both samples look similar, although the hysteresis loop is a little smaller and shifts to lower relative pressure for pure titania compared to S-doped sample, which suggests a smaller pore size and broader pore distribution. BJH pore-size analyses performed on the adsorption branch show that the S-doped and undoped titania exhibit a mean pore diameter of 7.0 and 6.2 nm, respectively. Excluding bigger pores, the pore size distribution of S-doped titania is more uniform and narrower than that of the undoped titania film. The titania films show a small amount of pores in the range of 20-70 nm probably from the fusing of small pores during the calcination,[290] or from gaps between crystallites. Although bigger pores always mean smaller surface area, they share similar BET surface areas, which is 190 $m^2/g$ for the S-$TiO_2$ and 187 $m^2/g$ for the undoped $TiO_2$ film. The pore volumes are 0.50 $cm^3/g$ for S-$TiO_2$ and 0.55 $cm^3/g$ for $TiO_2$ and the lower pore volume of S-$TiO_2$ is due to the lack of macropores. The results of

parameters calculated from the sorption isotherms are summarized in Table 5-1 below.

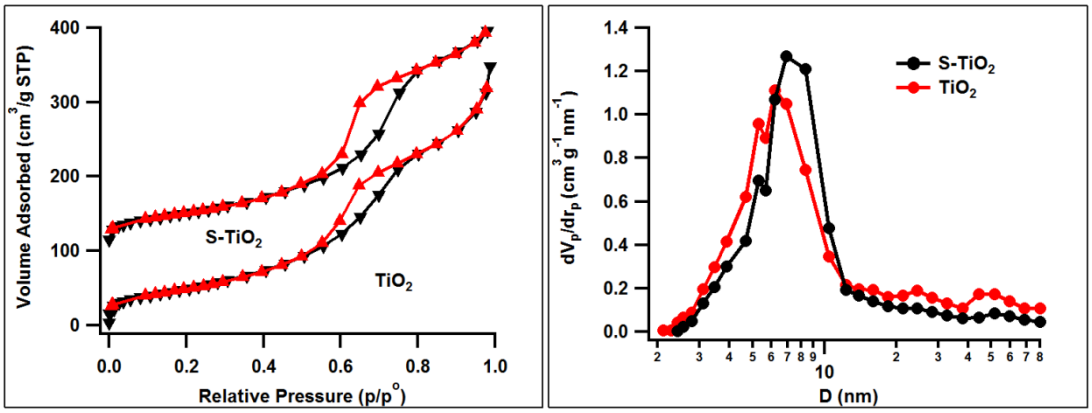


**Figure 5-8 $N_2$ adsorption–desorption isotherms (data offset for clarify) and pore size distribution of S-$TiO_2$ and $TiO_2$ after final calcination.**

### *5.2.8 Ellipsometry measurement*

Table 5-1 also lists the results from modelling of ellipsometry measurements. Both of the films before calcination show a similar thickness around 415 nm. After calcination, the thickness decrease due to the combustion of template and shrinkage of inorganic network. The titania film has a thickness of 215 nm, which corresponds reasonably well with work by others, as the films were aged under medium relative humidity during synthesis.[291] The S-doped film has a larger thickness of 317 nm, which is increased by almost 50 % compared to that of the undoped film. The shrinkage of the film was around 48 % for undoped and only 25 % for S-doped titania according to the film thickness, indicating the S-modification favours the maintenance of the mesoscopic structure of the films. The refractive index found from model fitting was used to calculate the porosity of the mesoporous $TiO_2$ thin films through equation 2.31. For S-doped titania film, the refractive index is 1.47 while that for the pure titania film is 1.55. The porosity for titania films is 74% and for S-doped one is as high as 78%. To the best of our knowledge, this is the largest porosity of mesoporous titania films reported.[106, 288, 292]

**Table 5-1 Textural properties of S doped and undoped titania films.**

| *Sample* | *Thickness before calcination (nm)* | *Thickness after calcination (nm)* | *Porosity (%)* | *Pore size (nm)* | *Surface area ($m^2/g$)* | *Pore volume ($cm^3/g$)* |
|---|---|---|---|---|---|---|
| S-$TiO_2$ | 418±2 | 317±1 | 78 | 7.0 | 189.51 | 0.50 |
| $TiO_2$ | 412±2 | 215±1 | 74 | 6.2 | 186.79 | 0.55 |

## *5.2.9 UV-Vis transmission and absorbance*

Figure 5-9 shows the absorbance and transmission of S-doped and pure titania films on glass slides. The S-modification improved the light absorbance over the whole spectral range. From the absorbance curves, a clear shift of the band onset in the direction of the visible region of the spectrum is observed for the S-doped samples, suggesting the dopant results in band-gap narrowing effects.[293, 294] The transmission also confirmed the red-shift of the absorbance of the film arising from the doping modification. S-$TiO_2$ has a higher absorbance and 10 % lower transmission compared to the undoped film over the whole visible region, probably due to the doping effects and around 47 % improvement of thickness indicated by the ellipsometry measurements above.

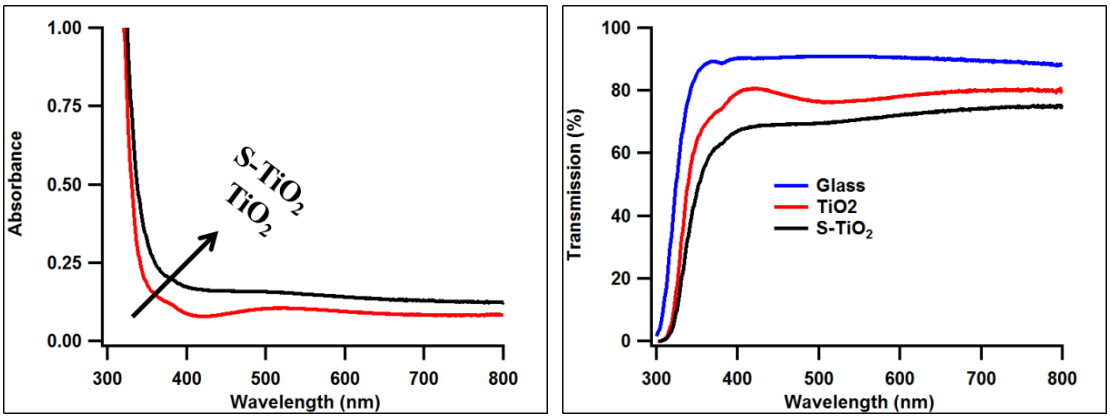


**Figure 5-9 Absorbance and transmission of S doped and undoped titania films on glass slide.**

## *5.2.10 Water contact angle*

The photocatalytic and hydrophilic properties of the $TiO_2$ materials are closely correlated and act in the same direction. Therefore, the surface wettability of S-doped and undoped films were tested by contact angle measurements. As shown in Figure 5-10, the contact angle of S doped and undoped films were 23 and 47 º respectively. The decrease of 24 º is a great improvement, as we did not do any further treatment to the film surface to achieve this hydrophilic surface.

Sakai et al. used anodic polarization to treat the surface of titania film and obtained a 7-15 º decrease of water contact angle.[295] Yu et al. used HCl solution to treat the surface of titania film and obtained ~7º decrease of water contact angle.[296] The more hydrophilic surface of the S-doped titania films will further affect the photocatalytic activity.[297]

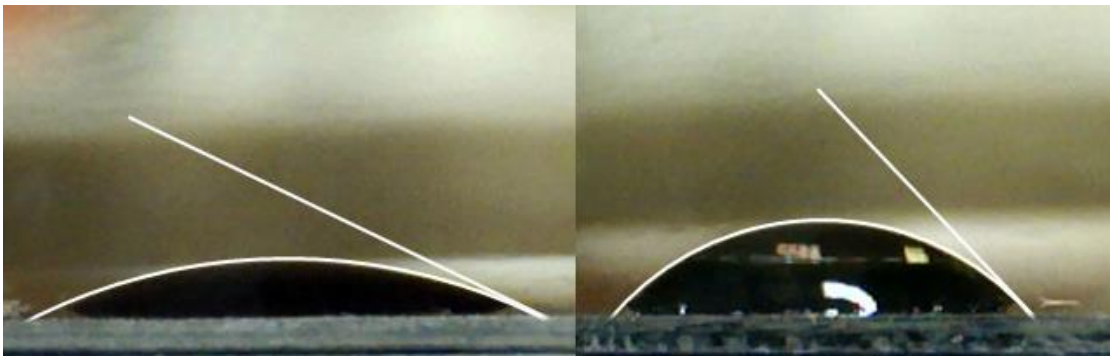

**Figure 5-10 Contact angle of water resting on S doped and undoped films.**

### *5.2.11 Photocatalytic activity*

The photocatalytic activity of these films under the irradiation of 1 sun intensity from a solar simulator was investigated. Methylene blue is a representative of a class of dyestuffs that are resistant to biodegradation. In Figure 5-11, the S-$TiO_2$ film exhibits higher activity in the degradation of methylene blue than the $TiO_2$, showing the promoting effect of the S-modification. Although the S-$TiO_2$ did not have an as well crystallized anatase structure as the undoped sample, which slows the transfer of photocharges from bulk to surface,[298] the improved the photocatalytic efficiency could be explained by the following reasons: Firstly, S-$TiO_2$ has a better defined mesoporous structure and the ordered mesopore channels facilitate fast intraparticle molecular transfer. Bian et al. fabricated Bi doped $TiO_2$ nanocrystallines with ordered mesoporous structure by EISA method for visible light photocatalyst. They think the ordered mesoporous channels also facilitated the diffusion of reactant molecules.[285] Secondly, the S-modification further increased the pore size and porosity and the large pore size will facilitate the access and diffusion of large organic molecules.[299, 300] Thirdly, the S-modification resulted in a slight red-shift of the band gap of the film and thus, the catalyst could be easily activated by visible lights and finally, the S-modification induced a more hydrophilic surface which allows aqueous solutions to wet the pore surfaces more efficiently and thus more

•OH groups can be generated so the hydrophilicity benefits the photocatalytic activity, even for degradation of hydrophobic molecules.[297]

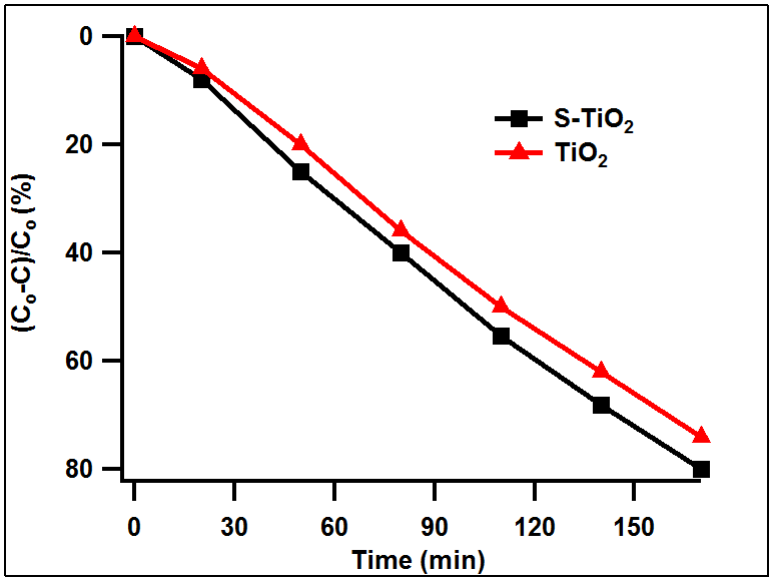


**Figure 5-11 Photocatalytic degradation of methylene blue aqueous solution on S doped and undoped films.**

The films were tested several times to determine the recyclability of the photocatalysts. The tests were run only for 150 minutes to obtain the performance comparison. As the concentration drops below 80% of the initial value the reaction will become diffusion limited and thus reaching 100% degradation would require considerably more time. Between each test, the films were briefly rinsed with water and dried. After use in three cycles for the photocatalytic degradation of methelene blue, the S-doped titania film did not show any significant loss of photocatalytic activity, as shown in Figure 5-12. This result is comparable with other's work. Han et al. prepared S-doped titania films templated by Tween 80 by dip-coating using sulphuric acid as the sulphur source.[301] The film is porous but not ordered. After three cycles, the S-doped titania film had around 5 % decrease of photocatalytic acitivity. Lee prepared S-doped 5-nm titania nanoparticle and shows 8% phtocatalytic activity loss after fifteen runs of the RB 5 degradation reaction.[302] The little loss of photocatalytic activity indicates mechanically stable and reusable under these experimental conditions, which is important to its practical environmental applications.

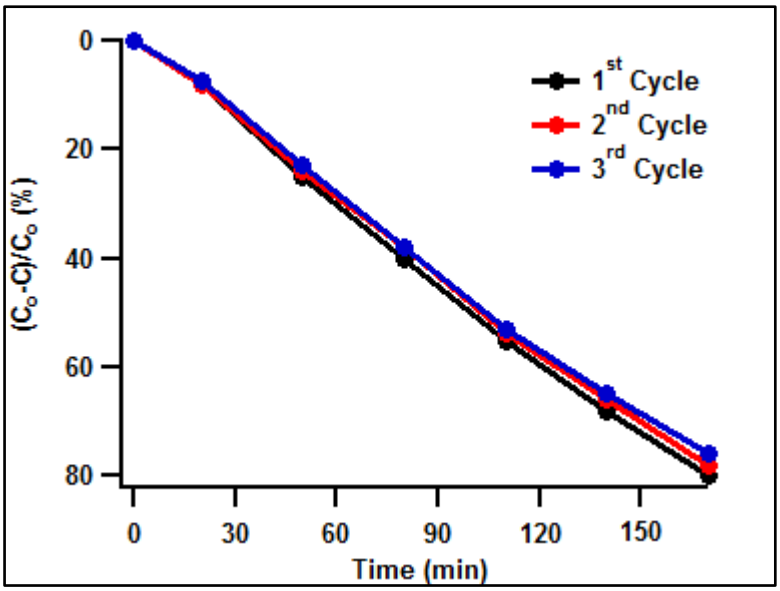


**Figure 5-12 Three cycles for the photocatalytic degradation of methylene blue using the same S-doped titania film.**

## 5.3 Conclusion

S-doped titania thin films with a cubic Pn3m phase mesostructure were prepared and applied in sun-light-driven photocatalysis. By using sulfuric acid as the S source, sulphur was successfully and uniformed doped into titania films at a level of S/Ti atomic ratio 0.19/1. Due to the modifying effects of sulphur doping, the S-$TiO_2$ film had a thickness of 317 nm and showed an anatase phase in the walls, extremely smooth surface (root mean square roughness <1nm), large, open pores (7.0 nm diameter), large surface area (190 $m^2$/g), ultrahigh porosity (78%) and relatively little thickness shrinkage after calcination (25%). However, the pure titania had a wormlike mesostructure and exhibited a large amount of pore collapse due to the growth of bigger crystallites in the wall domains compared to those in the S-doped film. It had a rougher surface, smaller pores and larger thickness shrinkage after calcination due to pore restructuring during calcination. The photocatalytic activity was measured by degrading methylene blue aqueous solution under a solar simulator and the S-doped titania film had an improved efficiency compared to that of the undoped film. This is because the S-modification favours formation of films with a better ordered mesostructure, bigger pore size, higher porosity, red-shift of band gap and more hydrophilic surface. However, the position/location of S in S-doped titania sample is uncertain. Some reports suggest that sulfur may exist in more than one oxidation state ($S^{2-}$,

$S^{4+}$ or $S^{6+}$) in $TiO_2$ depending on the synthetic conditions or the types of S precursor.[303] So, characterization such as XPS should be used to further confirm the the S oxidation state in titania.

To further improve the efficiency of photocatalysts, improvement of the degree of crystallization without loss of surface area is needed, as the formation of anatase and the improvement of crystallization of anatase in the films can increase the photocatalytic activity.[304, 305] However, the increase of crystallite size is invariably accompanied with the reduction of the surface area and detrimentally affects the ordering of the mesostructure, which will decrease the photoreactivity. So, balancing the two factors should be considered to find optimized parameters. Moreover, the variation of the amount of S-doping to find an optimum amount is important since the amount of S-doping is one of the most important parameters for doped titania, as it affects the optical properties for doped materials.[276, 281] As well as pollutant degradation, the S-doped photocatalyst could also be trialled for water-splitting, anti-bacterial surfaces, self-cleaning, and anti-fogging surfaces.[133]

Except for using S-doped film as a photocatalyst, the application of S-doped film as the blocking or buffer layer to increase DSSC efficiency has also been suggested,[306, 307] considering the cubic mesostructure and low thickness. Kim et al. used cubic mesostructured titania film with a thickness 300 nm as the blocking layer for DSSC.[307] They found the use of meso-$TiO_2$ allowed more light to be transmitted through the FTO glass and decreased the roughness of FTO glass to improve the adhesion between the FTO layer and nanocrystalline titania layer. Ahn et al. prepared a randomly structured mesoporous titania film with a thickness of 550 nm for use as an interfacial layer between the FTO and the nanocrystalline $TiO_2$ layer.[306] The roughness of the FTO glass was significantly reduced, which improved the interfacial adhesion between the titania nanocrystallite layer and the FTO, leading to a decreased interfacial resistance. In our case, using the mesostructured S-doped film as the interfacial layer is a possible way to optimize the solar cells that are prepared in chapter 4.

# Chapter 6 S-Doped Mesoporous $TiO_2$ Films Prepared by Dip-coating for DSSC

Mesostructured titania films can be easily prepared by dip or spin coating. By repeating coating processes, organized mesoporous titania thin films with a thickness of 1 - 5 μm can be obtained.[106] For titania films , with only 1 μm thickness, application in a DSSC shows a highest efficiency of 4.04 % by Zukalová et al, which is about a 50 % increase compared to that of traditional films of the same thickness made from randomly oriented anatase nanocrystals.[108] However, not all ordered mesoporous films published have such a high efficiency. Most of them have efficiency in the range of 1-3% for 1 μm-thick films.[105, 106] For thinner films (< 1 μm), such as films with 500 nm-thickness, they were mainly applied into all (or quasi)-solid-state DSSC and show an efficiency less than 1%.[308, 309] Because the diffusion length of excitons in a semiconducting polymer electrolyte is usually at a nanometre length scale, the electron acceptor must be in contact with polymer at a nanometre length scale to achieve efficient charge separation.[310]

Doping of titania has be an shown to been effective way to extend the spectral response of titania to visible light.[143] A number of metal or non-metal dopants were previously studied and showed an improved photocatalytic activity under visible light.[145, 311-315] Some of the doped titanias were also applied into DSSC and showed a promising increase in efficiency, such as N, C, Zn, Al, Nb etc.[94, 316, 317] Among all the doping elements for DSSC, N is still under special attention, because doping N into the $TiO_2$ crystal structure can perfect the oxygen deficiency and decrease the back reaction.[152] Sulfur shares a similar doping effect as N in photocatalysts,[143] but no S doped titania thin films applied in DSSC have been reported so far. From Chapter 5, ordered mesoporous S-doped titania films were successfully made and they show an improved photocatalytic activity as sun-light-driven photocatalysts, so these films were also applied in DSSC in the hope of improving the efficiency of the DSSC.

## 6.1 Experimental

The S-doped titania films were prepared by dip coating according to the method described in section 5.2 of Chapter 5. However for application in DSSC, thicker films were needed, so repeated coating steps were carried before the final calcination at 450°C. Final calcination was only done after reached the number of layers. GISAXS, ellipsometry, AFM, UV/Vis spectrometry, and $N_2$ adsorption and desorption were used to characterize the samples.

According to the report by Krins et al,[232] thermal treatment after each coating can partly open the pore, which allows the inorganic precursor to fill in the pore in the next coating step. They suggested refilling the pores with Pluronic P123 solution between depositions of two layers may hinder the pore blocking which occurs during the second coating. So, the "filling pore" process was attempted to obtain a better ordered mesostructure in the multi-layered films. Pluronic P123 was dissolved into ethanol at a concentration of 2 mM. Then, 1-layer films after an initial thermal treatment but prior to final calcination were dipped into the Pluronic P123 solution at a speed of 60mm/min and dried at room temperature for half an hour before the second titania coating. No final calcination was taken for the films prepared with the filling-pore process. GISAXS, ellipsometry measurement, AFM, TEM were used to study the influence of the "filling pore" process on the morphology and structure of films.

After final calcination, the mesoporous films with different numbers of layers were applied in DSSCs and characterized by IV curves and IPCE. The absorbed dye quantity was also tested by UV/Vis spectrometry.

## 6.2 Results and Discussion

### *6.2.1 The effects of "filling pore" process*

#### 6.2.1.1 GISAXS

Figure 6-1 shows GISAXS image of a 2-layer S-$TiO_2$ films on a silicon wafer substrate prepared with the "filling pore" process, and corresponding intensity profile in the $Q_z$ and $Q_{xy}$ directions. The GISAXS and corresponding intensity

profile of 2-layer S-$TiO_2$ films prepared without the “filling pore” process was shown in Figure 2-7.

From the two figures below the anisotropy in the scattering suggests that the film is compressed in the vertical direction as the scattering peaks at 0.09 $Å^{-1}$ with a d-spacing of 7 nm in this direction, while a sharper diffraction ring is seen at 0.03 $Å^{-1}$ with a d-spacing of 21 nm in the in-plane cut. Both the film in Figure 2-7 and Figure 6-1 are better ordered in-plane, as peaks at ~0.03 $Å^{-1}$ is much sharper than peak at 0.09 $Å^{-1}$ in the in-plane cut direction can be observed. For film synthesised without using the “filling pore” process, there is one more shoulder at around 0.06 $Å^{-1}$ in the in-plane cut direction, suggesting a better ordering in the mesostructure in this film than in the film prepared without using the “filling pore” process. However in neither case do the films have extensive long range mesostructural ordering.

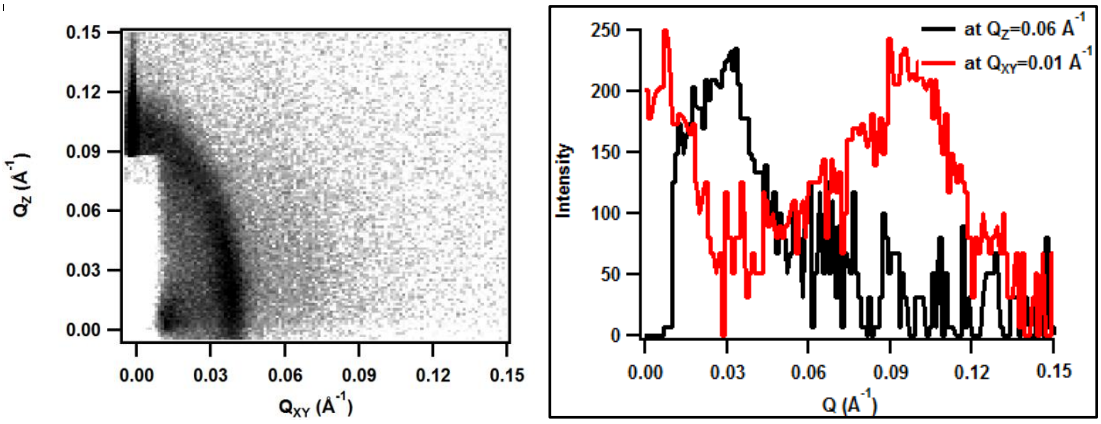


**Figure 6-1 GISAXS image (left) and corresponding intensity profile in the $Q_z$ and $Q_{xy}$ directions (right) of a 2-layer S-$TiO_2$ film prepared usingthe “filling pore” process on a silicon wafer substrate.**

### 6.2.1.2 TEM

Figure 6-2 shows TEM images of the 2-layer S-$TiO_2$ film prepared with and without the filling pore process. These are typical images of the two samples, the other parts of these sample show the same results. From the images, it can be seen that both of the films have a high porosity, the pore size is around 5 - 8 nm and uniformly distributed, which is in accordance with the results of pore size distribution of 1-layer film in chapter 5. The 1-layer film has a mean pore diameter ~7.0 nm. Both of them display a wormlike pore structure and no ordered

mesostructures were observed. This is in agreement with the GISAXS results. However, no big differences can be noticed between the two samples.

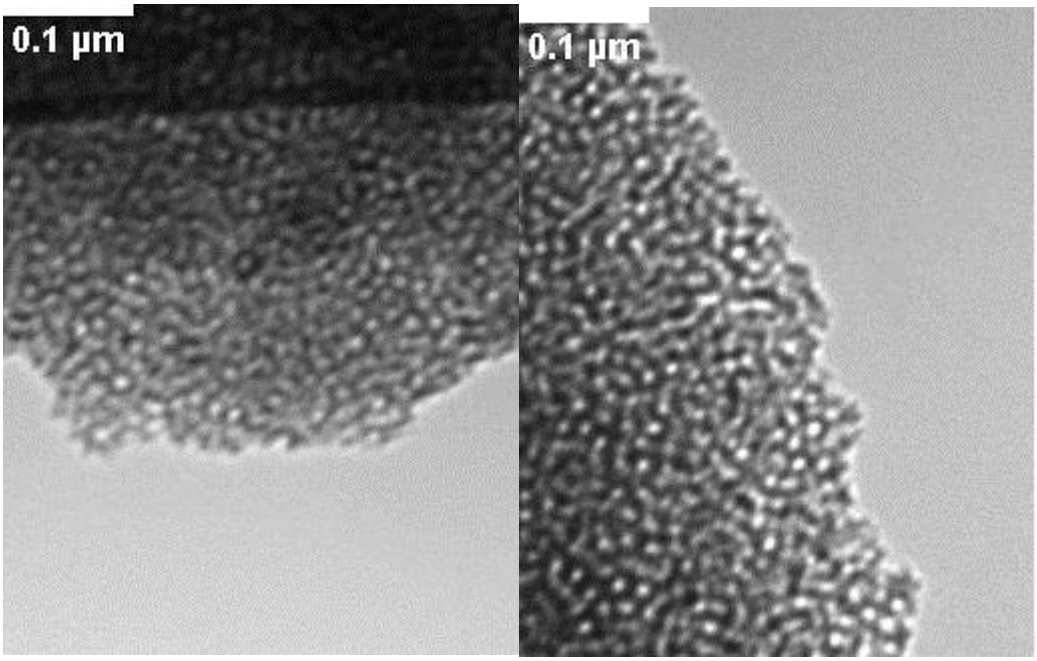


**Figure 6-2 TEM images of 2-layer S-$TiO_2$ films prepared with (left) and without (right) the "filling pore" process.**

### 6.2.1.3 AFM

Figure 6-3 compares the AFM images of 2-layer S-$TiO_2$ films prepared with and without the "filling pore" process. Both of them display a smooth surface and are highly porous with pores open to surface. The RMS roughness for films prepared with or without "filling pore" process are around 1 and 8 nm respectively, indicating the film prepared using the "filling pore" process had a rougher surface.

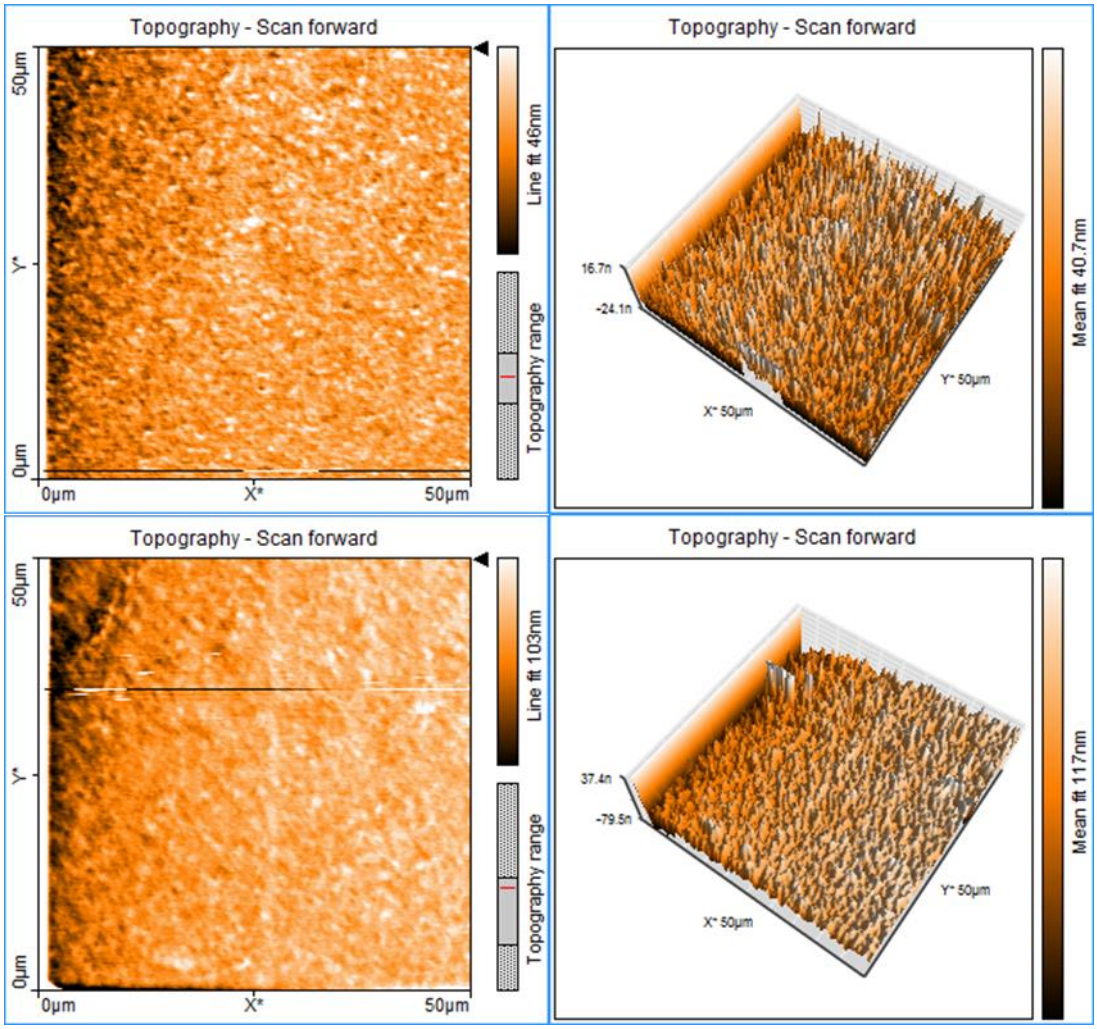


**Figure 6-3 AFM images of 2-layer S-$TiO_2$ films prepared with (top) and without (bottom) the "filling pore" process on silicon wafer substrate.**

### 6.2.1.4 Ellipsometry measurement

The film thickness was estimated by an ellipsometry measurement. The film made without using the filling pore process has a thickness of 477±3 nm, and the thickness of film prepared with the filling process is similar at 482±5 nm. Both of them have a refractive index around 1.6. The porosity was calculated according to equation 2.31 in Chapter 2, which is around 71%. Compared to the porosity of a 1-layer film, the porosity decreased a little, due to the pore filling during the repeated coating procedure.[2]

All the above results confirmed that the processes of filling the pore with surfactant solution did not have a large influence on the film mesostructure, thickness and optical properties, although it did increase the surface roughness. The aim of the "filling pore" process in this experiment was to prepare a

mesoporous film with better ordering, according to the report in the paper by Krins et al. However, no evidence was found to support this theory in our case and it adds to the complications of the film preparation, so this process was not adopted in the later experiments.

## *6.2.2 S-Doped Meso-$TiO_2$ Multilayer Films for DSSC*

### 6.2.2.1 GISAXS

Figure 6-4 shows GISAXS images of 3-layer and 4-layer S-$TiO_2$ films on a silicon wafer substrate and the corresponding intensity profile in the $Q_z$ and $Q_{xy}$ directions. From the two figures below, the anisotropy in the scattering suggests that the mesostructure in the film is compressed in the vertical direction as the scattering peaks at 0.09 $Å^{-1}$ in this direction, while a sharper diffraction ring is seen at 0.03 $Å^{-1}$ in the in-plane cut. Both of the films are better ordered in-plane, as the peak at ~0.03 $Å^{-1}$ is much sharper than the peak at 0.09 $Å^{-1}$ in the in-plane cut direction, suggesting larger domain sizes in the horizontal direction. For 3-layer film, there is one more shoulder visible at around 0.06 $Å^{-1}$ in the scattering in the in-plane cut direction, suggesting better ordering in this mesostructure than in the 4-layer film.

However, for 5-, 6- and 7-layer film (Figure 6-5), the order of mesostructure lost due to the multiple coating and calcination steps. In combination with the GISAXS pattern for a 1-layer film in Figure 5-2 and 2-layer film in Figure 2-7, all the films (less than 5 layers) are compressed in the vertical direction and have a peak at 0.09 $Å^{-1}$ with a d-spacing of 7 nm in this direction and a peak at 0.03 $Å^{-1}$ with a d-spacing of 21 nm in direction of in-plane cut. The typical unidirectional mesostructure shrinkage in the vertical direction, commonly observed during drying/calcinations of thin films.[288, 318, 319] The degree of ordering decreased with the increase of layers and was completely lost after 5 layers. This is a normal phenomenon for multilayer deposition of surfactant templated films by dip or spin coating,[109, 110] as the formation of crystallites that exceed the size of the inorganic framework domains during multiple calcination process, which induced the mesostructural degradation.

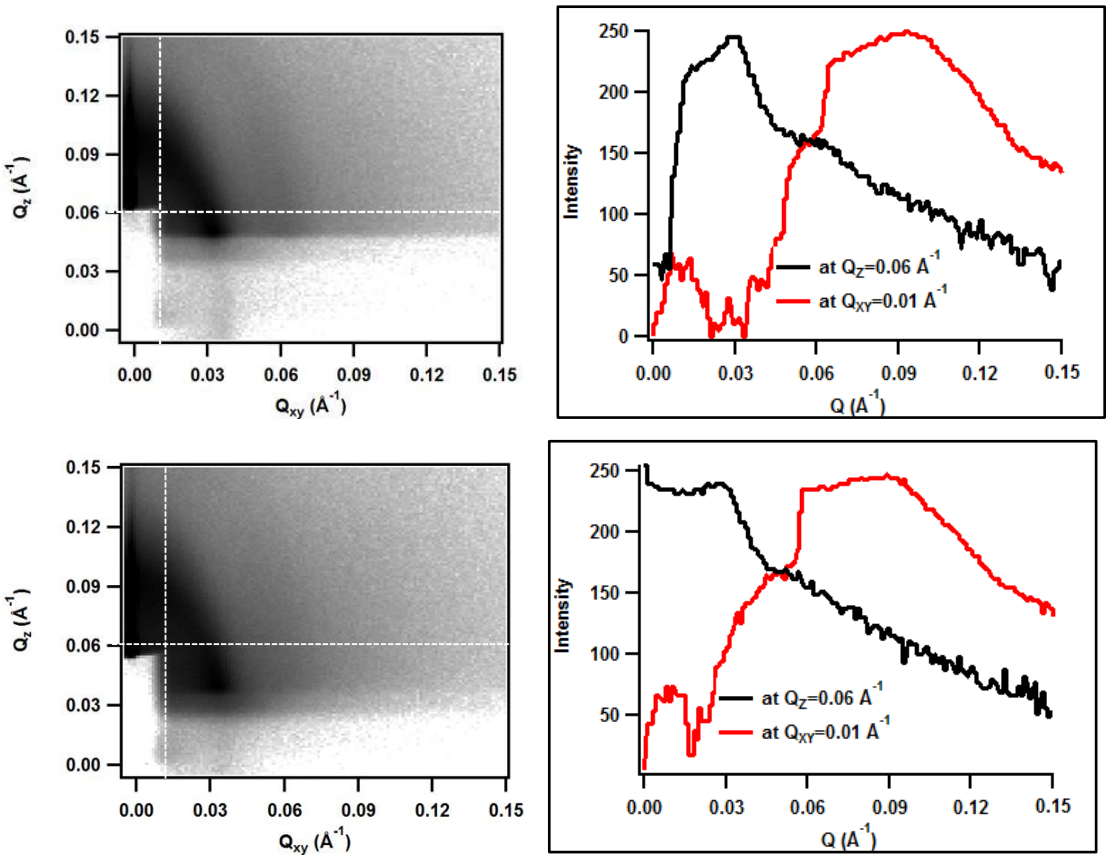


**Figure 6-4 GISAXS images (left) and corresponding intensity profiles in the $Q_z$ and $Q_{xy}$ directions (right) for 3-layer (top) and 4-layer (bottom) S-$TiO_2$ films on a silicon wafer substrate.**

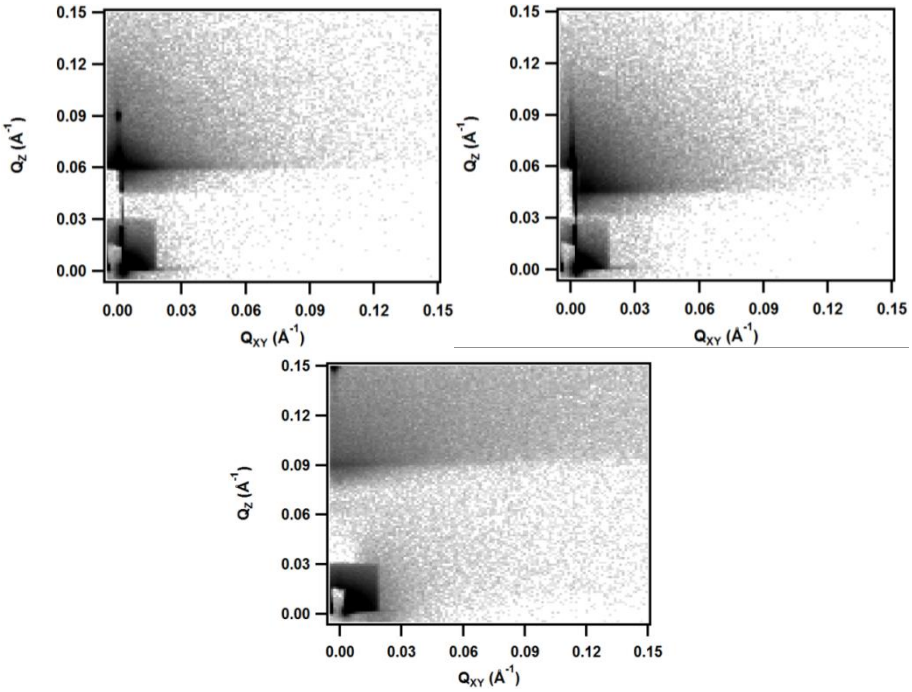


**Figure 6-5 GISAXS images (left) from 5-layer, 6-layer (right) and 7-layer (bottom) S-$TiO_2$ films on a silicon wafer substrate.**

### 6.2.2.2 Film thickness

The values of film thickness were obtained from the ellipsometry result. Figure 6-6 shows the relationships between dip coating cycles and the thickness of S-doped titania films on silicon wafer substrates after the final calcination step. As can be seen, the thickness of the film increases linearly with an increase in coating cycle from 317 nm for one cycle up to 1.5 µm for seven cycles. The gradient is around 165 nm per coating, which is relatively low compared to work by others.[106] Dewalque et al. found an increase of around 234 nm per layer for a mesoporous titania film templated by Pluronic P123. But, the thickness of the first layer has a relatively high value due to the effects of improved mesostructure maintenance resulting from S doping as seen previously in chapter 5. The total thickness of multilayer films is lower than the thickness reported for mesoporous titania films templated using Pluronic P123 as the template,[108, 292, 320] due to the lower gradient.

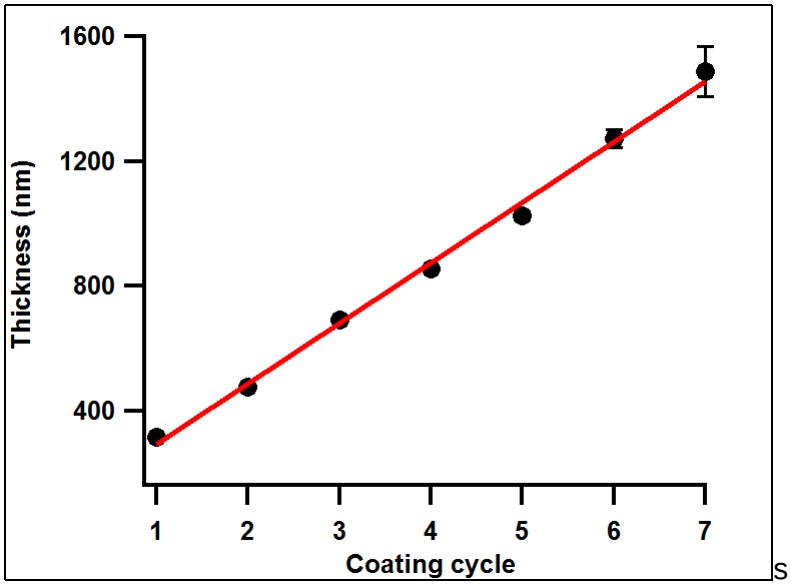


**Figure 6-6 Relationship between dip coating cycles and thickness of the S-$TiO_2$ films on a silicon wafer after the final calcination step.**

### 6.2.2.3 AFM

When S-$TiO_2$ films are used in DSSC, FTO glass with blocking layer was normally used as the substrate rather than Si wafers. Figure 6-7 shows AFM images of films with different layers deposited on FTO glass with blocking layer. All of them show a uniform surface. The roughness increases with the increase in

number of layers due to the collapse and re-structuring of pores during repeated calcination. The RMS roughness of 2-layer film is 3.48 nm and increases to 13.67 nm for an 8-layer film. For 2-layer film, the surface is very smooth and many uniformly distributed pores can be seen, but the phenomenon of pore collapse is very obvious for a 7-layer film. It is interesting that the 7-layer film seems to have a meso/macropores hierarchical structure, due to the collapse of mesopores and some macropoeres occursed. Moreover, there are many small cracks in the surface of the 8-layer film, which is normal for thicker films obtained by repeated coating and calcination methods. Zhang et al. prepared mesoporous titania film by spin coating and observed large cracks for thicker film due to the repeated coating.[110]

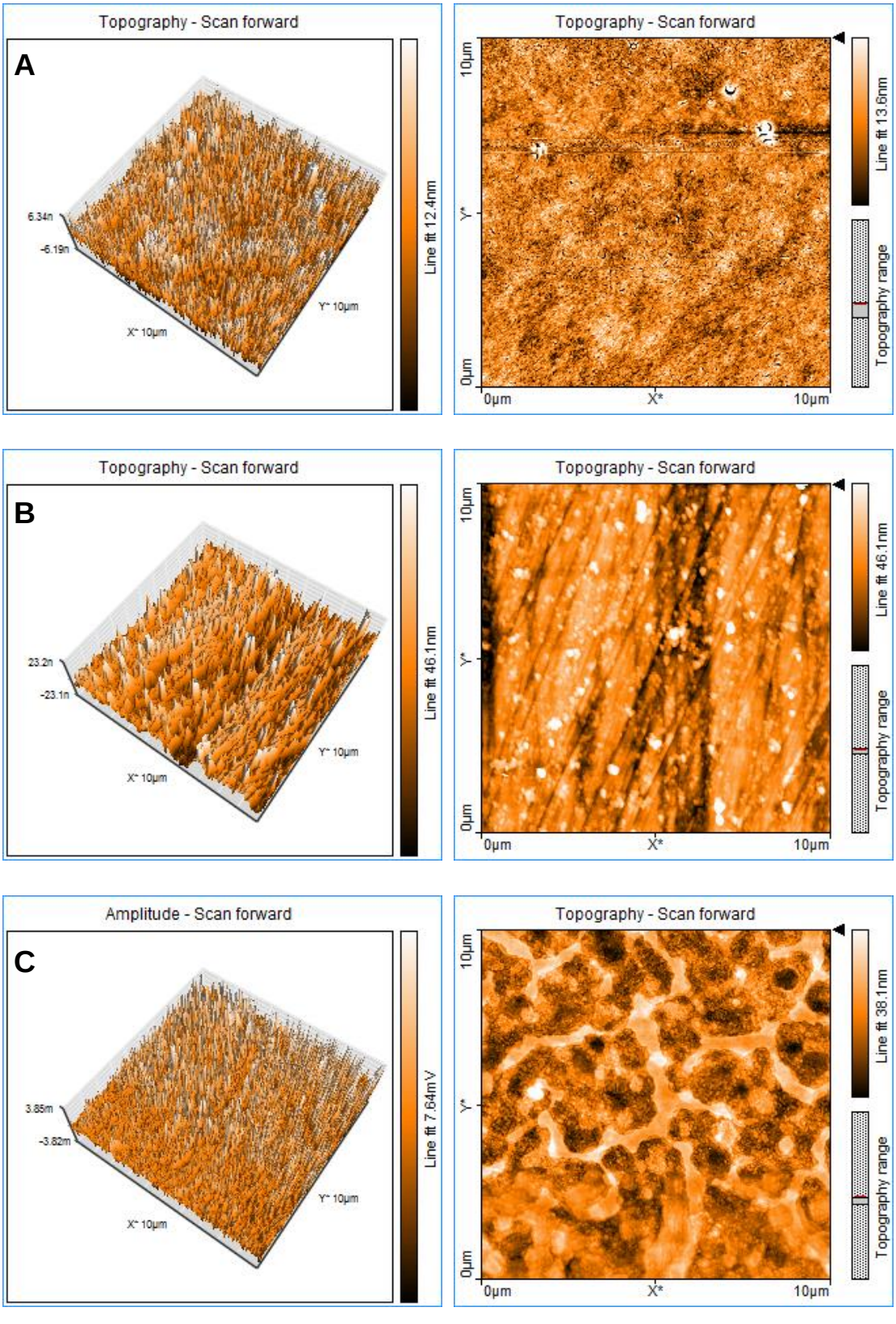
Topography - Scan forward
A
6.34n
-6.19n
X* 10µm
Y* 10µm
Line fit 12.4nm
Topography - Scan forward
10µm
Y*
0µm
0µm
X*
10µm
Line fit 13.6nm
Topography range
Topography - Scan forward
B
23.2n
-23.1n
X* 10µm
Y* 10µm
Line fit 46.1nm
Topography - Scan forward
10µm
Y*
0µm
0µm
X*
10µm
Line fit 46.1nm
Topography range
Amplitude - Scan forward
C
3.85m
-3.82m
X* 10µm
Y* 10µm
Line fit 7.64mV
Topography - Scan forward
10µm
Y*
0µm
0µm
X*
10µm
Line fit 38.1nm
Topography range

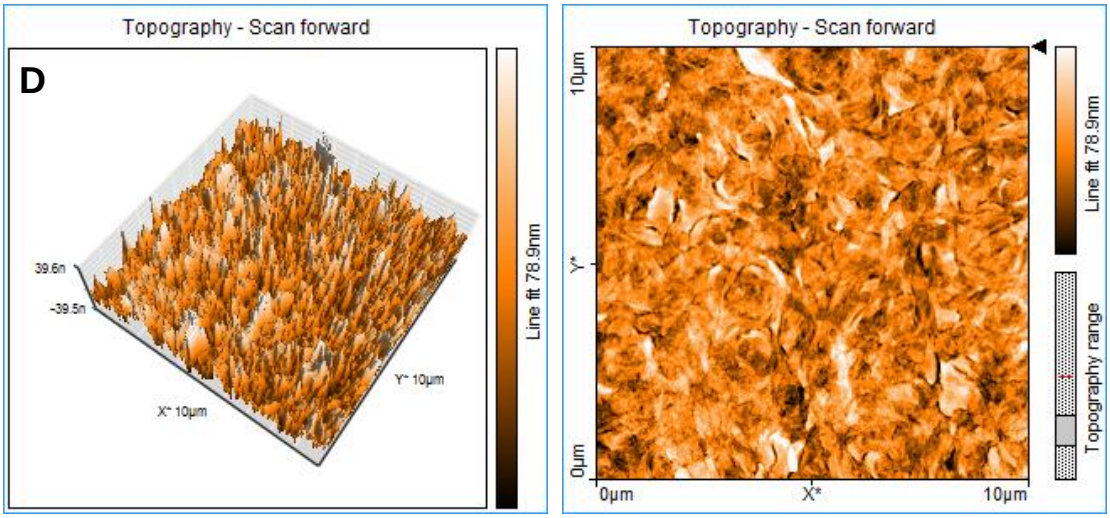


**Figure 6-7 AFM images of different films on FTO glass with blocking layer. (A) 2-layer, (B) 4-layer, (C) 7-layer and (D) 8-layer S-$TiO_2$ films without final calcination.**

### 6.2.2.4 UV-Vis absorbance

The absorbance of S-$TiO_2$ films with different numbers of layers on glass slides before the final calcination step is shown in Figure 6-8 (left). With an increase in number of layers, the absorbance increases mainly due to the higher thickness. However, the absorbance of these films is not high compared to film with a thickness at the micrometre level, so most of the light will pass through the cell rather than being harvested by the dyes to generate electrons when applied these films into DSSC. For a 2-layer film deposited on FTO glass with a blocking layer after the final calcination step, the absorbance before and after dye uptake is shown in Figure 6-8 (right). The improved absorbance after dye uptake is obvious and is observed due to the light harvesting ability of the dye, but the improvements was not very large, as the film is thin (less than 500 nm) and only limited amounts of dye molecules can be absorbed.

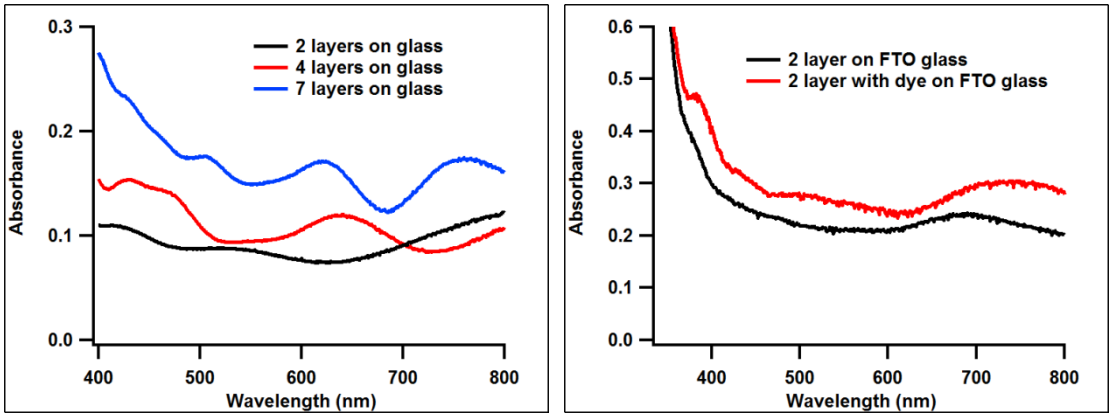


**Figure 6-8 UV-Vis absorbance of S-$TiO_2$ films with different numbers of layers on glass before the final calcination step (left); absorbance of 2 layer films after final calcination before and after dye uptake (right).**

### 6.2.2.5 $N_2$ adsorption and desorption

Figure 6-9 shows the $N_2$ adsorption and desorption isotherms and BJH pore size distribution of a powder generated by scratching several 7-layer films off the substrate after the final calcination. The BET surface area is only 73 $m^2/g$ and total pore volume is 0.16 $cm^3/g$, which are much lower than that found for a 1-layer film in Table 5-1. This is probably due to the collapse of the pores during the repeated calcination and infilling with new material at each subsequent coating step. The isotherms show a broad capillary condensation step in the range of 0.4-0.9, indicating the presence of mesopores with a wide distribution of pore size.[229] The pronounced H1 desorption hysteresis loop suggests the existence of mesopores with open-ended cylindrical shapes in this sample.[230] BJH pore size analyses were performed on the adsorption branch, shown in Figure 6-9. The median pore size is 6.21 nm, while that of the 1-layer film is 7.0 nm. The decrease of pore size is because the continueous growth of crystallites in walls area during the repeated calcination. Zukalová et al. fabricated organized mesoporous titania film. The mean pore diameter of the 1-layer and 2-layer film is 7.3 nm but decreased to 6.7 nm for 3-layer film. [108] However, there are also some bigger pores with sizes in the range of 10 to 60 nm, probably from the merging of small pores during the calcination.[290] This is also in accordance with AFM results.

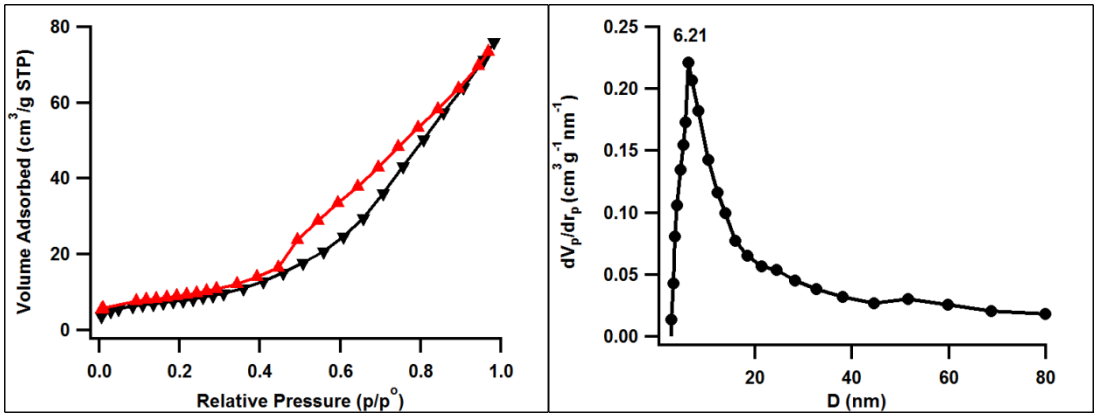


**Figure 6-9 $N_2$ adsorption and desorption isotherms and BJH pore size distribution from a powder generated from 7-layer films after final calcination.**

### 6.2.2.6 IV and IPCE

Figure 6-10 shows the IV curves and IPCE of DSSC made from different photoelectrodes prepared using the multilayered films. The photovoltaic properties of DSSC with different photoelectrodes are also shown in Table 6-1. With the increase of number of film layers, the short current and the open voltage decreased. The decrease of open voltage is probably because the thicker electrode may increase charge recombination between injected electrons and electroactive agents, due to low drift mobility of electrons in the film, which limits the conversion efficiency.[321] The decrease in the short current is mostly affected by reduced dye loading. The increase in number of film layers decreased the dye uptake, probably due to the decrease in the specific surface area. The IPCE of cells made with a 2-layer and a 7-layer film is shown in Figure 6-10. The IPCE results are in agreement with the IV curves. The cell made from a 2-layer film has the highest efficiency, 0.78%, due to the highest dye loading. This efficiency for 7-layer film with a thickness ~1.3 µm is much lower than the values generally reported for cells made from dip-coated surfactant-templated titania films.[105, 106] Zukalová et al applied 1 µm mesoporous titania into DSSC and showed an efficiency of 4.04 %.[1] Dewalque et al. obtained an conversion efficiency of 1.9 % by using 1 µm mesoporous titania into DSSC.[106] Some reasons are possible: firstly, the dye loading of films is not high due to the low specific surface area and collapsing of pores; Secondly, the films have low light absorbance to favour the harvesting of protons by dye molecules; Thirdly, the doping of sulphur may increase the defects of titania, which will influence the charge transfer

characteristics of photogenerated electrons from the dye into the titania.[322] However, for the 2-layer film based DSSC, the efficiency of 0.78 % is not so bad due to the relative high dye loading and porosity, considering the 500 nm thickness and 1 $cm^2$ active area in our case. The cell area of DSSC from Zukalová's work is 0.158 $cm^2$ and that from Dewalque is 0.2064 $cm^2$.

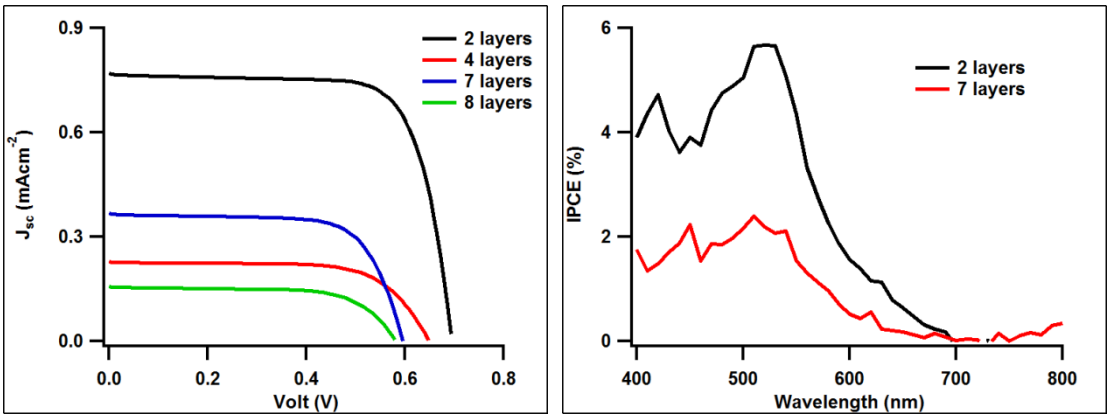


**Figure 6-10 The IV curves and IPCE of DSSC made from different photoelectrodes.**

**Table 6-1 Photoelectric properties of DSSC with photoelectrodesmade from films with different numbers of dip-coated layers.**

| *Sample* | *$J_{sc}$(mA/cm$^2$)* | *$V_{oc}$(mV)* | *FF (%)* | *η (%)* | *Dye uptake(nmol/cm$^2$)* |
|---|---|---|---|---|---|
| 2-layer | 0.782 | 693 | 73.45 | 0.78 | 12.0 |
| 4-layer | 0.230 | 648 | 67.80 | 0.23 | 3.1 |
| 7-layer | 0.373 | 597 | 68.87 | 0.37 | 4.4 |
| 8-layer | 0.159 | 580 | 66.07 | 0.06 | 4.8 |

## 6.3 Conclusion

To obtain better ordered mesostructures, the effects of the "filling pore" process were studied by GISAXS, ellipsometry, TEM, and AFM. From the results, the degree of mesostructural ordering for films made without the "filling pore" process decreased when applying the "filling pore" process and surface roughness increased. The thickness and porosity were however, similar compared to films made without the "filling pore" process. So the "filling pore" process was not used in later experiments. Thicker film up to 1.6 µm were made by repeated coating and investigated by GISAXS, AFM, UV-Vis and $N_2$

adsorption and desorption. The film thickness had a linear relationship with the number of layers in the films and the gradient was 165 nm per layer. In the GISAXS patterns all of the films had a higher ordering in the in-plane cut direction than the vertical cut direction, indicating the mesostructures in the films were compressed in the vertical direction. The ordering of the mesostructures decreased during the multiple coating processes and the mesostructure ordering was lost for film with greater than 5 layers. With the increase of film thickness, the film had higher absorbance and a rougher surface, but cracks appeared in the 8-layer film. Due to the collapse and re-structuring of pores in repeated calcination and infilling by subsequent coating steps, the specific surface area and pore volume decreased as the number of layers increased, which induced a lower dye loading for the thicker films. When these films were applied in DSSC, the solar conversion efficiencies were lower than the previously reported values. The 2-layer film showed the best cell performance due to the higher dye loading compared to the other films.

In this experiment, cells with a good efficiency were not obtained as expected, mainly due to the pore collapse, restructuring and in-filling during the repeated coating and partial calcination steps. Some suggestions for further work to improve this system are given here. Apart from modification of the synthesis parameters which need to be tightly controlled to make ordered surfactant-templated multilayer films, such as humidity control, reagents adjustment, the S-doped titania multilayer films may be more applicable in other applications. Firstly, the S-doped titania multilayer films can be used as solar photocatalysts, From Chapter 5, the S-doped titania with 1 layer was used as a solar photocatalyst and a promising result was obtained. It is known that the thickness of films has a great influence on their photocatalytic activity,[323] so investigation the influence of thickness for S-doped titania films on the performance of photoreactivity would be an interesting study. The hierarchical structure of the 7-layer film, revealed by the AFM measurements may be a particular advantage in this application due to the more rapid rates of mass transfer allowed through meso/macroporous structures. Secondly, the S-doped film with thickness around 500 nm could be applied in a solid-state DSSC that utilizes solid hole-collectors in place of liquid electrolytes. The film thickness

normally used in solid-state DSSC is around 500 nm and a mesoporous titania film made by dip or spin coating has previously showed a good efficiency in such cells according to literature.[324] The mesoporous thin film has open, uniformly sized pores enable effective infiltration of an organic phase. In this chapter, the 2-layer film has a thickness of 500 nm and highly porous, so applying them in solid-state DSSC has potential to achieve higher photon conversion efficiencies.

# Chapter 7 Meso-$TiO_2$ and Nanowire Composite Films Self-assembled at Air-Water Interface for DSSC

Most free-standing inorganic oxide films are surfactant-templated and based on mesoporous silica, however, for non-silica species, including titania, interfacial film growth is much less developed. In our previous work, a series of unsupported mesostructured surfactant-polymer films and silica films were synthesized at the air-water interface.[247, 252, 325-327] Here, we have expanded this method to prepare titania films templated by surfactant/polymer. Initially, the free-standing surfactant/$TiO_2$ films from titania precursor in aqueous solution were successfully fabricated, but there was not enough titania left after calcination due to the quick hydrolysis reaction of titania precursor in aqueous solution. To solve this problem, titania seed solution was used instead of the titania precursor and templated by CTAB/SDS/PEO. Interestingly, the unsupported titania films (FS-$TiO_2$) are composed of both nanowires and nanoparticles. After calcination the films contain an anatase phase with high surface area and remain intact, with thickness around 8.2 μm. When the film was put into a bilayer photoelectrode in DSSC, the FS-$TiO_2$ shows a better cell performance compared to a standard colloidal titania (Degussa P25) film and commercial Dyesol titania film.

## 7.1 Experimental

### *7.1.1 Free-standing surfactant/$TiO_2$ films from titania precursor*

CTAB, SDS and PEI were dissolved in ultrapure deionised water to give 0.1 M CTAB, 0.1 M SDS and 100 g/l PEI stock solution respectively. Although the CTAB/PEI mixture alone forms films at the solution interface, no film was observed when adding TIPR, TIBU or TIBDD to this solution. Different parameters, such as concentration of reagents and pH were adjusted but still no films were observed. However, films were observed when using CTAB/SDS mixedsurfactant solutions with PEI and titania precursors.

The two surfactant solutions were mixed and diluted to prepare a CTAB/SDS solution with 5.25 mM CTAB and 2.25 mM SDS. The polymer solution was then

added to the mixed surfactant solution to give a final concentration of CTAB and SDS of 3.5 mM and 1.5 mM respectively. After a short period of stirring, TIPR, TIBU or TIBDD was added to the solution to give the final concentration of 24.3 mM or 48.6 mM, but no film formed when adding TIBDD as it forms precipitates immediately. As the hydrolysis reaction of TIPR is much quicker than TIBU, TIBU was chosen for the later experiments. The surfactant/$TiO_2$ solution was then poured into a petri dish with a diameter of 50 mm over a plastic mesh. Several hours later, films were observed on the surface and precipitate formed at the bottom of the solution. Films were removed from the solution surface by lifting the open plastic mesh and dried in the air at room temperature. Dried films were then calcined at 450 ºC in air for 3 h with a ramp speed of 1 ºC/min and a natural cool down. To optimize the parameters, the concentration of CTAB, SDS, PEI were varied. Two kinds of polymers, SPEI, and LPEI were used and no pH adjustment was made to the solution. The neutron reflectivity patterns for films grown at air/water surface were used to characterize the film in situ. TGA was taken to characterize the dried surfactant/$TiO_2$ films.

### *7.1.2 Free-standing titania films from titania colloidal solutions*

3 ml TIPR was added dropwise to 40 ml 0.1 M HCl solution at room temperature with vigorous stirring. After stirring another 30 min in a bottle sealed by a lid, the solution was aged at a certain temperature (40, 70 or 100 ºC) overnight to form a clear titania seed solution. CTAB, SDS and PEO were dissolved in ultrapure deionised to give 0.1 M CTAB, 0.1 M SDS and 100 g/l PEO solution respectively. Normally the seed solution aged at 70 ºC was used if not otherwise specified.

To prepare CTAB/SDS/PEO/$TiO_2$ films, a mixture of 3.5 ml CTAB and 1.5 ml SDS solutions were diluted into 17 ml $H_2O$ and then 8 ml PEO and 10 ml titania colloidal solution were added separately (to give a final surfactant concentration of 12.5 mM, PEO 2 wt.% and $TiO_2$ 2.5 mM). This solution was poured into an 8 cm diameter polystyrene dish over a piece of plastic mesh after a short period of stirring. Films grew at the air-liquid interface within several hours and were removed from the solution surface by lifting the open plastic mesh and dried in the air at room temperature. Dried films were then calcined at 450 ºC in air for 3 h with a ramp speed of 1 ºC/min and a natural cool down.

TEM, DLS, AFM. SEM, TGA, XRD and $N_2$ adsorption and desorption were taken to characterize the samples.

### *7.1.3 Free-standing titania films for DSSC*

As there is only a small amount of titania left after calcination for surfactant/$TiO_2$ films from titania precursor solution, only titania films produced from colloidal solution were used in DSSCs. A bilayered $TiO_2$ photoelectrode was used in this experiment. The first layer was deposited on FTO glass (3 × 2.5 $cm^2$) with a blocking layer on top, from a Solaronix-paste by the doctor blade method: 'magic tape' was used to mark out a 1 cm wide strip on the glass and control the film thickness and the paste spread over this space by a sharp edge. The film was initially put into an oven for 30 min at 450 ºC. To minimize the effects of the first layer on the cells performance, a single piece of FTO glass with one coating was cut into two small pieces (1.5 × 2.5 $cm^2$). Then a second layer from home-made paste was coated on top. In the case of free-standing titania (FS-$TiO_2$), a drop of Milli-Q water was applied to moisten the surface before putting the dried unsupported titania film on the top of the initial film layer. This caused the unsupported films to lie flat on the substrate due to its hydrophilic property. After that, the FS-$TiO_2$ photoelectrode was calcined at 450 ºC in air for 3 h with a ramp speed of 1 ºC/min and a natural cool down. To make a comparison, the second piece of substrate was coated in a home-made paste prepared from commercial Degussa P25 titania nanoparticles as the second layer by doctor-blade method. The preparation of Degussa P25 titania paste was described in section 4.1 of chapter 4. After that, the Degussa P25 photoelectrode was calcined under the process described in section 4.2.2 as well. Another comparison photoelectrod is the film with thickness ~10 µm made from Dyesol paste according to the literature.[328]

The photoelectrodes were put into DSSC and measured by IV curves and IPCE. Cells were repeated 3-5 times to obtain the right trends. The dye absorbance of photoelectrodes was also tested.

Pervoskite electrolytes such as $CsSnI_{3-x}F_x$ have been found to be an effective hole-conductor for solid-state DSSC in 2012 by Chung et al..[329, 330] Here, free-standing titania films with $CsSnI_{3-x}F_x$ in the film were attempted to prepare. A

small amount of $CsSnI_{3-x}F_x$ solid particles were added into a CTAB/SDS/PEO/$TiO_2$ solution, but no film was formed and some white cottony materials formed in the solution. This is probably because the surfactant surface adsorption is very sensitive to the addition,[329, 331] or because the $CsSnI_{3-x}F_x$ reacts in acid solution as some people consider the $CsSnI_3$ as the metallic solids. [332] Also the colour of $CsSnI_{3-x}F_x$ solid is black and it became dark brown after being dissolved in organic solvent, the solution is dark brown, but the solution became white when adding the $CsSnI_3$ into CTAB/SDS/PEO/$TiO_2$ solution. No deep research was done due to the failure of this experiment.

## 7.2 Results and Discussion

### *7.2.1 Free-standing $TiO_2$/surfactant films from titania precursor*

#### 7.2.1.1 Neutron reflectivity of interfacial films

The neutron reflectivity patterns collected on INTER at ISIS, for films grown at air/water surface using LPEI are shown in Figure 7-1. In general the LPEI films show little evidence of long range mesostructural ordering. Only a broad peak at around 0.106 $Å^{-1}$ can be observed, giving the spacing between adjacent repeat units of 5.9 nm if a lamellar film structure is assumed.

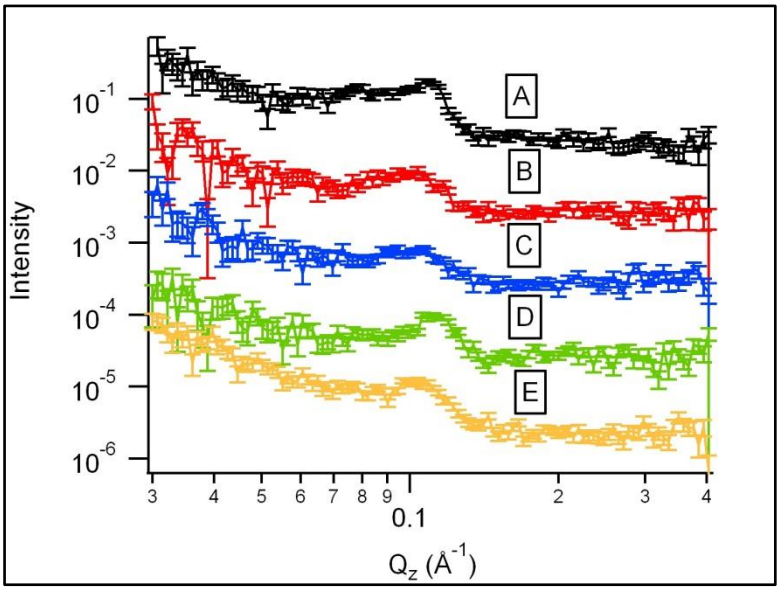


**Figure 7-1 Neutron reflectivity patterns of CTAB 3.5 mM/SDS 1.5 mM films grown at air/water surface Sample A is synthesized from 5 g/l LPEI and 24.3 mM TIBU, while sample B is prepared from the same amount of LPEI without TIBU. 10 g/l LPEI was**

**used in samples C, D and E, but sample C was made from 24.3 mM TIBU, D without TIBU and E from 48.6 mM TIBU.**

Time-resolved neutron reflectivity data of a film grown using 5 g/l SPEI as the polymer, with no added titania precursor is shown in Figure 7-2. It is found that the film has a good mesostructural order. In the first ten minutes after mixing, two distance peaks at 0.09 and 0.12 $Å^{-1}$ and a broad weak peak at 0.18 $Å^{-1}$ can be observed. This phase is a cubic Im3m phase with unit cell 9.9 nm since the three peaks are almost related by $1:\sqrt{2}:2$. The intensity of the peak at 0.09 $Å^{-1}$ decreases slowly in the first 30 min and quickly in the next 30 min, when the intensity of the peak at 0.12 $Å^{-1}$ behaves oppositely. After 30 min, the peak at 0.18 $Å^{-1}$ disappeared and a new peak at 0.14 $Å^{-1}$ grows quickly. The intensity of peak at 0.12 $Å^{-1}$ decreases gradually after around one hour. The final pattern of films, which has two peaks (0.09 and 0.14 $Å^{-1}$) with the second peak still showing traces of evolution, is shown in the right graph of Figure 7-2. All of these changes indicate that a phase transformation is occurring within the interfacial film, however, the final mesostructure of films need more evidence to analyse the structure present, as the mesostructure after 60 min is still changing and only two peaks are found.

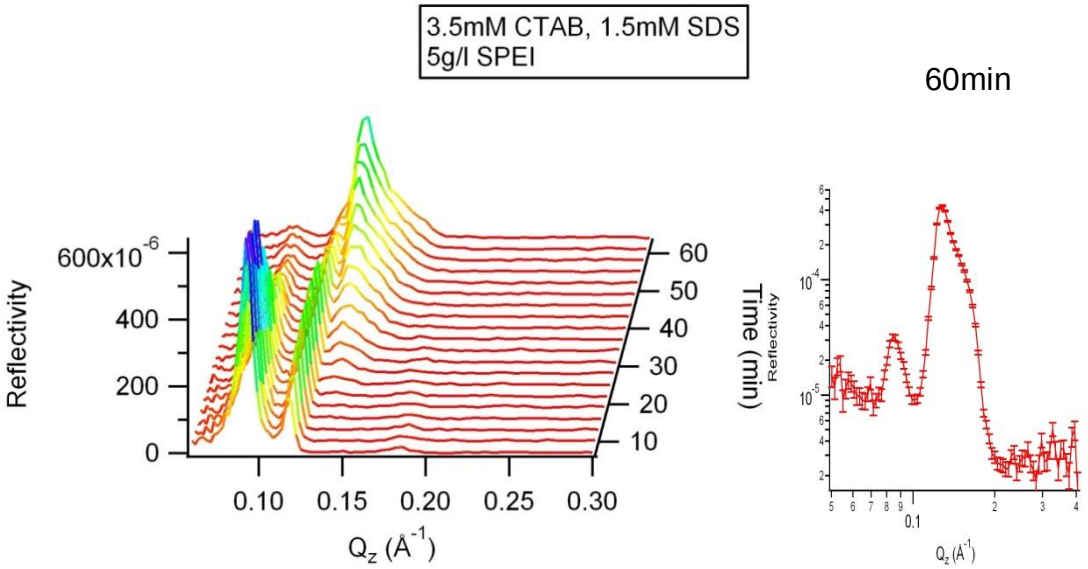


**Figure 7-2 Evolution of the CTAB/SDS/ SPEI film grown at air/water surface (left) and a higher resolution reflectivity pattern at 60 min (right).**

With CTAB/SDS as surfactants, the effects of the concentration of SPEI and TIBU on the evolution of CTAB/SDS/SPEI/$TiO_2$ film at air/water surface were investigated by neutron reflectivity.

Figure 7-3.A shows reflectivity from a film grown at the air/water surface synthesized from 3.5mM CTAB/1.5mM SDS/5g/l SPEI/24.3mM TIBU. In the first half an hour, only one distinct peak at 0.12 $Å^{-1}$ appears and the shape has little change. The intensity of this peak increases in first 30 min then decreases when a new peak at 0.14 $Å^{-1}$ grows in. The new peak grows quickly, while the peak at 0.12 $Å^{-1}$ disappeared gradually. Moreover, another weak peak at 0.09 $Å^{-1}$ starts to form at 100 min, although it grows really slowly and is difficult to notice. However its presence can be confirmed by the pattern at 154 min. The mesostructure of film with the second still showing traces of evolution at 154 min looks quite similar as the one in Figure 7-2.

Figure 7-3.B shows reflectivity from a film grown at the air/water surface synthesized with the same concentration of surfactant-polymer complex as in sample A, but with 48.6 mM TIBU added. After mixing, the film has one distinct peak at 0.09 $Å^{-1}$ and two weaker peaks at 0.12 and 0.18 $Å^{-1}$, which can be indexed to a cubic Im3m phase. The intensity of the first two peaks increases for 10 min then changes little. Although the changes of the patterns are small after 10 min, some wrinkles occur in the region of 0.12-0.18 $Å^{-1}$, which can be confirmed by the higher resolution pattern at 60 min as belonging to four peaks at 0.09, 0.12, 0.14 and 0.18 $Å^{-1}$. This means a new peak at 0.14 $Å^{-1}$ formed, but it is difficult to index the four peaks as a pure cubic phase. As the speed of evolution of the film is really slow, we scan it again after 236 min to obtain the final structure. Two obvious peaks at 0.09 and 0.14 $Å^{-1}$ are observed, which is almost the same as the films with lower concentration or without TIBU.

Figure 7-3.C shows reflectivity for a film grown at the air/water surface synthesized with the same concentration of CTAB/SDS/TIBU as sample A, but increasing the amount of SPEI to 10 g/l. In the whole time-resolved process, two peaks at 0.09 and 0.12 $Å^{-1}$ are always observed, possibly indicating the cubic Im3m phase. The first peak is much weaker and its intensity decreases with time while the other one behaves oppositely. Half an hour after mixing, a new peak at 0.14 $Å^{-1}$ begins to form and its intensity increases with time. The three peaks are

also shown in the pattern at 60 min. The final structure of this film, shown in the pattern at 195 min, has two peaks at 0.09 and 0.14 $Å^{-1}$, which is almost the same as the films of the other two graphs in Figure 7-3.

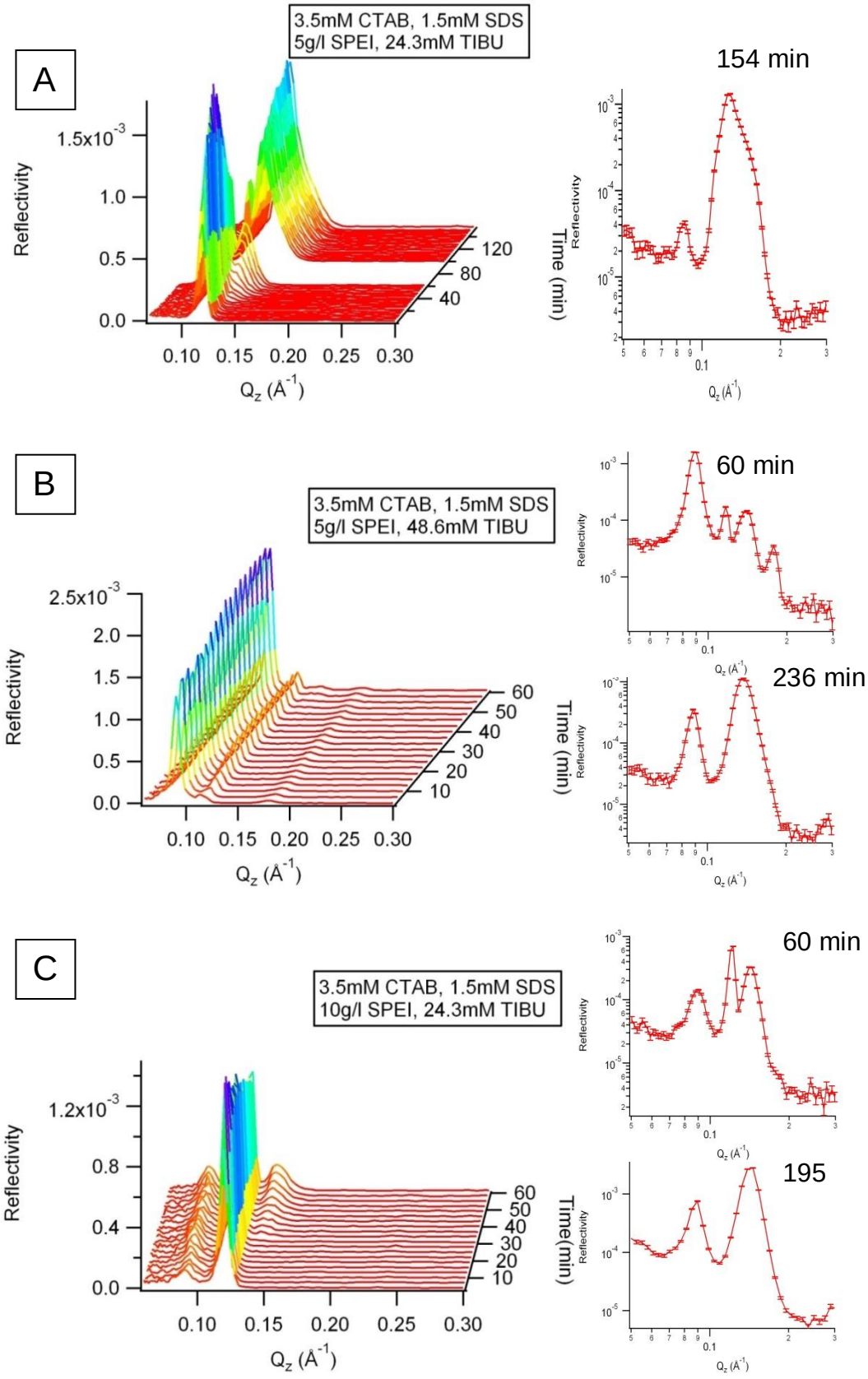


**Figure 7-3 Evolution of the CTAB/SDS/SPEI/$TiO_2$ film grown at air/water surface (left) and reflectivity patterns at different times (right). Concentrations of materials are indicated on each graph.**

All of these films with different amount of titanium precursor or polymer indicated a phase transformation occurring from cubic Im3m to another phase within the interfacial film, although the variation of peaks intensity and numbers are totally different from each other. Compared with the film without adding TIBU, they have the same process of mesostructure transformation, but the structure for films with addition of titania changed more slowly, so adding titania has greatly affected the process of film mesostructure transformation. The phase transformation was also observed in our group's work,[333] and higher concentration of surfactant solution were used to template silica film.

With different amount of TIBU and SPEI, the evolutions of different samples have different structural transfer processes but have the same final structure. So, it can be concluded that the amount of TIBU and SPEI greatly affects the process of structure evolution in inorganic surfactant/polymer films rather than the final structure. Most of the structural changes observed must be due to drying rather than titania polymerisation since similar structural changes are observed in the film without titania addition, suggesting either that little titania is incorporated into the films or that the rapid titania condensation finishes in times short enough that the final structure of the film is not perturbed although the mechanism by which is forms can be altered.

#### 7.2.1.2 TGA of dried film

To test these possibilities TGA measurements were made on these films after recovery from the solution surface and drying. Figure 7-4 shows the TGA curves of dried CTAB/SDS/SPEI/$TiO_2$ films. Although the concentration of reagents changed, there is only a small amount of titania left after calcination, because hydrolysis reaction of titania precursor in aqueous solution is very quick and the titania form precipitates without interacting with surfactants. This limits the potential of these films and does not meet the aim of this project, so no further work was continued using titania precursors directly in film formation.

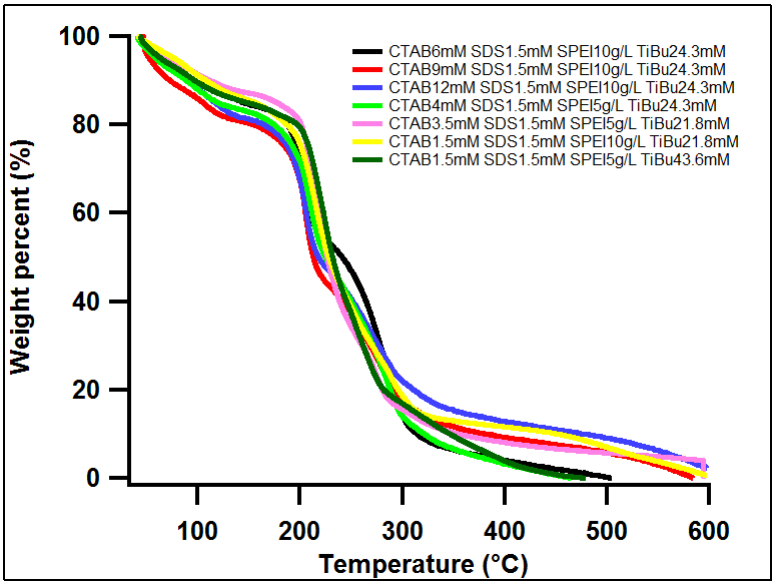


**Figure 7-4 TGA curves of dried CTAB/SDS/PEI/$TiO_2$ films.**

## *7.2.2 Free-standing titania films from titania colloidal solution*

### 7.2.2.1 Titania seed solution

To prepare the films a titania nanoparticle solution was initially prepared. Since the pH of the resultant solution (~ 1) is below the point-of-zero charge (pzc) of titania (pzc ~ 6-7), the titania seeds are positively-charged. TEM images of the seed solution show particles with diameters between 2.5-4 nm, shown in Figure 7-5. However, DLS measurements suggest the seeds rapidly form clusters which are ~14.3 nm diameter with a dispersity of 0.25. DLS of seed solution aged at 40 and 100 ºC are ~12.3 and ~21.6 nm with a dispersity of 0.25 and 0.22 respectively, demonstrating that the size aggregation process increase with the increase of aging temperature.

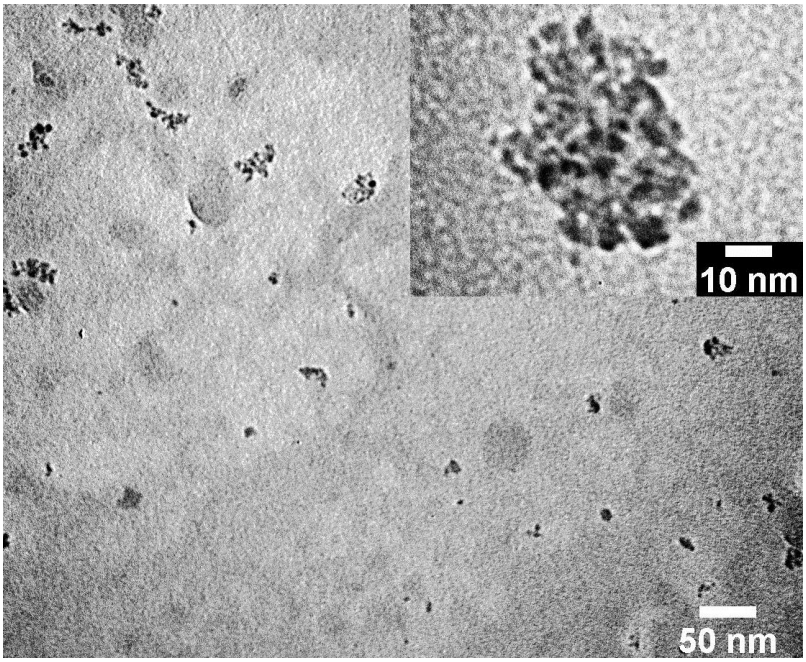


**Figure 7-5 TEM image of titania seed solution prepared at 70 ºC.**

### 7.2.2.2 Morphology

Photographs of free-standing films at different stages are shown in Figure 7-6 A, B and C. At first, uniform films formed at the air-interface of the white surfactant/polymer mixture and can be demonstrated from the macroscopic wrinkles visible in the surface (Image A). Then, the robust film was lifted and dried in air keeping the shape of the dish (Image B). Noticeably, the FS-$TiO_2$ film retains its shape after calcination (Image C).

The calcined FS-$TiO_2$ film has an estimated thickness of ~ 8.2 µm measured by cross-sectional SEM (Figure 7-6 D). AFM (Figure 7-6 E) demonstrates that the calcined film has a smooth surface with a 31.9 nm RMS roughness and a long nanowire is seen running parallel to the surface. This wire is more than 13 µm long with a diameter between 40 and 150 nm. The nanowire surface is not smooth, as seen for previously reported “naked“ nanowires [334] since some nanoparticles adhere to the nanowire, which is also the reason for the large variation in rod diameter.

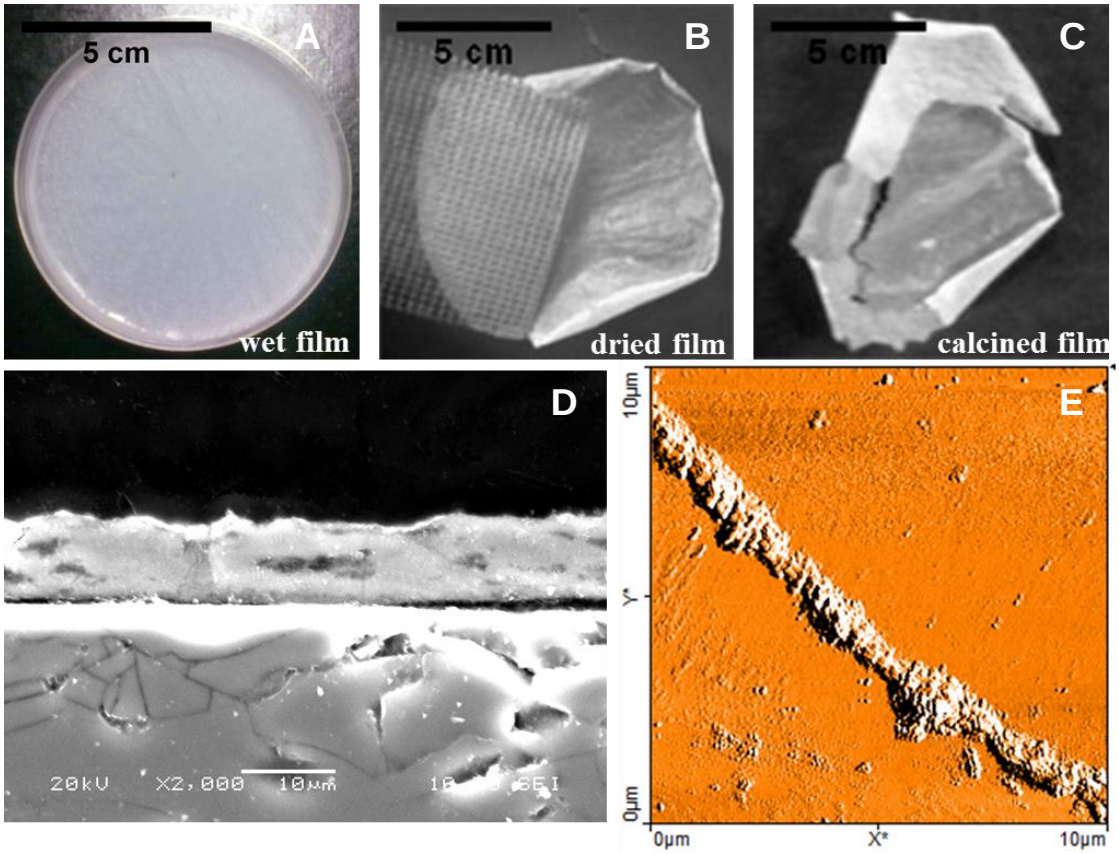


**Figure 7-6 Photographs of free-standing films at different stages (A,B and C); SEM cross-sectional image (D) and AFM surface images of calcined film (E).**

### 7.2.2.3 TGA

Figure 7-7 shows the TGA of dried composite films suggests 25 wt.% titania remains after heating to 450 ºC. From the TGA pattern, water evaporates in the temperature range 100 - 220 ºC, combustion of the template occurs until 370 ºC followed by condensation and crystallization of the $TiO_2$ structure ending at 500 ºC. From 500 ºC onwards, the residual mass from the composite film is 22 wt. % $TiO_2$. The mass ratio of $TiO_2$ and template calculated from TGA is 2:5.

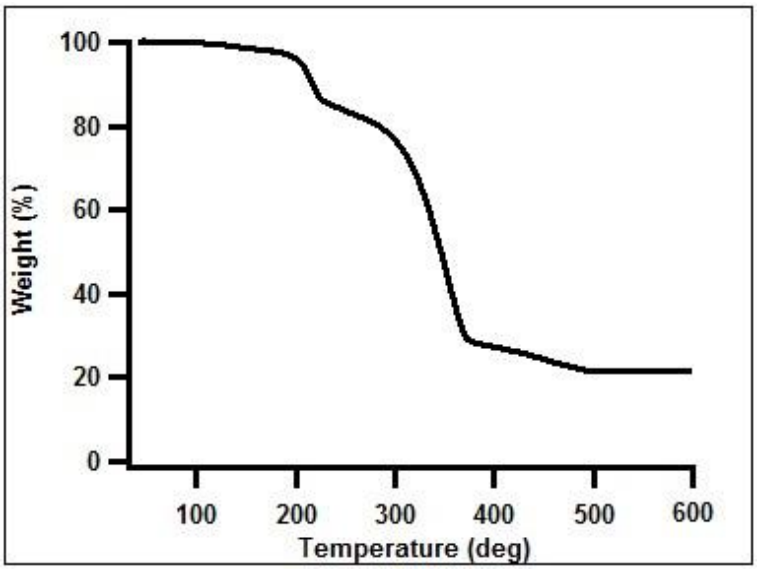


**Figure 7-7 TGA curve of dried surfactant/titania films.**

### 7.2.2.4 XRD

Figure 7-8 shows the XRD of a powdered, calcined FS-$TiO_2$ film. The diffraction peaks (101), (004), (200), and (220) can be unambiguously assigned to the anatase form of $TiO_2$ (JCPDS card no. 21-1272). The relatively broad peaks suggest the calcined film has a nanocrystalline structure with a crystal size ~ 6.1 nm according to the Scherrer formula.

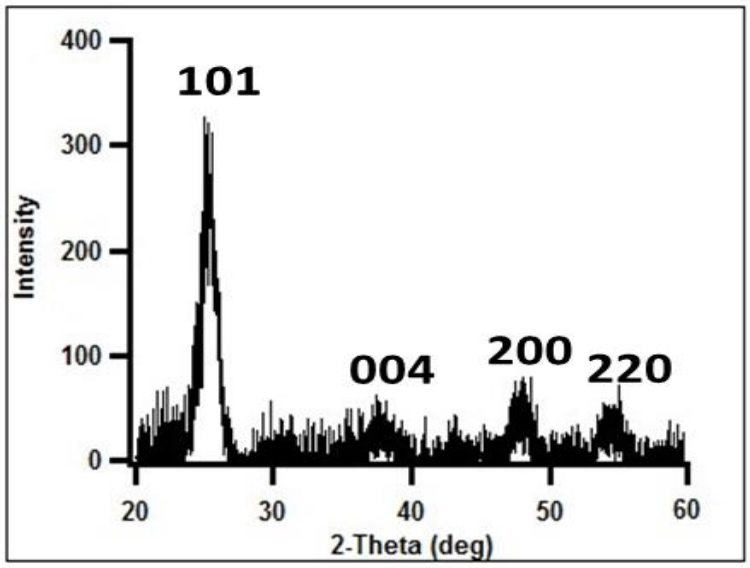


**Figure 7-8 XRD curve of calcined FS-$TiO_2$.**

#### 7.2.2.5 TEM

The morphology and structure of the calcined FS-$TiO_2$ film are further confirmed by TEM and selected-area electron diffraction patterns (SAED). As shown in Figure 7-9, the typical FS-$TiO_2$ film is composed of nanowires and a branched nanoparticle network, which roughens the surface of the nanowire. The diameter of the nanowire structures ranges from 40-200 nm and the length is on the order of micrometers, in agreement with the AFM data. A magnified image (Image A), shows the long axis of the nanowire, (in the direction marked by the lines) with a diameter of 40 nm. It is important to note that that these nanowire/nanoparticle composites are nanoporous due to the formation of unsymmetrical pores associated with the interparticle spaces. Nanoparticles, with diameter around 6-8 nm, gather on the body of the nanowire and form branches from the nanowire surfaces. The presence of nanoparticles (with some circled) are also shown in the high-resolution image in Image B. The size of nanoparticles is in agreement with the XRD results. The branched nanoparticle aggregates help bind the nanowires together to form continuous films. In Image C, a nanoparticle (circled) acts as a bridge to connect the two separate nanowires. Image C and D also indicate that the nanoparticles are fully crystalline, with a lattice spacing of 0.35 nm corresponding to the (101) crystal plane, which is also verified by the inset SAED pattern in Image C. The larger nanowire structure is not as well crystallized as the nanoparticles although it also has an anatase nanocrystalline structure. The clear crystalline rings in the inset SAED pattern in Image D are attributed to the (101), (004), (200) and (211) planes of the anatase phase, respectively. The difference in the degree of crystallization between nanoparticles and nanowires may result from different polymer and surfactant content in the nanowire compared to the branched nanoparticle regions. Adsorption of surfactant on the initial $TiO_2$ nanoparticles will influence the surface energies of titania nuclei and thus alter the crystallization, as the formation of anatase titania from an amorphous precursor has a surface nucleation-dominated crystallization behaviour.[335]

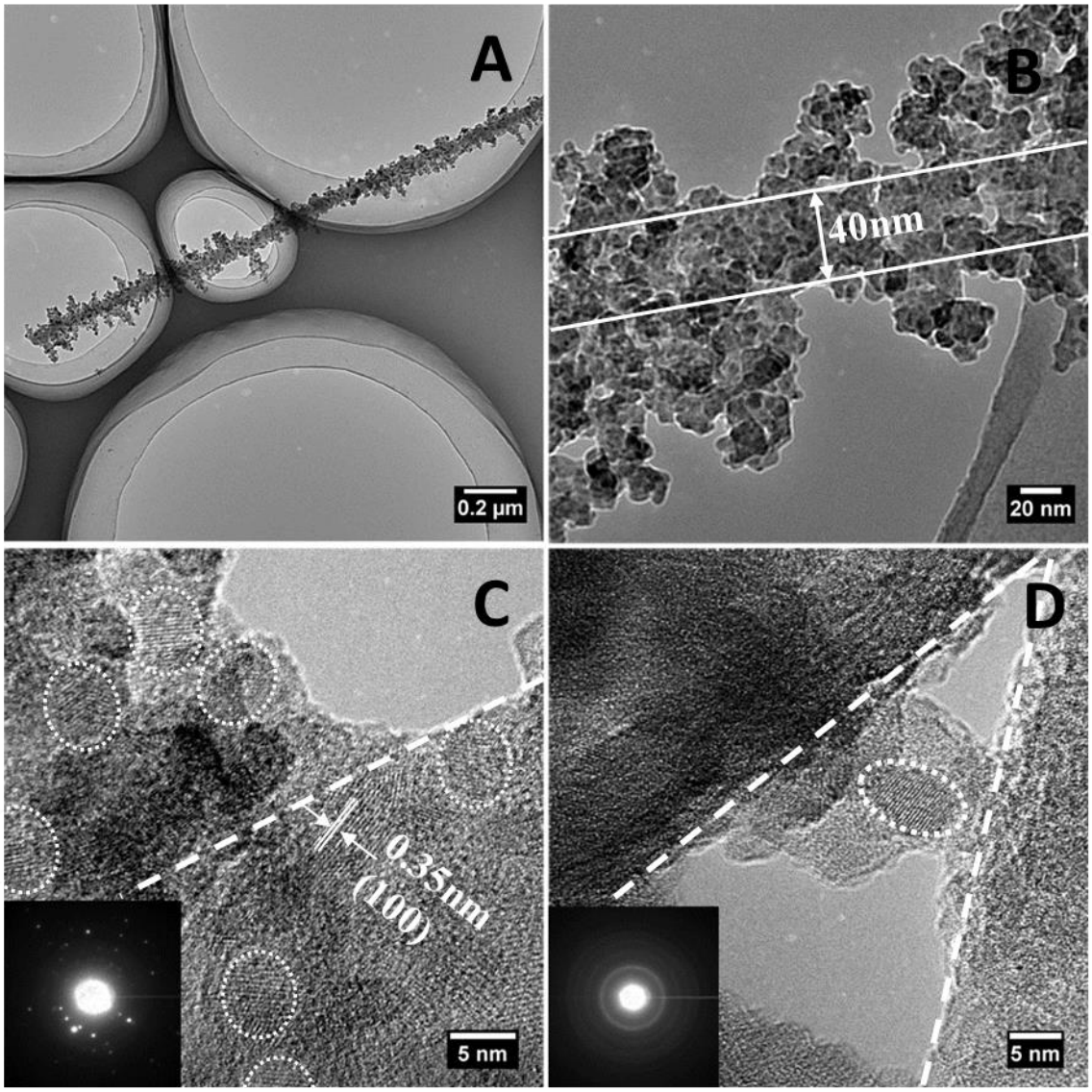


**Figure 7-9 TEM images of calcined FS-$TiO_2$ with SAED patterns inset.**

### 7.2.2.6 $N_2$ adsorption and desorption

The nitrogen ads/desorption isotherms of calcined FS-$TiO_2$ prepared from different seed solutions are presented in Figure 7-10 (left). The films made from seed solution aged at 40, 70 and 100 ºC were named FS-$TiO_2$-40, FS-$TiO_2$-70 and FS-$TiO_2$-100 respectively. It is noticeable that all the titania composites show the type IV isotherm with type H2 hysteresis loop according to IUPAC classification indicating interconnected pores.[336] All of them have high BET surface area and the film FS-$TiO_2$-70 has the highest value. Its surface area is up to 190 $m^2/g$, which is more than 4 times higher than the commercial Degussa P25 nanoparticles (46 $m^2/g$) and at least twice that of titania nanowires alone (10-100 $m^2/g$) according to literature.[337] The high surface area may result from the porous

structure and roughened nanowire surface. The pore-size distribution of FS-$TiO_2$ film powders were analysed using the BJH method and displayed in Figure 7-10 (right). For the typical film FS-$TiO_2$-70, the predominate pore size is around 5.28 nm and mesopores are probably attributed to the inter-particle gaps in the assemblies of nanoparticle branches and nanowires,[338] which is also in accordance with TEM results. With the increase of the ageing temperature, the pore size increased. This also confirms that the pores were introduced by the voids between particles.[33] The voids between particles increased due to the increase of particle size as the higher ageing temperature induced a bigger particle size in the seed solutions. The results of nitrogen ads/desorption are also summarized in Table 7-1.

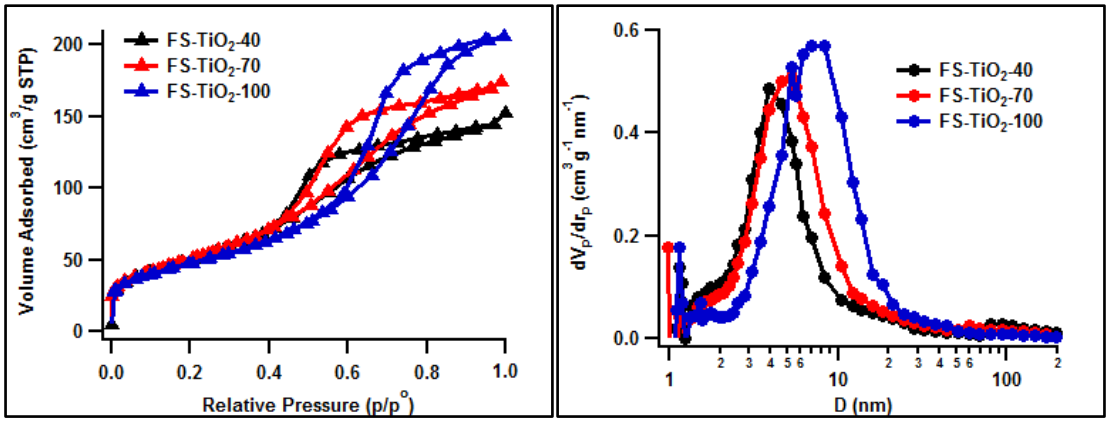


**Figure 7-10 $N_2$ ads/desorption isotherms (left) and BJH pore size distribution (right) of FS-$TiO_2$ films fabricated from different seed solutions.**

**Table 7-1 The parameters calculated from the nitrogen ads/desorption isotherms.**

| *Sample* | *$S_{BET}$ ($m^2$/g)* | *Pore volume ($cm^3$/g)* | *Peak pore size (nm)* |
|---|---|---|---|
| FS-$TiO_2$-40 | 187 | 0.24 | 3.88 |
| FS-$TiO_2$-70 | 190 | 0.28 | 5.28 |
| FS-$TiO_2$-100 | 171 | 0.32 | 8.33 |

Films with high surface area and a porous structure will facilitate mass transfer making them useful for many applications, such as faster diffusion to the active sites during catalysis[339] and allows the capture of more dye molecules to improve the efficiency of solar cells.[35]. Below in section 7.2.3 we explore the potential application of these films as photoanodes for 1 $cm^2$ DSSCs.

### 7.2.2.7 Mechanism for film formation

The overall CTAB/SDS concentration in the film forming solutions is 0.0125 M, and at this concentration the mixed surfactant solution contains small mixed micelles in solution [340] although other work in our group has found a mixture of larger aggregates and small micelles in 0.01 M CTAB/SDS solutions without added polymer.[247] Contrast variation small angle neutron scattering and ultrasmall angle neutron scattering was used to demonstrate that the mixed surfactant solution separates into small ellipsoidal micelles which contain 90 % CTAB (with radii 25 and 33Å) and larger mixed ellipsoidal aggregates (1.5 × 0.5 microns) with a 7:3 molar ratio of CTAB:SDS. At higher total surfactant concentration (0.05 M) the formation of large multilamellar vesicles is favoured by addition of PEO however addition of this polymer was not investigated at the lower surfactant concentration. With the addition of PEO, several environments are available to influence the crystallisation and clustering of the nanoscopic titania seeds. Preferential adsorption of surfactant on crystal faces of nanoparticles may favour growth as nanowires along a preferred direction, similar to the growth of gold nanorods from initial seeds.[341, 342] However work on hydrothermal synthesis of $TiO_2$ nanorods on substrates has shown that elongated nanorod growth is favoured by PEO in solution while addition of SDS causes elongation but also fusing of nanorods attached to substrates in hydrothermal synthesis.[114] CTAB also favours aggregation of nanoparticles into nanowires, since CTAB addition to solution phase titania nanorod syntheses in ethylene glycol caused formation of nanorods with a rough surface.[343] The presence of the PEO in our solutions therefore may promote nanorod growth and the presence of SDS and CTAB the fusion of further nanoparticles to the rods. Intercalation of the polymer in the nanorod would explain the lower degree of crystallinity as the rods form from fusion of nanoparticles interacting with the polymer. Nanoparticles incorporated into the large surfactant aggregates or surfactant micelles grow and crystallise to form the nanoparticle network. Forced by the solvent evaporation, the titania hybrid nanowires, dispersed particle aggregates, micelles and PEO migrate to the surface of solution to form films within a few hours after mixing and this surface layer condenses due to the continuous evaporation of water. During this process, PEO, wrapped around the micelles and nanoparticles, plays an

important role to hinder the electrostatic repulsion between charged wires and seeds and bind them together to form strong films.[252] The wet films can be easily lifted by a mesh and dried in air to obtain thick and robust titania hybrid films. After calcination the titania hybrid nanowires became anatase nanowires and titania nanoparticle branches served as a binder between nanowires to form intact films. The overview of the mechanistic scheme of FS-$TiO_2$ films suggested above is shown in Figure 7-11.

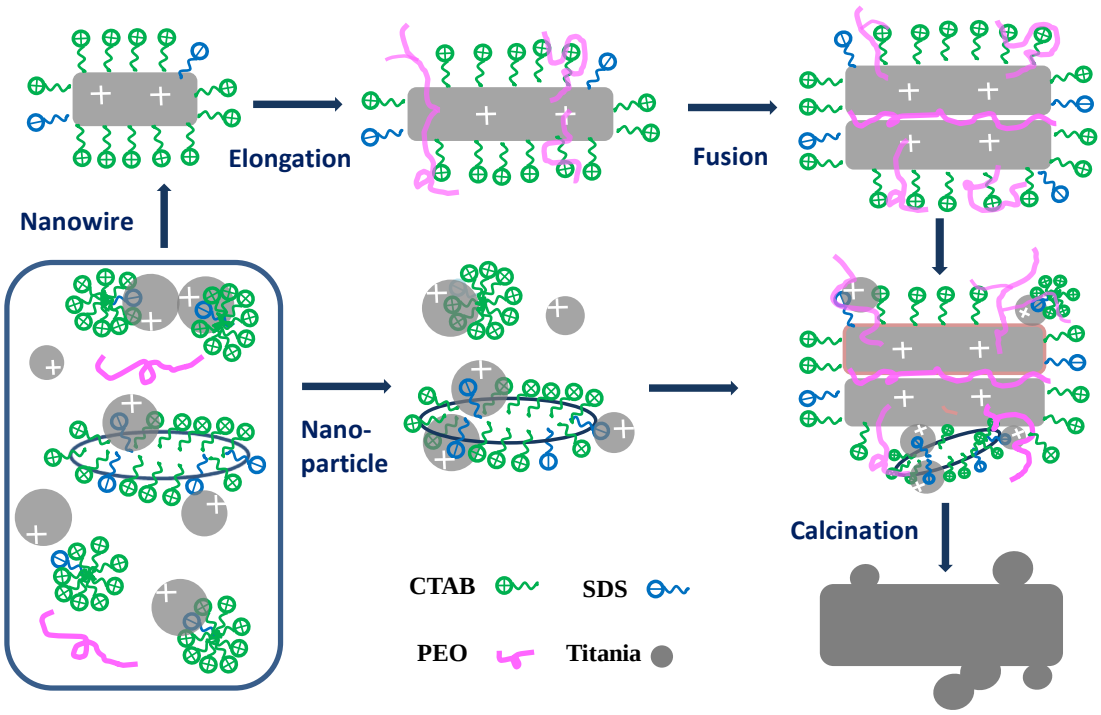


**Figure 7-11 Scheme showing the mechanism of unsupported titania nanowire/nanoparticle composite film growth.**

### *7.2.3 Free-standing titania films in DSSCs*

Figure 7-12 shows SEM cross-sectional image of the first and second layer of the bilayer photoelectrode prepared from the Degussa P25 film. The initial layer is around 2 µm, and as this substrate was split in half after the initial film was deposited, this thickness is the same for the two solar cells subsequently prepared from FS-$TiO_2$ and Degussa P25 films. The thickness of the secondary Degussa P25 film is around 8.2 µm, which is similar to that of the FS- $TiO_2$ film.

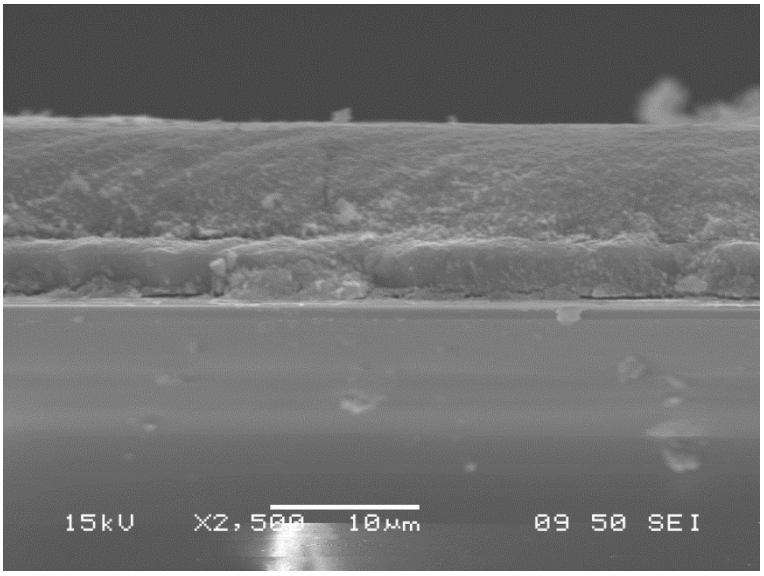


**Figure 7-12 SEM cross-sectional image of a bilayer photoelectrode prepared from a Degussa P25 film deposited on an initial layer of $TiO_2$.**

Figure 7-13 shows the IV curves and IPCE of FS-$TiO_2$-70, Degussa P25 and Dyesol cells. The dye uptake of the three electrodes was 195, 125 and 100 nmol/$cm^2$ for FS-$TiO_2$-70, Degussa P25 and Dyesol films respectively, calculated by desorbing the dyes in 0.1M KOH solution. This suggests 56 % more dye was absorbed by the FS-$TiO_2$-70 film than the Degussa P25 layer and that is 95 % than Dyesol film. Both the short current and open voltage of FS-$TiO_2$-70 film cell are the highest among the three cells. In particular, the short current of FS-$TiO_2$-70 cell is 9.32 mA which is ~14% higher than that found for the Degussa P25 cell (7.95 mA) and Dyesol cell (7.82 mA). The total global efficiency is 3.99 % compared to 3.50 % from the cell prepared using the Degussa P25 layer and 3.19 % from Dyesol cell. These better photoelectrical performances are due to the higher dye uptake and faster electron transfer in the nanowire structure found in the FS-$TiO_2$-70 films [47].The improved short current does not correspond with the improved dye uptake, rather it results from the fact that the higher surface area also means more back reactions occur which reduce the short current.[344] The IPCE of the FS-$TiO_2$-70, Degussa P25 and Dyesol cells is shown in Figure 7-13 (right) and is in accordance with the efficiency result. In general, the IPCE of the FS-$TiO_2$-70 cell is higher than that of the Degussa P25 and Dyesol cell over the whole wavelength range due to their different light capture ability, due to the adsorbed dye amounts, which is in agreement with the IV results. In the blue and

visible wavelength range, the FS-$TiO_2$-70 cell has an obviously higher IPCE than the Degussa P25 cell. At 530 nm, the peak of the adsorption spectrum for the N719 dye used in these cells occurs and the IPCE for the FS-$TiO_2$-70 cell is 15% higher than the Degussa P25 cell and 23% than the Dyesol cell. The results of the three cell performance were also summarized in Table 7-2.

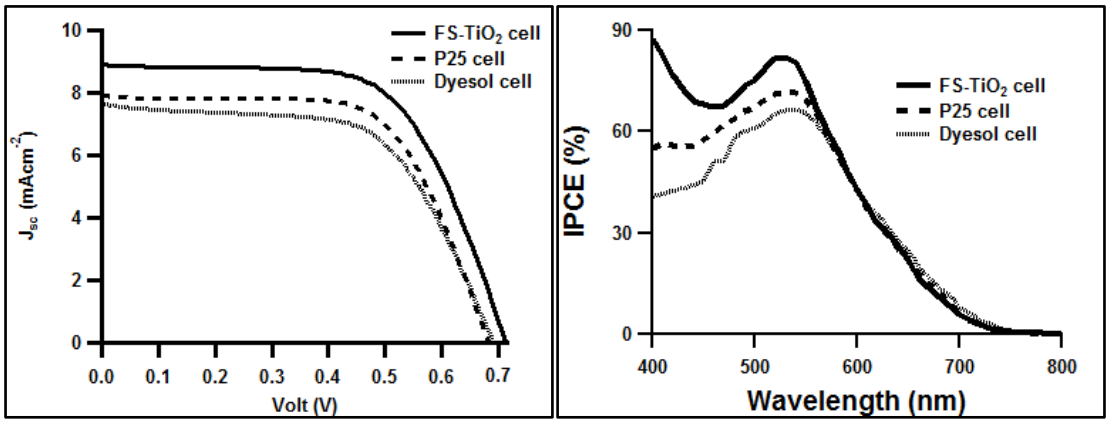


**Figure 7-13 IV curves and IPCE of DSSC made from FS-$TiO_2$-70, Degussa P25 and Dyesol films**

**Table 7-2 Photoelectric properties of DSSC made from FS-$TiO_2$-70, Degussa P25 and Dyesol films.**

| *Sample* | *Film thickness (μm)* | $J_{sc}$ *(mA)* | $V_{oc}$ *(mV)* | *FF (%)* | *Efficiency (%)* | *Dye-uptake (nmol/cm²)* | *IPCE at 530 nm (%)* |
|---|---|---|---|---|---|---|---|
| FS-$TiO_2$ | 2 + 8.2 | 8.96 | 720 | 62 | 3.99 ±0.12 | 195 ±3 | 82.2 |
| P25 | 2 + 8.2 | 7.95 | 677 | 64 | 3.50 ±0.18 | 125 ±2 | 71.7 |
| Dyesol | 10 | 7.82 | 691 | 60 | 3.19 ±0.15 | 100 ±2 | 66.6 |

## 7.3 Conclusion

Free-standing surfactant/polymer templated titania films were successfully made either from a titania precursor or a seed solution. Although the films made using a titania precursor have an ordered mesostructure, there is only a small amount of titania left after calcination. This suggests the failure of trying to make free-standing titania film from titania precursor due to the rapid hydrolysis reaction in water leading to poor titania incorporation into the films. So, a titania seed solution was used as the titania source to prepare free-standing titania films containing larger amounts of titania. This is a novel method adopted to successfully fabricate free-standing robust titania nanowire/nanoparticle

composite films. Films are composed of ~25 wt.% of titania when freshly prepared and retain their macroscopic shape, with a thickness around 8.2 μm after calcination. The nanoparticle component acts as a binder between nanowires which grow during synthesis. This allows formation of unsupported intact porous titania films even after heat treatment at 450 ºC for 3 h. Moreover, calcined films contain an anatase crystal phase and have a high surface area (190 $m^2/g$) with the structure composed of one-dimensional long nanowires (more than 13μm in length and ca. 40nm in diameter) and mesoporous nanoparticle branches (peak pore size at 5.28nm). When the film is used as the second layer in bilayered photoelectrode DSSC, the short current of FS-$TiO_2$-70 cell is 9.32 mA which is ~14% higher than that found for the other two nanoparticle films. The total global efficiency is 3.99 % compared to 3.50 % from the cell prepared using the Degussa P25 layer and 3.19 % from Dyesol cell. The IPCE at 530 nm is 15% higher than the Degussa P25 cell and 23% than the Dyesol cell. The improved performance is due to higher dye uptake in the FS-$TiO_2$ films and possibly also more rapid electron transfer in the nanowire structures, compared to the nanoparticle films.

The 1D nanostructure can increase the electron transport. To further confirm this, the differences in electron transport and back reaction should be measured. From the experiments, we changed the parameter of titania seed solution which can affect the pore size and surface area, so other testing and application in DSSC should be taken to investigate the influences. By changing the other parameters such as concentration of reagents, pH, it is possible that the tuning of size of nanowires and the titania amount in as-prepared hybrid film could be changed to obtain stronger films with better properties to put into more applications.

Except changing the parameters of film formation solution, the strength improvement of films could be attempted by adding some silicon source in reagents solution to prepare $TiO_2/SiO_2$ film. The silicon precursor reacts relatively slowly in acid solution and interacts with surfactants strongly,[345] also it will not crystallize during calcination and people in our group made very robust mesostructured silica from this method.[333] These suggest it will be a good way to

make the robust and mesoporous titania film by adding a small amount of silicon precursor or treat the titania hybrid film by exposure to silica precursor vapour.

# Chapter 8 Conclusion and Future Work

Mesoporous titania powder or film with various mesostructure have been fabricated via different approaches. When applied the structured titania into DSSCs or photocatalysts, the influence of film's morphology, mesostructure, porosity and optical property on the performance of DSSC and photocatalyst were investigated using many characterization methods.

## 8.1 Meso-$TiO_2$ powder made from water-ethanol solution

Meso-$TiO_2$ was made from water-ethanol solution by using the P123 as the template. The effects of volume ratio between ethanol and water, and aging temperatures on mesostructure of calcined samples were studied. All the samples do not have ordered mesostructure. From the TGA results, the aging temperatures do not affect the inorganic/organic weight ratio in the as-prepared materials. For a typical sample, it has an anatase phase with crystal size ~ 19 nm and obtains a specific surface area 101 $m^2/g$ with a mean pore diameter of 3.1 nm. The formation of the relatively small pores is due to the pore collapse during calcination. Although these meso-$TiO_2$ are not well-ordered, they are well-crystallized and retain some mesoporosity. These materials therefore should have higher active performance compared to bulk titania in many applications. Some further ways could be attempted to improve the long range ordering, such as lowering the calcination temperature to reduce the collapse of pores, using CASH method [29] in the calcination process to help maintain better ordering and adding chelating complex in the reagents to slow the hydrolysis reaction of titanium precursor.[13]

## 8.2 Ordered mesoporous titania and nanoparticle composite films prepared by doctor-blading for DSSC

Ordered 2D-hexagonal mesoporous titania powders were synthesized vis EISA method and templated by P123. The aging time on the mesostructure of as-prepared sample were investigated by SAXS. Increasing the age time favours the degree of long range ordering but it has little effects when the ageing time is

longer than 6 days. After calcination, the meso-$TiO_2$ aged for 6 days has anatase crystallite with a size ~7 nm and high surface area 149 $m^2/g$ with a mean pore diameter of 8.33 nm. By mixing this meso-$TiO_2$ with Degussa P25 titania and preparing meso-$TiO_2$ and nanoparticle composite films by doctor-blading, the films become more porous, rougher, have higher surface area and stronger scattering effects compared to pure P25 film. Most importantly, the amount of dye loading increased with the fraction of meso-$TiO_2$. When applying these films as the scattering layer for DSSCs, the photovoltaic performances improved by the introduction of meso-$TiO_2$ into P25 films. Considering the porosity, surface area, scattering effects and the degree of compactness of the film, the optimum cell was obtained by introducing 50 wt.% meso-$TiO_2$, which shows an increase of short current from 8.36 to 11.96 $mA/cm^2$ and efficiency from 3.85 to 4.93 % compared to cell with the Degussa P25 film.

To our knowledge, this is the first time using mesoporous titania and nanoparticle composite films as the scattering layer for DSSCs. Although some promising results were obtained, there are still some points which could be improved. In the process of titania paste preparation, annealing of the film is needed to remove the organic compounds, although the meso-$TiO_2$ was calcined at 450 °C already, so using the as-prepared meso-$TiO_2$ directly in the paste could simplify the fabrication process. To further improve the efficiency of solar cells, post treatment is a proven convenient and applicable approach.[74]

## 8.3 Ordered meso-$TiO_2$ thin films by dip coating from aqueous solution

Ordered meso-$TiO_2$ films were made by dip coating from aqueous solution and templated by F127 without a subsequent ageing process. The withdrawal speed of dip coating, amounts of titanium salt in precursor solution, calcination temperature affected the mesostructure. The typical film has a cubic Im3m mesostructure and a meso/macroporous structure that could benefit the efficient transport of guest species to framework binding sites. However, the film has a very rough surface and low thickness ~ 130 nm, which limits their potentials. Before putting the film into application, many modifications on preparation process should be made, such as tuning the viscosity of precursor solution to

obtain thicker film and changing the surface chemistry and the wettability of substrate to prepare smoother film.

## 8.4 Ordered S-Doped meso-$TiO_2$ thin film prepared by dip-coating for photocatalyst

S-doped titania thin films with a cubic Pn3m phase mesostructure were prepared by dip coating via EISA method and templated by P123. By using sulfuric acid as the S source, sulphur was successfully and uniformed doped into titania films at a level of S/Ti atomic ratio 0.19/1. The modification effects on mesostructure, morphology, optical property, hydrophility and photoreactivity of film were studied. The S-$TiO_2$ film has a thickness of 317 nm with a smooth surface and has anatase crystallize ~4.5 nm, mean pores diameter 7.0 nm, specific surface area 190 $m^2/g$ and porosity 78%. The solar photocatalytic activity was measured by degrading methylene blue and the S-doped titania film has an improved efficiency compared to that of the undoped film, because the S-$TiO_2$ film has a better ordered mesostructure, bigger pore size, higher porosity, red-shift of band gap and more hydrophilic surface compared to pure titania film.

So far as we know, this is the first time that S-doped titania thin films with a cubic Pn3m phase mesostructure was successfully made and applied as solar photocatalyst. To further improve the efficiency of photocatalysis, it is worthy to try to improve the crystallization of S-$TiO_2$ film and tune the amount of S-doping. The ordered S-$TiO_2$ film can also be applied into other application of photocatalysis,[133] such as water-splitting, anti-bacteria, and used as the blocking or buffer layer for DSSC.[306, 307]

## 8.5 S-Doped meso-$TiO_2$ films prepared by Dip-coating for DSSC

To obtain better ordered mesostructures, the effects of the “filling pore” process on the mesostructure, morphology, porosity and optical property of films were studied. The degree of long range ordering decreases and surface roughness increases after introduction of the “filling pore” process. So the “filling pore” process does not show a promising result. Thicker film up to 1.6 μm were made by repeated coating and investigated. The film thickness has a linear

relationship with the number of layers in the films and all the films are compressed in the vertical direction. With the increase of film thickness, many properties are changed due to the collapse and re-structuring of pores in repeated calcination: Firstly, the ordering of the mesostructure decreases until being lost for film with greater than 5 layers; Secondly, the film has higher absorbance and a rougher surface, but cracks appear in the 8-layer film; Thirdly, the specific surface area and pore volume decrease, which induces a lower dye loading for the thicker films. When these films were applied in DSSC, the 2-layer film shows the best cell performance due to the higher dye loading compared to the other films, but the conversion efficiency is still not good due to the low dye uptake.

Although the efficiency of DSSC is not good, this is still the first time using S-doped titania thin films for DSSCs. To improve the efficiency, modification of the synthesis parameters are needed to make ordered surfactant-templated multilayer films, such as humidity control, reagents adjustment. Moreover, the multilayer films may be put in other applications, such as photocatalyst or solid state DSSC.[324]

## 8.6 Meso-$TiO_2$ and nanowire composite films self-assembled at air-water interface for DSSC

Free-standing surfactant/polymer templated titania films were successfully made either from a titania precursor or a seed solution. The film made using a titania precursor has an ordered mesostructure, but it is crashed into powder after calcination. However, the film made using a titania seed colloidal retains the macroscopic shape after calcination and a possible mechanism is proposed. The calcined film is composed of titania nanowire/meso-$TiO_2$ composites and the nanoparticle component acts as a binder between nanowires. The film is composed of ~25 wt.% of titania when freshly prepared and has a thickness around 8.2 μm after calcination. Moreover, the calcined film has a high surface area (190 $m^2/g$) with the structure composed of one-dimensional long nanowires (more than 13μm in length and ca. 40nm in diameter) and mesoporous nanoparticle branches (peak pore diameter at 5.28 nm). When the film is used in DSSC, the cell performance is better than the cell prepared using the Degussa

P25 layer or Dyesol film due to higher dye uptake in the FS-$TiO_2$ films and possibly also more rapid electron transfer in the nanowire structures, compared to the nanoparticle films.

This is a novel method to fabricate anatase titania nanowire/nanoparticle films with high surface area and use them in DSSC application. Some further work needs to be carried out. The fact that 1D nanoastructure can increase the electron transport needs to be confirmed by later experiments. The film is still not robust enough which limits many applications. So, modifications are required to obtain stronger films, such as change the synthesis parameters, adding some silicon source in reagents solution to prepare $TiO_2$/$SiO_2$ film, treating the titania hybrid film by exposure to silica precursor vapour to let more inorganic keep in the hybrid film.[326]

## 8.7 ZnO films self-assembled at air-liquid interface

Free-standing surfactant/polymer templated ZnO hybrid films were successfully fabricated and a possible mechanism was proposed. Films are composed of ~15 wt.% of ZnO when freshly prepared. The procedure of decomposition of organics and ZNAC is not fully finished until ~550 ºC. After calcination at 600 ºC, the ZnO has a wurtzite phase with a crystal size of 27.4 nm. The film is composed of rough spheres with uniform size distribution around 100-200 nm. The spheres are composed of assembled elongated ZnO nanoparticles and have a surface area around 20 $m^2$/g, which is much higher than commercial ZnO nanoparticles.

To the best of our knowledge, this is also the first time to prepare free-standing ZnO film. However, due to the limited time, no further work was done on these materials. ZnO aggregated spheres have strong scattering effects, which can be used in DSSC. Before using the free-standing ZnO films into DSSC, adjustments of synthesis parameters to obtain robust ZnO film will be required. Moreover, the free-standing ZnO hybrid film could also have potential for direct use in applications, such as UV emitters and lithium batteries.[254, 255]

## 8.8 Overall summary

Mesoporous metal-oxides with different geometries were successfully made by various synthesis processes:

1. Mesoporous titania powder was made from ethanol/water solvent;
2. Ordered 2D-hexagonal mesoporous titania powder was prepared via EISA method and put into a thick film by doctor-blading;
3. Ordered cubic Im3m mesoporous titania thin film was fabricated by dip coating from aqueous solution;
4. Ordered cubic Pn3m S-doped mesoporous titania film was made via EISA method by dip-coating;
5. Free-standing mesoporous titania nanoparticle and nanowire composite film was fabricated by self-assembled at air-water interface;
6. Free-standing ZnO rough sphere film was prepared by self-assembled at air-water interface.

The nanostructure, morphology, porosity and optical property of meso-$TiO_2$ were investigated to obtain optimized materials. When applying these optimized materials for photocatalysts or DSSCs, some promising results have been obtained due to the excellent properties of these materials, such as high surface area, ordered mesostructure. However, work cannot be perfect and scientists say no ends in science, some further work to extend the projects or optimize the materials would be carried out in future.

# References


1. R. Jose, V. Thavasi and S. Ramakrishna, *J Am Ceram Soc*, 2009, **92**, 289-301.
2. R. Zhang, A. A. Elzatahry, S. S. Al-Deyab and D. Zhao, *Nano Today*, 2012, **7**, 344-366.
3. M. Pagliaro, G. Palmisano, R. Ciriminna and V. Loddo, *Energ Environ Sci*, 2009, **2**, 838-844.
4. X. Chen and S. S. Mao, *Chem Rev*, 2007, **107**, 2891-2959.
5. A. P. Alivisatos, *Science*, 1996, **271**, 933-937.
6. A. Kolmakov and M. Moskovits, *Annu. Rev. Mater. Res.*, 2004, **34**, 151-180.
7. J. G. Lu, P. Chang and Z. Fan, *Mater Sci Eng R*, 2006, **52**, 49-91.
8. G. Ai, W.-T. Sun, Y.-L. Zhang and L.-M. Peng, *Chem Commun*, 2011, **47**, 6608-6610.
9. P. Roy, S. Berger and P. Schmuki, *Angew Chem Int Edit*, 2011, **50**, 2904-2939.
10. U. Ozgur, Y. I. Alivov, C. Liu, A. Teke, M. A. Reshchikov, S. Dogan, V. Avrutin, S. J. Cho and H. Morkoc, *J Appl Phys*, 2005, **98**, 041301-041103.
11. N. V. Golubko, M. I. Yanovskaya, I. P. Romm and A. N. Ozerin, *J Sol-gel Sci Techn*, 2001, **20**, 245-262.
12. B. E. Yoldas, *J Mater Sci*, 1986, **21**, 1087-1092.
13. S. Doeuff, M. Henry, C. Sanchez and J. Livage, *J Non-cryst Solids*, 1987, **89**, 206-216.
14. Y. Sakamoto, M. Kaneda, O. Terasaki, D. Y. Zhao, J. M. Kim, G. Stucky, H. J. Shin and R. Ryoo, *Nature*, 2000, **408**, 449-453.
15. T. Froschl, U. Hormann, P. Kubiak, G. Kucerova, M. Pfanzelt, C. K. Weiss, R. J. Behm, N. Husing, U. Kaiser, K. Landfester and M. Wohlfahrt-Mehrens, *Chem Soc Rev*, 2012, **41**, 5313-5360.
16. V. Meynen, P. Cool and E. F. Vansant, *Micropor Mesopor Mat*, 2009, **125**, 170-223.
17. L. Leibler, H. Orland and J. C. Wheeler, *The Journal of chemical physics*, 1983, **79**, 3550-3558.
18. C. J. Brinker, Y. Lu, A. Sellinger and H. Fan, *Adv Mater*, 1999, **11**, 579-585.
19. P. C. A. Alberius, K. L. Frindell, R. C. Hayward, E. J. Kramer, G. D. Stucky and B. F. Chmelka, *Chem Mater*, 2002, **14**, 3284-3294.
20. D. Chen, L. Cao, F. Huang, P. Imperia, Y.-B. Cheng and R. A. Caruso, *J Am Chem Soc*, 2010, **132**, 4438-4444.
21. A. H. Lu and F. Schüth, *Adv Mater*, 2006, **18**, 1793-1805.
22. F. Schüth, *Chem Mater*, 2001, **13**, 3184-3195.
23. Z. Zhang, F. Zuo and P. Feng, *J Mater Chem*, 2010, **20**, 2206-2212.
24. Y. Xia and R. Mokaya, *J Mater Chem*, 2005, **15**, 3126-3131.
25. M. C. Orilall, N. M. Abrams, J. Lee, F. J. DiSalvo and U. Wiesner, *J Am Chem Soc*, 2008, **130**, 8882-8883.
26. J. Qiu, W. Yu, X. Gao and X. Li, *Nanotechnology*, 2007, **18**, 295604.
27. M. Nedelcu, J. Lee, E. J. Crossland, S. C. Warren, M. C. Orilall, S. Guldin, S. Hüttner, C. Ducati, D. Eder and U. Wiesner, *Soft Matter*, 2009, **5**, 134-139.
28. Y.-G. Guo, Y.-S. Hu and J. Maier, *Chem Commun*, 2006, 2783-2785.
29. J. Lee, M. C. Orilall, S. C. Warren, M. Kamperman, F. J. DiSalvo and U. Wiesner, *Nat Mater*, 2008, **7**, 222-228.

30. K. Wang, M. Wei, M. A. Morris, H. Zhou and J. D. Holmes, *Adv Mater*, 2007, **19**, 3016-3020.
31. Y. Zhou and M. Antonietti, *J Am Chem Soc*, 2003, **125**, 14960-14961.
32. C. Liu, L. Fu and J. Economy, *J Mater Chem*, 2004, **14**, 1187-1189.
33. J. Yu, G. Wang, B. Cheng and M. Zhou, *Appl Catal B: Environ*, 2007, **69**, 171-180.
34. H. Li, Z. Bian, J. Zhu, D. Zhang, G. Li, Y. Huo, H. Li and Y. Lu, *J Am Chem Soc*, 2007, **129**, 8406-8407.
35. B. O'Regan and M. Gratzel, *Nature*, 1991, **353**, 737-740.
36. K. Kalyanasundaram, EPFL Press, Lausanne, 2010.
37. L. Perez-Lombard, J. Ortiz and C. Pout, *Energ Buildings*, 2008, **40**, 394-398.
38. A. Hagfeldt, G. Boschloo, L. C. Sun, L. Kloo and H. Pettersson, *Chem Rev*, 2010, **110**, 6595-6663.
39. D. E. Carlson and C. R. Wronski, *Appl Phys Lett*, 1976, **28**, 671-673.
40. K. L. Chopra, P. D. Paulson and V. Dutta, *Prog Photovoltaics*, 2004, **12**, 69-92.
41. M. A. Green, *Third generation photovoltaics: advanced solar energy conversion*, Springer, 2003.
42. M. GrÄtzel, *Accounts Chem Res*, 2009, **42**, 1788-1798.
43. Z. Ning, Y. Fu and H. Tian, *Energ Environ Sci*, 2010, **3**, 1170-1181.
44. R. Faccio, L. Fernandez-Werner, H. Pardo and A. W. Mombru, *Recent Pat. Nanotechnology*, 2011, **5**, 46-61.
45. S. Ito, T. Murakami, P. Comte, P. Liska, C. Grätzel, M. Nazeeruddin and M. Grätzel, *Thin Solid Films*, 2008, **516**, 4613-4619.
46. A. Burke, S. Ito, H. Snaith, U. Bach, J. Kwiatkowski and M. Gratzel, *Nano Lett*, 2008, **8**, 977-981.
47. Q. F. Zhang and G. Z. Cao, *Nano Today*, 2011, **6**, 91-109.
48. M. Law, L. E. Greene, J. C. Johnson, R. Saykally and P. D. Yang, *Nat Mater*, 2005, **4**, 455-459.
49. A. B. F. Martinson, J. W. Elam, J. T. Hupp and M. J. Pellin, *Nano Lett*, 2007, **7**, 2183-2187.
50. L. M. Fraas and L. D. Partain, *Solar cells and their applications*, Wiley. com, 2010.
51. N. Robertson, *Angew Chem Int Edit*, 2006, **45**, 2338-2345.
52. K. Hara, T. Sato, R. Katoh, A. Furube, Y. Ohga, A. Shinpo, S. Suga, K. Sayama, H. Sugihara and H. Arakawa, *J Phys Chem B*, 2003, **107**, 597-606.
53. K. Hara, M. Kurashige, S. Ito, A. Shinpo, S. Suga, K. Sayama and H. Arakawa, *Chem Commun*, 2003, 252-253.
54. T. W. Hamann, R. A. Jensen, A. B. F. Martinson, H. Van Ryswyk and J. T. Hupp, *Energ Environ Sci*, 2008, **1**, 66-78.
55. Z.-S. Wang, K. Sayama and H. Sugihara, *J Phys Chem B*, 2005, **109**, 22449-22455.
56. H. Nusbaumer, J. E. Moser, S. M. Zakeeruddin, M. K. Nazeeruddin and M. Gratzel, *J Phys Chem B*, 2001, **105**, 10461-10464.
57. S. Cazzanti, S. Caramori, R. Argazzi, C. M. Elliott and C. A. Bignozzi, *J Am Chem Soc*, 2006, **128**, 9996-9997.
58. Y. Tian and T. Tatsuma, *J Am Chem Soc*, 2005, **127**, 7632-7637.
59. T. Nakanishi, B. Ohtani and K. Uosaki, *J Electroanal Chem*, 1998, **455**, 229-234.
60. G. Oskam, B. V. Bergeron, G. J. Meyer and P. C. Searson, *J Phys Chem B*, 2001, **105**, 6867-6873.

61. K. Imoto, K. Takahashi, T. Yamaguchi, T. Komura, J.-i. Nakamura and K. Murata, *Sol Energ Mat Sol C*, 2003, **79**, 459-469.
62. T. N. Murakami, S. Ito, Q. Wang, M. K. Nazeeruddin, T. Bessho, I. Cesar, P. Liska, R. Humphry-Baker, P. Comte, P. Pechy and M. Gratzel, *J Electrochem Soc*, 2006, **153**, A2255-A2261.
63. A. Kongkanand, R. M. Dominguez and P. V. Kamat, *Nano Lett*, 2007, **7**, 676-680.
64. K. Suzuki, M. Yamaguchi, M. Kumagai and S. Yanagida, *Chem Lett*, 2003, **32**, 28-29.
65. Y. Saito, W. Kubo, T. Kitamura, Y. Wada and S. Yanagida, *J Photochem Photobiol A Chem*, 2004, **164**, 153-157.
66. Q. H. Li, J. H. Wu, Q. W. Tang, Z. Lan, P. J. Li, J. M. Lin and L. Q. Fan, *Electrochem Commun*, 2008, **10**, 1299-1302.
67. W. J. Hong, Y. X. Xu, G. W. Lu, C. Li and G. Q. Shi, *Electrochem Commun*, 2008, **10**, 1555-1558.
68. H. Ago, K. Petritsch, M. S. P. Shaffer, A. H. Windle and R. H. Friend, *Adv Mater*, 1999, **11**, 1281-1285.
69. K. Bouzek, K. M. Mangold and K. Juttner, *Electrochim Acta*, 2000, **46**, 661-670.
70. K. Kitamura and S. Shiratori, *Nanotechnology*, 2011, **22**, 195703.
71. Q. D. Tai, B. L. Chen, F. Guo, S. Xu, H. Hu, B. Sebo and X. Z. Zhao, *ACS Nano*, 2011, **5**, 3795-3799.
72. L. Kavan, J. H. Yum and M. Gratzel, *ACS Nano*, 2011, **5**, 165-172.
73. M. K. Nazeeruddin, A. Kay, I. Rodicio, R. Humphry-Baker, E. Mueller, P. Liska, N. Vlachopoulos and M. Graetzel, *J Am Chem Soc*, 1993, **115**, 6382-6390.
74. S. A. Boden and D. M. Bagnall, IEEE, 2006, pp. 1358-1361.
75. S. Chattopadhyay, Y. Huang, Y. Jen, A. Ganguly, K. Chen and L. Chen, *Mater Sci Eng R*, 2010, **69**, 1-35.
76. K. Forberich, G. Dennler, M. C. Scharber, K. Hingerl, T. Fromherz and C. J. Brabec, *Thin Solid Films*, 2008, **516**, 7167-7170.
77. F. T. Li, L. G. Wang, S. S. Fu, Z. Y. Huo and Y. Z. Gu, *J. Chin. Chem. Soc*, 2011, **58**, 408-411.
78. G. Rothenberger, P. Comte and M. Grätzel, *Sol Energ Mat Sol C*, 1999, **58**, 321-336.
79. M. K. Nazeeruddin, F. De Angelis, S. Fantacci, A. Selloni, G. Viscardi, P. Liska, S. Ito, B. Takeru and M. Grätzel, *J Am Chem Soc*, 2005, **127**, 16835-16847.
80. H.-J. Koo, J. Park, B. Yoo, K. Yoo, K. Kim and N.-G. Park, *Inorg Chim Acta*, 2008, **361**, 677-683.
81. Z.-S. Wang, H. Kawauchi, T. Kashima and H. Arakawa, *Coordin Chem Rev*, 2004, **248**, 1381-1389.
82. H. Zhang, Y. Han, X. Liu, P. Liu, H. Yu, S. Zhang, X. Yao and H. Zhao, *Chem Commun*, 2010, **46**, 8395-8397.
83. C. J. Barbé, F. Arendse, P. Comte, M. Jirousek, F. Lenzmann, V. Shklover and M. Grätzel, *J Am Ceram Soc*, 1997, **80**, 3157-3171.
84. T. Le Bahers, F. Labat, T. Pauporte, P. P. Laine and I. Ciofini, *J Am Chem Soc*, 2011, **133**, 8005-8013.
85. A. J. Frank, N. Kopidakis and J. van de Lagemaat, *Coordin Chem Rev*, 2004, **248**, 1165-1179.
86. X. Chen and S. Mao, *Chem. Rev*, 2007, **107**, 2891-2959.
87. L. Malfatti, P. Falcaro, H. Amenitsch, S. Caramori, R. Argazzi, C. A. Bignozzi, S. Enzo, M. Maggini and P. Innocenzi, *Micropor Mesopor Mat*, 2006, **88**, 304-311.

88. Y. Xia, P. Yang, Y. Sun, Y. Wu, B. Mayers, B. Gates, Y. Yin, F. Kim and H. Yan, *Adv Mater*, 2003, **15**, 353-389.
89. A. R. Uhl, Y. E. Romanyuk and A. N. Tiwari, *Thin Solid Films*, 2011, **519**, 7259-7263.
90. P. Péchy, T. Renouard, S. M. Zakeeruddin, R. Humphry-Baker, P. Comte, P. Liska, L. Cevey, E. Costa, V. Shklover, L. Spiccia, G. B. Deacon, C. A. Bignozzi and M. Grätzel, *J Am Chem Soc*, 2001, **123**, 1613-1624.
91. D. S. Tsoukleris, I. M. Arabatzis, E. Chatzivasiloglou, A. I. Kontos, V. Belessi, M. C. Bernard and P. Falaras, *Sol Energy*, 2005, **79**, 422-430.
92. S. K. Dhungel and J. G. Park, *Renew Energ*, 2010, **35**, 2776-2780.
93. J.-K. Lee, B.-H. Jeong, S.-i. Jang, Y.-G. Kim, Y.-W. Jang, S.-B. Lee and M.-R. Kim, *J Ind Eng Chem*, 2009, **15**, 724-729.
94. K. H. Ko, Y. C. Lee and Y. J. Jung, *J Colloid Interf Sci*, 2005, **283**, 482-487.
95. W. Guo, L. Q. Wu, Z. Chen, G. Boschloo, A. Hagfeldt and T. L. Ma, *J Photochem Photobiol A Chem*, 2011, **219**, 180-187.
96. S. R. Gajjela, K. Ananthanarayanan, C. Yap, M. Gratzel and P. Balaya, *Energ Environ Sci*, 2010, **3**, 838-845.
97. J. Zhang, Y. Deng, D. Gu, S. Wang, L. She, R. Che, Z.-S. Wang, B. Tu, S. Xie and D. Zhao, *Adv Energy Mater*, 2011, **1**, 241-248.
98. S. Agarwala, M. Kevin, A. S. W. Wong, C. K. N. Peh, V. Thavasi and G. W. Ho, *ACS Appl Mater Inter*, 2010, **2**, 1844-1850.
99. T. K. Yun, S. S. Park, D. Kim, Y.-K. Hwang, S. Huh, J. Y. Bae and Y. S. Won, *J Power Sources*, 2011, **196**, 3678-3682.
100. J.-Y. Liao, B.-X. Lei, D.-B. Kuang and C.-Y. Su, *Energ Environ Sci*, 2011, **4**, 4079-4085.
101. S. R. Gajjela, C. Yap and P. Balaya, *J Mater Chem*, 2012, **22**, 10873-10882.
102. F. Huang, D. Chen, X. L. Zhang, R. A. Caruso and Y.-B. Cheng, *Adv Fun Mater*, 2010, **20**, 1301-1305.
103. J. Jiu, S. Isoda, F. Wang and M. Adachi, *J Phys Chem B*, 2006, **110**, 2087-2092.
104. B. Smarsly, D. Grosso, T. Brezesinski, N. Pinna, C. Boissière, M. Antonietti and C. Sanchez, *Chem. Mater*, 2004, **16**, 2948-2952.
105. M. Zukalová, J. Procházka, A. Zukal, J. H. Yum and L. Kavan, *Inorg Chim Acta*, 2008, **361**, 656-662.
106. J. Dewalque, R. Cloots, F. Mathis, O. Dubreuil, N. Krins and C. Henrist, *J Mater Chem*, 2011, **21**, 7356-7363.
107. M. Zukalova, J. Prochazka, A. Zukal, J. H. Yum, L. Kavan and M. Graetzel, *Journal of The Electrochemical Society*, 2010, **157**, H99-H103.
108. M. Zukalová, A. Zukal, L. Kavan, M. K. Nazeeruddin, P. Liska and M. Grätzel, *Nano Lett*, 2005, **5**, 1789-1792.
109. B. Chi, L. Zhao, J. Li, J. Pu, Y. Chen, C. C. Wu and T. Jin, *J Nanosci Nanotechnol*, 2008, **8**, 3877-3882.
110. Y. Zhang, Z. Xie and J. Wang, *Nanotechnology*, 2009, **20**, 505602.
111. K. Zhu, N. R. Neale, A. Miedaner and A. J. Frank, *Nano Lett.*, 2007, **7**, 69-74.
112. T.-S. Kang, A. P. Smith, B. E. Taylor and M. F. Durstock, *Nano Lett*, 2009, **9**, 601-606.
113. X. Feng, K. Shankar, O. K. Varghese, M. Paulose, T. J. Latempa and C. A. Grimes, *Nano Lett*, 2008, **8**, 3781-3786.
114. B. Liu and E. S. Aydil, *J Am Chem Soc*, 2009, **131**, 3985-3990.
115. M. A. Fox and M. T. Dulay, *Chem Rev*, 1993, **93**, 341-357.

116. M. R. Hoffmann, S. T. Martin, W. Choi and D. W. Bahnemann, *Chem Rev*, 1995, **95**, 69-96.
117. M. Umar and H. A. Aziz, *Photocatalytic Degradation of Organic Pollutants in Water*, 2013.
118. J.-M. Herrmann, *Catal Today*, 1999, **53**, 115-129.
119. U. G. Akpan and B. H. Hameed, *J Hazard Mater*, 2009, **170**, 520-529.
120. A. Mills and S. Le Hunte, *J photoch Photobio A*, 1997, **108**, 1-35.
121. N. Xu, Z. Shi, Y. Fan, J. Dong, J. Shi and M. Z. C. Hu, *Ind Eng Chem Res*, 1999, **38**, 373-379.
122. C.-C. Wang, Z. Zhang and J. Y. Ying, *Nanostruct Mater*, 1997, **9**, 583-586.
123. T. Peng, D. Zhao, K. Dai, W. Shi and K. Hirao, *J Phys Chem B*, 2005, **109**, 4947-4952.
124. W. Zhou, F. Sun, K. Pan, G. Tian, B. Jiang, Z. Ren, C. Tian and H. Fu, *Adv Fun Mater*, 2011, **21**, 1922-1930.
125. J. G. Yu, Y. R. Su and B. Cheng, *Adv Fun Mater*, 2007, **17**, 1984-1990.
126. X. Wang, J. C. Yu, C. Ho, Y. Hou and X. Fu, *Langmuir*, 2005, **21**, 2552-2559.
127. J. Joo, S. G. Kwon, T. Yu, M. Cho, J. Lee, J. Yoon and T. Hyeon, *J Phys Chem B*, 2005, **109**, 15297-15302.
128. N. Wu, J. Wang, D. N. Tafen, H. Wang, J.-G. Zheng, J. P. Lewis, X. Liu, S. S. Leonard and A. Manivannan, *J Am Chem Soc*, 2010, **132**, 6679-6685.
129. S. Y. Chae, M. K. Park, S. K. Lee, T. Y. Kim, S. K. Kim and W. I. Lee, *Chem Mater*, 2003, **15**, 3326-3331.
130. Y. Sakatani, D. Grosso, L. Nicole, C. Boissiere, G. J. de A. A. Soler-Illia and C. Sanchez, *J Mater Chem*, 2006, **16**, 77-82.
131. Z. Liu, X. Zhang, S. Nishimoto, M. Jin, D. A. Tryk, T. Murakami and A. Fujishima, *J Phys Chem C*, 2007, **112**, 253-259.
132. R. Abe, *J photoch Photobio B*, 2010, **11**, 179-209.
133. M. Anpo and M. Takeuchi, *J Catal*, 2003, **216**, 505-516.
134. A. Zaleska, *Recent Patents on Engineering*, 2008, **2**, 157-164.
135. D. Chatterjee and S. Dasgupta, *J photoch Photobio B*, 2005, **6**, 186-205.
136. D. Dvoranova, V. Brezova, M. Mazúr and M. A. Malati, *Appl Catal B: Environ*, 2002, **37**, 91-105.
137. S. Klosek and D. Raftery, *J Phys Chem B*, 2001, **105**, 2815-2819.
138. J. Yu, Q. Xiang and M. Zhou, *Appl Catal B: Environ*, 2009, **90**, 595-602.
139. J. C. Yu, G. Li, X. Wang, X. Hu, C. W. Leung and Z. Zhang, *Chem Commun*, 2006, **0**, 2717-2719.
140. V. Puddu, R. Mokaya and G. Li Puma, *Chem Commun*, 2007, **0**, 4749-4751.
141. S. In, A. Orlov, R. Berg, F. García, S. Pedrosa-Jimenez, M. S. Tikhov, D. S. Wright and R. M. Lambert, *J Am Chem Soc*, 2007, **129**, 13790-13791.
142. Y. Choi, T. Umebayashi and M. Yoshikawa, *J Mater Sci*, 2004, **39**, 1837-1839.
143. R. Asahi, T. Morikawa, T. Ohwaki, K. Aoki and Y. Taga, *Science*, 2001, **293**, 269-271.
144. Q. Zhang, J. Wang, S. Yin, T. Sato and F. Saito, *J Am Ceram Soc*, 2004, **87**, 1161-1163.
145. J. C. Yu, J. Yu, W. Ho, Z. Jiang and L. Zhang, *Chem Mater*, 2002, **14**, 3808-3816.
146. R. Long and N. J. English, *J Phys Chem C*, 2010, **114**, 11984-11990.
147. X. Hong, Z. Wang, W. Cai, F. Lu, J. Zhang, Y. Yang, N. Ma and Y. Liu, *Chem Mater*, 2005, **17**, 1548-1552.

148. D. Li, H. Haneda, N. K. Labhsetwar, S. Hishita and N. Ohashi, *Chem Phys Lett*, 2005, **401**, 579-584.
149. W. Zhongbiao, D. Fan, Z. Weirong, W. Haiqiang, L. Yue and G. Baohong, *Nanotechnology*, 2009, **20**, 235701.
150. K. J. Edler and S. J. Roser, *Int Rev Phys Chem*, 2001, **20**, 387-466.
151. B. Yang, K. Edler, C. Guo and H. Z. Liu, *Micropor Mesopor Mat*, 2010, **131**, 21-27.
152. H. Tian, L. Hu, C. Zhang, W. Liu, Y. Huang, L. Mo, L. Guo, J. Sheng and S. Dai, *J Phys Chem C*, 2010, **114**, 1627-1632.
153. K. J. Edler and B. Yang, *Chem. Soc. Rev.*, 2013, **42**, 3765-3776.
154. M. J. Henderson, D. King and J. W. White, *Langmuir*, 2004, **20**, 2305-2308.
155. C. Kan, X. Liu, G. Duan, X. Wang, X. Yang and L. Lu, *J. Colloid Interface Sci.*, 2007, **310**, 643-647.
156. H. Ji, X. Liu, X. Wang, L. Lu and X. Yang, *Colloid Surf. A*, 2011, **392**, 242-249.
157. H. Ji, X. Liu, X. Wang and X. Yao, *Rare Metals*, 2011, **30**, 225-228.
158. N. Kasai and M. Kakudo, *X-ray diffraction by macromolecules*, Kodansha, 2005.
159. M. Brune, F. Schmidt-Kaler, A. Maali, J. Dreyer, E. Hagley, J. Raimond and S. Haroche, *Phys Rev Lett*, 1996, **76**, 1800-1803.
160. C. Suryanarayana and M. G. Norton, *Microsc Microanal*, 1998, **4**, 513-515.
161. P. Beckmann and A. Spizzichino, *Norwood, MA, Artech House, Inc., 1987, 511 p.*, 1987, **1**.
162. J. Lu, E. Lee and R. Thomas, *Acta Crystallogr A*, 1996, **52**, 11-41.
163. I. K. Robinson, in *Characterization of Materials*, John Wiley & Sons, Inc., 2002.
164. J. Penfold and R. Thomas, *J Phys Condens Matter*, 1999, **2**, 1369-1412.
165. S. Park, D. H. Lee, J. Xu, B. Kim, S. W. Hong, U. Jeong, T. Xu and T. P. Russell, *Science*, 2009, **323**, 1030-1033.
166. K. Vegso, P. Siffalovic, M. Benkovicova, M. Jergel, S. Luby, E. Majkova, I. Capek, T. Kocsis, J. Perlich and S. V. Roth, *Nanotechnology*, 2012, **23**, 045704.
167. N. Krins, J. D. Bass, B. Julian-Lopez, P. Evrar, C. Boissiere, L. Nicole, C. Sanchez, H. Amenitsch and D. Grosso, *J Mater Chem*, 2011, **21**, 1139-1146.
168. Beamline I22 instrument specifications, http://www.diamond.ac.uk/Home/Beamlines/I22/status.html,.
169. T. C. Huang, H. Toraya, T. N. Blanton and Y. Wu, *J Appl Crystallogr*, 1993, **26**, 180-184.
170. D. S. Sivia, ed., *Elementary Scattering Theory*, Oxford University Press, 2011.
171. G. E. Bacon, *Experimental Magnetism*, 1979, **1**, 1-68.
172. A. Nelson, *J Appl Crystallogr*, 2006, **39**, 273-276.
173. J. R. P. Webster, Introduction to neutron reflectivity.
174. S. Huard, *Polarization of Light, by Serge Huard, pp. 348. ISBN 0-471-96536-7. Wiley-VCH, January 1997.*, 1997, **1**.
175. H. Tompkins and E. A. Irene, *Handbook of ellipsometry*, William Andrew, 2005.
176. H. Fujiwara, *Spectroscopic ellipsometry: principles and applications*, John Wiley & Sons, 2007.
177. D. Aspnes, *Handbook of Optical Constants of Solids*, 1985, **1**, 89.
178. D. Aspnes, J. Theeten and F. Hottier, *Phys Rev B*, 1979, **20**, 3292-3302.
179. P. Hauge, *Surf Sci*, 1980, **96**, 108-140.
180. K. Liu, W. Zhou, K. Shi, L. Li, L. Zhang, M. Zhang and H. Fu, *Nanotechnology*, 2006, **17**, 1363.
181. B. J. Berne and R. Pecora, *Dynamic light scattering: with applications to chemistry, biology, and physics*, Courier Dover Publications, 1976.

182. K. S. Schmitz, 1990.
183. B. Nail, Dynamic Light Scattering, http://chemwiki.ucdavis.edu/Analytical_Chemistry/Instrumental_Analysis/Microscopy/Dynamic_Light_Scattering.
184. J. H. Roe, J. H. Epstein and N. P. Goldstein, *J Biol Chem*, 1949, **178**, 839-845.
185. R. F. Egerton, *Electron energy-loss spectroscopy in the electron microscope*, Springer, 2011.
186. T. F. Anderson, *Transactions of the New York Academy of Sciences*, 2012, **13**, 130-134.
187. P. Buseck, J. Cowley and L. R. Eyring, *High-Resolution Transmission Electron Microscopy: And Associated Techniques*, Oxford University Press, USA, 1989.
188. L. Reimer and H. Kohl, *Transmission electron microscopy: physics of image formation*, Springer, 2008.
189. J. W. Edington, *Practical electron microscopy in materials science*, Van Nostrand Reinhold Company, 1976.
190. D. C. Joy and A. D. Romig Jr, *Principles of analytical electron microscopy*, Plenum Publishing Corporation, 1986.
191. J. Goldstein, D. E. Newbury, D. C. Joy, C. E. Lyman, P. Echlin, E. Lifshin, L. Sawyer and J. R. Michael, *Scanning electron microscopy and X-ray microanalysis*, Springer, 2003.
192. D. B. Williams and C. B. Carter, *The Transmission Electron Microscope*, Springer, 1996.
193. G. Binnig, C. F. Quate and C. Gerber, *Phys Rev Lett*, 1986, **56**, 930-933.
194. E. Meyer, *Prog Surf Sci*, 1992, **41**, 3-49.
195. M. Radmacher, R. Tillamnn, M. Fritz and H. Gaub, *Science*, 1992, **257**, 1900-1905.
196. D. Rugar and P. Hansma, *Phys Today*, 1990, **43**, 23-30.
197. B. Lippens, B. Linsen and J. H. Boer, *J Catal*, 1964, **3**, 32-37.
198. S. J. Gregg and K. S. W. Sing, eds., *Adsorption, Surface Area and Porosity*, ACADEMIC PRESS, 1982.
199. T. Leppäjärvi, I. Malinen, J. Kangas and J. Tanskanen, *Chem Eng Sci*, 2012, **69**, 503-513.
200. P. T. M. Nguyen, D. D. Do and D. Nicholson, *J Phys Chem C*, 2011, **115**, 4706-4720.
201. D. PERRIN, B. GILBERT, W. PURDY and R. NEEB, 1983.
202. D. Chen, F. Huang, Y.-B. Cheng and R. A. Caruso, *Adv Mater*, 2009, **21**, 2206-2210.
203. M. J. Abdelhamid Sayari, Thomas J. Pinnavaia, ed., *Nanoporous materials II* elsevier, 2000.
204. G. Jiang, Z. Lin, C. Chen, L. Zhu, Q. Chang, N. Wang, W. Wei and H. Tang, *Carbon*, 2011, **49**, 2693-2701.
205. T. Tsoufis, G. Tuci, S. Caporali, D. Gournis and G. Giambastiani, *Carbon*, 2013, **59**, 100-108.
206. X. Zhang, J. Liu, B. Xu, Y. Su and Y. Luo, *Carbon*, 2011, **49**, 1884-1893.
207. J. Ju, X. Chen, Y. Shi and D. Wu, *Fuel*, 2013, **108**, 850-854.
208. J. Zheng, Y. Yi, W. Wang, K. Guo, J. Ma and R. Li, *Micropor Mesopor Mat*, 2013, **171**, 44-52.
209. J. C. Groen, L. A. A. Peffer, J. A. Moulijn, R. Pérez, amp, x and J. rez, *Micropor Mesopor Mat*, 2004, **69**, 29-34.

210. G. Leofanti, M. Padovan, G. Tozzola and B. Venturelli, *Catal Today*, 1998, **41**, 207-219.
211. K. S. W. S. Ferdi Schuth, and Jens Weitkamp, ed., *Handbook of porous solids*, WILEY-VCH Verlag GmbH, 2002.
212. I. Langmuir, *J Am Chem Soc*, 1918, **40**, 1361-1403.
213. E. Shkol'nikov and E. Sidorova, *Doklady Physical Chemistry*, 2007, **412**, 4-7.
214. J. E. S. S. Lowell, Martin A. Thomas and Matthias Thommes, ed., *Characterization of porous solids and powders:surface area, pore size and density*, Kluwer Academic Publishers, 2004.
215. S. Lowell and J. E. Shields, *Powder surface area and porosity*, Chapman & Hall, 1991.
216. C. Duval, ed., *Inorganic thermogravimetric analysis*, 1963.
217. G. Höhne, W. F. Hemminger and H.-J. Flammersheim, *Differential scanning calorimetry*, Springer, 2003.
218. M. A. Green, *Englewood Cliffs, NJ, Prentice-Hall, Inc., 1982. 288 p.*, 1982, **1**.
219. M. Grätzel, *J photoch Photobio B*, 2003, **4**, 145-153.
220. J. Nelson, *The physics of solar cells*, World Scientific, 2003.
221. M. Bachman, *INRF application note Engineering of Microworld at the University of California. Irvine*, 1999.
222. E. Crepaldi, G. de AA Soler-Illia, D. Grosso, F. Cagnol, F. Ribot and C. Sanchez, *J. Am. Chem. Soc*, 2003, **125**, 9770-9786.
223. S. S. Soni, G. Brotons, M. Bellour, T. Narayanan and A. Gibaud, *J Phys Chem B*, 2006, **110**, 15157-15165.
224. C. Sanchez, C. Boissière, D. Grosso, C. Laberty and L. Nicole, *Chem Mater*, 2008, **20**, 682-737.
225. Y.-F. Lee, K.-H. Chang, C.-C. Hu and K.-M. Lin, *J Mater Chem*, 2010, **20**, 5682-5688.
226. A. Patterson, *Phys Rev*, 1939, **56**, 978-982.
227. J. C. Yu, X. Wang and X. Fu, *Chem Mater*, 2004, **16**, 1523-1530.
228. K. Liu, M. Zhang, K. Shi and H. Fu, *Mater Lett*, 2005, **59**, 3308-3310.
229. T. Horikawa, D. D. Do and D. Nicholson, *Adv Colloid Interfac*, 2011, **169**, 40-58.
230. J. Liu, T. An, G. Li, N. Bao, G. Sheng and J. Fu, *Micropor Mesopor Mat*, 2009, **124**, 197-203.
231. K. Liu, H. Fu, K. Shi, F. Xiao, L. Jing and B. Xin, *J Phys Chem B*, 2005, **109**, 18719-18722.
232. N. Krins, M. Faustini, B. Louis and D. Grosso, *Chem Mater*, 2010, **22**, 6218-6220.
233. L. Zhao, Y. Yu, L. Song, M. Ruan, X. Hu and A. Larbot, *Appl Catal A: Gen*, 2004, **263**, 171-177.
234. S.-B. Jung, T.-J. Ha, J.-B. Seon and H.-H. Park, *Micropor Mesopor Mat*, 2008, **111**, 188-193.
235. T. P. Chou, Q. Zhang, G. E. Fryxell and G. Z. Cao, *Adv Mater*, 2007, **19**, 2588-2592.
236. P. Carcia, R. McLean, M. Reilly and G. Nunes, *Appl Phys Lett*, 2003, **82**, 1117-1119.
237. Z. Fang, Y. Wang, X. Peng, X. Liu and C. Zhen, *Mater Lett*, 2003, **57**, 4187-4190.
238. B. Yang and K. J. Edler, *Chem Mater*, 2009, **21**, 1221-1231.
239. B. M. D. O'Driscoll, E. Milsom, C. Fernandez-Martin, L. White, S. J. Roser and K. J. Edler, *Macromolecules*, 2005, **38**, 8785-8794.

240. S. Chakraborti, P. Joshi, D. Chakravarty, V. Shanker, Z. A. Ansari, S. P. Singh and P. Chakrabarti, *Langmuir*, 2012, **28**, 11142-11152.
241. E. A. Meulenkamp, *J Phys Chem B*, 1998, **102**, 5566-5572.
242. A. Sinhamahapatra, A. K. Giri, P. Pal, S. K. Pahari, H. C. Bajaj and A. B. Panda, *J Mater Chem*, 2012, **22**, 17227-17235.
243. K. Kaneko, *J Membrane Sci*, 1994, **96**, 59-89.
244. L. Xu, Z. Li, Q. Cai, H. Wang, H. Gao, W. Lv and J. Liu, *CrystEngComm*, 2010, **12**, 2166-2172.
245. C. Chen, P. Liu and C. Lu, *Chem Eng J*, 2008, **144**, 509-513.
246. K. C. Barick, M. Aslam, V. P. Dravid and D. Bahadur, *J Phys Chem C*, 2008, **112**, 15163-15170.
247. M. J. Wasbrough, K. J. Edler, A. M. Hawley, J. A. Holdaway and G. J. Price, *Soft Matter*, 2013, **8**, 3357-3362.
248. M. S. Mohajerani, A. Lak and A. Simchi, *J Alloy Compd*, 2009, **485**, 616-620.
249. C. He, T. Sasaki, Y. Shimizu and N. Koshizaki, *Appl Surf Sci*, 2008, **254**, 2196-2202.
250. B. Liu and H. C. Zeng, *J Am Chem Soc*, 2003, **125**, 4430-4431.
251. Z. Li, Y. Xiong and Y. Xie, *Inorg Chem*, 2003, **42**, 8105-8109.
252. B. M. D. O'Driscoll, E. A. Nickels and K. J. Edler, *Chem. Commun.*, 2007, 1068-1070.
253. Q. Zhang, T. P. Chou, B. Russo, S. A. Jenekhe and G. Cao, *Angewandte Chemie*, 2008, **120**, 2436-2440.
254. H.-M. Xiong, X. Zhao and J.-S. Chen, *J Phys Chem B*, 2001, **105**, 10169-10174.
255. A. A. ElBellihi, W. A. Bayoumy, E. M. Masoud and M. A. Mousa, *B Kor Chem Soc*, 2012, **33**, 2949-2954.
256. M. Wei, Y. Konishi, H. Zhou, M. Yanagida, H. Sugihara and H. Arakawa, *J Mater Chem*, 2006, **16**, 1287-1293.
257. F. Sauvage, D. Chen, P. Comte, F. Huang, L.-P. Heiniger, Y.-B. Cheng, R. A. Caruso and M. Graetzel, *ACS Nano*, 2010, **4**, 4420-4425.
258. W.-Y. Cheng, J. R. Deka, Y.-C. Chiang, A. Rogeau and S.-Y. Lu, *Chem Mater*, 2012, **24**, 3255-3262.
259. Z. Gao, Z. Wu, X. Li, J. Chang, D. Wu, P. Ma, F. Xu, S. Gao and K. Jiang, *CrystEngComm*, 2013, **15**, 3351-3358.
260. S.-H. Han, S. Lee, H. Shin and H. Suk Jung, *Adv Energy Mater*, 2011, **1**, 546-550.
261. Y. J. Kim, M. H. Lee, H. J. Kim, G. Lim, Y. S. Choi, N.-G. Park, K. Kim and W. I. Lee, *Adv Mater*, 2009, **21**, 3668-3673.
262. B. Smarsly, D. Grosso, T. Brezesinski, N. Pinna, C. Boissière, M. Antonietti and C. Sanchez, *Chem Mater*, 2004, **16**, 2948-2952.
263. K. Narayan, M. T. Anderson and C. J. Brinker, *Chem Mater*, 1996, **8**, 1682-1701.
264. S. Y. Choi, M. Mamak, N. Coombs, N. Chopra and G. A. Ozin, *Adv Fun Mater*, 2004, **14**, 335-344.
265. S. Mohd Ibrahim, A. Masrom, B. Mazinani, S. Radiman, F. Md Jamil, A. Beitollahi, N. Negishi and N. Yahya, *Res Chem Intermediat*, 2013, **39**, 1003-1014.
266. S. Guldin, S. Huttner, P. Tiwana, M. C. Orilall, B. Ulgut, M. Stefik, P. Docampo, M. Kolle, G. Divitini, C. Ducati, S. A. T. Redfern, H. J. Snaith, U. Wiesner, D. Eder and U. Steiner, *Energ Environ Sci*, 2011, **4**, 225-233.
267. H. Zhou, C. Wang, Z. Feng, S. Li and B. Xu, *Surf Coat Tech*, 2012, **207**, 34-41.

268. J. Lee, M. Orilall, S. Warren, M. Kamperman, F. DiSalvo and U. Wiesner, *Nature Materials*, 2008, **7**, 222-228.
269. M. Zhou, J. Yu, S. Liu, P. Zhai and L. Jiang, *J Hazard Mater*, 2008, **154**, 1141-1148.
270. E. P. Barrett, L. G. Joyner and P. P. Halenda, *J Am Chem Soc*, 1951, **73**, 373-380.
271. X.-D. Gao, X.-M. Li, X.-Y. Gan, Y.-Q. Wu, R.-K. Zheng, C.-L. Wang, Z.-Y. Gu and P. He, *J Mater Chem*, 2012, **22**, 18930-18938.
272. E. Hosono, S. Fujihara, I. Honma and H. Zhou, *Adv Mater*, 2005, **17**, 2091-2094.
273. I. G. Yu, Y. J. Kim, H. J. Kim, C. Lee and W. I. Lee, *J Mater Chem*, 2010, **21**, 532-538.
274. W.-Q. Wu, B.-X. Lei, H.-S. Rao, Y.-F. Xu, Y.-F. Wang, C.-Y. Su and D.-B. Kuang, *Sci Rep*, 2013, **3**, 1352.
275. J. van de Lagemaat, K. D. Benkstein and A. J. Frank, *J Phys Chem B*, 2001, **105**, 12433-12436.
276. J. C. Yu, W. Ho, J. Yu, H. Yip, P. K. Wong and J. Zhao, *Environ Sci Technol*, 2005, **39**, 1175-1179.
277. A. Schleife, P. Rinke, F. Bechstedt and C. G. Van de Walle, *J Phys Chem C*, 2013, **117**, 4189-4193.
278. Y. W. Sakai, K. Obata, K. Hashimoto and H. Irie, *Vacuum*, 2008, **83**, 683-687.
279. P. Periyat, S. C. Pillai, D. E. McCormack, J. Colreavy and S. J. Hinder, *The Journal of Physical Chemistry C*, 2008, **112**, 7644-7652.
280. N. Umezawa, A. Janotti, P. Rinke, T. Chikyow and C. G. Van de Walle, *Appl Phys Lett*, 2008, **92**, 041104.
281. H. Li, X. Zhang, Y. Huo and J. Zhu, *Environ Sci Technol*, 2007, **41**, 4410-4414.
282. V. Pore, M. Ritala, M. Leskela, S. Areva, M. Jarn and J. Jarnstrom, *J Mater Chem*, 2007, **17**, 1361-1371.
283. C. W. Dunnill, Z. A. Aiken, A. Kafizas, J. Pratten, M. Wilson, D. J. Morgan and I. P. Parkin, *J Mater Chem*, 2009, **19**, 8747-8754.
284. J. Tang, Y. Wu, E. W. McFarland and G. D. Stucky, *Chemical communications*, 2004, 1670-1671.
285. Z. Bian, J. Zhu, S. Wang, Y. Cao, X. Qian and H. Li, *J Phys Chem C*, 2008, **112**, 6258-6262.
286. J. H. Pan and W. I. Lee, *Chem Mater*, 2006, **18**, 847-853.
287. M. A. Carreon, S. Y. Choi, M. Mamak, N. Chopra and G. A. Ozin, *J Mater Chem*, 2007, **17**, 82-89.
288. D. Grosso, G. de AA Soler-Illia, E. Crepaldi, F. Cagnol, C. Sinturel, A. Bourgeois, A. Brunet-Bruneau, H. Amenitsch, P. Albouy and C. Sanchez, *Chem. Mater*, 2003, **15**, 4562-4570.
289. K. Wang, M. Morris and J. Holmes, *Chem. Mater*, 2005, **17**, 1269-1271.
290. B. Schwenzer, L. Wang, J. S. Swensen, A. B. Padmaperuma, G. Silverman, R. Korotkov and D. J. Gaspar, *Langmuir*, 2012, **28**, 10072-10081.
291. E. L. Crepaldi, G. J. d. A. A. Soler-Illia, D. Grosso, F. Cagnol, F. Ribot and C. Sanchez, *J Am Chem Soc*, 2003, **125**, 9770-9786.
292. D. Fattakhova-Rohlfing, M. Wark, T. Brezesinski, B. M. Smarsly and J. Rathousk ý, *Adv Fun Mater*, 2007, **17**, 123-132.
293. T. Ohno, M. Akiyoshi, T. Umebayashi, K. Asai, T. Mitsui and M. Matsumura, *Appl Catal A: Gen*, 2004, **265**, 115-121.
294. T. Umebayashi, T. Yamaki, H. Itoh and K. Asai, *Appl Phys Lett*, 2002, **81**, 454-456.

295. N. Sakai, A. Fujishima, T. Watanabe and K. Hashimoto, *J Phys Chem B*, 2001, **105**, 3023-3026.
296. J. Yu and X. Zhao, *Mater Res Bull*, 2001, **36**, 97-107.
297. K. Guan, *Surf Coat Tech*, 2005, **191**, 155-160.
298. J. Tang, Y. Wu, E. W. McFarland and G. D. Stucky, *Chem Commun*, 2004, **0**, 1670-1671.
299. X. Min, H. Li, W. Jian-Qiang, W. Ying, G. Ling, Z. Jian-hua and Z. Zhi-Gang, *Nanotechnology*, 2008, **19**, 185604.
300. G. J. d. A. A. Soler-Illia, C. Sanchez, B. Lebeau and J. Patarin, *Chem Rev*, 2002, **102**, 4093-4138.
301. C. Han, M. Pelaez, V. Likodimos, A. G. Kontos, P. Falaras, K. O'Shea and D. D. Dionysiou, *Appl Catal B: Environ*, 2011, **107**, 77-87.
302. H. U. Lee, S. C. Lee, S. H. Choi, B. Son, S. J. Lee, H. J. Kim and J. Lee, *Appl Catal B: Environ*, 2013, **129**, 106-113.
303. M. Jalalah, M. Faisal, H. Bouzid, A. A. Ismail and S. A. Al-Sayari, *Mater Res Bull*, 2013, **48**, 3351-3356.
304. J.-G. Yu, H.-G. Yu, B. Cheng, X.-J. Zhao, J. C. Yu and W.-K. Ho, *J Phys Chem B*, 2003, **107**, 13871-13879.
305. T. Ohno, T. Mitsui and M. Matsumura, *Chem Lett*, 2003, **32**, 364-365.
306. S. H. Ahn, H. Jeon, K. J. Son, H. Ahn, W.-G. Koh, D. Y. Ryu and J. H. Kim, *J Mater Chem*, 2011, **21**, 1772-1779.
307. Y. J. Kim, Y. H. Lee, M. H. Lee, H. J. Kim, J. H. Pan, G. I. Lim, Y. S. Choi, K. Kim, N.-G. Park, C. Lee and W. I. Lee, *Langmuir*, 2008, **24**, 13225-13230.
308. E. Lancelle-Beltran, P. Prené, C. Boscher, P. Belleville, P. Buvat and C. Sanchez, *Adv Mater*, 2006, **18**, 2579-2582.
309. H. J. Snaith and L. Schmidt-Mende, *Adv Mater*, 2007, **19**, 3187-3200.
310. E. Lancelle-Beltran, P. Prené, C. Boscher, P. Belleville, P. Buvat, S. Lambert, F. Guillet, C. Boissière, D. Grosso and C. Sanchez, *Chem Mater*, 2006, **18**, 6152-6156.
311. X. Li and F. Li, *Environ Sci Technol*, 2001, **35**, 2381-2387.
312. J. Choi, H. Park and M. R. Hoffmann, *J Phys Chem C*, 2009, **114**, 783-792.
313. M. Takeuchi, H. Yamashita, M. Matsuoka, M. Anpo, T. Hirao, N. Itoh and N. Iwamoto, *Catal Lett*, 2000, **67**, 135-137.
314. J. B. Varley, A. Janotti and C. G. Van de Walle, *Adv Mater*, 2011, **23**, 2343-2347.
315. A.-W. Xu, Y. Gao and H.-Q. Liu, *J Catal*, 2002, **207**, 151-157.
316. X. Lü, X. Mou, J. Wu, D. Zhang, L. Zhang, F. Huang, F. Xu and S. Huang, *Adv Fun Mater*, 2010, **20**, 509-515.
317. W. Guo, Y. Shen, G. Boschloo, A. Hagfeldt and T. Ma, *Electrochim Acta*, 2011, **56**, 4611-4617.
318. D. Grosso, G. J. de A. A. Soler-Illia, F. Babonneau, C. Sanchez, P. A. Albouy, A. Brunet-Bruneau and A. R. Balkenende, *Adv Mater*, 2001, **13**, 1085-1090.
319. M. Klotz, P.-A. Albouy, A. Ayral, C. Ménager, D. Grosso, A. Van der Lee, V. Cabuil, F. Babonneau and C. Guizard, *Chem Mater*, 2000, **12**, 1721-1728.
320. J. Yu, J. C. Yu, W. Ho and Z. Jiang, *New J Chem*, 2002, **26**, 607-613.
321. C. Longo, J. Freitas and M.-A. De Paoli, *J photoch Photobio A*, 2003, **159**, 33-39.
322. J. Weidmann, T. Dittrich, E. Konstantinova, I. Lauermann, I. Uhlendorf and F. Koch, *Sol Energ Mat Sol C*, 1999, **56**, 153-165.
323. S. S. Soni, M. J. Henderson, J.-F. Bardeau and A. Gibaud, *Adv Mater*, 2008, **20**, 1493-1498.

324. J. H. Yum, P. Chen, M. Grätzel and M. K. Nazeeruddin, *ChemSusChem*, 2008, **1**, 699-707.
325. K. J. Edler, M. J. Wasbrough, J. A. Holdaway and B. M. D. O'Driscoll, *Langmuir*, 2009, **25**, 4047-4055.
326. B. Yang and K. J. Edler, *Chem Mater*, 2009, **21**, 1221-1231.
327. B. Yang, J. A. Holdaway and K. J. Edler, *Langmuir*, 2013, DOI: 10.1021/la4001329.
328. T. A. G. Risbridger, F. A. Castro and P. J. Cameron, *J Phys Chem C*, 2012, **116**, 22253-22260.
329. I. Chung, B. Lee, J. He, R. P. Chang and M. G. Kanatzidis, *Nature*, 2012, **485**, 486-489.
330. G. Armstrong, A. R. Armstrong, P. G. Bruce, P. Reale and B. Scrosati, *Adv Mater*, 2006, **18**, 2597-2600.
331. H. Chakraborty and M. Sarkar, *Langmuir*, 2004, **20**, 3551-3558.
332. I. Chung, J.-H. Song, J. Im, J. Androulakis, C. D. Malliakas, H. Li, A. J. Freeman, J. T. Kenney and M. G. Kanatzidis, *J Am Chem Soc*, 2012, **134**, 8579-8587.
333. B. Yang, J. A. Holdaway and K. J. Edler, *Langmuir*, 2013, **29**, 4148-4158.
334. E. Zampetti, S. Pantalei, A. Muzyczuk, A. Bearzotti, F. De Cesare, C. Spinella and A. Macagnano, *Sensors Actuators B*, 2013, **176**, 390-398.
335. M. Fernández-García, X. Wang, C. Belver, J. C. Hanson and J. A. Rodriguez, *J Phys Chem C*, 2007, **111**, 674-682.
336. C. G. Göltner, B. Smarsly, B. Berton and M. Antonietti, *Chem. Mater.*, 2001, **13**, 1617-1624.
337. H. B. Wu, H. H. Hng and X. W. Lou, *Adv Mater*, 2012, **24**, 2567-2571.
338. Y. Zhou and M. Antonietti, *J. Am. Chem. Soc.*, 2003, **125**, 14960-14961.
339. D. M. Antonelli and J. Y. Ying, *Angew. Chem. Intl. Ed.*, 1995, **34**, 2014-2017.
340. V. Tomašić, I. Štefanić and N. Filipović-Vinceković, *Colloid Polym Sci*, 1999, **277**, 153-163.
341. B. D. Busbee, S. O. Obare and C. J. Murphy, *Adv Mater*, 2003, **15**, 414-416.
342. A. Gole and C. J. Murphy, *Chem Mater*, 2004, **16**, 3633-3640.
343. W. Baoxiang, R. Zbigniew, F. Jon Otto, D. K. Kenneth and Y. Yingda, *Nanotechnology*, 2012, **23**, 075706.
344. Z.-S. Wang, H. Kawauchi, T. Kashima and H. Arakawa, *Coord. Chem. Rev.*, 2004, **248**, 1381-1389.
345. K. J. Edler, T. Brennan, S. J. Roser, S. Mann and R. M. Richardson, *Micropor Mesopor Mat*, 2003, **62**, 165-175.